Chloride Ingress Into Submerged Concrete Under Sustained Load

By

Andrew Karam

A thesis

Presented to the University of Ottawa in partial fulfillment of the requirements for the degree of

Master of Applied Science in Civil Engineering

uOttawa

Department of Civil Engineering
University of Ottawa
Ottawa, Ontario, Canada
K1N 6N5

January 2014

Abstract

A harsh, cold, and icy environment is of no surprise to the conditions of a winter climate, where the wide use of de-icing salts on roads and highways allows for the initiation of chloride-induced corrosion of the reinforcement of concrete structures; a reduced service life, loss of structural integrity, visible damages, and ultimately structural failure are among the many unwanted effects of rebar corrosion. Chloride ingress into concrete has been extensively studied for the last four decades; however, most of the relevant research to date does not take into account the effects of sustained loading on chloride transport properties. Therefore, the objectives of this study were to investigate the influence of sustained compressive and tensile stresses on chloride ingress into concrete, and ultimately to understand what the effect of sustained stress is on chloride penetration depth, on chloride concentration by % weight of concrete, and on apparent diffusion coefficients by comparing results to those of unloaded control specimens.

To achieve these objectives, six post-tensioned and four non-reinforced control concrete beams were constructed with different water-to-cement (w/c) ratios and completely submerged in a 4-5% de-icing salt (NaCl) solution for 12 weeks, allowing chloride transfer to be completely governed by continuous diffusion. The effects of supplementary cementing material on chloride ingress are also studied. Concrete beams were post-tensioned to induce variable sustained compressive and tensile stresses along the beam. After 12 weeks of exposure, beams were fractured at specific locations and sprayed with a 0.1N silver nitrate ($AgNO_3$) solution to determine average penetration depths; chloride concentration profiles were obtained from potentiometric titration of grinded powder samples.

Apparent chloride diffusion coefficients were then obtained from the results of spraying $AgNO_3$ and titration, the latter by non-linear regression curve-fitting to Fick's second law of diffusion. A good agreement between results from both methods reveals that the use of $AgNO_3$ in field is acceptable in predicting the rate of chloride ingress in concrete sustaining stress. The chloride diffusivity for each profile, relative to that of the unstressed section, was related to the compressive and tensile stresses in the concrete section. The experimental results indicate the dependence of chloride ingress and concentration on the type and level of sustained stress. An analysis of the results to study the effects of the w/c ratio using colourimetric (silver nitrate spray) and potentiometric titration methods was also completed.

Acknowledgments

First and foremost, I would like to express my deepest gratitude to my thesis supervisor, Dr. Beatriz Martín-Pérez for her continued support, guidance, knowledge, inspiration, and financial support throughout the course of my studies and research. Her willingness to always make herself available through email and meetings, and her tremendously helpful suggestions allowed for a very pleasurable experience, and should not go unnoticed. Thank you for being such a down-to-earth and kind person, your efforts to help me advance in my career will not be forgotten.

I would like to thank *Harris Rebar* for providing post-tensioning tendons and anchors, *Sika® Canada* for providing industrial strength waterproof membranes, Michel Ross from *Sika® Canada* who helped me install said membrane, *Russel Metals Inc.* for the steel bearing plates, and Dr. Pouria Ghods from Carleton University for his help in lending profile grinding equipment.

I would like to acknowledge the Bank of Montréal (BMO), the Queen Elizabeth II Graduate Scholarship in Science and Technology (QEII GSST), and the University of Ottawa Admission Scholarship for their respectable financial support.

I would also like to thank all my friends, co-workers, students, and co-op students who generously helped me in the lab while performing chloride analysis and experiments. The help, guidance, and friendly advice from Muslim Majeed in the Structures Lab, Christine Séguin in the Environmental lab, and John Loop should not go unnoticed. Without all of you, I would not have been able to complete my experiments in a timely or accurate manner.

Finally, special thanks go out to my family and friends who have graciously supported me throughout my numerous years of study. Without their love, support, and encouragement I would not be where I am today, and would not have come this far. A very special thanks goes to my father, who helped me construct the plywood forms for this project; without him I would have no interest in construction or concrete.

Table of Contents

List of Tables

List of Figures

Notations

The following symbols are used in this thesis:

A	=gross cross-sectional area of concrete (mm^2)
A_C	=net cross-sectional area of concrete (mm^2)
A_{PR}	=change in area due to Poisson's ratio effects (mm^2)
A_T	=total change in cross-sectional area of concrete (mm^2)
C (x,t)	=total chlorides at depth x at time t (kg/m^3)
Cl (%)	=total chlorides by % weight of concrete (%)
C_O	=initial chloride concentration in concrete (%)
C_S	=chloride concentration at the surface x=0 (%)
D	=diffusion coefficient (m^2/s)
D_{app}	=apparent diffusion coefficient (m^2/s)
D_i & D_o	=apparent diffusion coefficients for section *i*(stressed) and *o*(untresse), respectively (m^2/s)
D_{ref}	=reference diffusion coefficient (m^2/s)
$e_{(x)}$	=eccentricity of the tendon at abscise *x*
E_C	=elastic modulus of concrete (MPa)
erf	=error function
F	=Faraday's constant (9.6548×10^4 J/Vmol)
f'c	=cylinder compressive strength of concrete (MPa)
f'r	=modulus of rupture (MPa)
f't	=cylinder tensile splitting strength of concrete (MPa)
h	=height of cross-section (mm)
$I_{(x)}$	=gross moment of inertia at distance x
Ig	= gross moment of inertia of uncracked section (mm^4)
k	=permeability coefficient
N	=exact normality of 0.05N $AgNO_3$ solution
n	=porosity
P	=load to cause the specific loading stress needed (N)
q	=mass transport rate, or the flux of chloride ions ($kg/m^2 \cdot s$)
R	=universal gas constant (8.314 J/molK)

t	=time of exposure (days)
T	=absolute temperature (°C)
U	=potential difference across samples (V)
V_1	= volume of consumed 0.05N $AgNO_3$ at the equivalence point for concrete sample titration (mL)
V_2	=volume of consumed 0.05N $AgNO_3$ at the equivalence point for blank titration (mL)
W	=mass of concrete sample (g)
w/c	=water-to-cement ratio
x	=depth or distance from exposed surface (mm)
x_i	=penetration depth of stressed section (cm)
x_o	=penetration depth of unstressed section (cm)
z	=electrical charge (ionic valence) of diffusing ions
γ_c	= density of concrete (kg/m^3)
ε	=strain (mm/mm)
ε_x & ε_y	=transverse and axial strains, respectively (mm/mm)
μ_e	=elastic Poisson's ratio
$\sigma_{c,t}(x,h)$	=compressive and tensile stresses induced by post-tensioning (MPa)

Chapter 1 - Introduction

1.1 Background

The effect of chloride-induced reinforcement corrosion on concrete structures is a major issue plaguing concrete infrastructure around the world. In Canada, billions of dollars are spent annually on the upkeep, maintenance, and repair of reinforced concrete (RC) structures that have been deteriorated by corrosion (Schweitzer, 2009). Despite being more durable than steel and timber structures, RC and prestressed (PS) concrete structures are more vulnerable to the unwanted effects of corrosion caused by chloride ingress from de-icing salts or seawater. Rebar corrosion can also result from carbonation of the concrete cover, the interaction of carbon dioxide gas with concrete; this is a slower and less relevant process that will not be discussed in this research. In Canada, the main cause of rebar degradation and overall loss of structural integrity of RC and PS concrete structures is from the regular use of de-icing salts (Environment Canada, 2006). De-icing salts are widely used on highway decks and roads and can be transported to other RC structures such as parking garages by motor vehicles.

The corrosion of steel reinforcement leads to deterioration of the structure with very visible signs that may include: concrete fracture, cracking, water leakage, salt staining (rust), delamination, spalling and loss of cover, and reduction of concrete section among other visible signs. Loss of concrete cross section and steel due to corrosion has a huge impact on the integrity of the structure and overall section capacity, strength, and ductility. As a result, the safety, serviceability, and service life of the structure is greatly reduced. Although very rare, failure can occur if the reduction in flexural and shear capacity becomes lower than the required safe and serviceable load capacity. One of the most visible and unavoidable sign that is most important to the initiation of corrosion and deterioration of RC is cracking. Permeability is also an important property because it significantly affects the ability of the concrete to prevent corrosion of reinforcement; average ISAT intrinsic permeability values for concrete range from $1x10^{-17}$ to $1x10^{-18}$ m^2, depending on the w/c ratio of the concrete (Claisse, Ganjian, & Adham, 2003). Along with how porous the concrete is, cracking is one of the main factors that affects the rate of chloride ion penetration and reduces the initiation time of rebar corrosion.

Although, when concrete is properly placed, compacted, cured, and is uncracked it becomes almost impermeable, although not waterproof. The appearance of cracks in concrete causes it to become vulnerable to the processes of reinforcement corrosion by allowing the chloride ions to reach the rebar substantially quicker than uncracked concrete. However, the purpose of this research focuses on the factors that affect the apparent diffusion coefficient (D_{app}) in stressed uncracked concrete. Past research has focused on the determination of chloride penetration rates and diffusion coefficients on unloaded concrete specimen; however, new research on concrete specimens loaded in compression, tension, shear, or flexure is required to accurately simulate and model chloride ingress in real world conditions.

1.2 Causes and Mechanisms of Corrosion

As mentioned above, the main cause of steel rebar corrosion in RC is the chloride attack mainly from chlorides in de-icing salts, but can also come from other sources. Chlorides can be incorporated into the concrete mix by contaminated 'salty' ingredients such as seawater, or can penetrate into the hardened concrete from harsh surrounding saline environments. Concrete as a building material is alkaline in nature and produces a self sustaining passive layer of protective oxide on the steel surface which reduces the corrosion rate to a minimum level (Broomfield, 2007). Cloride ions act to break down this passive layer and act as a catalyst for the corrosion process. There are many mechanisms that govern the chloride penetration rate into concrete such as suction, porosity, capilliary action, and diffusion. This rate can also be affected by factors such as: cracking, crack location and orientation, and loading.

Chloride ions are able to penetrate deep into the concrete cover and reach the reinforcing steel due to the fact that concrete is a porous material. Using different cement pastes or adding mineral admixtures to the concrete allow for a less porous concrete and act to lessen the chloride permeablility. Figure 1.1 shows the ingress of chloride ions into concrete and their effects on the deterioration and corrosion of the reinforced concrete section.

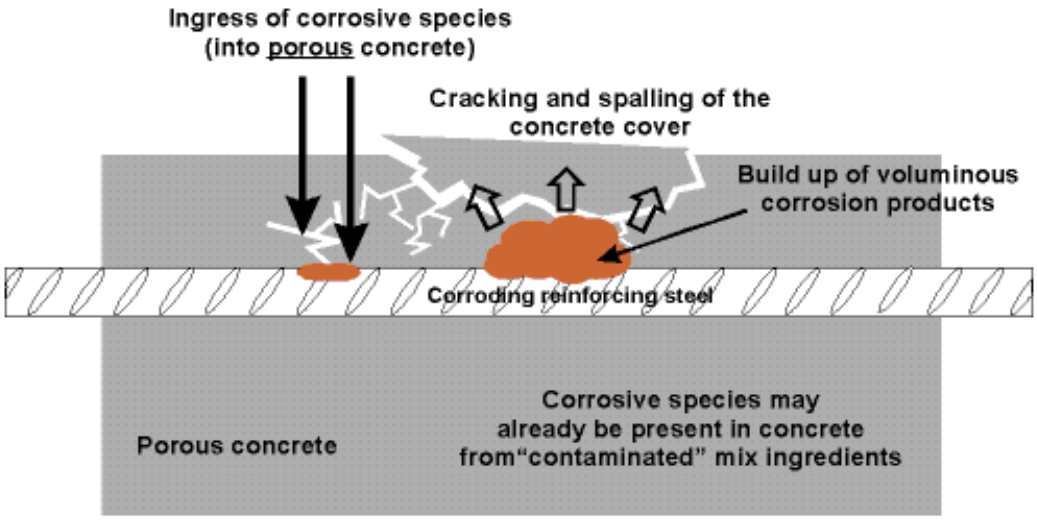

Figure 1.1: Corrosion damage mechanism and deterioration of RC (Tullmin, 2002)

Rebar deterioration can cause many visibly unwanted effects as well as compromising the structural integrity of the section that is corroded, which can lead to failure and reduced service life of the structure. Service life can be defined as the period of time during which a structure meets or exceeds the minimum requirements it was designed for; which can be limited by technical, functional, or economical reasons (Nagi & Kilgour, 2008). Technical requirements are related to the structural integrity and ability of the structure to withstand service loads during its service life; corrosion plays the biggest role in limiting the technical service life of a structure (Nagi & Kilgour, 2008). Service life models developed over the years, such as the model developed by Tutti (1982), frequently divide the mechanism of corrosion into an initiation period and a propagation period. The initiation period is the time from initial exposure to chlorides until adequate chloride contamination has accrued (the threshold concentration); the onset of corrosion occurs once the chloride threshold at the level of reinforcing steel has been reached, upon which the propagation period begins. Figure 1.2 illustrates this idealized model and the stages that define each period of contamination, ultimately leading to structural collapse and failure if no repairs or precautions are taken during the propagation period.

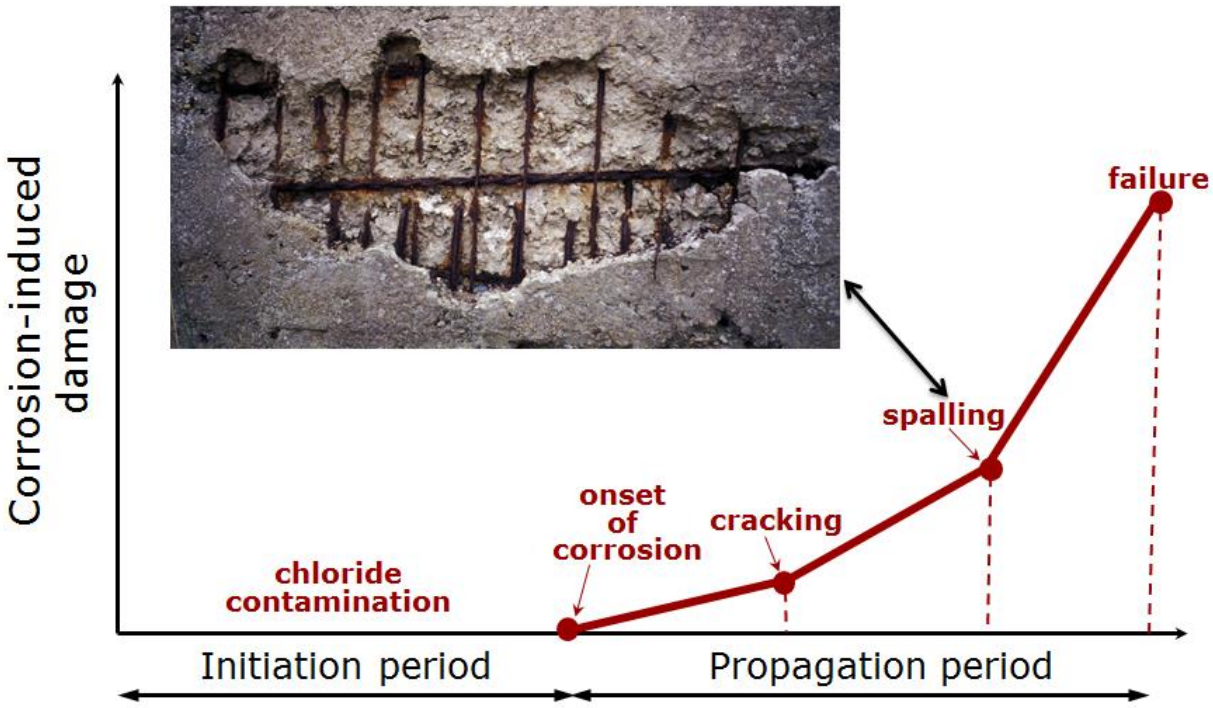

Figure 1.2: Idealized two-stage mechanism of corrosion over time

The duration of the initiation period can be influenced by factors such as: thickness and quality of concrete cover, surface chloride concentration, extent and size of cracks in concrete, rate of chloride ingress (D_{app}), and the chloride threshold. To date, the chloride threshold level has not been accurately quantified, it depends on various factors in the concrete; no accepted standardized procedure exists for the determination of said threshold level (Angst, Vennesland, Elsener, & Larsen, 2009). If diffusion is the main mechanism of chloride ingress, then the estimated time for corrosion initiation and the duration of the initiation period can be calculated using Fick's 2nd law of diffusion; which in turn will allow for the apparent diffusion coefficient to be found.

1.3 Objectives and Scope of Research

Corrosion is usually idealized as a two stage process; in service life modelling of reinforcement corrosion, the modelling of the initiation stage corresponding to chloride ingress is always done neglecting the actual loads a structure is carrying. To accurately predict and model the chloride ingress into real world structures under services conditions, the effects of external loads on the chloride transport in concrete should be considered (Wang, Lu, Jin, & Bai, 2011). The work presented in this thesis aims at better understanding chloride ingress in concrete sustaining loads and at how to model and prolong this initiation phase of rebar corrosion in RC and PS concrete structures. This is accomplished by using experimentally collected chloride content data from concrete samples under different stress levels and analyzing the data to develop a relationship between the apparent chloride diffusion coefficient and sustained compressive and tensile stresses.

The research presented here investigates the influence of sustained compressive and tensile stresses on chloride ingress and transfer properties into concrete; it applies and takes into consideration past experiences and suggestions from similar experiments done by Dr. Bruno Cousin of the Université Montpellier, France. It seeks to understand what the effect of sustained stress is on chloride penetration depth, on chloride concentration by % weight of concrete, and on apparent diffusion coefficients by comparing results to those of unloaded control specimens. To achieve this objective, six post-tensioned and four non-reinforced control concrete beams were constructed with different water-to-cement (w/c) ratios and exposed to a de-icing salt (NaCl) solution for 12 weeks. The beams were specifically designed with a tapered cross section and an eccentric post-tensioning tendon to allow for variation in compressive and tensile stresses along each beam. After the three-month period of exposure, each beam was fractured at various cross sections and analyzed for chloride content by spraying silver nitrate to determine average penetration depths, and by conducting potentiometric titrations on extracted concrete powder to determine chloride concentrations.

1.4 Outline of Thesis

Chapter 2 presents the review and synthesis of relevant literature on the topic of chloride ingress into loaded and unloaded concrete, as well as a minor review of the behaviour and transport properties of chlorides in cracked concrete. The review focuses on newly published experimental studies that deal with the effect of sustained compressive, tensile, and flexural stress on concrete and its effect on chloride transport properties.

Chapter 3 presents the experimental program designed to specifically produce results that are directly related to the scope of the research. It includes a detailed description of each concrete beam that was constructed, the materials used, and the casting and curing regime. Details of the equipment used and experimental procedures are described, along with data collection of the chloride ingress and concentration.

Chapter 4 presents the collected data from the experimental program along with a detailed description and discussion of the pertinent trends that were observed. Chapter 5 seeks to analyze and assess chloride ingress properties and trends by means of chloride ingress modelling.

Finally, major conclusions and notable trends with respect to the effect of sustained stress on chloride ingress into concrete are listed in Chapter 6. Recommendations for future work are given as well; how to improve the accuracy of the results obtained from this research by improving experimental fault.

Chapter 2 – Literature Review

2.1 Chloride Transport Mechanisms

In order to accurately predict the durability of concrete, it is important to understand the many different transport mechanisms that govern the ingress of chlorides into concrete. Concrete by nature is a porous heterogeneous material that allows fluids, ions, or gases to move through its microstructure by means of cracks, microcracks, pores and voids, and defects in the concrete. Limiting the movement of these fluids is one of the main functions that a durable RC structure must provide throughout its service life.

Several laboratory tests and in-situ inspections have shown that the chlorides incorporated into the concrete mix that were once thought to be bound, insoluble, and harmless have an effect on the total amount of chlorides present (Buckley, Carter, Wilson, & Scantlebury, 2007). These chlorides are released by the carbonation and leaching of fluids and contribute to the total chloride content limit; the threshold concentration that leads to corrosion of reinforcement (Poulsen & Mejlbro, 2006). Concrete design codes around the world have now taken this information into consideration; CSA A23.1-04 specifies that the amount of water-soluble chlorides from mix ingredients is limited to 0.015% and 0.06% by mass of cementing material for RC and PS, respectively.

Some of the different transport mechanisms of chlorides into uncracked concrete as described by Poulsen & Mejlbro (2006) and Otieno et al. (2010) include:

2.1.1 Diffusion

Diffusion is the process driven by a difference in the concentration of chloride ions in various zones, the influence of a concentration gradient. Chlorides will always move from an area of high concentration to an area of low concentration until equilibrium is reached, provided that the concrete is fully or partially saturated. Diffusion is often regarded as the main transport mechanism governing chloride ingress into concrete (Poulsen & Mejlbro, 2006). In combination with other mechanisms, diffusion contributes to chloride transport in concrete under most exposure conditions. Diffusion is also responsible for the transport of oxygen in concrete to the steel surface, allowing the initiation of corrosion. The rate of diffusion of oxygen is determined by the pore structure and size distribution in the concrete as well as the moisture content (Richardson, 2002).

For steady-state scenarios, the modelling of gaseous or ionic diffusion in concrete is well described by Fick's 1st law of diffusion (Eq. 2.1), which states that the chloride flux q is proportional to the concentration gradient. The negative prefix means that diffusion occurs opposite to the concentration gradient. However, the assumptions made in Fick's 1st law are generally not representative of the real mechanism of diffusion; these assumptions include a steady-state regime, pure diffusion, and an isotropic medium.

For non-steady state scenarios, the modelling of ionic diffusion in concrete is done using Fick's 2nd law of diffusion (Eq. 2.2); it states that for a semi-infinite homogeneous medium the rate of change of concentration with respect to time and spatial position is proportional to the concentration gradient. Figure 2.1 shows a visual representation of Fick's 2nd law of diffusion.

$$q = -D\frac{\partial C}{\partial x} \tag{2.1}$$

$$\frac{\partial C}{\partial t} = \frac{\partial}{\partial x}\left(D\frac{\partial C}{\partial x}\right) \tag{2.2}$$

where q = mass transport rate, or the flux of chloride ions (kg/m^2·s)

D = diffusion coefficient (m^2/s)

$\partial C/\partial x$ = concentration gradient (kg/m^3/m)

C = Concentration of fluid (ion or gas) (kg/m^3)

x = depth or distance from exposure surface (m)

t = time of exposure (s)

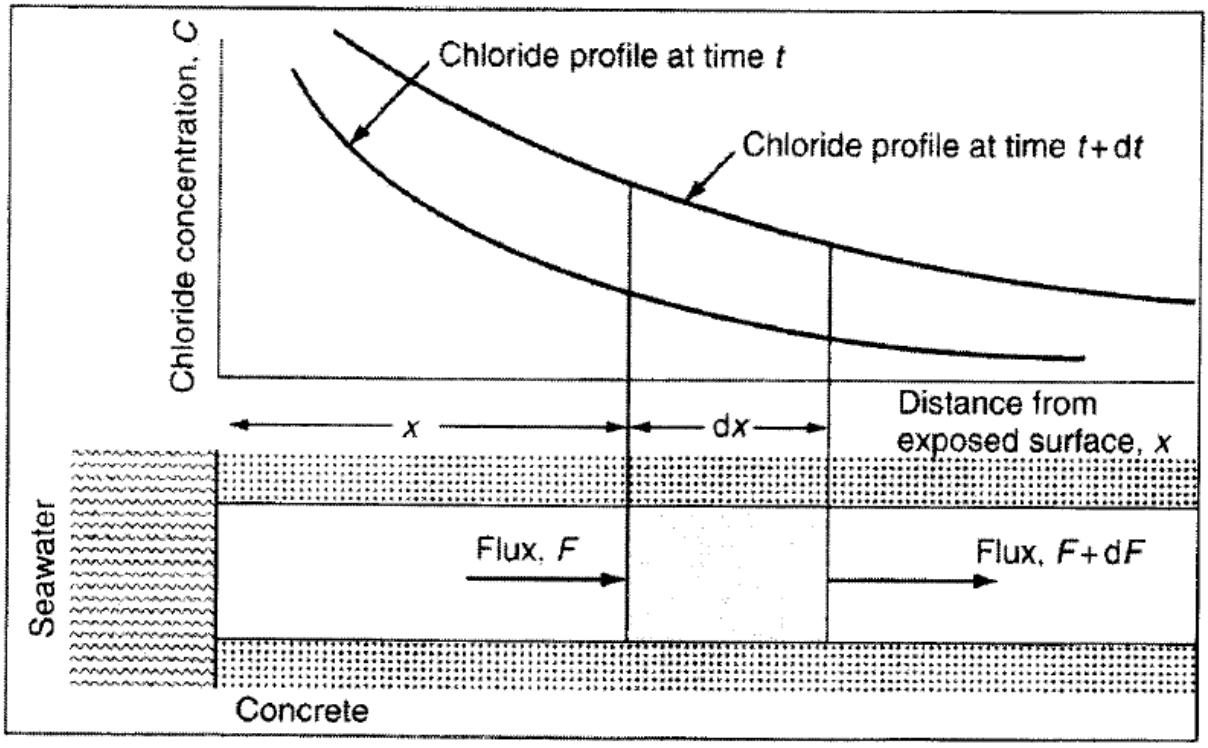

Figure 2.1: Fick's 2nd law of diffusion expresses that the change in chloride concentration per unit time is equal to the change of flux per unit length (Poulsen & Mejlbro, 2006)

To model pure diffusion in submerged concrete, a closed form analytical solution to Fick's 2nd law given specific initial and boundary conditions was developed by Crank (1975). It is one of the most widely used equations to model pure diffusion in concrete; an in-depth explanation of Crank's error function solution can be seen in Section 2.4 of this chapter.

2.1.2 Permeation

Permeation is the process driven by a difference in the hydraulic pressure externally applied to fully saturated concrete in various zones and depths. Chlorides will always move through pore spaces, cracks, and defects in the concrete; from higher hydraulic pressure zones to lower hydraulic pressure zones (pressure gradient). Permeation is an important transfer parameter to consider when designing water retaining concrete structures such as retaining walls or holding tanks, where fluid seepage can be detrimental or catastrophic. D'Arcy's law can be used to calculate the average velocity of fluid flow in the concrete:

$$\bar{v} = \left(\frac{k}{n}\right)\left(-\frac{dh}{dx}\right) \tag{2.3}$$

where k = permeability coefficient

n = porosity

h = hydraulic head

x = distance

2.1.3 Migration

Migration is the process driven by a difference in electrical potential between two points, also known as electro-migration, electro-diffusion, or accelerated diffusion. Chlorides will always move from areas of high electric potential to areas of low electric potential. Migration of chlorides may occur when subjected to stray electric fields such as in subway tunnels, or can be artificially induced in laboratory-accelerated chloride tests. In laboratory tests, migration and diffusion may occur simultaneously, however migration accounts for the majority of the flux of chlorides. The Nernst-Planck equation is used to determine the velocity of chloride ion transfer in accelerated chloride tests:

$$v = \left(D\frac{zF}{RT}\right)\left(\frac{dU}{dx}\right) \tag{2.4}$$

where v = velocity of the ionic species

D = diffusion coefficient of the ionic species

z = electrical charge (ionic valence) of diffusing ions

F = Faraday's constant (9.6548 x 10^4 J/Vmol)

T = absolute temperature

U = potential difference across the sample

x = distance variable

R = universal gas constant (8.314 J/molK)

2.1.4 Convection

Convection is the process driven by a difference in moisture content. If all other parameters are kept constant, water contaminated with chlorides (or any solute) will always move from a high moisture content zone to a lower one. Convection occurs at a much faster pace than pure diffusion, as chloride ions move with the water flow (Deif, 2010). The process can be mathematically described by:

$$\frac{\partial C}{\partial t} = -\bar{v}\frac{\partial^2 C}{\partial x^2} \quad (2.5)$$

where C = concentration of solute at depth x at time t

$\bar{v}$ = average velocity vector of fluid flow

The capillary absorption of chlorides due to convection has an important role in the movement of chloride ions, particularly when concrete is subjected to wetting and drying cycles. Wick action, a special case that may occur during a wetting and drying cycle, is the transport of chlorides from a concrete surface that is exposed to a water/salt solution to a drying face. The pore liquid of the concrete moves towards a surface exposed to evaporation, resulting in an accumulation of chlorides near the drying face of the concrete.

2.1.5 Combined Transport Mechanisms

In reality, the chloride ion transport mechanisms described above do not act in isolation; more than one mechanism may be active at any given time, either in similar or different sections along the flow path of the concrete. To act alone would be an over-simplification of what occurs in exposed concrete, where wetting and drying cycles are common (Otieno, Alexander, & Beushausen, 2010). However, pure diffusion (along with permeation as a minor secondary transport mechanism) can be obtained when concrete is fully submerged in a saline/chloride solution for its entire service lifetime (Kim & Stewart, 2000). Knowing this, pure diffusion can easily be recreated in laboratory environments to determine the rate of chloride ingress into concrete. Despite the fact that the diffusion equation is only applicable to saturated concrete, Fick's 2nd law has been applied to evaluate the rate of chloride ingress during combined chloride transport and/or predict the penetration of chloride in long-term exposure (Bioubakhsh, 2011). Hence, an apparent diffusion coefficient (D_{app}) is used in Crank's error function solution to take into consideration all these assumptions.

Currently, research on combined transport mechanisms has not been without challenges. New models and testing methods need to be developed to predict and asses the simultaneous movement of the particles that occur during mixed modes of transport. Combined transport properties are usually physically quantified by considering chloride penetration profiles that show the distribution of chlorides with depth from the concrete surface during different times of exposure (Otieno, Alexander, & Beushausen, 2010).

2.2 Effect of External Loading on Chloride Transport

Chloride ingress into concrete has been extensively studied for the last four decades; however, most of the relevant research to date does not take into account the effects of sustained loading on chloride transport properties. New and prominent research by Wang et al. (2011) and Deif (2010) aims to understand how the transport mechanisms explained in the previous section are affected by external loading and induced stresses. External loading can alter the microstructure of the cover concrete by inducing crack formation along the paste-aggregate interface, causing microcracking formation and propagation, or by the opening or closing of pores based on the type of loading. These effects, coupled with exposure to an aggressive chloride-filled environment, aid in the acceleration of chloride ion transport and subsequently corrosion initiation. Previous attempts have been made to establish an accurate relationship between chloride transport and the applied stress; results have been conflicting as reported in the literature (Wang, Lu, Jin, & Bai, 2011), which establishes a need for more data and experimental results to validate this relationship.

Some of these conflicting views on the effect of external loading and stress on concrete permeability and transport properties can be summarized as follows:

- The chloride transport rate, in terms of the rapid chloride permeability test (RCPT), increased with an increase in compressive stress; stress levels below that of 75% of the compressive strength had an insignificant effect on the RCPT results (Samaha & Hover, 1992).
- The chloride transport rate, in terms of the RCPT, was almost identical between the unloaded control specimen and that of concrete that was subjected to 90% of its compressive strength (Saito & Ishimori, 1995).
- The D_{app} was found to be around 40% higher in beams sustaining higher flexural stress than that of unloaded prestressed beams (Cousin & Martin-Perez, 2010).
- The D_{app}, under sustained flexural load, is relatively higher in the tension zone than that in the compression zone. With an increase in stress level, the chloride D_{app} decreases in the compression zone, and marginally increases in the tension zone (Gowripalan, Sirivivatnanon, & Lim, 2000).

These discrepancies in chloride diffusivity and transport rate can be attributed to the many different experimental methods and approaches used by each researcher. For example, the

concrete cylinders in the studies carried out by Saito & Ishimori (1995) and Samaha & Hover (1992) were subjected to uniaxial compression and then unloaded before the RCPT. A major limitation in this approach is that once concrete has been unloaded the characteristics of the microcracks present in the concrete change (Wang, Lu, Jin, & Bai, 2011). Depending on the compressive stress level applied, microcracks present can partially or completely close up upon unloading. However, if the loading applied causes enough residual strain to develop in the concrete, then crack recovery after unloading of the specimen will not occur; the inconsistent values obtained can be attributed to this phenomenon. Also, the permeability of concrete increases with the increase of residual strains (Saito & Ishimori, 1995); this suggests that chloride ingress into concrete structures is indeed influenced by the type of loading whether sustained or removed.

According to the results obtained from Gowripalan et al. (2000), compressive and tensile stresses (induced by flexural loading) have noticeably different effects on the chloride transport mechanisms. Compressive stresses hinder chloride diffusion by the reduction of porosity in the concrete, while tensile stresses allow an easier and hindrance free diffusion process that can be attributed to the damage caused by flexural loading at the aggregate-paste interface. Again, the minor discrepancies between the results obtained in the experiments done by Cousin & Martin-Perez (2010) and Gowripalan et al. (2000) can be attributed to the difference in the concrete beam specimens tested, exposure conditions, and experimental methods; generally, results from both experiments conclude that an increase in tensile stress causes higher chloride penetration depths. Table 2.1 shows the average chloride front depth on the tensile side of each beam section for different loading levels for the experiment done by Cousin & Martin-Perez (2010). Diffusion is a time-dependant phenomenon, therefore as time progresses, chlorides will continue to penetrate and diffuse deeper into the prestressed beam. After one week of exposure the results are scattered, but after three weeks a general trend of an increase in penetration depth with increased load can be observed. However, in addition to diffusion being time-dependant, this may be due to the fact that the applied flexural load de-compressed the beam that was initially presetressed, opening up pores; further experiments are needed to confirm a more precise relation.

Table 2.1: Depth of the chloride penetration front for prestressed beams subjected to flexural loading, tension side (Cousin & Martin-Perez, 2010)

Load (kN)	Section	Depth at 1 week		Depth at 3 weeks	
		average	Standard deviation	average	Standard deviation
0	1	10.5	1.0	12.2	2.3
	2	10.0	0.9	7.9	1.6
	3	11.5	1.0	11.9	1.1
	4	5.0	2.3	13.2	1.5
	5	9.5	0.7	13.0	1.0
3	1	8.8	0.3	20.3	2.5
	2	8.4	0.8	12.5	1.0
	3	9.2	1.2	14.0	2.4
	4	-	-	13.9	1.4
	5	8.6	2.2	14.8	2.2
5	1	7.9	1.0	15.2	2.4
	2	8.2	1.4	14.7	1.5
	3	-	-	15.4	1.2
	4	9.1	0.9	14.0	1.4
	5	12.6	1.4	14.7	1.4
7	1	7.0	1.6	13.4	2.0
	2	5.7	1.0	13.9	2.0
	3	7.6	1.8	15.9	1.3
	4	8.1	1.2	14.5	1.6
	5	7.4	0.8	13.3	1.9

A recent study done by Wang et al. (2011) seeks to add more experimental data to further validate the relationship and influence of stress on chloride ingress; the investigation was done on concrete sustaining compressive and flexural loads exposed to a 5% accelerated salt fog chamber for two months. Under service conditions, concrete structures may be subjected to various loading conditions where compressive and flexural loading play different roles; therefore, the study of these loading conditions is crucial to the understanding of chloride transport in real concrete structures (Wang, Lu, Jin, & Bai, 2011). Table 2.2 shows the details of the specimens that were used in the experiment, where series A sustained compressive loads by means of post-tensioning, series B sustained flexural loads by means of four-point bending, and series C was used as an unloaded control series. Parameter λ_σ in Table 2.2 is a stress level index that is a ratio between the applied stress and the strength of the concrete.

Table 2.2: Stresses in concrete series A (compressive) and series B (flexural) (Wang, Lu, Jin, & Bai, 2011)

Specimen	W/C ratio	f_c (MPa)	σ_c (MPa)	λ_σ
A41	0.4	28.50	6.27	0.220
A42	0.4	28.50	10.45	0.367
A43	0.4	28.50	14.64	0.514
A51	0.5	21.70	4.79	0.221
A52	0.5	21.70	7.98	0.368
A53	0.5	21.70	11.18	0.515
Specimen	W/C ratio	f_t (MPa)	σ_t (MPa)	λ_σ
B41	0.4	2.58	0.576	0.223
B42	0.4	2.58	1.036	0.402
B43	0.4	2.58	1.290	0.500
B51	0.5	2.14	0.667	0.312
B52	0.5	2.14	1.015	0.474
B53	0.5	2.14	1.291	0.603

Chloride concentration results can be seen in Figure 2.2. It can be seen that stress applied to the concrete does indeed have a significant effect on the chloride transport properties. For series A, an increase in compressive stress caused a decrease in concentration at a given depth, especially for concretes with a higher w/c. Again, this may be attributed to the effect of compression on the

closure of microcracks and pores in the concrete. For series B, an increase in flexural stress caused a rapid increase in concentration at a given depth, especially for concretes with a higher w/c. Also, the control series C was always lower than series B at any given depth. Under flexural stress the microcracks in the interfacial transition zone between aggregates and the cement paste open and become unstable causing an increase in the connectivity of pores in concrete and accelerating the diffusion process (Mehta & Monteiro, 2006). These findings are similar to those of Gowripalan et al. (2000) and Lim et al. (2000). Also, the D_{app} showed very similar trends as the chloride concentration profiles for each series of specimens, with a 10% reduction under compression and a 16% increase under flexural loads (w/c =0.5). A linear relationship was found between the apparent diffusion coefficient and compressive/flexural stress.

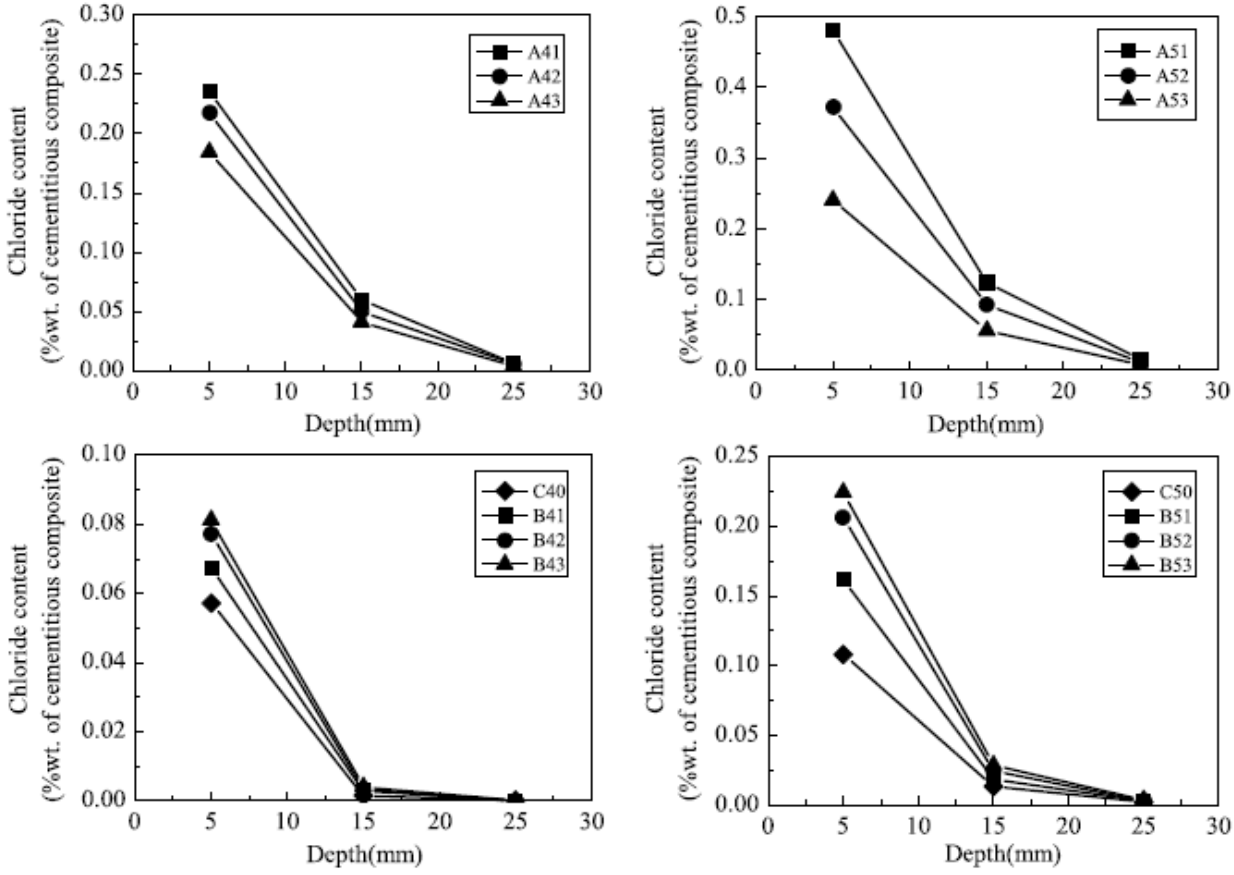

Figure 2.2: Chloride profiles for Series A (0.4 w/c upper left; 0.5 w/c upper right) and Series B &C (0.4 w/c bottom left; 0.5 w/c bottom right) (Wang, Lu, Jin, & Bai, 2011)

Currently, there is no established chloride transport model that includes the effects of different sustained loading conditions. A preliminary model was created on the basis of the study completed by Wang et al. (2011), which seeks to build upon models that have already been developed. Factors

such as: concrete age, temperature, relative humidity, D_{app} dependency on chloride concentration, and external load can be seen in the model. It was found that the model correlates well with the experimental D_{app} values. A more detailed look at this model will be seen in Section 2.4 of this chapter.

Some of the important conclusions made by Wang et al. (2011) include:

- Under sustained compressive stresses, the chloride concentration decreases with an increase of compressive stress up to 55% of the compressive strength.
- Under sustained flexural stress, the chloride concentration increases rapidly with the increase in flexural stress.
- Similarly to the chloride concentration profiles, the D_{app} decreases with the increase of compressive stress and increases with the increase of flexural stress.
- A successful preliminary empirical model was developed to predict the chloride diffusion process under different loading conditions and factors.

The conclusions made from the preceding studies suggest that when chloride ingress models are used to predict the service life of concrete structures, the stress state of the service structure should be taken into account; the transport parameters from in-situ structures under service conditions are more desirable than those from the laboratory (Wang, Lu, Jin, & Bai, 2011).

2.2.1 Effects of Sustained In-Service Loads

Bridge decks and parking garages are examples of common concrete structures that are very susceptible to the effects of chloride-induced corrosion of reinforcing steel. In Canada, the regular de-icing, wetting and drying cycles, and freezing and thawing cycles that these structures are subjected to have detrimental effects on concrete durability, and in turn the service life of the structure. A recent study done by Deif (2010) establishes a relationship between the rate of chloride ingress in concrete and the strains induced in the concrete deck under sustained in-service loads. The experiment simulated a small-scale bridge deck split into three different strips, each with a different w/c ratio. The deck was subjected to three wetting and drying cycles of chlorides, where each RC strip was simply supported and loaded to create both positive and negative bending moment regions in the slab. Figure 2.3 shows the strain gauges and loading conditions, while Figure 2.4 shows the sustained moment and shear forces that each slab was subjected to. Section (0) refers to the unloaded control section, while sections (2), (4), (7), and (8) are subjected to bending

moments of 12.5kN·m, 25.0kN·m, -25.0kN·m, and -12.5kN·m, respectively. It is also important to note that section (7) was cracked in all three strips; the negative moment indicates compression at the bottom of the slab, resulting in the tension face being subjected to chlorides.

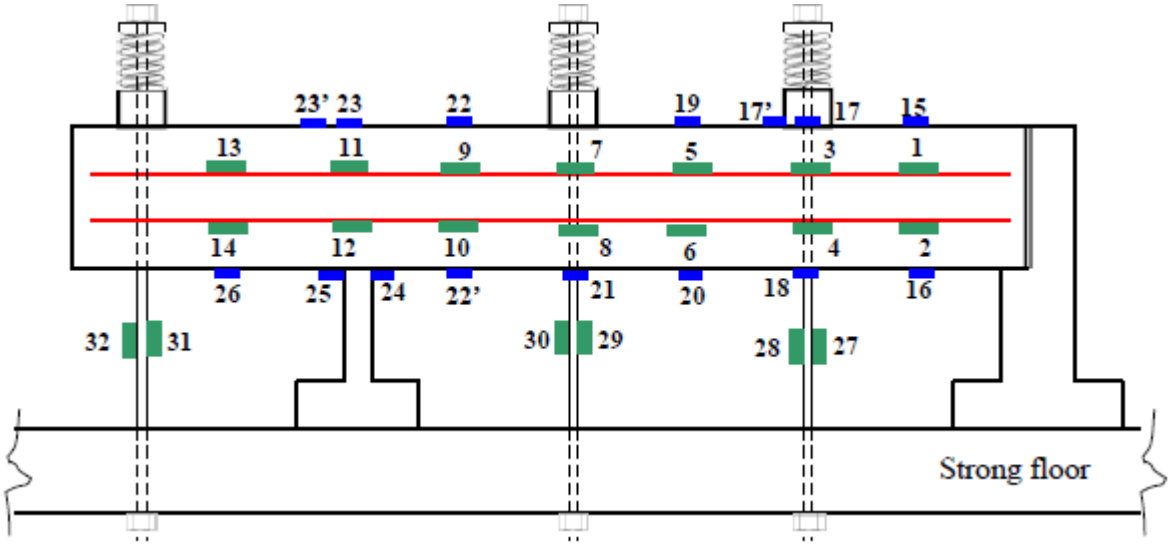

Figure 2.3: Location of strain gauges and loading cells (Deif, 2010)

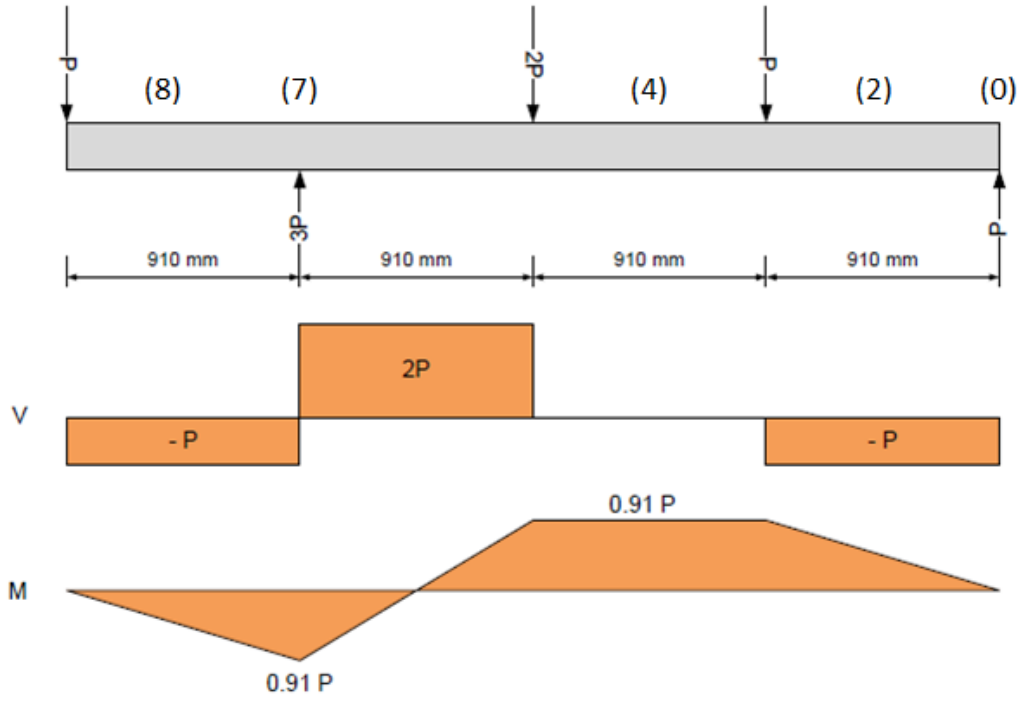

Figure 2.4: Moment and shear diagrams for applied load on RC slab (P = 27.5kN) (Deif, 2010)

Some of the important conclusions made by Deif (2010) that can be incorporated into the data bank of knowledge in the field of chloride ingress into concrete sustaining mechanical loads include:

- Chloride transport into concrete for this study was assumed to comply with Fick's 2nd law of pure diffusion; however, according to the results the diffusion in concrete containing cracks (section 7) does not follow Fick's 2nd law.
- The D_{app} is affected by the stress level and whether the exposed concrete surface is subjected to compressive, tensile, shear, or a combination of stresses. The highest diffusion coefficients were found in the cracked tension zones, uncracked tension zones second highest, and compression zones lowest.
- The D_{app} decreases with increasing time of exposure with respect to both sets of results obtained from spraying silver nitrate on fresh concrete cores and titrating concrete powder samples.
- The D_{app} decreases with lower w/c ratio with respect to both sets of results from the silver nitrate spraying and titration.
- With the exception of section (7), there were good agreements between the results from the silver nitrate spraying and titration methods with respect to relative diffusivity between loaded and unloaded sections (Eq. 2.8 in Section 2.4 of this chapter). This relationship revealed that spraying silver nitrate can be used to estimate the diffusion coefficient for a particular concrete during a specific estimated amount of time; this method can only be used if the concrete is exposed to chlorides for at least one year.
- There were also good agreements between the results from the silver nitrate spraying and titration methods with respect to the relation of diffusivity and bending moment ratios (D/D_o and M/M_{cr}). Higher diffusivity ratios between stressed and unstressed D_{app} corresponded to sections under tension, while lower ratios were found for sections subjected to pure compression. The combination of shear and compressive stresses caused the ratio to increase from that of pure compression.
- The chloride penetration rate increases with concrete microcracking, which can be seen in core samples from section (8) that were uncracked under tension.

Future considerations on chloride ingress research could include the effects of different aggregate sizes, types, and shapes; chloride ingress into masonry structures; effects of splashing and runoff;

structures under pure shear stress; and continuous studies (longer than three years) on projects outside the laboratory in the real world (Deif, 2010).

2.2.2 Effects of Microcracking

Microcracks can be present in concrete due external and internal factors such as: shrinkage, bleeding, thermal gradients, freezing and thawing cycles, alkali-aggregate reactions, sulphate attack, external loading, and the general interaction of concrete with its surrounding environment. Under an applied stress, microcracks that originally existed in the concrete after being casted (plastic shrinkage) and exposed to the environment may propagate and produce an interconnected series of pathways for chlorides to flow (Lim, Gowripalan, & Sirivivatnanon, 2000). These load-induced microcracks add to the randomly sized, arranged, and connected pore system that already exists in concrete; the microcracks occur mainly at the paste-aggregate interface and can extend into the mortar as higher stresses are applied (Samaha & Hover, 1992). Figure 2.5 shows a sketch of the different types of microcracking that can occur in concrete based on the abovementioned internal and external factors. The effect of microcracking on the transport properties of concrete, whether induced by compressive, tensile, or shrinkage stresses, is an important parameter that has been gaining more and more research significance and should not be overlooked.

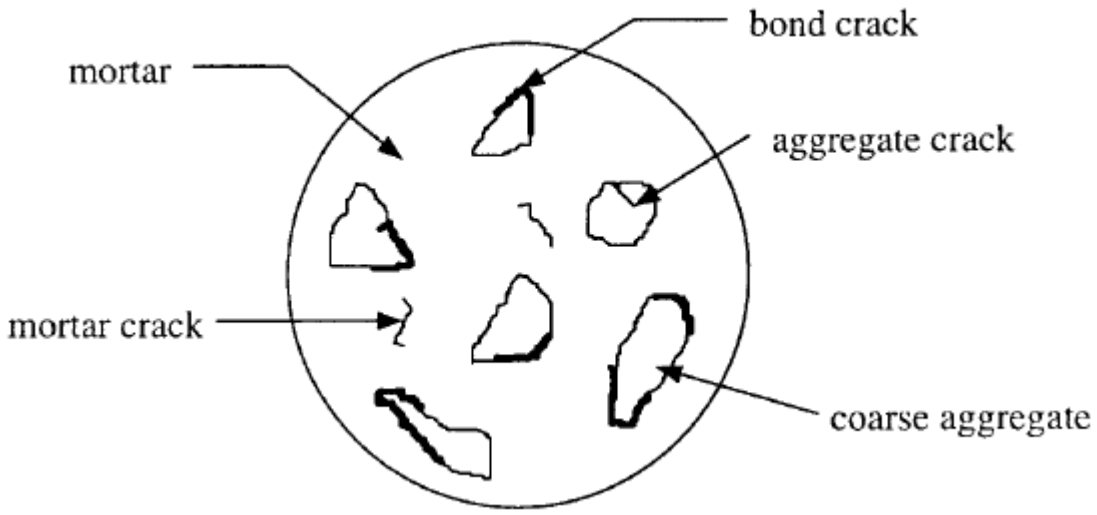

Figure 2.5: Different types of microcracks in concrete (Lim, Gowripalan, & Sirivivatnanon, 2000)

In uncracked concrete beams subjected to flexural loading, there is an increase in chloride penetration in the tensile stress zone due to the damage caused at the paste-aggregate level (tensile microcracking); this also encourages corrosion on the tensile reinforcement because of the

damage at the steel-concrete interface caused by external flexural loading (Francois & Arliguie, 1999). Compressed longitudinal reinforcement in concrete beams subjected to flexural loads are not usually affected by corrosion for this reason, provided that there is sufficient concrete cover. However, it's a known fact that tensile stresses and microcracking caused by external flexural loads play a significant role in the penetration of chlorides and tensile reinforcement corrosion, especially when macro flexural cracking occurs and cracks widen. Subsequently, the effect of microcracking on permeability and chloride transport under compressive stresses is not as straight forward and is subjected to conflicting views in the literature. An early experiment done by Samaha & Hover (1992), briefly described in the above section, gives important findings on the effect of uniaxial compression on microcracking on chloride transport. Samaha & Hover (1992) found that:

- Higher strength concrete is not necessarily less permeable than lower strength concrete with respect to RCPT results. Compressive strength and resistance of concrete to mass transport are independent properties.
- Higher rates of water absorption were found as compressive stress increased, also causing an increase in total porosity as microcracks continued to develop in the concrete.
- The proportion of aggregate in the concrete mix has a significant effect on RCPT results.
- Internal microcracking damage caused by oven-drying shrinkage has a greater effect on chloride transport than the damage caused by short term loading of concrete that is air-dried cured.
- Microcracking steadily increased with applied compressive loading, starting with bond cracking and producing mortar cracking as compressive stress increased up until failure. Extensive mortar cracking is directly related to the concrete's resistance to water flow and chloride transport.
- Microcracks caused by compressive stresses did not affect mass transport properties at load levels below 75% of the concrete compressive strength. Concrete became 15-20% less resistant to chloride transport when compressive loading was above 75% of the compressive strength (Samaha & Hover, 1992).

However, as mentioned before, there were limitations on the experiments done by Samaha & Hover (1992). They did not attempt to characterize microcracks during compressive loading; it would be more appropriate to characterize the microcracks during compressive testing so that a more realistic depiction of the influence of microcracks on the permeability of concrete can be

established (Lim, Gowripalan, & Sirivivatnanon, 2000). The non-destructive method of microcrack evaluation used in the experiments done by Lim et al. (2000) was developed by Loo (1992). The method provides a quantitative indication of the extent of microcracking during compressive testing; it's based on the assumption that the change in cross-sectional area of a prismatic concrete specimen under uniaxial compression is equal to the sum of the elastic change in cross-sectional area due to Poisson's ratio effects and expansion due to microcracking (Lim, Gowripalan, & Sirivivatnanon, 2000). The expression can be explained with the following equations:

$$\Delta A_T = \Delta A_C + \Delta A_{PR} \tag{2.6}$$

$$\varepsilon_{cr} = 2(\varepsilon_x - \mu_e \varepsilon_y) \tag{2.7}$$

where A_T = total change in cross-sectional area of concrete

A_C = change in area due to microcracking

A_{PR} = change in area due to Poisson's ratio effects

ε_{cr} = specific crack area

ε_x & ε_y = transverse and axial strains, respectively

μ_e= elastic Poisson's ratio

During compressive loading, the critical stress is the level of stress at which instability occurs (around 75-90% of f'_c); more and more microcracks propagate into the mortar, eventually leading to failure due to the collapse of the remaining load paths taken up by microcracks (Samaha & Hover, 1992). The conflicting results on how compressive stress affects chloride permeability in concrete can be attributed to the fact that neither of the studies done by Samaha & Hover (1992) and Saito & Ishimori (1995) attempted to determine this critical stress in their test specimens. The chloride permeability of concrete after it is unloaded is influenced by this critical stress threshold. When the critical stress is exceeded in a concrete specimen, large chloride permeability values are measured; when the critical stress is not exceeded, the increase in chloride permeability is not significant in spite of the large increase in microcracks (Lim, Gowripalan, & Sirivivatnanon, 2000). Therefore, the low RCPT charges found in the studies done by Samaha & Hover (1992) and Saito & Ishimori (1995) can be explained by the fact that the critical stress was not reached in either specimen.

Figure 2.6 shows the microcrack observations found in two different studies compared to that of the present one done by Lim et al. (2000). The present study shows very similar trends, with some slight variations in crack length elongation given the same applied stress on similar strength concretes. Concrete in all three studies have a definite critical stress threshold above which crack length dramatically increases. Figure 2.7 shows a visual representation of these cracks for a 100 mm diameter (10 mm thick) concrete specimen subjected to a compressive stress (a) below and (b) above the specific critical stress level. Just as seen in the different microcracking examples of Figure 2.5, The increase in the amount and length of microcracking at the paste-aggregate level as well as in the mortar, can be clearly seen under the examination of an optical microscope (magnification of 20-40x).

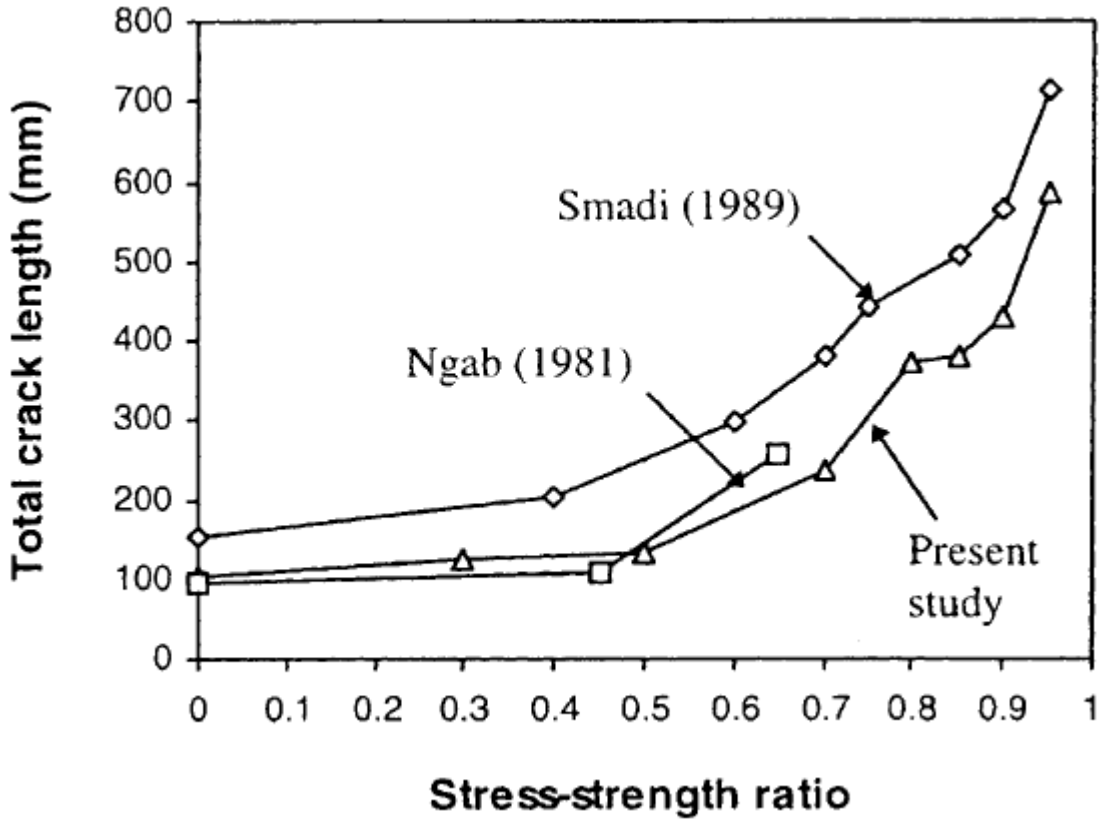

Figure 2.6: Relationship between total microcrack length and stress-strength ratio (Lim, Gowripalan, & Sirivivatnanon, 2000)

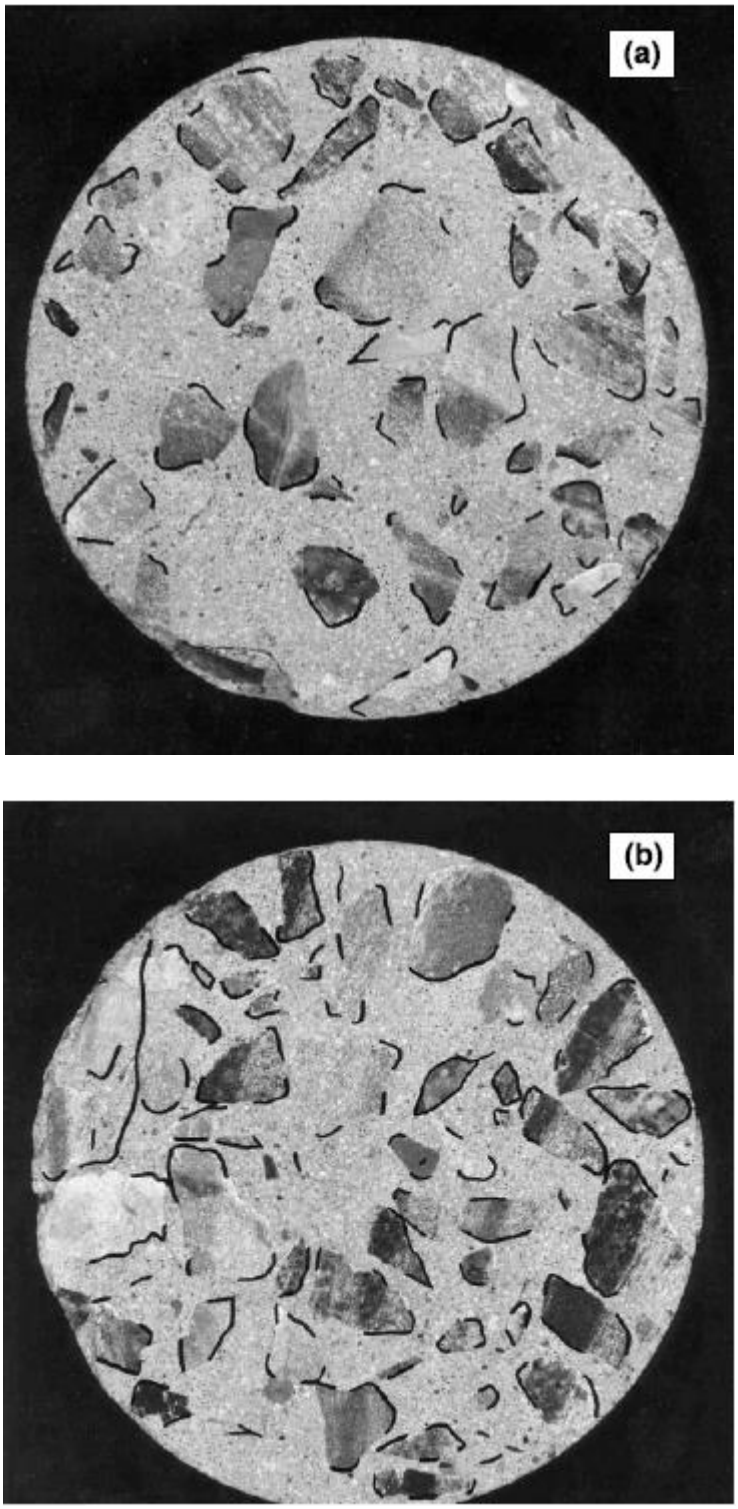

Figure 2.7: Typical cracking maps (a) 0.7f'c (b) 0.95f'c (Lim, Gowripalan, & Sirivivatnanon, 2000)

With the addition of the aforementioned microcrack and critical stress assessment and evaluation methods, some of the new findings in accordance to the study completed by Lim et al. (2000) include:

- Chloride permeability of a concrete is influenced by whether the specimen is loaded or unloaded at the time of testing.
- Depending on the stress level at which the concrete is subjected, microcracks can close completely or partially after unloading. The ability of microcracks to 'close' and 'open' may have a greater effect (more sensitive) on chloride permeability than its crack length when relating permeability to stresses in concrete.
- When a concrete specimen is unloaded completely from $0.5f'_c$, the specific crack recovery is 100%, microcracks close back up completely. However, when unloaded between $0.70\text{-}0.95f'_c$, it can be seen that cracks only partially close up; this can be attributed to exceeding the critical stress level and the remaining residual strains.
- The critical stress was found to be exceeded when concrete cylinders were loaded to a compressive stress level between $0.80\text{-}0.95f'_c$. However, there were some specimens where the critical stress was not reached when subjected to $0.80\text{-}0.85f'_c$.
- After it is unloaded, the chloride permeability of a concrete appears to be influenced by the occurrence of the critical stress. When the critical stress is exceeded, a large RCPT value is measured; when the critical stress is not exceeded, the increase in RCPT values measured is insignificant based on the large increase in microcracking.

2.3 Effect of Cracking on Chloride Transport

There are many factors that determine the chloride penetration rate into cracked concrete, and there has been new research that provides sound findings. Some of these factors include the type of loading (static, cyclic, dynamic, etc.), crack width, depth of cover, crack orientation (transverse or longitudinal to reinforcement), and the use of high performance concrete (HPC) to reduce overall porosity. Some of the sources of cracks in concrete include reinforcement corrosion, weathering processes such as freezing and thawing, chemical reactions, shrinkage, and mechanical loading (Poursaee & Hansson, 2008). Often, the dynamic and static loading experienced in structures commonly affected by corrosion will cause cracks in the concrete. Coupled with a harsh environment, static loads from snow deposits or parked cars as well as dynamic loads from moving vehicles cause an excess of stress on the structure. The stress and fatigue from cyclic loading form cracks in the concrete, increasing the penetration rate of chlorides, which is an unfavourable yet inevitable outcome.

Below are the findings of several researchers on the contribution of these factors on the overall chloride penetration rate and the initiation of the corrosion process.

2.3.1 Mechanical Loading and Stress

During their service life RC structures are subjected to many forms of mechanical stresses, which alone usually do not cause significant deterioration or corrosion. Structures are designed to resist these stresses; however in time these applied dynamic and static loads will cause cracks to form. Cracks cause an increase in the permeability of concrete as well as facilitate the path for chloride and water ingress. In reality these mechanical stresses are present at all times, and therefore it is beneficial to study the chloride transport and permeability into concrete as the specimen is being loaded.

An excellent experiment was done by Hoseini, Bindiganavile, & Banthia (2009) that illustrates how the effects of different cases of mechanical stress on a cracked concrete specimen influence fluid permeability in concrete. The experiment included results of the effect of loading types, admixtures, and crack dimensions on the permeability of water in concrete. Although the experiment dealt with the transport of water, the results can be co-related to that of the transport of chloride ions in water. The stresses caused by internal forces such as concrete shrinkage, creep, and thermal effects were ignored to simplify the analysis.

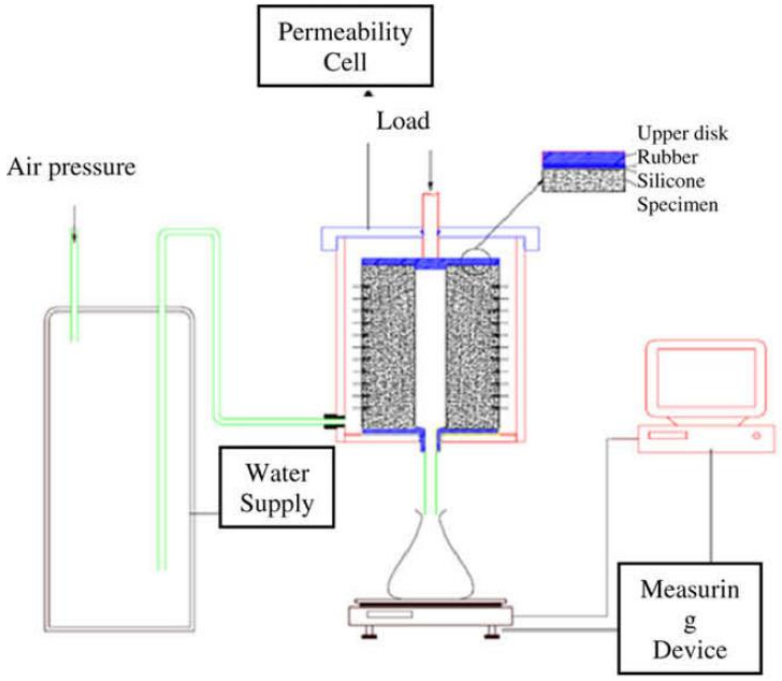

Figure 2.8: Mechanical stress test apparatus for measuring concrete permeability (Hoseini, Bindiganavile, & Banthia, 2009)

Figure 2.8 shows the test apparatus and set-up by Hoseini et al. (2009), which measures the concrete permeability under 18 MPa of compression. Other test methods by different researchers measured permeability under tension and flexure.

The transport and cracking properties are both directly influenced by the type of applied stress (compression, tension, or flexure), the loading level with respect to the ultimate capacity, and the rate of loading. A concrete permeability threshold stress was found for each type of specimen, which is a significant finding. It showed that at low levels of loading beneath the threshold, the permeability did not significantly increase and that crack formation was minimal. As the load increased to the threshold, there is a significant rise in the concrete permeability and larger cracks form.

This threshold can be seen in Figure 2.9 at about 40% of the ultimate stress for concrete made with OPC (ordinary Portland cement), where Kermani (1991) investigated the permeability of a stressed concrete specimen after being unloaded. He found that the permeability was related to the applied stress, and identified threshold levels of three types of concrete specimens (Hoseini, Bindiganavile, & Banthia, 2009).

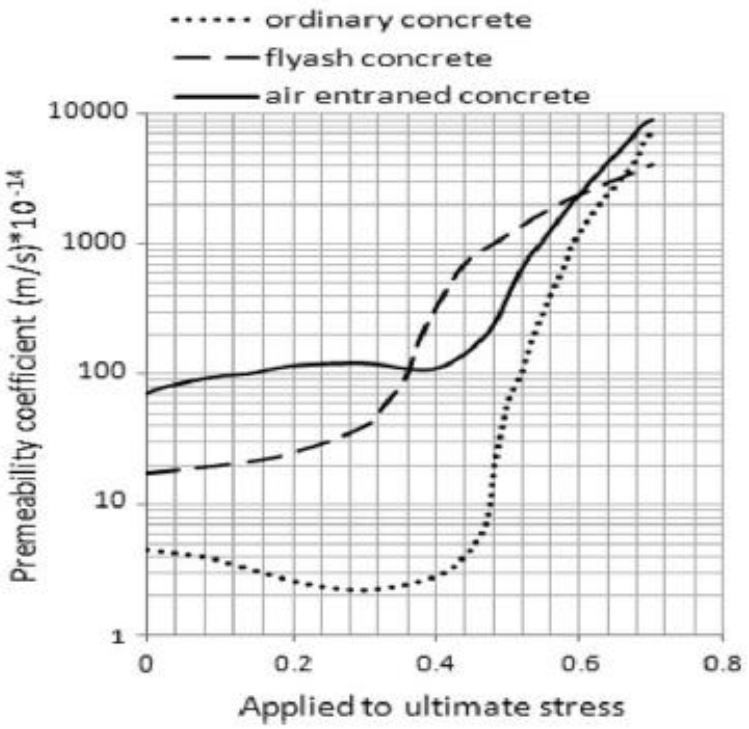

Figure 2.9: Effect of compressive stress on concrete permeability (Hoseini, Bindiganavile, & Banthia, 2009)

Some of the conclusions made by Hoseini, Bindiganavile, & Banthia (2009) include:

- Applied stress causes a slight decrease followed by a sudden increase in permeability past the threshold stress, which varies from 30%-80% of the ultimate stress capacity.
- Cyclic loading has a greater effect on permeability than monotonic loading.
- Up to the threshold stress, permeability under loading is less than permeability measured after the load is removed/unloaded.
- There is also a threshold value for crack width, where permeability is low before the threshold and increases greatly after the threshold. This value ranges from 50-100 μm.
- Permeability is not dependant on crack length, only crack width.

For future tests and further understanding of fluid permeability of concrete under stress, there should be some focus on how the compressive strength of concrete affects crack initiation and the threshold crack width, which is so important to permeability rates. Also, since fluid permeability in concrete is a slow process the possibility of a freeze and thaw cycle could occur in reality. The effect of internal cracking due to freeze/thaw exposure on chloride migration was studied by Jacobsen et

al. (1996). The authors observed an increase in the rate of chloride migration of the order of 2.5-8 times larger for non-air entrained concretes, and they modelled this increase fairly well by using a square grid crack pattern model to characterize the cracks.

2.3.2 Cyclic Loading

Applications where dynamic loading conditions occur, such as in marine conditions or parking garages, need to be successfully modelled for chloride penetration rates. Structures that are exposed to de-icing salts such as bridges and parking garages are subjected to high seasonal peaks of chloride exposure, and varying dynamic mechanical loads with frequent rest periods.

A preliminary experiment done by Kuter, Geiker, Olesen, & Al (2005) presents the results of the effect of crack opening and closing caused by dynamic mechanical loading on chloride ingress into cracked concrete. Different frequencies of load application were used to simulate dynamic loading, while one load application per hour was used to simulate a static crack. Ingress influencing parameters, such as static crack width, were kept constant to determine the full effect of cyclic loading on chloride ingress.

The sudden opening and closing of cracks exhibit a different chloride transport mechanism than that of a static crack. Closing of a crack leads to overpressure along the crack face, and if closure takes place at a high rate, not only will the chlorides be pressed out of the crack but also forced into the crack faces. This is called ‘pumping’. The roughness of the crack face determines how the solution will flow inside the concrete; frictional resistance has an effect on chloride ingress as well.

Figure 2.10 shows the results of the pumping effect due to static and dynamic loads acting on cracks of concrete submerged in a chloride solution. Sketch (A) shows results for the high frequency beam, (B) low frequency beam, (C) ingress in crack face under immediate exposure, (D) ingress in crack face for a static crack, and (E) ingress in crack face for dynamic loading. Silver nitrate was used to have a visual representation of the chloride ingress.

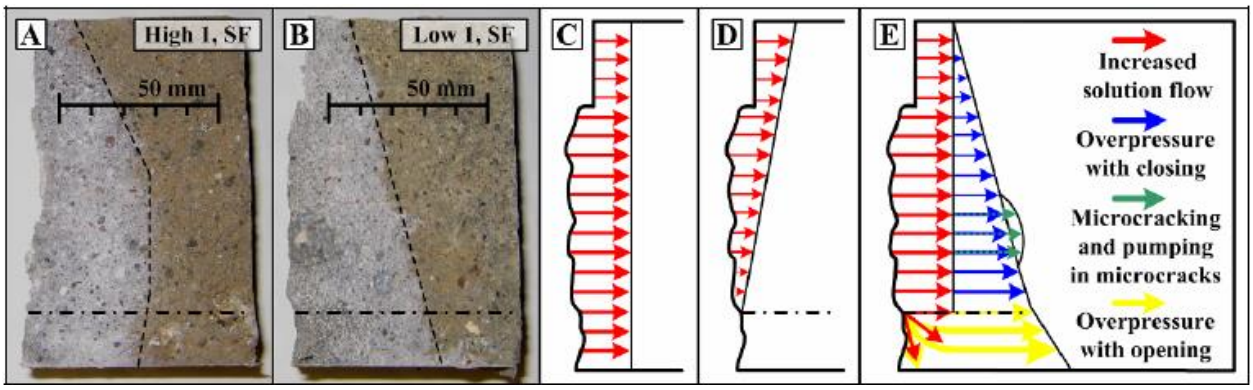

Figure 2.10: Chloride ingress shapes in static and dynamic load cases (Kuter, Geiker, Olesen, & Al, 2005)

Some conclusions made by Kuter, Geiker, Olesen, & Al (2005) include:

- It was determined that cyclic opening and closing of cracks could not be fully isolated because mechanical loading conditions were partly undefined causing microcracking to occur.
- Dynamic cyclic loading increases chloride ingress compared to static loading; this is especially true near the top of the crack and in the beam compression zones.
- The increased ingress caused by forced circulation and build-up of pressure is controlled by the frequency and rate of loading.
- Crack width is seen to be independent to chloride ingress when the beam is loaded dynamically.

2.3.3 Transverse and Longitudinal Cracks

Crack orientation is an important parameter in determining concrete durability and permeability rates. Various experimental tests have confirmed that corrosion initiates slower when penetrating transverse cracks rather than longitudinal cracks; generally, a greater area of rebar is exposed to chloride ions in a longitudinal crack that is situated directly above the rebar.

An experiment done by Djerbi et al. (2008) studied the effects of transverse cracks of concrete on chloride diffusion. The specimens used were ordinary concrete (OC), HPC, and HPC with added silica fume (HPCSF). The different specimens show the influence of w/c and admixtures to the diffusion coefficient of concrete. Table 2.3 shows the uncracked material properties of each sample measured at 28 days. It can be seen that the diffusion coefficient of HPC with silica fume was the

lowest, followed by HPC, and OC. This is to be expected as diffusion is directly related to the porosity of the uncracked concrete.

Table 2.3: Material properties and diffusion coefficient of uncracked concrete specimen (Djerbi, Bonnet, Khelidj, & Baroghel-bouny, 2008)

Material properties measured at 28 days and diffusion coefficient

	OC	HPC	HPCSF
Module of elasticity (GPa)	22	31	36
Compressive strength (MPa)	46	75	85.5
Dry apparent density (g/cm^3)	2.35	2.55	2.46
Open porosity measured by water saturation (%0	12.1	11.4	10.0
Diffusion coefficient (m^2/s)	1.8×10^{-12}	0.76×10^{-12}	0.26×10^{-12}

Controlled crack widths ranging from 30-250 μm were obtained using a splitting tensile test, and it was found that the diffusion coefficient increased as the crack width increased. This is expected as a wider crack will cause an increase in chloride penetration rates. Figure 2.11 shows the test set-up and the controlled splitting tensile test done on each specimen to obtain the desired crack widths needed for experimentation.

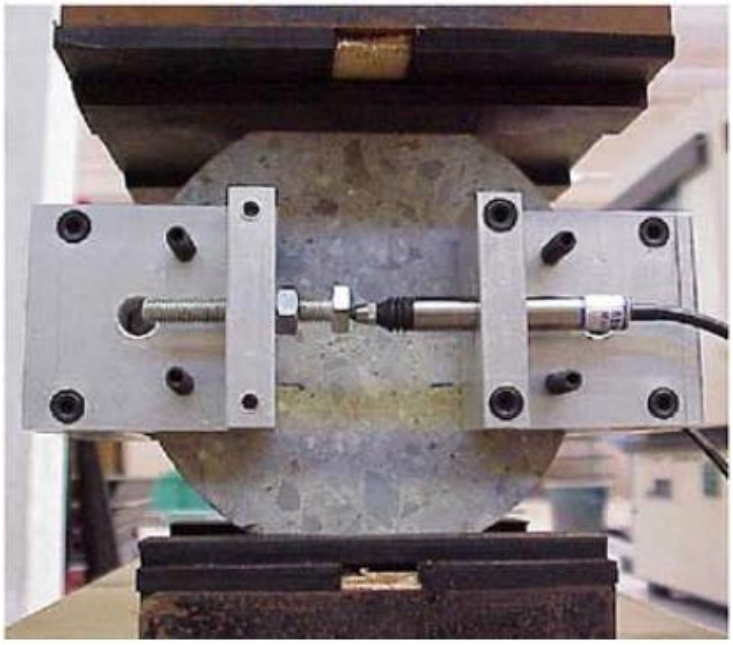

Figure 2.11: Concrete specimen tensile splitting test (Djerbi, Bonnet, Khelidj, & Baroghel-bouny, 2008)

However, at crack widths of 80 μm and larger, the diffusion coefficient (D_{cr}) is almost constant; this shows that D_{cr} is independent of concrete material properties when cracks are wide enough to allow chloride transport through the crack to be free-flowing, meaning that the concentration of chlorides in the crack wall is equal to the concentration at the exposed surface (Jin, Yan, & Wang, 2010). Figure 2.12 illustrates this phenomenon, where a bi-linear relationship can be used to represent the change in diffusion as the crack width increases.

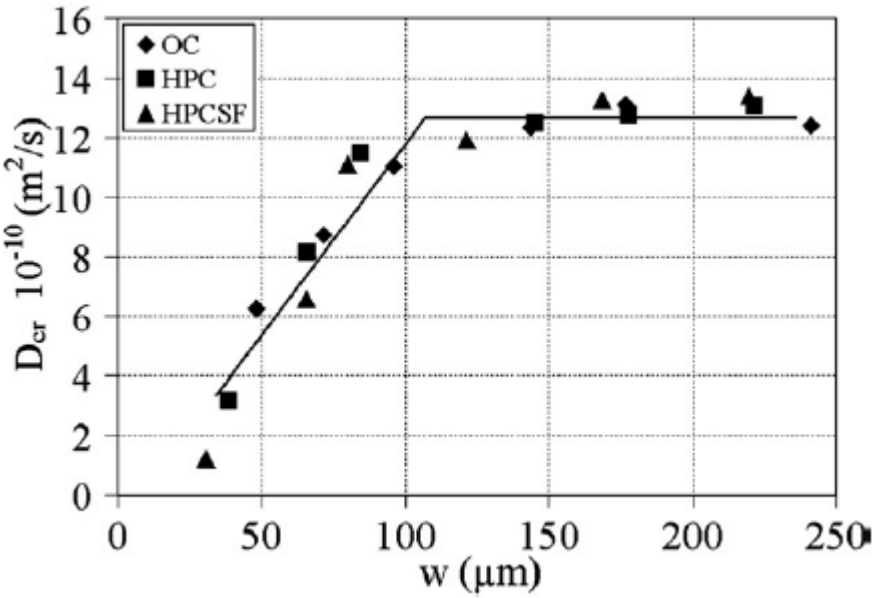

Figure 2.12: Diffusion coefficients as a function of crack width w (Djerbi, Bonnet, Khelidj, & Baroghel-bouny, 2008)

Some conclusions made by Djerbi et al. (2008) include:

- The chloride diffusion coefficient of cracked samples increases with increasing crack widths for all three specimens up to crack widths of approximately 80 μm. The time for chloride penetration is decreased, which decreases the initial time of corrosion initiation.
- For the entire range of data and for the same crack opening displacement, OC had a larger crack width than HPC and HPCSF.
- OC being more porous and permeable than HPC means that the diffusion ratio for cracked/uncracked specimens is lower in OC than HPC.
- The diffusion coefficient through a crack increases linearly for all types of concrete until 80-μm width, above which the diffusion coefficient is independent of material properties.

In addition to transverse cracking, structures such as continuously reinforced concrete pavements, parking garage slabs, and reinforced concrete sewer pipes can be affected by longitudinal cracking. This type of cracking is less common than transverse cracking due to the conditions needed to achieve such a large crack, but the outcome can be more devastating.

An experiment done by Poursaee & Hansson (2008) illustrates the performance of HPC and OPC when both subjected to longitudinal cracks parallel to the rebar. As mentioned before, the uncracked performance of HPC is always greater than OPC with respect to concrete permeability and corrosion protection. However, it was found that HPC does not have any added benefits over OC when both are subjected to longitudinal cracks, because the whole length of the bar is exposed to chlorides.

Table 2.4 shows the three specimens being tested; each specimen was tested with cracks parallel to and immediately above the rebar, perpendicular to the rebar, and without any cracks.

Table 2.4: Mix design for each concrete specimen (Poursaee & Hansson, 2008)

Component	OPC	HPC-slag	HPC-fly ash
Type 10 Portland, kg	355	-	-
Type 10SF Portland, kg	-	337	337
Slag, kg	-	113	-
Fly ash, kg	-	-	113
Sand, kg	770	718	718
Stone 20 mm, kg	1070	1065	1065
Water, L	153	158	158
Eucon MRC air entrainment	40 mL/100 kg cementitious	65 mL/100 kg cementitious	65 mL/100 kg cementitious
Water reducer	250 mL/100 kg cementitious	250 mL/100 kg cementitious	250 mL/100 kg cementitious
Superplasticizer	-	21 + 1.51	31 + 0.51
W/CM ratio	0.43	0.35	0.35

Among the various testing methods to determine chloride-induced corrosion, the amount of corrosion was estimated using electrochemical techniques such as a polymethylmethacrylate (PMMA) rod probing tool. Figure 2.13 shows the corrosion potential of each specimen, which was tested after 128 weeks of chloride exposure and a longitudinal crack width of approximately 0.1 mm. A more negative potential indicates higher corrosive activity, which confirms that HPC does

not provide better corrosion protection than OPC with respect to longitudinal cracks. Indeed, it is the increase in concrete cover (from 10 mm to 15 mm) which provides the additional protection.

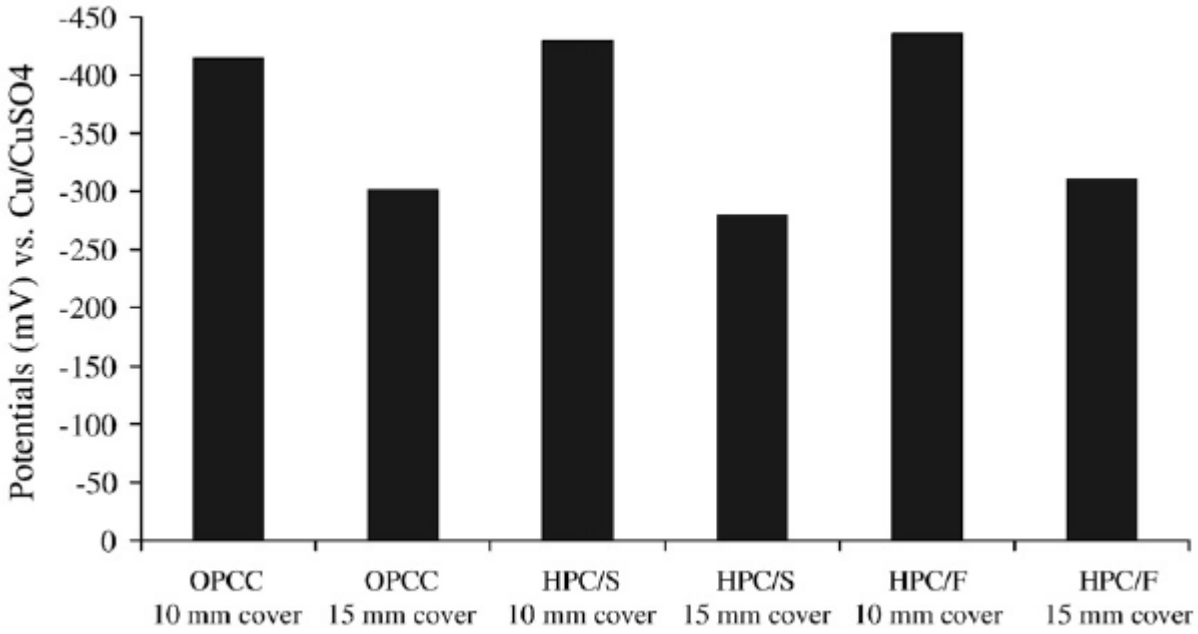

Figure 2.13: Corrosion potential in prisms with longitudinal cracks, 128 week exposure to de-icing salts (Poursaee & Hansson, 2008)

Some conclusions made by Poursaee & Hansson (2008) include:

- The cover depth influences the corrosion rate when the rebar is exposed to longitudinal cracks; however the local corrosion rate remains constant for all cover depths.
- HPC provides significantly greater protection against corrosion than OPC in uncracked concrete and concrete exposed to transverse cracking.
- HPC containing 25% fly ash and HPC containing 25% slag behave very similar in both cracked and uncracked concrete; therefore there is no advantage of one over the other.
- There is no significant difference between resistances of OPC and HPC when there is a longitudinal structural crack measuring 0.1 mm (below the allowable limit of 0.3 mm).
- Using concrete resistance as an indicator for longitudinal cracks is not recommended because the concrete resistances in HPC are higher than OPC, while the corrosion current densities of steel in all types of concrete are similar.

The relatively new research presented shows how chloride ingress, diffusion, and penetration rates are affected by factors such as crack width, crack orientation, porosity of concrete (OPC vs. HPC), and applied mechanical stresses. However, these experimental results are only useful in the advancement of service life prediction if they are successfully incorporated into an accurate numerical model.

2.4 Chloride Transport Modelling

The transport of chloride ions into concrete samples subjected to sustained loading is usually assumed to be one-dimensional in a semi-infinite medium complying with Fick's 2nd law of pure diffusion as seen in Eq. (2.2) (Wang, Lu, Jin, & Bai, 2011). When Eq. 2.5 is commonly resolved with the closed-form analytical solution first developed by Crank (1975), it can be expressed as:

$$C(x,t) = C_0 + (C_S - C_0)\left[1 - erf\left(\frac{x}{2\sqrt{D_{app}\cdot t}}\right)\right] \quad (2.6)$$

where *C(x,t)* = total content of chlorides at depth *x* after time *t* (s) (%)

C_0 = initial chloride concentration in concrete (%)

C_S = chloride concentration at the surface x = 0 (%)

D_{app} = apparent diffusion coefficient

erf = error function

Equation (2.6) can be further simplified by assuming that the initial condition $C(x > 0, t = 0) = 0$ ($C_0 = 0$) and boundary condition $C(x = 0, t > 0) = C_S$. With Eq. (2.6) one can find the chloride concentration at any depth for a given period of time assuming that the concrete is homogenous and that D_{app} and C_s remain constant in time and space. Since this assumption is not necessarily always true in concrete exposed to real conditions, the diffusion coefficient D obtained from Eq. (2.6) is substituted with an apparent diffusion coefficient (D_{app}) that is obtained by fitting chloride concentration profiles to Eq. (2.6) using the least-squares method. Sustained compressive and tensile stresses directly affect the value of D_{app} and C_s in Eq. (2.6); by altering the micro and macro structure of concrete, external loads alter the chloride penetration depths and concentration profiles used to theoretically calculate D_{app} and C_s values in Eq. (2.6). This model has successfully modelled pure diffusion in concrete under sustained load countless times, as seen in experiments done by Wang et al. (2011), Deif (2010), and Gowripalan et al. (2000). However, the fact that

concrete is a heterogeneous material that is vulnerable to cracking, makes chloride ingress into real world structures that are not permanently submerged a more complex process than that mathematically expressed in Eq. (2.6) (Deif, 2010).

Another way to determine chloride relative diffusivities is with the model proposed by Deif (2010), based on average chloride penetration depths obtained by spraying concrete samples with silver nitrate. The model is based on the assumptions that the chloride concentration at the boundary of colour change caused by the free chloride interaction with silver nitrate (colourimetric method) is the same for each sample, regardless of applied external loads. With this assumption, an estimate of the ratio between apparent diffusion coefficients of different samples can be obtained (Deif, 2010). If $C(x_i, t) = C(x_o, t)$, where x_i is the measured average chloride depth for loaded section *i* and x_o is the measured average chloride depth for the control unloaded section *o*, and assuming that C_s is the same for all sections, the following expression can be simplified from Crank's solution:

$$erf\left(\frac{x_i}{2\sqrt{D_i t}}\right) = erf\left(\frac{x_o}{2\sqrt{D_o t}}\right) \tag{2.7}$$

where D_i & D_o = apparent diffusion coefficients for section *i* and *o*, respectively.

x_i & x_o = average chloride penetration depths for section *i* and *o*, respectively.

The assumption of C_s being constant for all sections is valid if all the specimens are exposed to the same environment for the same amount of time. After more simplification and rearranging of Eq. (2.7), the relative value of the diffusivity for different sections of loaded and unloaded control specimens can be determined solely by using the penetration data obtained from the colourimetric method. This relation can be seen in the following equation:

$$\frac{D_i}{D_o} = \left(\frac{x_i}{x_o}\right)^2 \tag{2.8}$$

In recent years various models have been developed that attempt to predict the performance of concrete subjected to chloride exposure. However, there is currently no established model that incorporates sustained loading conditions into diffusion and service life prediction (Wang, Lu, Jin, & Bai, 2011). A preliminary model by Wang et al. (2011) has been proposed and can be expressed as follows:

$$D_{Cl} = D_{ref}(W/C\,, t_o) \cdot f_1(t) \cdot f_2(T) \cdot f_3(RH) \cdot f_4(C_{Cl}) \cdot f_5(\lambda_\sigma) \tag{2.9}$$

where D_{Cl} is the diffusion coefficient relating to the experimental D_{app}, D_{ref} is the reference chloride diffusion coefficient based on the ACI 365 service life prediction model, f_1 is the factor that accounts for the influence of concrete age (*t*) on chloride diffusion, f_2 is the factor that accounts for the effect of temperature (*T*) on chloride diffusion, f_3 is the factor that accounts for the effect of relative humidity (*RH*) on chloride diffusion, f_4 is the factor that accounts for the dependence of the chloride diffusion coefficient on the chloride concentration (C_{Cl}), and f_5 is the factor that accounts for the influence of external loads on the chloride diffusion (λ_σ) (Wang, Lu, Jin, & Bai, 2011). A more in depth look at equation (2.9) can be found in the study done by Wang et al. (2011).

To calculate the D_{Cl} and validate the proposed model in Eq. (2.9), Wang et al. (2011) determined all the necessary factors and parameters based on their experimental conditions. Figure 2.14 shows that the predicted chloride diffusion coefficients correlate well with the chloride diffusion coefficients obtained from experimental studies, rendering the preliminary model successful. However, further study on the effect of various mineral admixtures on the chloride diffusion coefficient should be fully investigated and added to the current model.

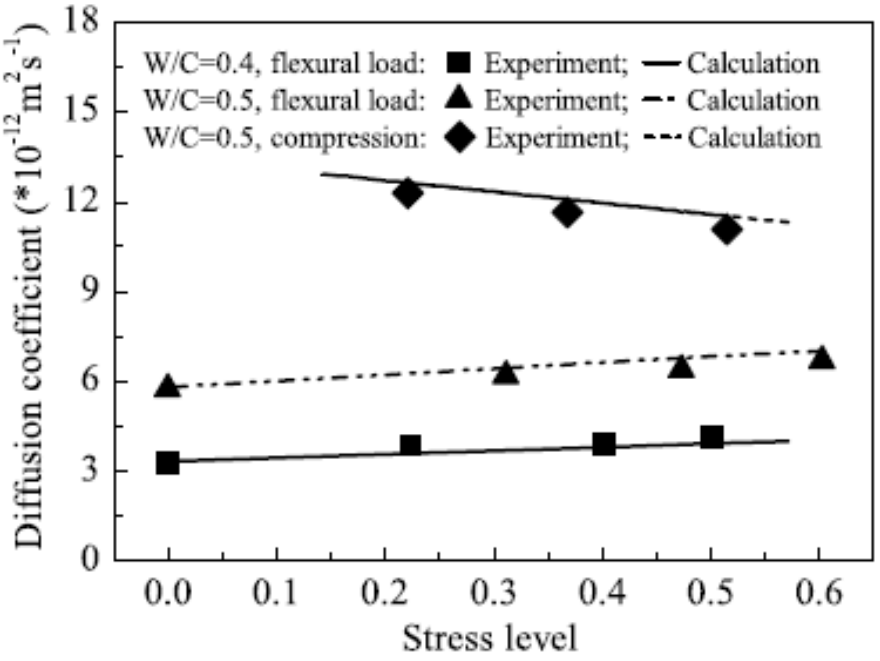

Figure 2.14: Comparison between predicted results and experimental results (Wang, Lu, Jin, & Bai, 2011)

2.5 Concluding Remarks

Based on the aforementioned studies presented in this review, it is clear that the application of external loads greatly influences the many different chloride transport mechanisms in concrete. This influence can be seen in the many studies on the effects of microcracking, different external loading conditions (sustained, cyclic, and unloaded), crack width and orientation, and porosity on chloride ingress and penetration rates. However, results have been conflicting in the literature; this can be seen in the experiments done by Samaha & Hover (1992), Saito & Ishimori (1995), and Lim et al. (2000). With the exception of the study carried out by Wang et al. (2011), there have not been prior attempts to relate chloride ingress properties to uncracked concrete under sustained compressive, tensile, and flexural loads. Therefore, the main objective of this work is to relate chloride ingress and diffusion values of concrete to the influence of sustained compressive and tensile stresses; this will act to further validate studies that seek to determine an accurate relationship between chloride ingress and sustained stress.

Chapter 3 – Experimental Program

3.1 Overview of Experiment

In reinforced concrete structures and highways exposed to de-icing salts, chloride ingress into concrete is mainly governed by diffusion and absorption mechanisms. In this study, unlike real exposure where there are many wetting and drying cycles, concrete was fully submerged in a 4-5% chloride de-icing salt solution for 12 weeks, allowing chloride transfer to be completely governed by continuous diffusion. A total of six post-tensioned concrete beams and four non-reinforced concrete beams were constructed, each with different specifications. The different w/c ratios along with the sustained post-tensioning forces are the main parameters to study their effect on chloride ingress into the concrete. Water cement ratios of 0.35, 0.40, and 0.50 were used; three concrete beams of each ratio were constructed along with a single beam of w/c of 0.50 with the addition of ground granulated blast-furnace slag to study the effects of supplementary cementing material on chloride ingress. Lastly, out of the three beams with similar w/c ratios, one was used as an unloaded control sample, while the other two beams were post-tensioned, inducing variable sustained compressive and tensile stresses along the beam.

This chapter presents a detailed description of how each concrete beam was constructed, the different materials used, and the experimental procedures and equipment needed for data collection and analysis.

3.2 Beam Specifications

To induce variable sustained compressive and tensile stresses, each beam was constructed according to the schematic provided in Figure 3.1. Beams measure 1 m in length and 100 mm in depth with a tapered cross section and one eccentric ½" post-tensioning strand (d = 12.7 mm). The large variation in stress applied to each beam allows for a broader range of data to be collected and analyzed for each post-tensioning load. Theoretical compressive (σ_c) and tensile (σ_t) stresses acting on the beams after post-tensioning were calculated with Eq. (3.1), which takes into account axial stress and the bending moment stress caused by the tendon eccentricity.

$$\sigma_{c,t}(x,h) = \frac{P}{A_c} \pm \frac{Pe(x)}{I(x)}\frac{h}{2} \tag{3.1}$$

where P is the post-tensioning force (kN), A_C is cross sectional area at abscise *x*, *h* is the height of the cross-section at abscise *x*, *e(x)* is the eccentricity of the tendon at abscise *x* with respect to the N.A. (neutral axis) of the uncracked section, and *I(x)* is the moment of inertia of the uncracked cross-section.

A graphical representation of the theoretical compressive and tensile stresses induced by a post-tensioning force of 130 kN can be seen in Figure 3.2. Maximum stresses can be found at the critical section (smallest cross-section) at a length of 150 mm, and minimum stresses can be found at the largest cross-section at a length of 1000 mm; compression is positive, while tension is negative.

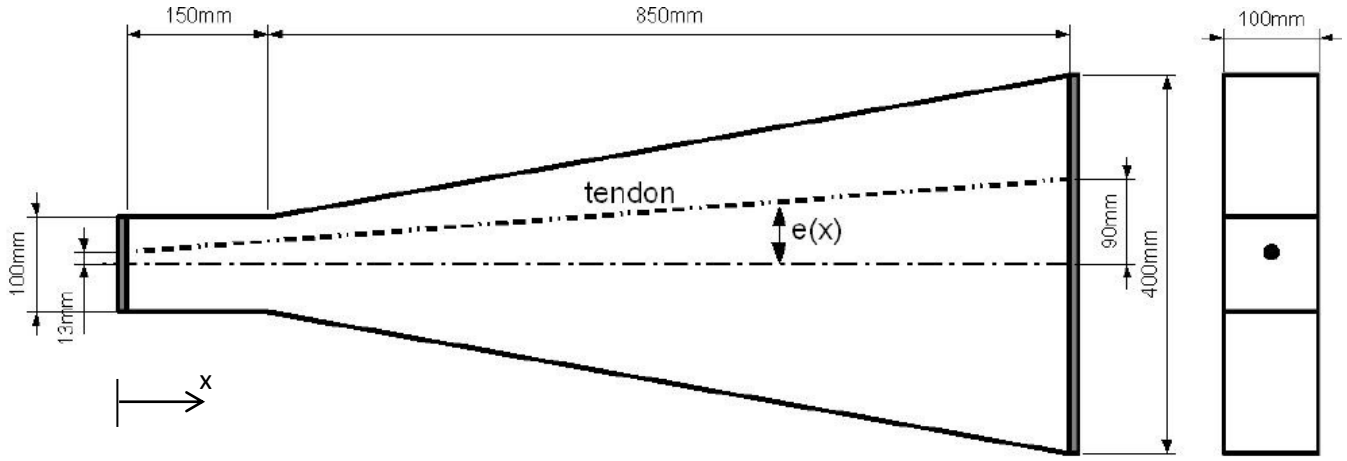

Figure 3.1: Beam specifications and dimensions

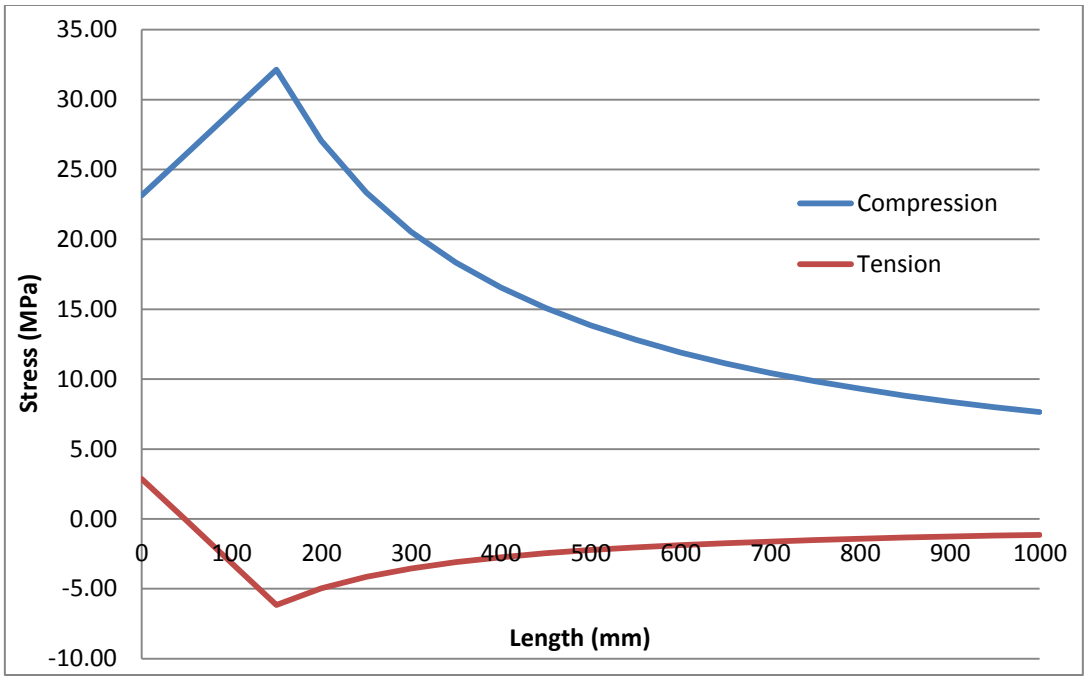

Figure 3.2: Compressive and tensile stress distribution along the entire length of the beam (P = 130 kN)

A tabular representation of the theoretical compressive and tensile stresses induced by a post-tensioning force of 130 kN can be seen in Table 3.1. Where $A(x)$ is the gross cross section at abscise x, without subtracting the area of the ½" tendon, and $A_C(x)$ is the net concrete cross section at abscise x, subtracting the area of the ½" tendon.

Table 3.1: Compressive and tensile stress distribution along the entire length of the beam (P = 130 kN)

						A		Ac	
x (mm)	h(x) (mm)	A(x) (mm^2)	Ac(x) (mm^2)	e(x) (mm)	I(x) (mm^4)	σ_c (MPa)	σ_t (MPa)	σ_c (MPa)	σ_t (MPa)
0	100	10000	9823	13.00	8.33E+06	23.14	2.86	23.37	3.09
50	100	10000	9823	16.85	8.33E+06	26.14	-0.14	26.38	0.09
100	100	10000	9823	20.70	8.33E+06	29.15	-3.15	29.38	-2.91
150	100	10000	9823	24.55	8.33E+06	32.15	-6.15	32.38	-5.92
200	117	11764	11588	28.40	1.36E+07	27.05	-4.95	27.22	-4.79
250	135	13529	13352	32.25	2.06E+07	23.35	-4.13	23.48	-4.01
300	153	15294	15117	36.10	2.98E+07	20.54	-3.54	20.64	-3.44
350	170	17059	16882	39.95	4.14E+07	18.33	-3.09	18.41	-3.01
400	188	18823	18646	43.80	5.56E+07	16.55	-2.74	16.61	-2.67
450	206	20588	20411	47.65	7.27E+07	15.08	-2.45	15.14	-2.40
500	223	22353	22176	51.50	9.31E+07	13.86	-2.22	13.90	-2.18
550	241	24117	23941	55.35	1.17E+08	12.81	-2.03	12.85	-1.99
600	259	25882	25705	59.20	1.44E+08	11.92	-1.87	11.95	-1.84
650	276	27647	27470	63.05	1.76E+08	11.14	-1.73	11.17	-1.70
700	294	29411	29235	66.90	2.12E+08	10.45	-1.61	10.48	-1.59
750	311	31176	30999	70.75	2.53E+08	9.85	-1.51	9.87	-1.48
800	329	32941	32764	74.60	2.98E+08	9.31	-1.42	9.33	-1.39
850	347	34706	34529	78.45	3.48E+08	8.83	-1.33	8.85	-1.32
900	364	36470	36293	82.30	4.04E+08	8.39	-1.26	8.41	-1.24
950	382	38235	38058	86.15	4.66E+08	8.00	-1.20	8.01	-1.18
1000	400	40000	39823	90.00	5.33E+08	7.64	-1.14	7.65	-1.12

3.2.1 Concrete Mix Design and Materials

Four different batches of normal density concrete with w/c ratios of 0.35, 0.40, and 0.50 were cast in this experiment; the fourth batch (w/c = 0.50) is identical to the third except for the addition of ground granulated blast-furnace slag (GGBS). Since the tendon is eccentric, the concrete cover on the top compressive face ranges from 25-110 mm. According to design standards in CSA A23.3-04, concrete that is continually submerged and exposed to chlorides but not to freezing and thawing, should be classified as C-3 exposure. However, since this is a short term laboratory controlled experiment that aims to determine the relationship between chloride ingress and stress, concrete classification and cover are not important parameters; tendons are also protected by a plastic duct to prevent reinforcement corrosion.

In order to determine appropriate water contents for each specific mix design, moisture and absorption contents were found for coarse and fine aggregates in accordance to the methods

described in CSA A23.2-04 experiments 6A, 11A, and 12A; the experimental procedure can be seen in Figure 3.3. However, it was found that the coarse aggregates were dirty and covered in dust, which would affect the concrete compressive strength if mixed with cement during casting. Coarse aggregates were hand washed and allowed to air dry for 24 hrs to SSD (saturated-surface dry) before usage in the mix; the aggregates can be seen in Figure 3.4.

Figure 3.3: Determining absorption and moisture contents of aggregates in the lab

Figure 3.4: (a) Coarse aggregate after washing and (b) After 24 hr of air drying to SSD

The proportions of the mix ingredients used for each batch are tabulated in Table 3.2; full details of the concrete mix design, material properties, and laboratory test results can be seen in Appendix A. The gradation curve for fine aggregates can be seen in Figure 3.5; sand in the laboratory was very fine, giving a FM of 1.49, therefore the minimum FM of 2.40, as given by the CSA A23.1-04 standard, was used in the concrete mix design.

Table 3.2: Concrete mix design proportions for each batch

Material	W/C			
	0.35	0.40	0.50	0.50
Water (kg/m^3)	133.0	153.6	197.0	197.0
Cement (kg/m^3)	400.0	400.0	400.0	340.0
Coarse aggregate (kg/m^3)	1056.0	1056.0	1056.0	1056.0
Fine aggregate (kg/m^3)	905.0	851.0	755.0	750.6
Blast Furnace Slag (kg/m^3)	-	-	-	60.0
Plasticizer (kg/m^3)	4.0	4.0	-	-

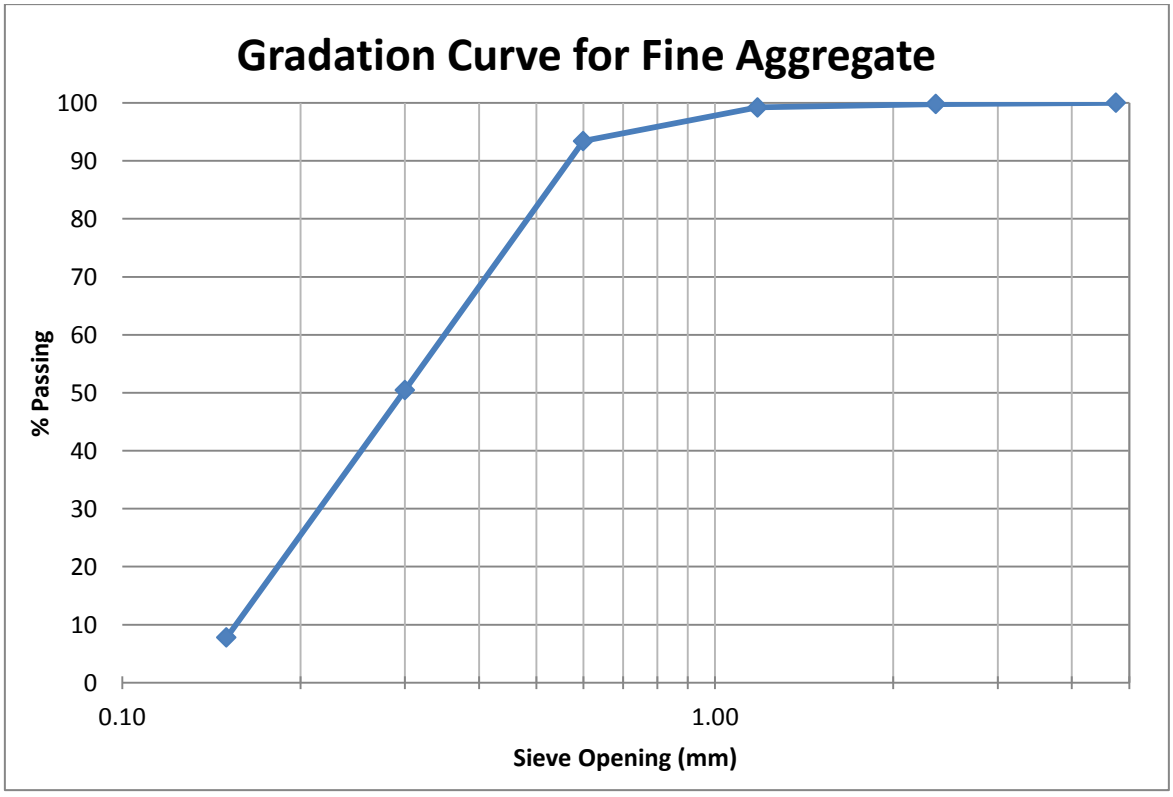

Figure 3.5: Gradation curve for fine aggregate

3.2.2 Casting and Curing

Specially designed formwork, constructed with plywood and nails, was built to meet beam specifications. The completed formwork ready for casting can be seen in Figure 3.6; it includes hooks for easy transport of the beams, a 0.152 mm plastic lining for easy beam removal from the forms and to protect the formwork for continued usage, one unbounded post-tensioning ½" strand, and bearing plates to protect against localized concrete crushing while post-tensioning. A total of four batches (according to Table 3.2) were cast using the same formwork, creating a maximum of three beams per cast.

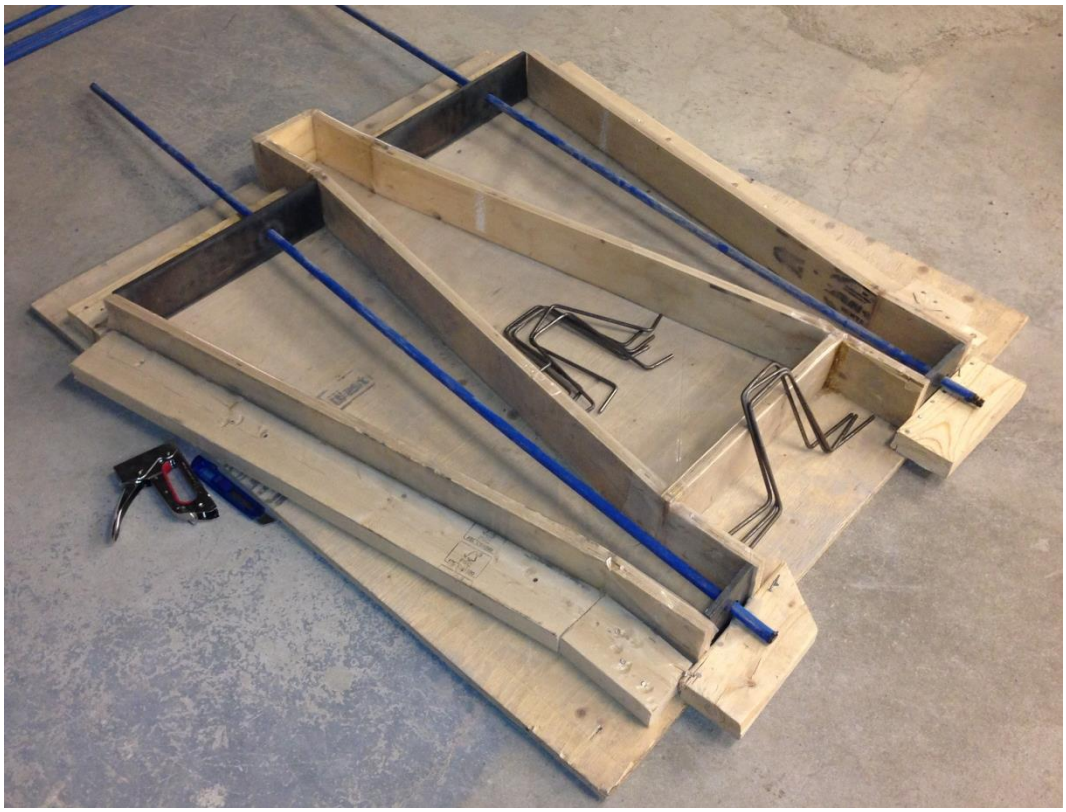

Figure 3.6: Completed formwork ready for concrete casting

The mixer used for casting was only large enough for 0.05 m^3 batches, therefore two separate but identical batches were cast to evenly fill the formwork and test cylinders (0.10 m^3) for each w/c; the batches are denoted by an a) and b) suffix as seen in Table A.2 of Appendix A. A complete listing of actual mix proportions from casting and succeeding casting notes can be seen in Appendix A. The formwork and test cylinders after casting and pouring of concrete, along with the concrete mixer used can be seen in Figure 3.7(a). One day after casting, each batch and subsequent test cylinders

were cured in the laboratory with a wet burlap cloth for 5 days as seen in Figure 3.7(b); the average temperature in the Structures Lab was 21°C with a RH of 25%. Burlap clothes were regularly soaked with water, and plastic sheets were later placed over the burlap cloth on future batches to prevent water from evaporating overnight. The completed beams after curing can be seen in Figure 3.8; a total of ten beams were constructed.

Figure 3.7: (a) Formwork after casting and levelling (b) Concrete being burlap cured in the lab

Figure 3.8: Ten concrete beams after curing and prior to post-tensioning, sealing, and material testing

Sand did not mix properly in the very first batch (batch 1a; w/c = 0.35); there was not enough water to allow the concrete ingredients to mix properly. The beam showed signs of major defects with respect to large pores (honeycombing) and sandy deposits as seen in Figure 3.9. Instead of discarding the beam and casting a new one, it was kept to study how poorly constructed beams in the field can affect chloride ingress under sustained load and reduced concrete durability conditions.

Figure 3.9: Poorly mixed concrete showing defects and large pores (batch 1a; w/c = 0.35)

3.2.3 Material Testing

Nine concrete cylinders (100 mm x 200 mm) and one concrete prism (100 mm x 100 mm x 400 mm) were prepared for each batch at the time of casting and were tested according to the methods seen in CSA A23.2-04-8C, 9C, 12C.

Three cylinders were tested each for 7 and 28-day compressive strengths (f'_c); 14 day tests were not performed because two data points are adequate to accurately represent concrete's increase in strength over time. Figure 3.10(a) shows the concrete cylinders from batch 1 (w/c = 0.35) after being tested in compression at 7 days . Since the concrete grinder in the lab was not functioning at the time of compression testing, steel caps with a rubber interior were used on rough and uneven surfaces of the concrete cylinders as seen in Figure 3.10(b); this was done to allow load to be distributed evenly on a flat surface. The average 28-day strengths obtained were 55.7 MPa, 57.0 MPa, 44.3 MPa, and 49.2 MPa for a w/c of 0.35, 0.40, 0.50, and 0.50+GGBS, respectively. The low compressive strength recorded for the concrete with w/c of 0.35, compared to that of the concrete with w/c of 0.40, is attributed to the problems encountered during mixing and the resulting poor-quality concrete (Figure 3.9) as discussed above. Figure 3.11 shows the compressive strength results for both 7 and 28 days for all w/c ratios; it can be seen that the addition of GGBS increases the compressive strength of the concrete as expected.

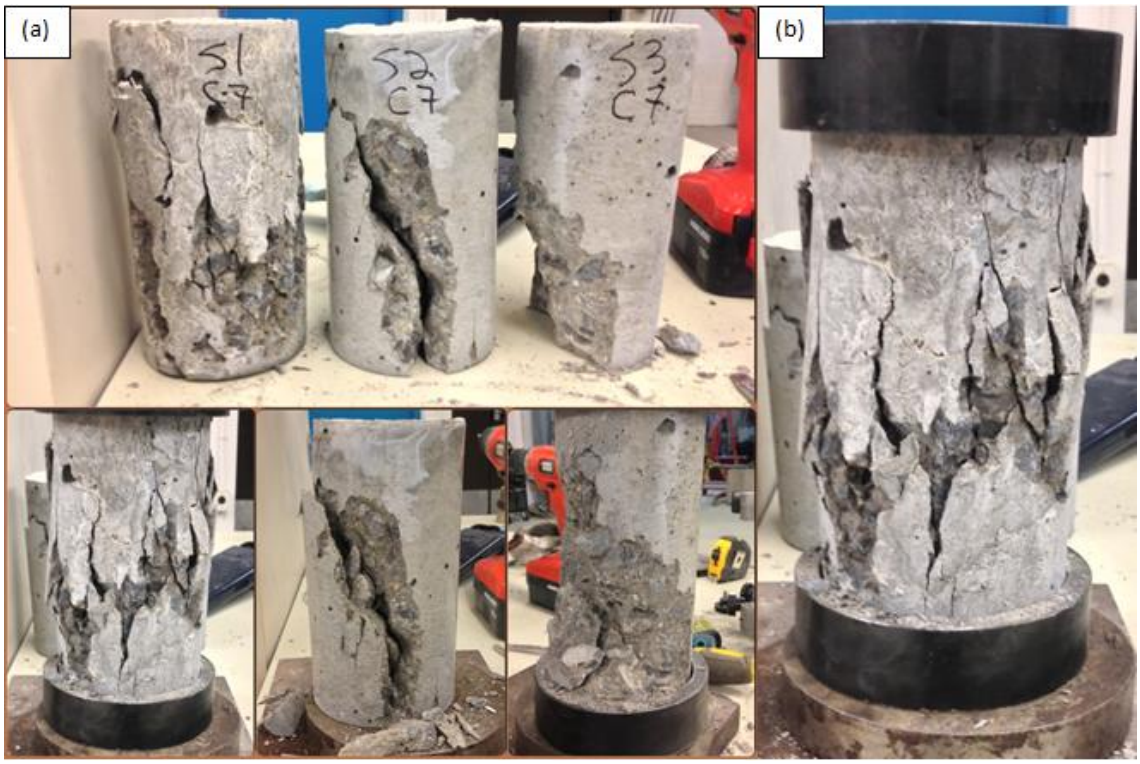

Figure 3.10: (a) Concrete cylinders after compression testing (b) Steel caps used on concrete cylinders

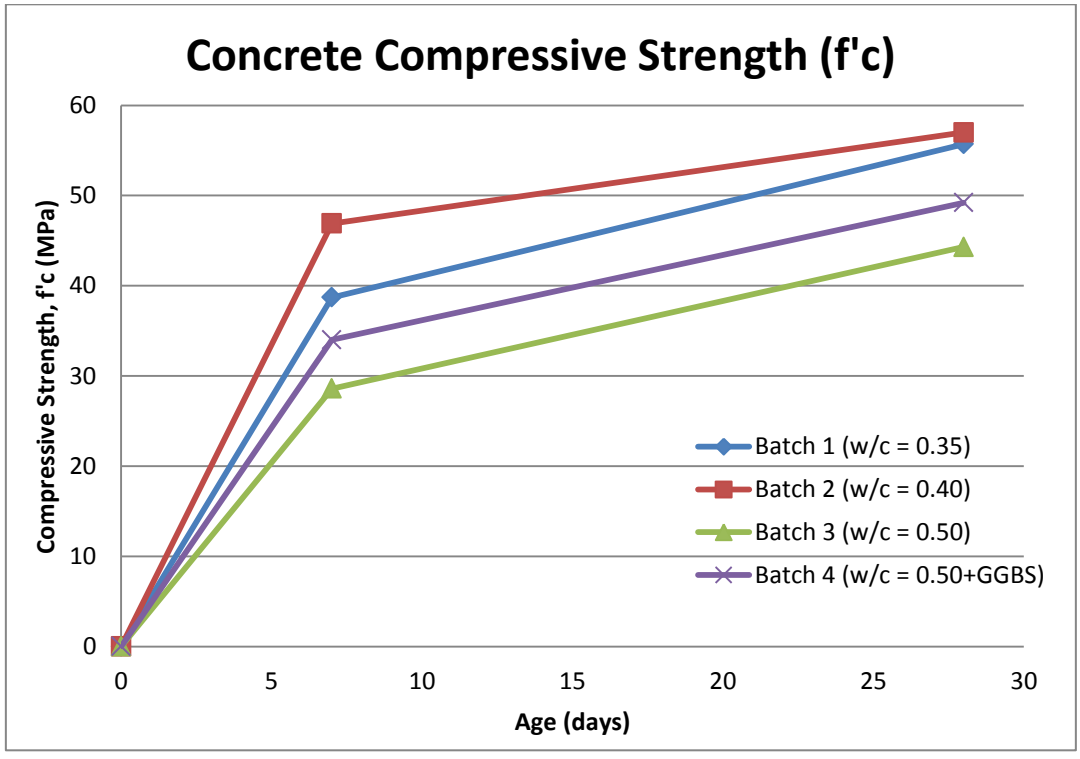

Figure 3.11: Compression test results for all w/c

Three cylinders were tested each for 38-day, 33-day, and 27-day splitting tensile strength (f'_t) for w/c of 0.35, 0.40, and 0.50, respectively. Figure 3.12 shows the test set up on the Galdabini 1890 loading machine, while Figure 3.13 shows the specimens from all batches and w/c ratios after the splitting tensile test . The average strengths obtained were 3.02 MPa, 2.96 MPa, and 3.07MPa for a w/c of 0.35, 0.40, and 0.5, respectively.

One prism was tested for 40-day, 35-day, and 29-day modulus of rupture of concrete (f'_r) for w/c of 0.35, 0.40, and 0.50, respectively. Figure 3.14 shows the test set up on the Galdabini 1890 loading machine. The average strengths obtained were 4.46 MPa, 3.84MPa, and 4.00MPa for a w/c of 0.35, 0.40, and 0.5, respectively. Batch 2 (w/c = 0.40), has the highest compressive strength, yet the lowest tensile strength and modulus of rupture; this can be attributed to human errors in material testing and loading; some concrete specimens were not loaded properly, reducing the obtained material strength. Although not measured at the same time, the modulus of rupture for each w/c concrete was higher than the corresponding splitting tensile strength as expected.

It is common knowledge that once concrete undergoes 28 days of curing and hydration it has substantially reached its ultimate compressive strength; therefore, any material testing done on or after 28 days should theoretically yield similar (but not identical) results. As seen above, testing days for tensile splitting and modulus of rupture tests were different for each w/c, however, they were all after or on 28 days.

Unexpectedly, the highest 28-day compressive strength was developed in the concrete with w/c of 0.40 from batch 2. This could be due to the fact that batch 2 was properly mixed and more consistent than batch 1 (w/c = 0.35). There was a learning curve between mixing the first and second batch of concrete; this is reflected in the poor quality and low compressive strength of batch 1.

Since batch 4 (w/c = 0.50+GGBS) was an unloaded control beam and did not sustain any load or post-tensioning, the f'_t and f'_r values were not needed, allowing only six cylinders to be cast for batch 4. All raw material testing data can be found in Appendix B, along with the equations used to determine the specific materials strengths. Table 3.4 shows a summary of all the relevant material data results.

Figure 3.12: Splitting tensile test performed on Galdabini 1890 loading machine

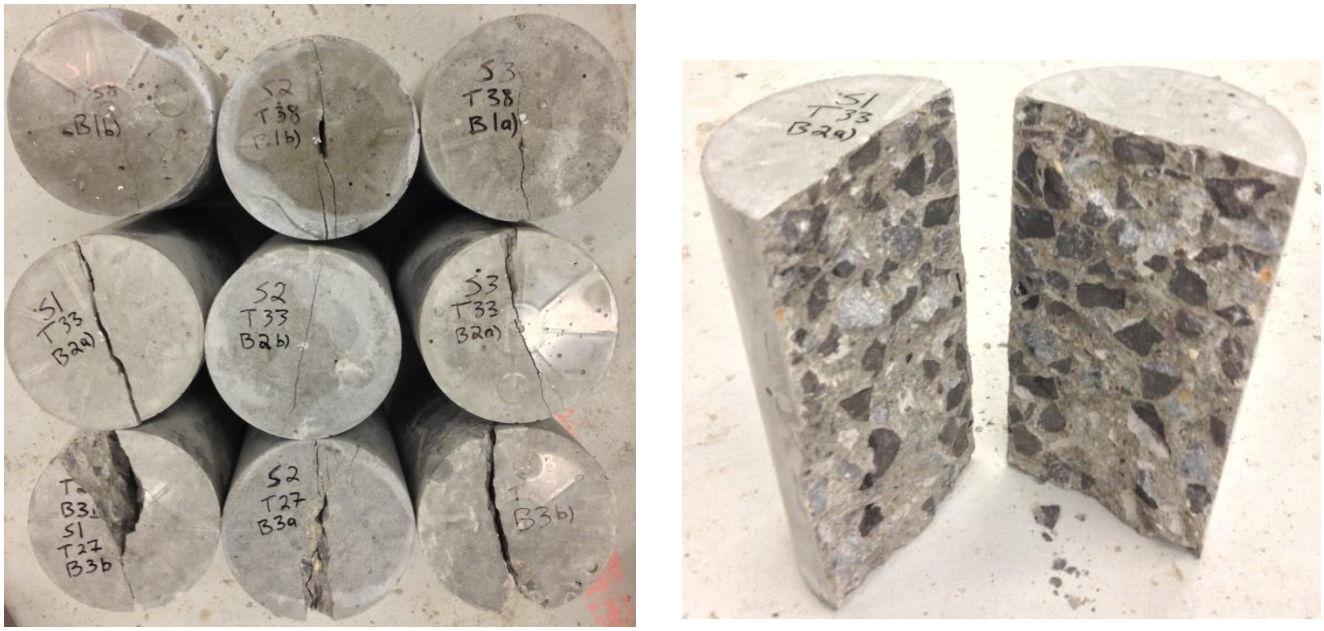

Figure 3.13: Concrete specimens after being failed by splitting tensile test

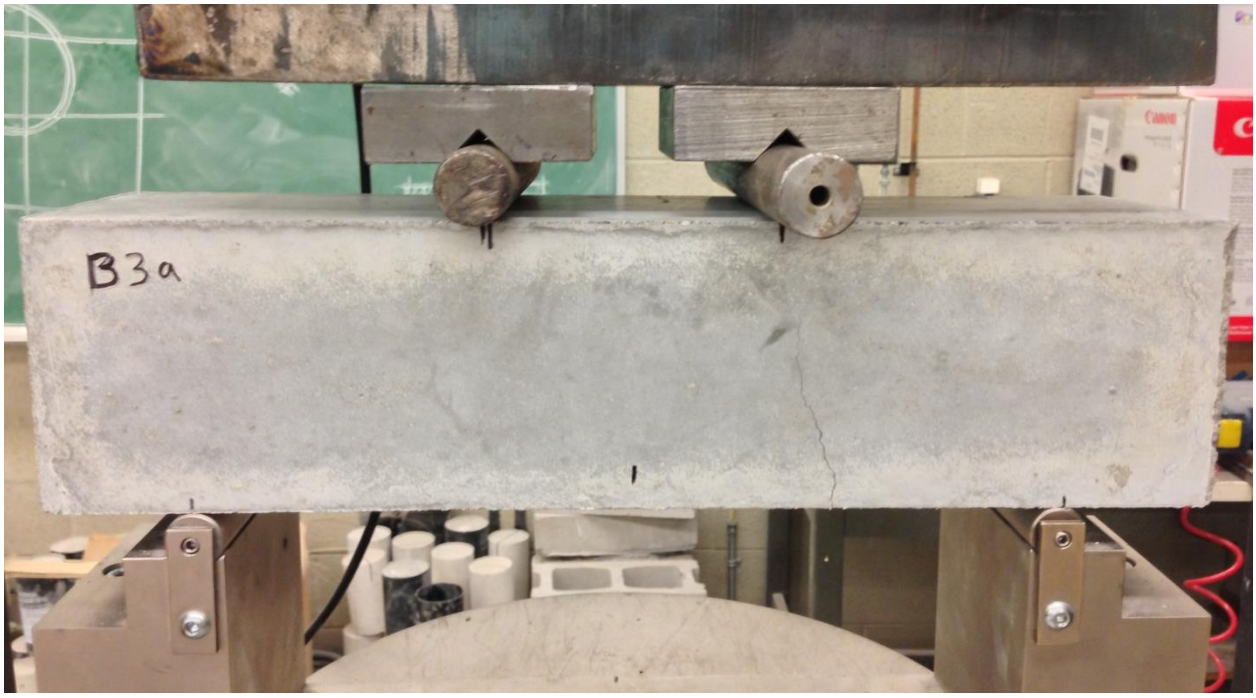

Figure 3.14: Modulus of rupture test being performed on Galdabini 1890 loading machine

The Galdabini 1890 loading machine only gives the option of a loading rate in mm/min. However, the A23.2-8C standard for determination of the modulus of rupture of a concrete prism under four-point loading gives a specific range of loading rates in MPa/min (0.85-1.2 MPa/min). In order to convert from MPa/min to mm/min loading rates, the elastic modulus (E_C) of the concrete must be known. A compressometer with a span length of 135 mm was initially used during compression testing to determine E_C. Raw compressometer data in accordance with ASTM C469/C469M-10 standards can be found in Appendix B; Figure 3.15 and Figure 3.16 show the graphical results obtained from the compressometer for two w/c ratios.

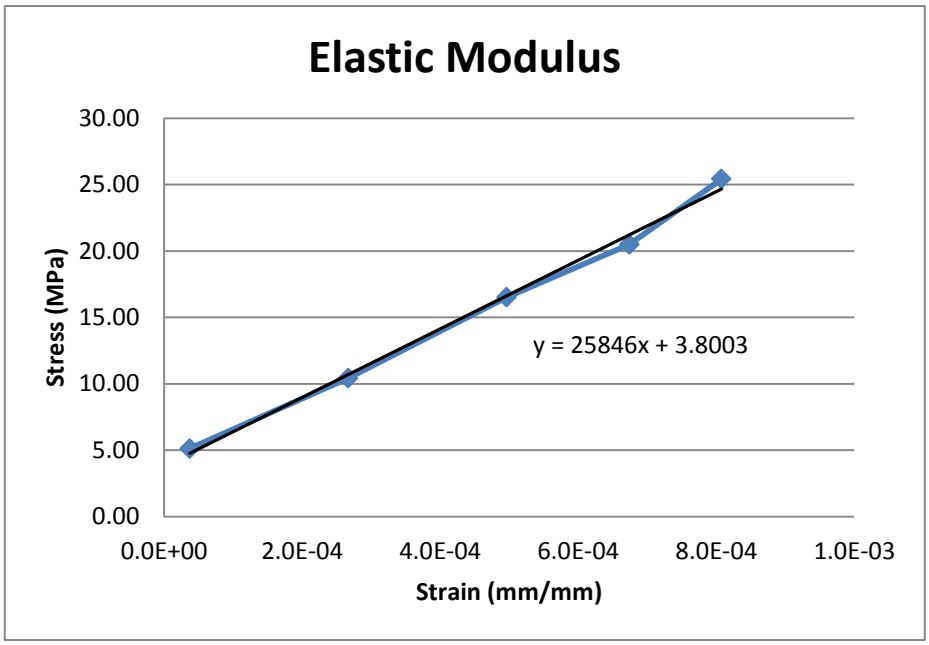

Figure 3.15: Elastic modulus determination for batch 2 (w/c = 0.40; 28day)

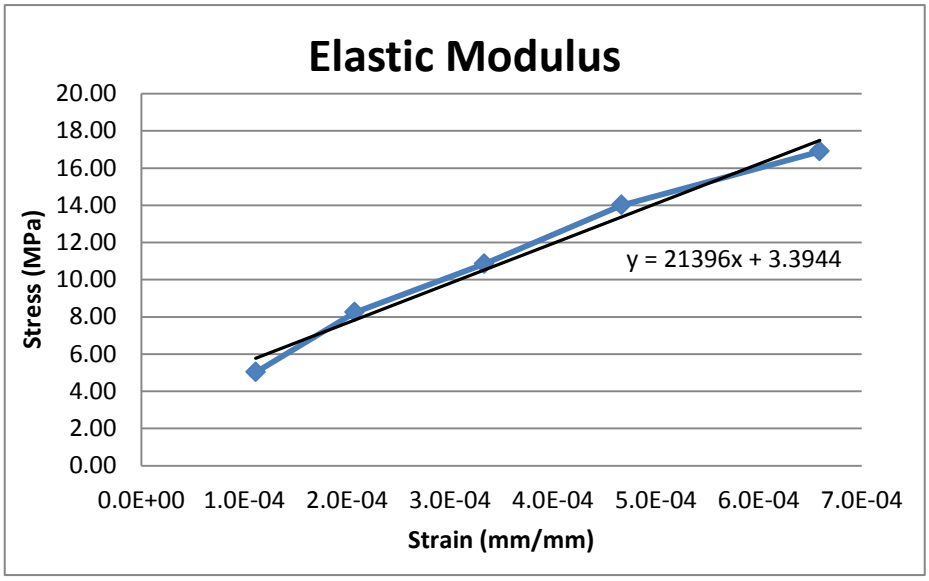

Figure 3.16: Elastic modulus determination for batch 4 (w/c =0.5; 7day)

Results from other batches at different ages did not give expected or valid deformations. Figure 3.15 and 3.16 show the most accurate determination of E_C out of all the trials, with values of 25.8 GPa and 21.4 GPa for w/c of 0.4 and 0.5, respectively. However, these results are still lower than the E_C calculated from the CSA A23.3-04 standard equations. Therefore, Eq. (3.3) is used to determine the E_C for each batch of concrete. Equations (3.2)-(3.7) determine the modulus of elasticity with respect to clause 8.6.2.2 of the CSA A23.3-04 design handbook and the conversion from MPa/min to mm/min:

$$\gamma_{C=} \frac{total\ mass\ of\ concrete\ mix\ ingregients\ (kg)}{total\ volume\ of\ batch\ (m^3)} \tag{3.2}$$

$$E_C = \left(3300\sqrt{f'_C} + 6900\right)\left(\frac{\gamma_C}{2300}\right)^{1.5} \tag{3.3}$$

$$I_G = \frac{bh^3}{12} \tag{3.4}$$

$$P = \frac{\sigma_{loading\ rate} \cdot I_G}{\left(\frac{d}{2}\right)a} \tag{3.5}$$

$$y = \frac{Pbx}{6E_C I_G L}(-x^2 - b^2 + L^2) \tag{3.6}$$

$$y_{total} = 2 \cdot y \tag{3.7}$$

where γ_C is the density of the concrete (kg/m^3), E_C is the modulus of elasticity of concrete (MPa), b and h are respectively the width and height of the concrete prism, I_G is the gross moment of inertia (mm^4), P is the load to cause the specific loading stress needed (N), L is the span of the prism, y is the deflection of the elastic curve at the application of load (mm), and y_{total} is the total deflection caused by superimposing both loads. Tables 3.3 and 3.4 summarize respectively the values of E_c and corresponding loading rates and the concrete material strengths obtained from the different methods.

Table 3.3: Summary of EC and loading rates

	γ_C (kg/m^3)	E_C (MPa)	y_{total} (mm)	Loading rate (mm/min)
Batch 1 (w/c=0.35)	2562.0	37070	0.0056	0.0056
Batch 2 (w/c=0.40)	2467.6	35354	0.0059	0.0059
Batch 3 (w/c=0.50)	2409.2	30960	0.0068	0.0068
Batch 4 (w/c=0.50+GGBS)	2392.6	31880	-	-

Table 3.4: Summary of concrete material strengths from different test methods

	7d Compression f'_c (MPa)	28d compression f'_c (MPa)	Tensile splitting f'_t (MPa)	Modulus of rupture f'_r (MPa)
Batch 1 (w/c = 0.35)	43.87	51.9	*1.74	**4.46**
	27.02	59.5	3.04	
	45.26	*47.34	2.99	
Average	**38.7**	**55.7**	**3.02**	
Batch 2 (w/c = 0.40)	51.16	58.76	2.50	**3.84**
	44.31	60.0	3.41	
	45.11	51.7	*2.00	
Average	**46.9**	**57.0**	**2.96**	
Batch 3 (w/c = 0.50)	24.5	45.7	*1.71	**$0.6\lambda\sqrt{f'_c} = 4.0$
	32.7	43.0	2.83	
	28.5	*34.0	3.31	
Average	**28.6**	**44.3**	**3.07**	
Batch 4 (w/c = 0.50)	32.5	49.6	-	-
	36.7	48.0	-	
	32.8	49.86	-	
Average	**34.0**	**49.2**	-	

* Cylinder was very inconsistent and/or was not rodded/compacted/loaded properly, therefore it was disregarded

** Prism was loaded too fast and caused instant failure, therefore use clause 8.6.4 of CSA A23.3-04

3.2.4 Waterproof Sealant

Beams were sealed with a high build, chemical, corrosion and abrasion-resistant liquid-applied polyurethane coating manufactured and donated by Sika® Canada. Sikagard® E.W.L (elastic waterproof lining) is a two-component (resin and activator) elastomeric coating that has been specifically designed for use in the demanding water and wastewater industries. It is one of the toughest waterproof membranes available, and is ideal for protection against the ingress of a high concentration of chlorides under continuous fully submerged conditions. Figure 3.17 shows the Sikagard® E.W.L product used.

Each beam was sealed with Sikagard® E.W.L on four sides to induce 1-D chloride ingress into the beam; 1-D ingress gives a clearer and more accurate depiction of chloride penetration depths, making the results much easier to observe and analyze. Figure 3.18 shows the direction of chloride ingress into the beam; since the transport direction is only in one plane (y-plane) there is no interference from chloride penetration from side planes (x-plane).

Figure 3.17: Sikagard® E.W.L polyurethane waterproof membrane containers

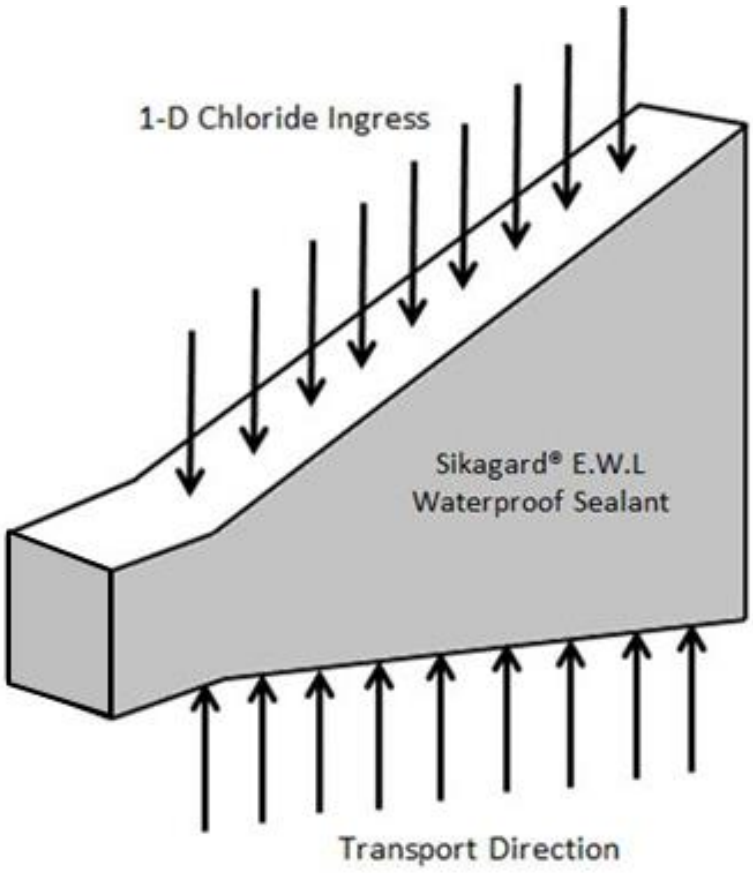

Figure 3.18: Visualization of 1-D chloride ingress into concrete beams

Sikagard® E.W.L has a pot life of 40 mins, therefore it is important to set up properly before application of the membrane. Paint rollers, tape, wooden lifters, plastic tarps, and cleaning products as seen in Figure 3.19(a) and (b) were set up before application. Figure 3.19(a) shows the beams before application, while figure 3.19(b) illustrates the completed beams patched up and ready for submergence. Figure 3.19(a) shows that three beams were sealed with Sikagard® E.W.L before post-tensioning, while the other beams were post-tensioned then sealed. Sikagard E.W.L is able to withstand up to 300% elongation and post-tensioning did not induce any cracks in the concrete, therefore either procedure is acceptable. To determine the ability of the sealant to effectively withstand the chloride exposure conditions (as will be seen in Section 3.4.1), one small test prism was sealed on four sides and exposed to chlorides; it was found that after one month of exposure 1-D chloride ingress was observed and the sealant was effectively preventing the transport of chlorides as it was designed to do.

Varisol industrial cleaning solution was used on the top and bottom surface of the beams (where chloride ingress was intended to occur); it is unknown how the reaction of varisol and concrete affect the ingress of chlorides, but it should be negligible since varisol completely evaporated after application.

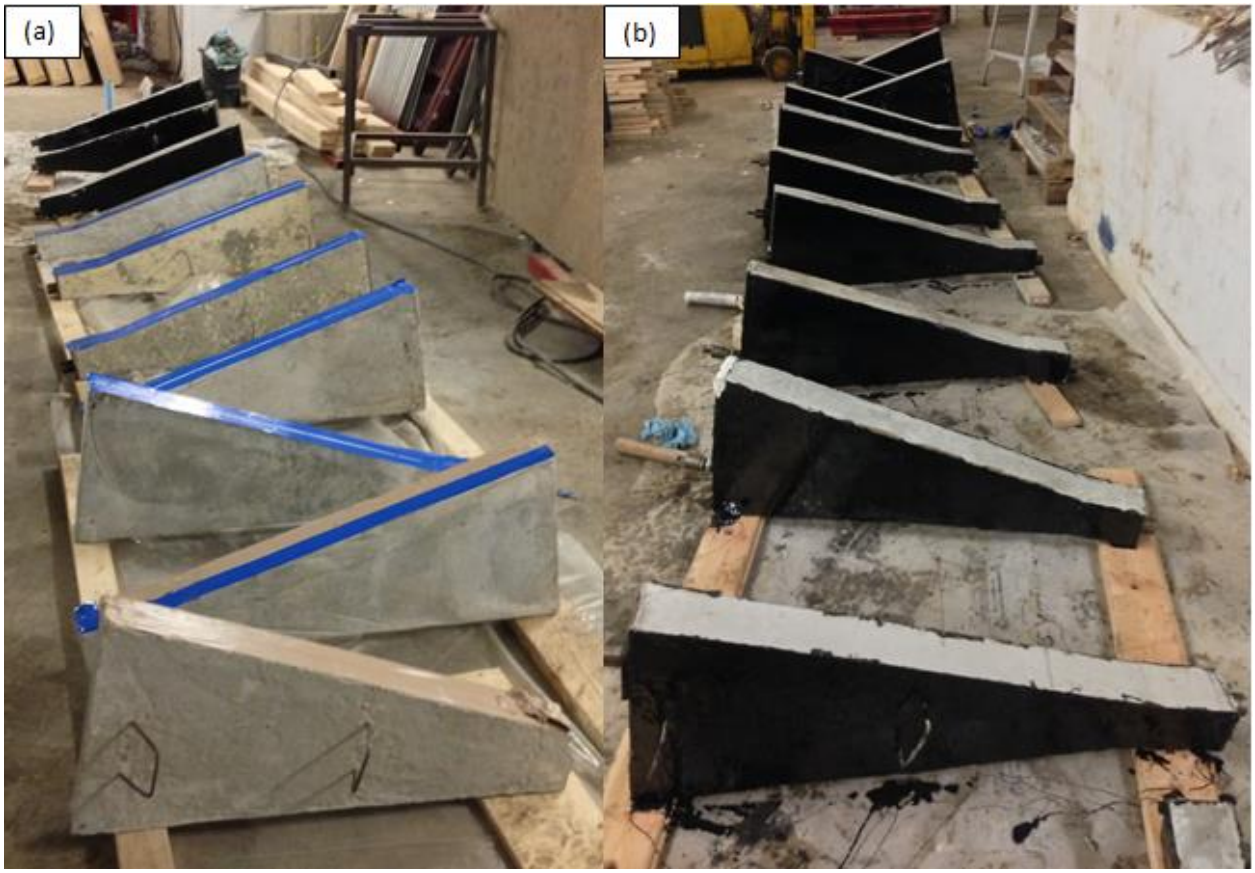

Figure 3.19: Application of Sikagard® E.W.L in Structures Lab (a) before and (b) after application

3.2.5 Post-Tensioning

Because beams are not reinforced other than having one ½" tendon, it is important that when being post-tensioned, compressive and tensile stresses in the concrete do not exceed the material strengths found in Table 3.4. If the post-tensioning force is too high concrete can crush under compressive stress or it can crack and fracture if tensile stresses are exceeded. Figure 3.20 shows the post-tensioning jacks and set up used to apply load to six concrete beams, where the main hydraulic jack applies the post-tensioning force, and the secondary hydraulic jack locks the force by means of a barrel and wedge anchorage.

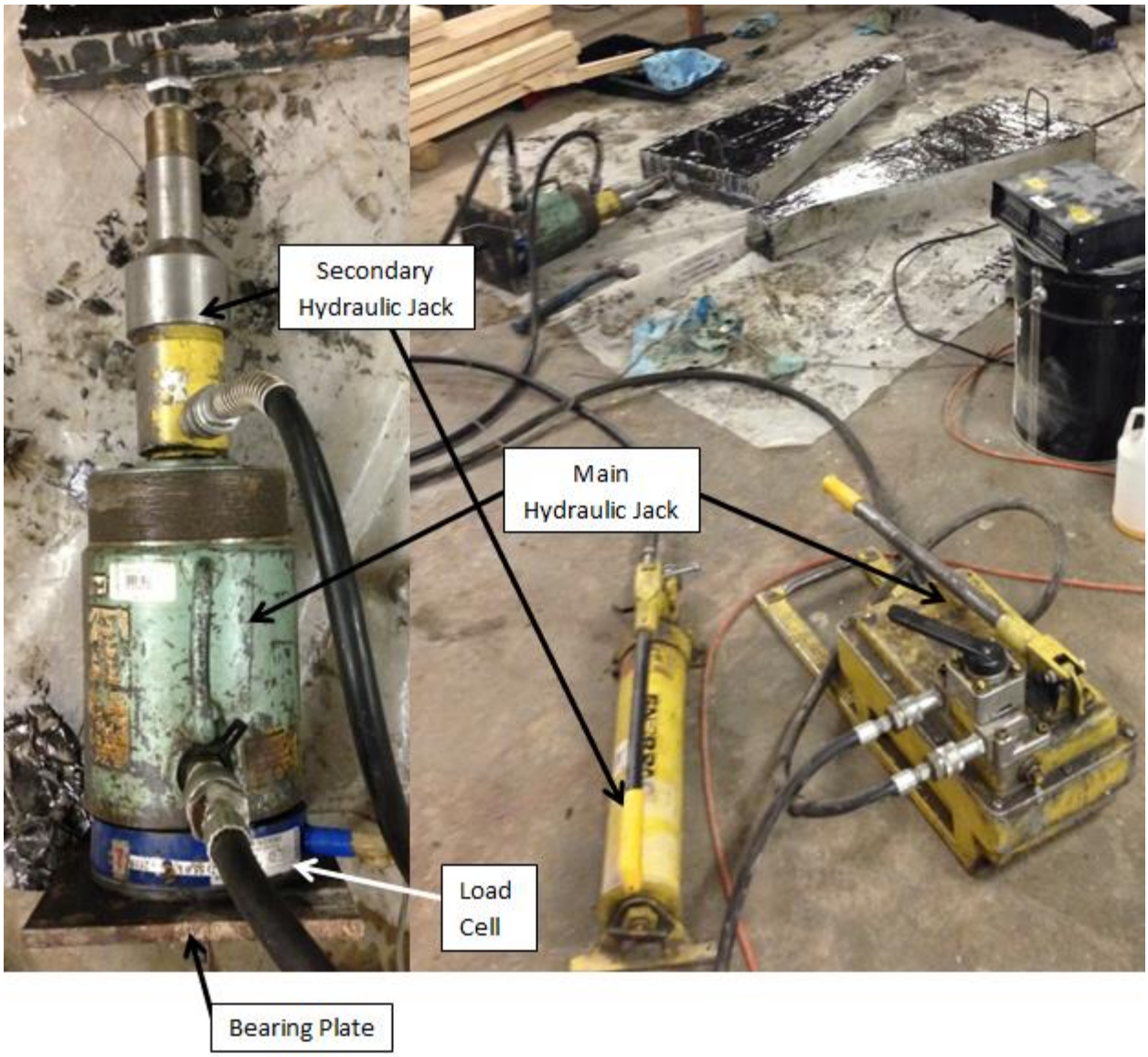

Figure 3.20: Post-tensioning hydraulic jacks and experimental set-up

A load cell as seen in Figure 3.20 was used to determine the post-tensioning load applied. Table B.5 in Appendix B shows the load cell calibration readings obtained from the Galdabini 1890 loading machine; it was found from the load cell calibration curve in Figure 3.21 that post-tensioning load = load cell readings/2.09. Table 3.5 shows the post-tensioning loads applied to each beam; there is a small loss of force once the secondary locking jack is activated due to relaxation of the tendon.

As seen in Table 3.5, post-tensioning loads of 153 kN and 130 kN were developed in beams 3 and 9, respectively. However, when using P = 153 kN and 130 kN in Eq. (3.1), tensile stresses of -7 MPa and -6 MPa are theoretically developed in the beam. This exceeds the material strengths found in Table

3.4; however, the beams did not crack or rupture. The reasoning behind this is that post-tensioning was done 10-15 days after the splitting tensile and modulus of rupture tests were performed, allowing concrete to develop more strength with age; it was difficult to intentionally crack the beams given the strength of the concrete and the maximum load capacity of the post-tensioning tendon. Material strength tests were not performed on the day of post-tensioning.

As discussed in the literature review, the application of external loading will cause compressive and tensile microcracking to occur that will directly impact the transport properties of chlorides into concrete. In order to accurately analyze trends it would be of benefit to determine the changes in concrete microstructure after compressive and tensile stress have been applied. Microcracking can be assumed based on critical stress values obtained experimentally (Lim et al, 2000), or can be determined with non-destructive methods such as mercury intrusion porosimetry or surface electrical resistivity. However, due to time constraints and the fact that stress varies along the length of each beam, microcracking was assumed to occur based on estimated critical stress values.

Table 3.5: Post-tensioning load obtained from hydraulic jacks

Beam Number	Load cell reading before locking	Load cell reading at locking	Post-tensioning force (kN)
2 (w/c =0.35)	76	72	**34**
3 (w/c =0.35)	330	320	**153**
5 (w/c =0.40)	77	71	**34**
6 (w/c =0.40)	168	158	**76**
8 (w/c =0.50)	78	73	**35**
9 (w/c =0.50)	280	270	**130**

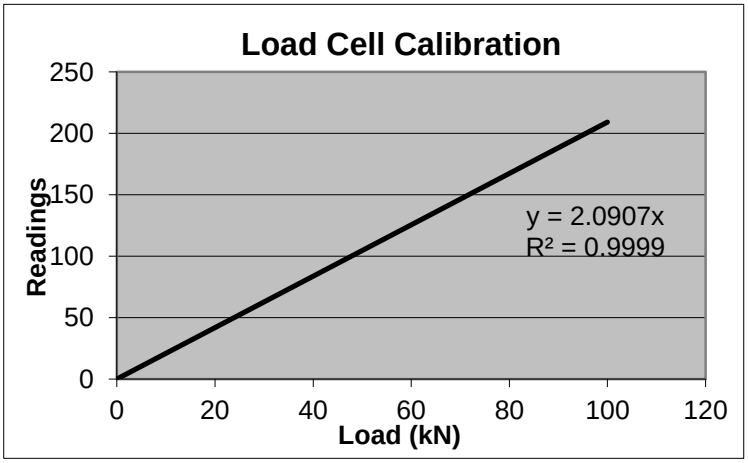

Figure 3.21: Load cell calibration curve

Before fracturing beams at various locations for analysis, as will be seen in Section 3.4.2, the post-tensioning force had to be loosened and de-stressed. In order to accomplish this, two separate systems were developed to release the load from the tendon. Figure 3.22(a) shows a steel plate which is hammered off with great force to create a gap, causing the tendon to relax and release the load. Figure 3.22(b) shows a bolt and fastener mechanism which is rotated into itself, slowly releasing the load and allowing the tendon to relax after every rotation. The bolt and fastener method only supported post-tensioning loads of 35 kN before rupturing. Since tendons were coated with grease inside the duct, they easily slid out of the duct to allow for beams to be fractured into smaller sections.

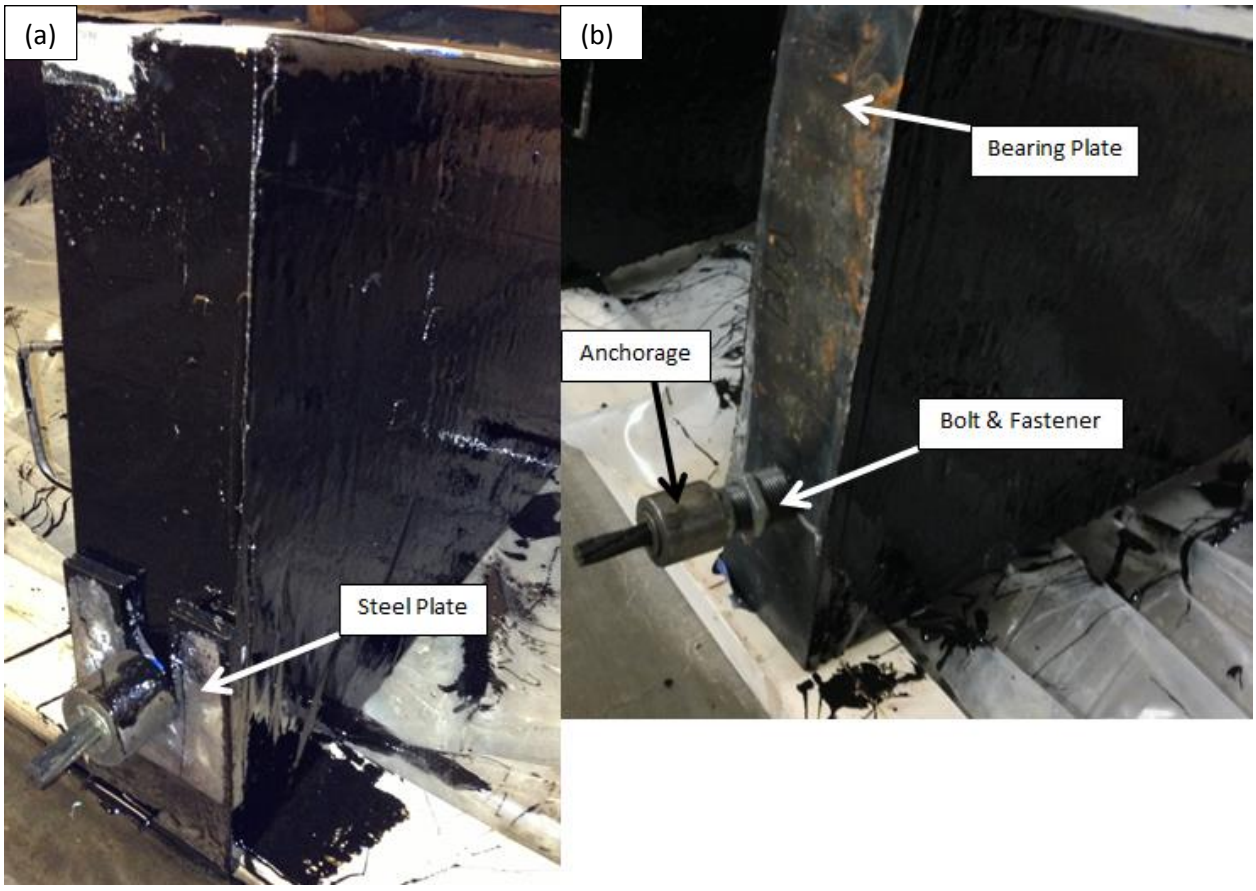

Figure 3.22: Anchorage and de-stressing systems (a) steel plate and (b) bolt & fastener

3.3 Experimental Grid

This experimental grid details and labels the ten beams that were constructed according to the previous section's specifications. The main parameter that affects the overall concrete mix design is the w/c ratio; different w/c ratios affect the concrete strength and porosity as seen in Table 3.6. As mentioned before, beam 10 has the addition of GGBS to the mix design of batch 3. Each w/c ratio has an unloaded control beam, an upper, and a lower bound post-tensioning force to allow for a wide range of sustained compressive and tensile stresses. Compressive strength results for w/c = 0.35 and tensile strength results for w/c = 0.40 do not give expected results; as mentioned before, inconsistency of batch 1 test cylinders likely caused a decrease in f'_c of w/c = 0.35, and inconsistent tensile splitting test results as seen in Table B.2 (Appendix B) contributed to the unreliable splitting tensile results for all w/c ratios. Beams 7 and 10 were unintentionally split at the critical section when transporting; since they were non-reinforced, they were extra vulnerable to cracking caused by sudden external forces. The consequences of this can be seen in the average chloride penetration depths in Appendix C.

Table 3.6: Summary of beam details for all the specimens used in the experiment

Specimen	w/c	Post-tensioning Load (kN)	Average 28-day Compressive Strength f'_c (MPa)	Average Splitting Tensile Strength f'_t (MPa)	Modulus of Rupture f'_r (MPa)
Beam 1	Batch 1 0.35	0	55.7	3.02	4.46
Beam 2		34			
Beam 3		153			
Beam 4	Batch 2 0.40	0	57.0	2.96	3.84
Beam 5		34			
Beam 6		76			
Beam 7	Batch 3 0.50	0	44.3	3.07	4.0
Beam 8		35			
Beam 9		130			
Beam 10	Batch 4 0.50	0	49.2	-	-

3.4 Evaluation of Chloride Ingress

The following sections describe the methodologies used to quantify the amount of chlorides in the concrete. The amount of chlorides penetrating the concrete cover as a result of the 12-week exposure condition was determined by two different methods; a qualitative colourimetric method, and a quantitative potentiometric titration method.

3.4.1 Chloride Exposure Conditions

Ten beams, as described in Table 3.6, were completely immersed for 12 weeks in a 4-5% NaCl (de-icing salt) solution, as seen in Figure 3.23. The immersion tank has dimensions of 1 m height x 2.55 m length x 1.4 m width, with a wall thickness of 20 cm. A special type of waterproof epoxy sealant, as seen in Figure 3.23, was painted inside of the tank to prevent water leakage; the masonry tank was also covered during the experiment to minimize water evaporation and therefore not leading to a consequent increase of the concentration of the NaCl solution.

Figure 3.23: Immersion of concrete beams into 4-5% NaCl solution

With the beams placed in the tank, preliminary volume calculations gave an estimate of roughly 1 m^3 or 1000 L of water up to the blue epoxy sealant. Therefore, in order to achieve a concentration of 5% NaCl, 53 kg of commercially available de-icing salt was initially added to the tank. As concrete became fully saturated with the 5% NaCl solution, chlorides began to ingress into the concrete and effectively diluted the solution in the tank. Therefore, NaCl concentrations in the tank were monitored weekly to ensure that the concentration remained relatively consistent. Figure 3.24 shows the fluctuating concentration conditions in the tank, while Table 3.7 shows the monitoring details along with the amounts of extra salts added to the tank to try and keep the NaCl concentration consistent. Initial additions and subsequent additions of de-icing salt into the tank did not completely dissolve into solution, leaving salt crystals at the bottom of the tank for the entire 12 weeks exposure. Great care was taken to manually crush salt and stir the tank regularly, but it was found that chloride concentrations at the bottom of the tank were greater than the surface.

NaCl concentrations were measured with Hach chloride titrator tabs for 1% NaCl, 25 mL samples were diluted 10x; Figure 3.25 shows the results for the first NaCl concentration taken after the initial 53 kg of salt was added. The initial tank concentration was not measured, but assumed to be 5% NaCl based on mass calculations. The initial drop in concentration is caused by the ingress of chlorides into chloride-free concrete; concentrations levels increased as the salt continued to slowly dissolve into solution.

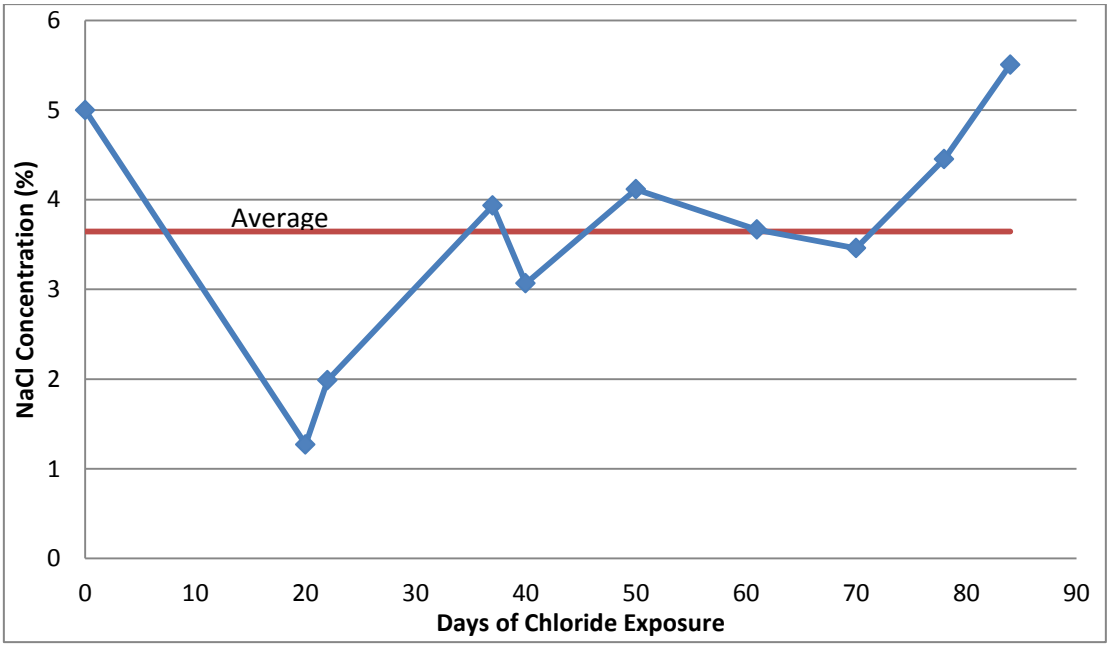

Figure 3.24: Measured NaCl concentrations in tank over entire exposure duration

Table 3.7: Summary of average NaCl concentration in tank over entire exposure duration

Date	Days of Exposure	Average Concentration NaCl (%)	Average Concentration Cl (%)	Notes
Feb-06	0	5.0	3.0	actual 5% concentration is unknown (added 53kg of NaCl/1053kg total mass)
Feb-26	20	1.27	0.762	added 27kg of salt, salt was not manually crushed
Feb-28	22	1.98	1.192	added 20kg of salt, salt manually crushed
Mar-15	37	3.93	2.36	tank stirred
Mar-18	40	3.06	1.84	tank not stirred before sample taken (added 10kg of salt)
Mar-28	50	4.11	2.47	tank not stirred before sample taken
Apr-08	61	3.66	2.20	tank not stirred before sample taken
Apr-17	70	3.46	2.076	tank not stirred before sample taken
Apr-25	78	4.45	2.672	tank not stirred before sample taken
May-01	84	5.50	3.304	tank not stirred before sample taken
	Average	**3.646**	**2.187**	

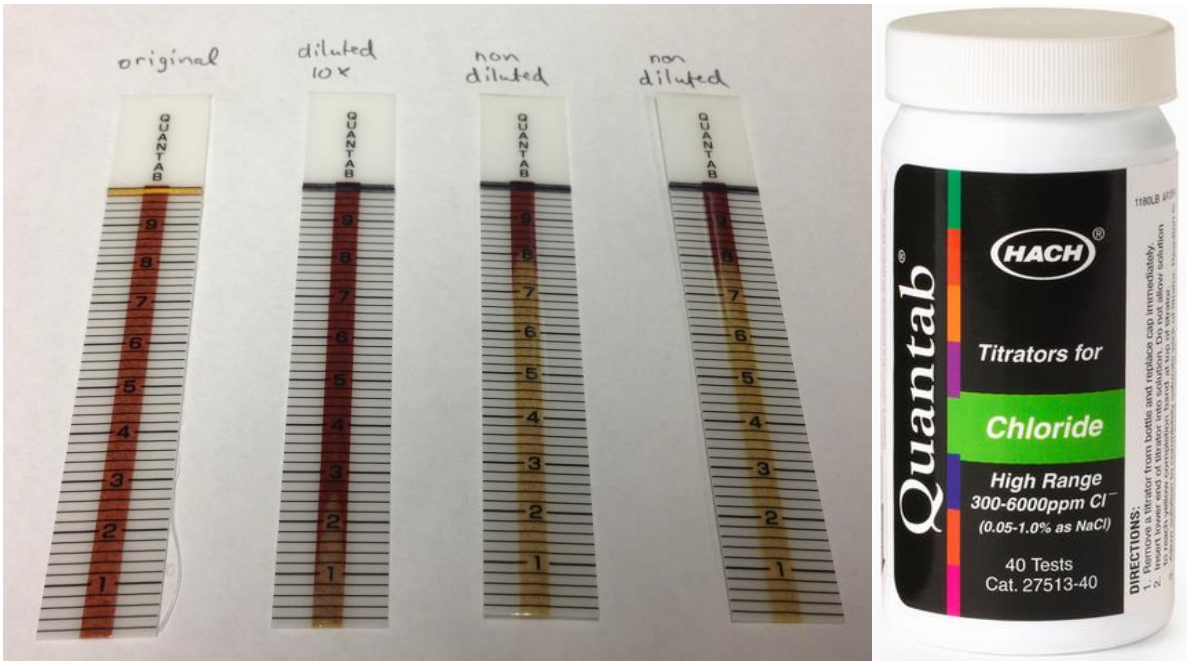

Figure 3.25: Chloride test strip results for February 26th, 2013 (Hach Company, 2013)

Figure 3.26 shows the fully submerged concrete beams after only one month exposure time; high levels of chlorides had caused significant rusting in a short time frame. Steel handles, bearing plates, post-tensioning tendons, and anchorage show signs of significant rust, with small localized clouds of negative chloride ions from solution attracted to and surrounding the positive metal steel handles.

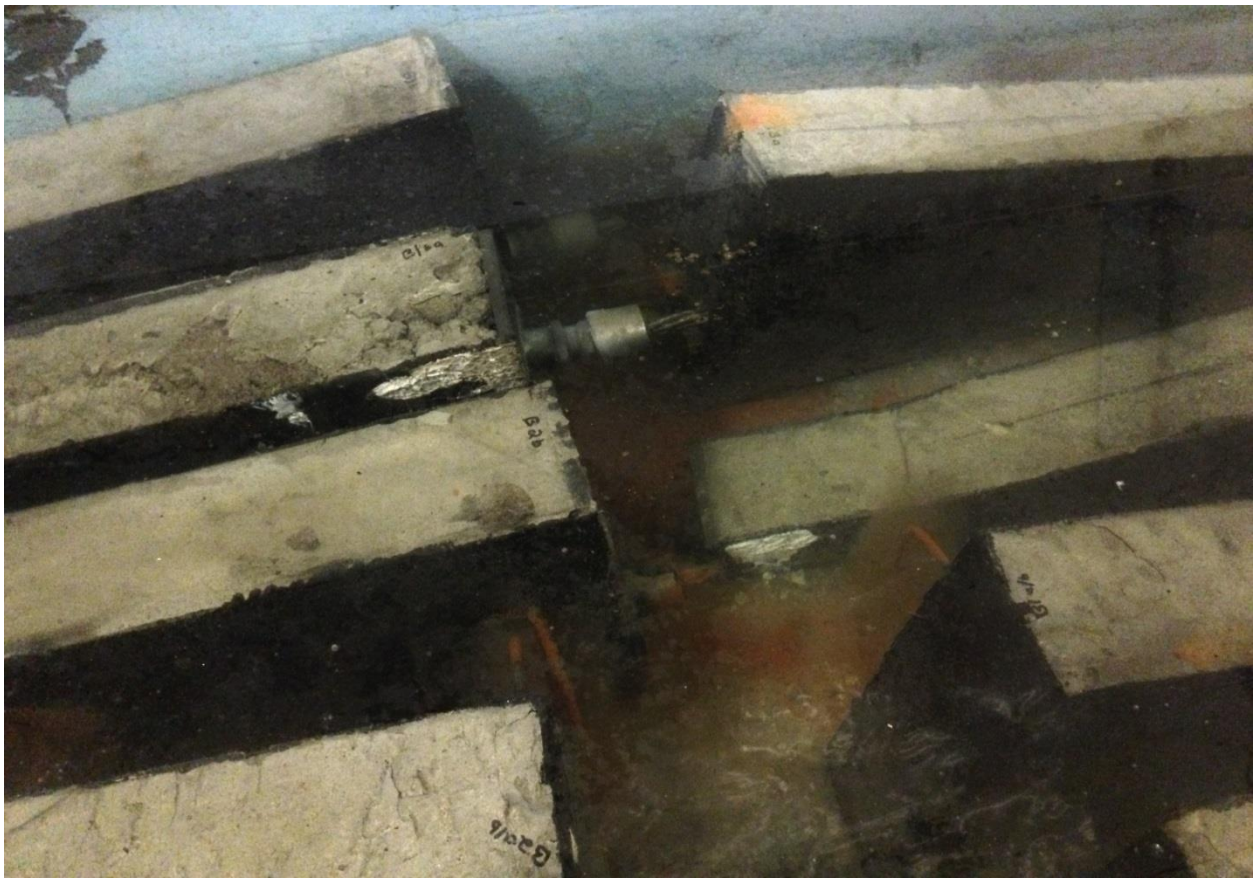

Figure 3.26: Submerged concrete specimens after one month exposure time

3.4.2 Colourimetric Method: Silver Nitrate Spray ($AgNO_3$)

After 12 weeks of exposure to a 4-5% NaCl solution, water was drained from the tank, and the beams were allowed to dry as seen in Figure 3.27. Salt residue was left over on the top face of each beam after drying, giving a white powdered look. In order to determine the average chloride penetration depth along the length of the beam, each beam was first fractured into five 200-mm sections (with the exception of 150 mm at the critical section) as illustrated in Figure 3.28. Figure 3.28 also shows how the compressive and tensile stress levels correspond to each sectional fracture of the beam, having high stresses at the critical section, and the lowest stresses at the largest cross-section of the beam.

Figure 3.27: Concrete beams drying after 12 weeks of exposure in tank

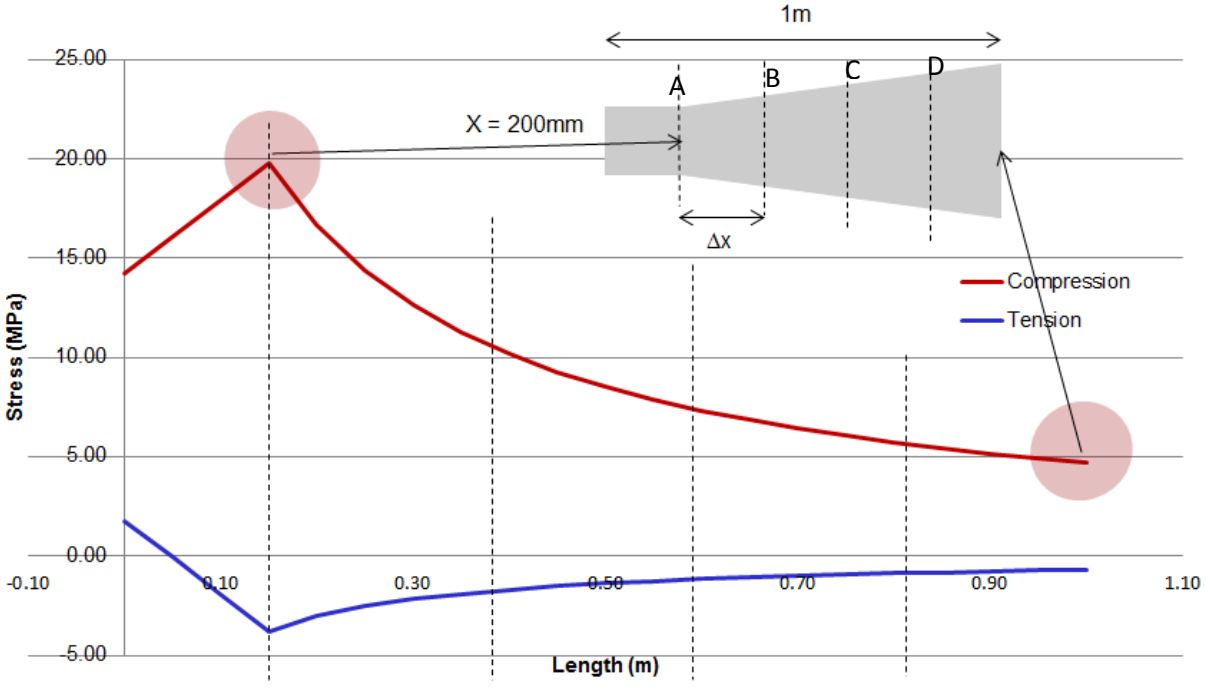

Figure 3.28: Determination of sectional cuts for average chloride penetration depths

Figure 3.29 shows how each beam was physically fractured in the lab, where (a) 5-mm notches were made on three sides of the beam with a disk diamond saw, (b) the beam was supported under critically weak sections and fractured with a sledgehammer at the midspan of the supports, and (c) the final product of all five sections after the post-tensioning duct was cut. Fracturing beams did not always give clean cuts, and it was later found that two 5-mm notches at the top and bottom face of the beam were sufficient; however, if beams were fully cut by a disk diamond saw, chloride-free zones would have become contaminated by concrete powder from a dry cut or water washing away free chlorides in a wet cut. Figure 3.30 shows all ten concrete beams after being fractured into sections.

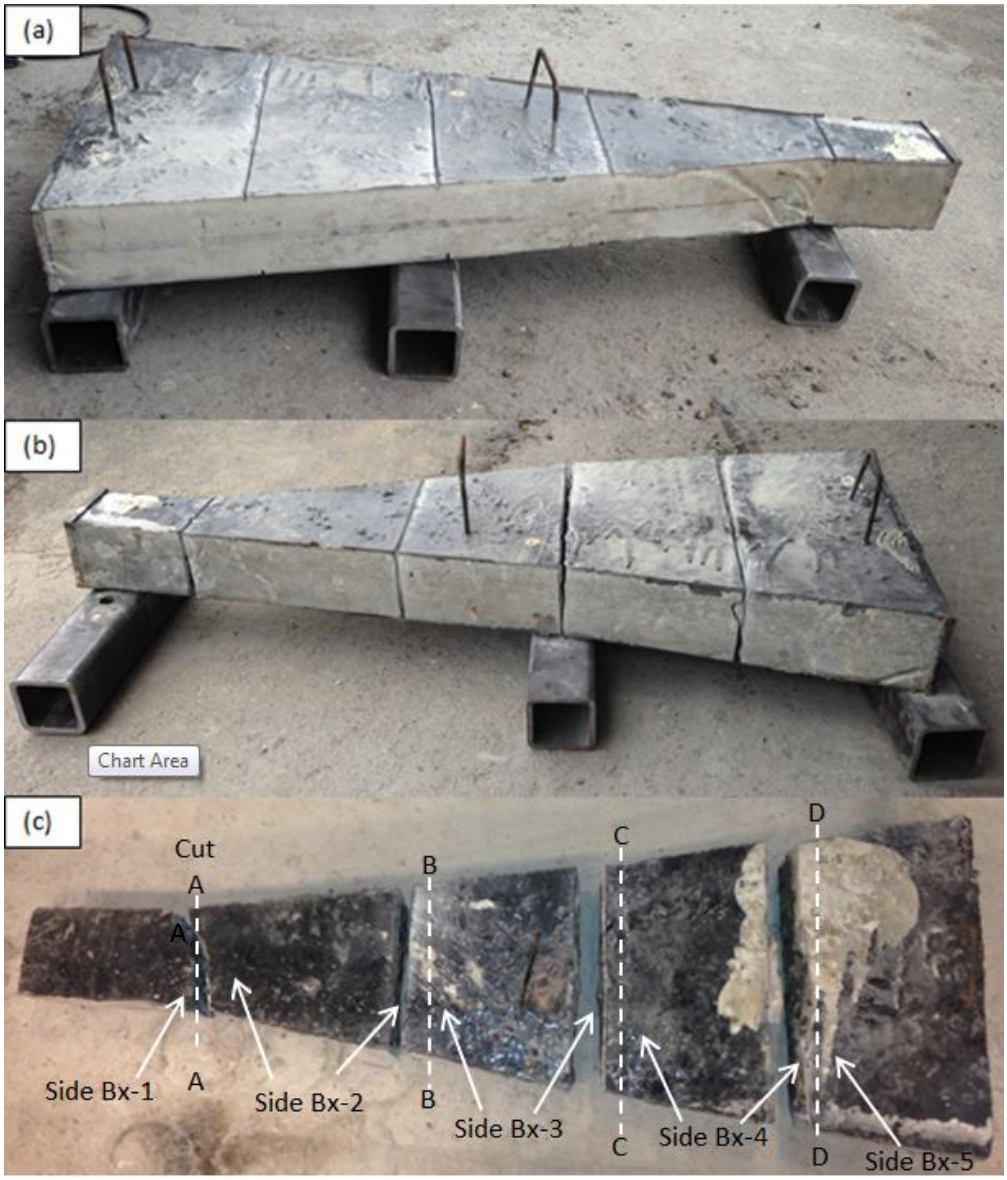

Figure 3.29: Fracturing beams in the lab into five 200-mm sections

Figure 3.30: All ten concrete beams completely fractured in the lab

The average depth of chloride penetration for each fractured section was determined by spraying a 0.1N (mole/L) silver nitrate ($AgNO_3$) solution on freshly split concrete samples. When free chlorides are present in the concrete pore solution, they react with silver nitrate to form a white/greyish precipitate (silver chloride). The chemical reaction that occurs is given by:

$$AgNO_3(aq) + NaCl(aq) \rightarrow AgCl \downarrow + NaNO_3(aq) \qquad (3.8)$$

This method is commonly referred to as the colourimetric method (Andrade et al. 1999), and it provides a quick and inexpensive way of estimating chloride contamination in concrete by measuring the depth of the colour change boundary (Deif, 2010). Spraying concrete with silver nitrate does not provide the value of chloride concentration; the depth represents the average penetration front of free chlorides (chlorides that are dissolved in the concrete pore solution and react with silver nitrate).

Figure 3.31 shows freshly fractured concrete sections being sprayed with a 0.1N silver nitrate solution in the lab, while figure 3.32 shows the chloride penetration front and colour change boundary in a fractured section of concrete. Chapter 4 and Appendix C outline visual and tabular

average penetration depths for all sections of all beams, while Figure 3.29(c) explains the labelling of each fractured beam.

Figure 3.31: Spraying silver nitrate (AgNO3) on freshly fractured concrete samples

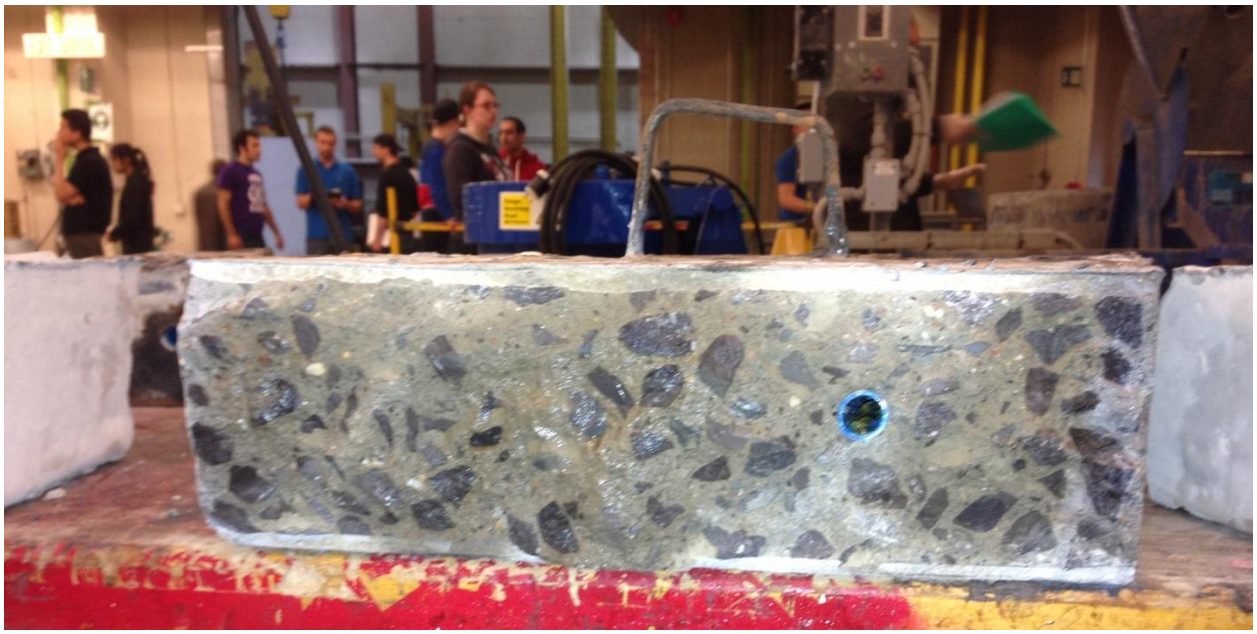

Figure 3.32: Section of concrete beam after being sprayed with silver nitrate

3.4.3 Potentiometric Titration: Chloride Concentration

The colourimetric method described above is a qualitative method that does not give actual chloride concentrations at different penetration depths. However, potentiometric titration is a quantitative method that does give an estimate of chloride concentrations at different penetration depths. The procedure used to carry out titrations for this study follows the ASTM C 1152/C 1152M-04 standard. The same fractured sections that were sprayed with silver nitrate were also used for titration chemical analysis.

In order to isolate for certain compressive and tensile stresses and simplify the chemical analysis, not all fractured sections were used to obtain a chloride concentration profile; Table 3.8 shows the methodology behind the selection of chloride concentration profiles. Chosen stress values for each w/c are approximate; actual stress values obtained are slightly different based on sectional fractures and different post-tension loads. Fractured sections corresponding to each estimated stress level can be seen in brackets, and the actual stress acting on each chosen section can be seen in Appendix C.

Table 3.8: Determination of chloride profile locations

w/c ratio	Compression			Tension		
	Lower stress (MPa)	Higher stress (MPa)	Unstressed control (MPa)	Lower stress (MPa)	Higher stress (MPa)	Unstressed control (MPa)
0.35	5.0 (B2-B;B2-3)	19.0 (B3-B;B3-2)	0 (B1-C;B1-3 and B1-B;B1-3)	1.5 (B2-A;B2-2)	3.0 (B3-B;B3-2)	0 (B1-A;B1-2)
0.40	5.0 (B5-B;B5-3)	19.0 (B6-A;B6-2)	0 (B4-B;B4-2 and B4-C;B4-3)	1.5 (B5-A;B5-1)	3.0 (B6-A;B6-2)	0 (B4-B;B4-2)
0.50	5.0 (B8-B;B8-3)	19.0 (B9-B;B9-2)	0 (B7-B;B7-3 and B7-C;B7-4)	1.5 (B8-A;B8-2)	3.0 (B9-B;B9-3)	0 (B7-C;B7-4)
0.50 + GGBS	-	-	0 (B10-B;B1-3 and B10-D;B10-4)	-	-	0 (B10-D;B10-5)

Titration was done on concrete sections that were ground into fine powder that passed a No. 20 sieve. An adjustable profile grinder, as seen in Figure 3.33(c), was used to create concrete powder in 5.0-mm depth intervals from the exposed surface to 5 mm below the colour change boundary of each specific section resulting from the $AgNO_3$ spray. Figure 3.33(a) shows the grinding process with the use of a steel plate to capture the powder and prevent it from being lost; Figure 3.33(b) shows the powder collection from a ground section. In order to obtain the 5 g of fine powder required by

the ASTM standard, more than one hole was needed. Powder samples were stored in labelled plastic bags until titration was carried out.

Figure 3.33: Profile grinding process used for each beam section to obtain concrete powder

Chemical analysis done on concrete powder obtained from the 5.0-mm depth interval samples provides an average chloride concentration value over the 5-mm depth. Therefore, if a powder sample is taken for a depth of 1.5 cm, then chlorides are assumed to be measured at a depth of 1.25 cm. This can be seen in the complete titration results for all sections found in Appendix D. Figure 3.34 shows the 2.0 mm deep holes created by the concrete profile grinder for section B4-3. To prevent contamination of samples and ensure each plastic bag only contains powder from 5.0 mm depth of sample, the profile grinder and concrete section were cleaned from excess powder every 5.0 mm with compressed air.

Figure 3.34: Holes created in concrete samples by profile grinder

As mentioned, potentiometric titration on concrete powder follows the ASTM C 1152/C 1152M-04 standard. However, the filtration step after the addition of nitric acid was skipped because it is a tedious and time consuming process; Climent et al. (2004) showed that there is not a significant difference in the results if the samples are titrated without filtration. Also, by eliminating the filtration step, common handling errors that could lead to solution losses are also eliminated (Climent, de Vera, Viqueira, & Lopez-Atalaya, 2004).

Instead of using a potentiometer as outlined in the ASTM standard, a microprocessor-controlled automatic titrator, the 794 Basic Titrino from Metrohm, was used (see Figure 3.35). The Volhard method as seen in the ASTM standard is more prone to human error when determining the equivalence point (E.P.) of a concrete sample solution; there are risks of misreading burettes and overshooting the titration effectively overlooking the E.P. As the E.P is reached equal additions of

titration solution will cause larger changes in the solution's millivoltmeter readings. However, the 794 Basic Titrino has the ability to detect low chloride concentrations and automatically vary the dosage for the titration solution (0.05N silver nitrate), automatically determine the E.P based on programmed parameters, and display precise results on a display screen. Preliminary measurements done by Deif (2010) compare the results obtained from the Volhard and automatic titration methods; results showed that although both methods give very similar chloride concentrations, concentrations obtained from the Volhard method are usually higher due to the aforementioned reasons. Therefore, according to Deif (2010), it is acceptable and more precise to use an automatic titrator to determine chloride concentrations in the concrete powder samples.

A Dynamic Equivalence Point Titration (DET) mode was programmed into the automatic titrator, where the titration solution dispenses in variable volume increments depending on the slope of the millivolt (mV) vs. volume (V) curve. The DET mode is recommended for titrations where the jumps in mV readings lie very close together or are very flat, and is suitable for most problems

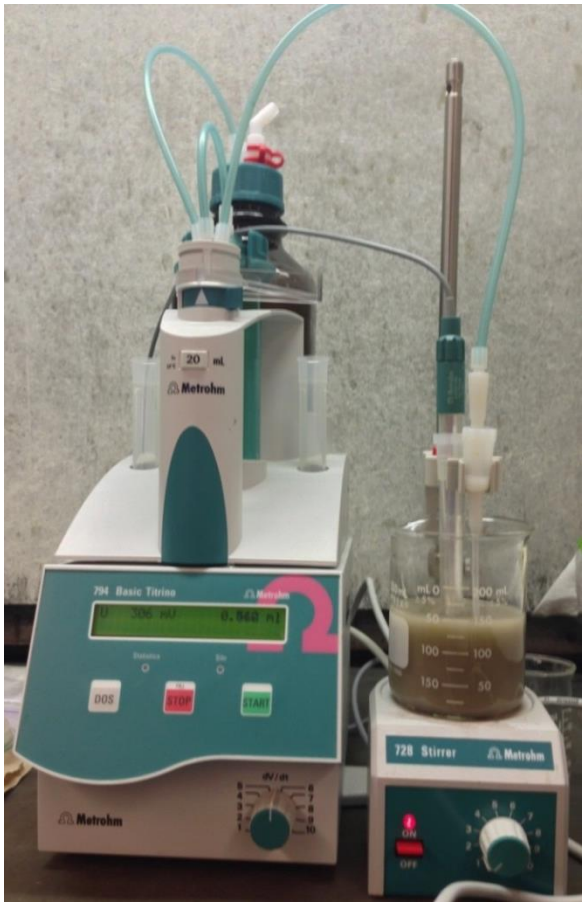

Figure 3.35: 794 Basic Titrino automatic potentiometric titrator

The following outlines the steps taken to determine the chloride concentration for this experiment, the chemical storage procedures, and the waste disposal and handling procedures. ASTM C114-07 recommends that the minimum weight of concrete sample to be analyzed be 5 g if the expected chloride content is below 0.15%; Figure 3.36 shows 5 g of concrete samples ready to be prepared for testing.

Preparation of sample

1. Pulverize concrete sample into fine powder, allow No.20 sieve passing (done in previous section)
2. Measure 5 g of sample and pour into 250 mL beaker
3. Add 75 mL of **distilled deionized water** to disperse sample
4. *Slowly* add 25 mL of 50% **nitric acid (1+1)** and stir with glass rod
5. Add 3 mL of 30% **hydrogen peroxide** if needed (beam 10, which has slag, was the only beam that required it)
6. Add 3 drops of **methyl orange** indicator and stir
7. Cover beaker with a watch glass and allow sample to **stand for 1-2 minutes**
8. Add drops of 50% nitric acid if a pink colour is **NOT** observed, and stir while dropping
9. Heat beaker rapidly to boiling, allow sample to boil for only a FEW seconds
10. Make blank determination using 75 mL of distilled deionized water
11. No filtering required (8.2 skipped)

Figure 3.37 shows the apparatus used to obtain distilled deionized water; this procedure removes unwanted chloride ions from the dispersing water that affect chloride concentration results. Also, to prevent loss of chlorides by volatilization, it is important to keep the beakers covered during digestion (step 7) and boiling (step 9). Watch glasses were used to cover beakers during digestion and boiling as seen in Figure 3.38 and 3.39, respectively.

Automatic titrator

12. Pipet 2 mL of 0.05N NaCl solution into cooled sample beaker
13. Place beaker on magnetic stirrer, allow the stirring motion to be gentle
14. Place mV reading probe and burette with 0.05N silver nitrate into the sample solution beaker
15. Start the automatic titration

16. Wait for titration to automatically stop, then take E.P (volume of $AgNO_3$ consumed) and mV readings
17. Clean probe and dispensing nozzle, properly dispose of analyzed solution, and start at step.1

50% Nitric Acid (1+1)

Should be tightly sealed and stored away from organics and bases, in a cool and dry place. Keep away from open flames and heat sources. Do not store above 23°C. Separate from acids, alkalies, reducing agents and combustibles.

30% Hydrogen Peroxide

Very reactive and must be kept in the fridge at all times. Only take as much as needed out for the day, and keep away from any open flames and heat sources. Separate from acids, alkalies, reducing agents and combustibles. Do not store above 8°C. Store in light-resistant containers.

0.1N and 0.05N Silver Nitrate

Keep containers tightly closed in a cool, dry, and well-ventilated area.

NaCl crystals

Harmless solids that can be stored with other chemicals in a cabinet.

Methyl orange indicator

Keep away from heat sources and open flames. Keep container tightly closed. Keep container in a cool, well-ventilated area. Do not store above 25°C. Keep away from oxidizing agents (hydrogen peroxide and nitric acid).

Waste disposal and handling

- There was approximately 15 L of waste (in aqueous form) in total, 3 L of waste a week.
- Any leftover chemicals not used during the day of titration were diluted and put into the waste container. 10% of the volume of sample as water was added before putting into waste container

- All materials, digested and undigested, went into the same waste container, making sure to add proper amounts of dilution water to the waste container
- Waste container was labelled with: **waste ID (inorganic acids (dilute) and metals (silver)- caution corrosive)**
- Waste container was left uncapped overnight in case of gaseous reactions still taking place
- Plastic lines of the automatic titrator were cleaned (from silver nitrate residue) each day before leaving the lab by running water through them
- At the end of each day, silver nitrate, nitric acid, methyl orange indicator, and salt solution were stored properly in the designated areas
- Since the probe is a separate metal electrode, it only requires storage in a dry place protected from dust; probe was cleaned with distilled deionized water before storage

Figure 3.36: Concrete samples ready for preparation

Figure 3.37: Apparatus used to obtain distilled deionized water for sample preparation

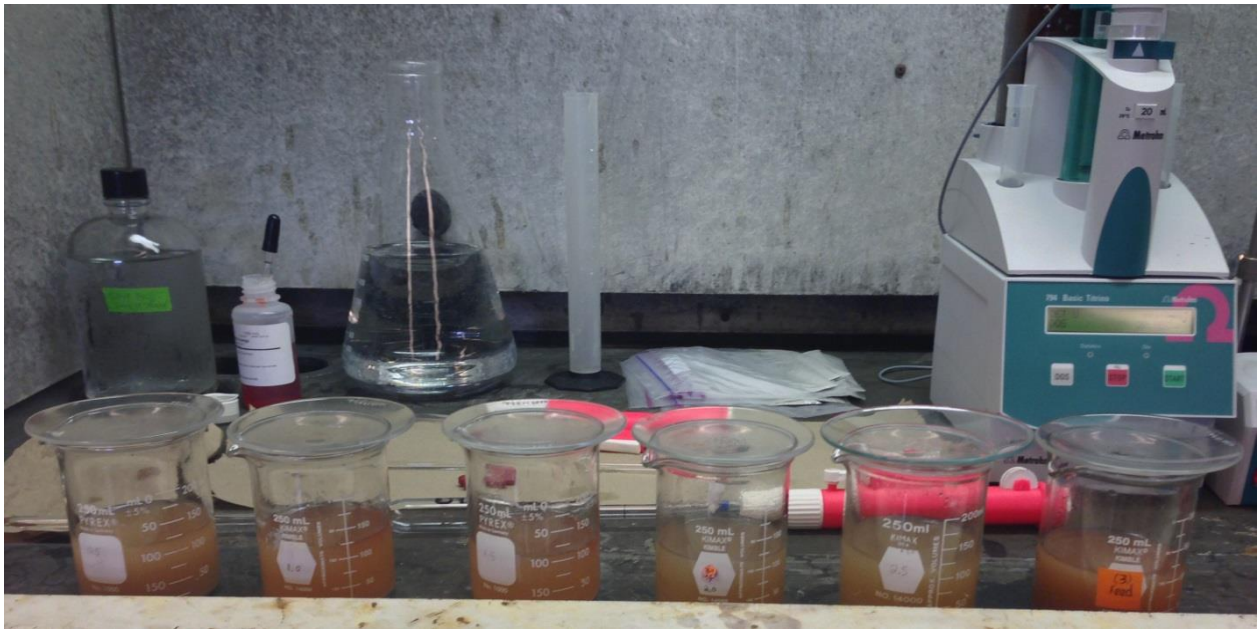

Figure 3.38: Prepared concrete samples digesting and ready to be boiled

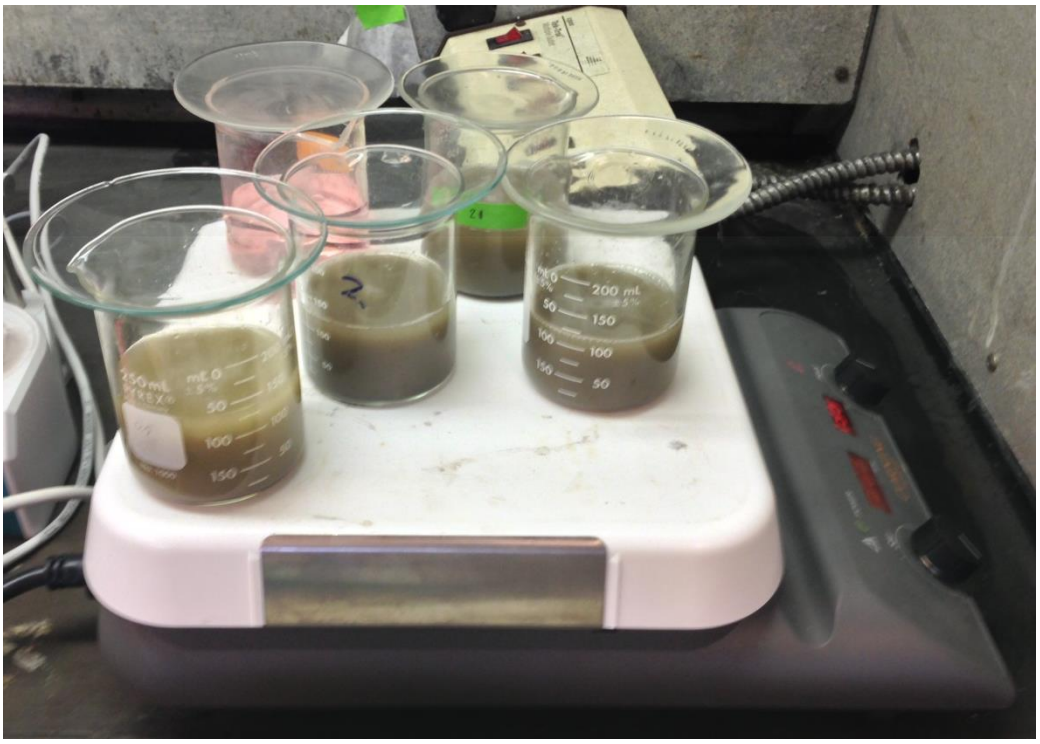

Figure 3.39: Concrete samples boiling and decomposing into solution before being titrated

The percentage of chloride content in each concrete powder sample can be calculated according to ASTM C114-07 as follows:

$$Cl(\%) = \frac{3.545[(V_1 - V_2)N]}{W} \tag{3.9}$$

where V_1 is the volume of consumed 0.05N $AgNO_3$ at the equivalence point for concrete sample titration (mL), V_2 is the volume of consumed 0.05N $AgNO_3$ at the equivalence point for blank titration (mL), N is the exact normality of 0.05N $AgNO_3$, and W is the mass of the concrete sample (g).

Chapter 4 – Experimental Results

4.1 Introduction

This chapter presents the experimental results obtained from conducting the data collection and experimental methods outlined in Chapter 3. Section 4.2.1 gives visual chloride penetration depth results from the colourimetric method for all fractured sections, while Section 4.2.2 gives chloride concentration results from the chosen profiles obtained from potentiometric titration.

4.2 Chloride Content Measurements

4.2.1 Colourimetric Method (Silver Nitrate Spray)

After 12 weeks of exposure in a 4-5% de-icing salt solution, beams were fractured at specific locations as detailed in Figure 3.29. In order to prevent dust and debris in the lab from contaminating the concrete, freshly fractured beams were quickly sprayed with a 0.1N solution of silver nitrate ($AgNO_3$) to determine the average chloride penetration depth at each section.

Figures C.1 through C.40 (Appendix C) show the chloride penetration depths for beams 1 through 10, respectively. The contaminated concrete can be identified by the whitish colour, with the colour change boundary from whitish silver chloride precipitate (contaminated concrete) to grey silver (chloride-free concrete) being the chloride penetration front. Loaded beams have a compressive and tensile face induced by eccentric post-tensioning; the compressive face is located near the blue post-tensioning duct, while the tensile face is below. Maximum compressive and tensile stresses occur at cut A (smallest section), while minimum stresses occur at cut D (largest section), as illustrated in Figure 3.28.

The white 'contaminated' areas on the left and right sides of each beam are attributed to the small notches made by a disk diamond saw, as seen in Figure 3.29, and should not be taken as chloride penetration. The critical section of beams 7 and 10 were cracked before submergence allowing the full cross-section to be quickly contaminated with chlorides; therefore, these sections are omitted from analysis. A summary of the maximum, minimum, and average chloride penetration depths as observed in the previous figures is tabulated in Appendix C. Results in Appendix C were measured directly from the physical specimen in the lab with a metric measuring tape.

For the majority of sections, chloride penetration depths obtained were reasonable and expected. However, Beam 2 (w/c = 0.35, 34 kN) gave higher than expected chloride penetration depths at both compressive and tensile regions, which can be explained by the inconsistency in the mix and major defects in the beam (batch 1 as explained in Chapter 3). Beam 9 (w/c = 0.50, 130 kN) also gave higher penetration depths when compared to other beams of similar w/c; the probability of compressive and tensile microcracks in this beam are very high, since the beam was subjected to a $0.73f'_C$ compressive stress, the highest percentage of the concrete compressive strength of all beams. Beam 3 (w/c = 0.35, 153 kN) incurred the second highest percentage with $0.68f'_C$, allowing the possibility of the very large chloride penetration depth on the tensile face to be due to tensile microcracking.

Figures 4.1 through 4.8 plot the average and maximum chloride penetration fronts on the bottom and top faces of all the tested beams. With very few exceptions, it can be seen from Figures 4.1 through 4.8 that the chloride penetration depths on the compression face are always deeper than on the tensile face. With the exception of beam 2 (the poorly constructed beam), the compression faces of the post-tensioned beams were all located at the bottom of the exposure tank, and the tension faces of the post-tensioned beams were located closer to the surface. The chloride concentration results of Section 4.2.2 prove that the chloride concentration at the bottom of the tank is higher than the surface; the majority of de-icing salt crystals settled on the bottom of the tank and slowly dissolved into solution, allowing for a larger concentration gradient and higher diffusion rates at the bottom of the tank. Therefore, the higher penetration depths on the compressive face of each beam cannot be solely attributed to the different effect that compressive and tensile stresses have on the microstructure of concrete. Knowing this, the bottom and top faces of the control beams were compared to the compression and tensile faces of post-tensioned beams, respectively. Again, tabular results of Figures 4.1 through 4.8 can be seen in Appendix C.

To illustrate the effects of the concrete water-to-cement ratio and sustained stress on the measured chloride penetration depths, the results displayed in Appendix C are plotted against the specific section length (distance to fracture location, in cm) in Figures 4.1 through 4.8. Figures 4.1 and 4.2 illustrate the average and maximum chloride penetration fronts on the bottom and top faces of the control beams, respectively. From Figures 4.1 and 4.2, a general trend is observed, in which the higher the w/c ratio, the higher chloride penetration depths are. Also, the effect of GGBS is very apparent, reducing the chloride penetration depths compared to the beams with similar w/c

and without the addition of GGBS. Figures 4.3 to 4.8 show the average and maximum chloride penetrations depths for the compressive and tensile faces of each of the beams with different w/c. From the figures, it can be seen that generally, the higher the compressive and tensile stress is, the higher the chloride penetration depth is for all w/c. However, for a w/c of 0.50, higher compressive stress caused a lower penetration depth (except for the beam subjected to 130 kN where microcracking most likely occurred); for a w/c of 0.40 and 0.50, no clear tensile stress trends can be observed for the penetration depths. The outliers and unexpectedly high chloride penetration depths found in Figure 4.3 and 4.4 are attributed to the inconsistency of beam 2. Note that the values in Figures 4.1 through 4.8 are discrete relative to each other, and the lines joining them do not necessarily imply trend values in between (Deif, 2010).

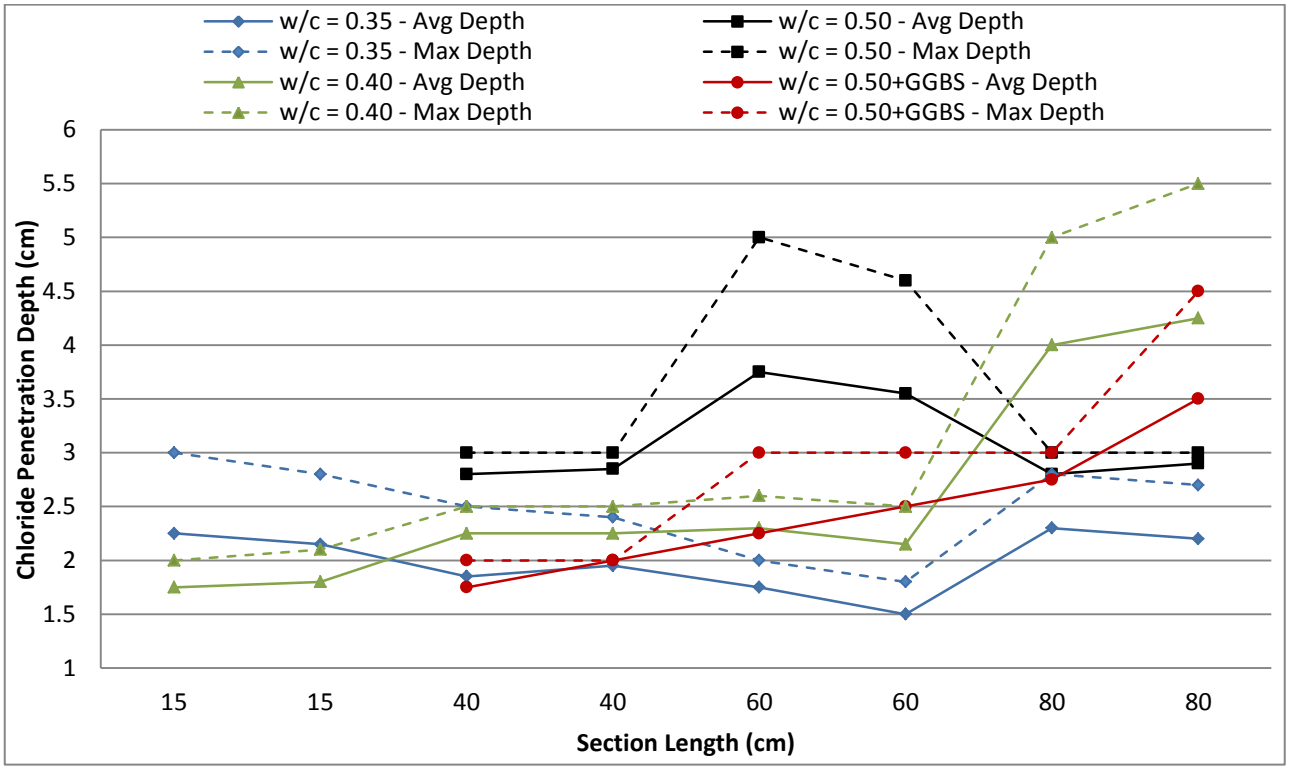

Figure 4.1: Average and maximum chloride penetration depths for bottom face of control beams

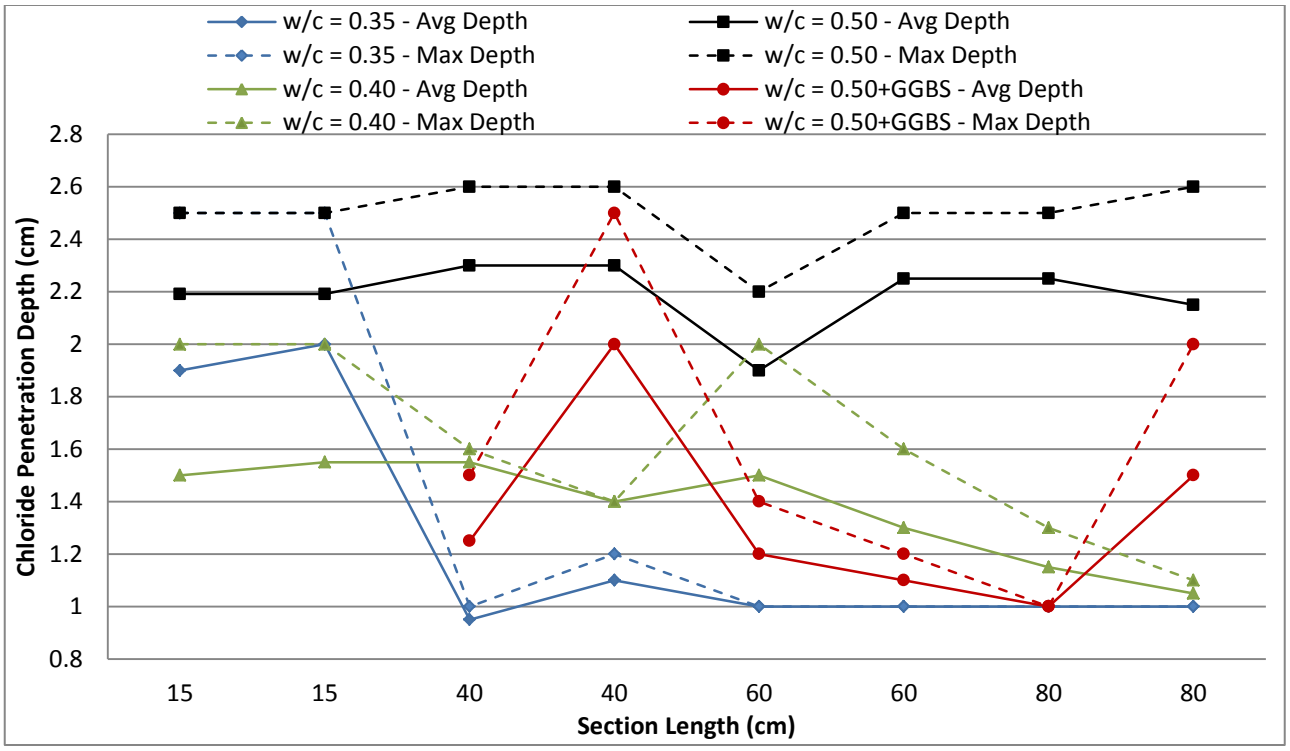

Figure 4.2: Average and maximum chloride penetration depths for top face of control beams

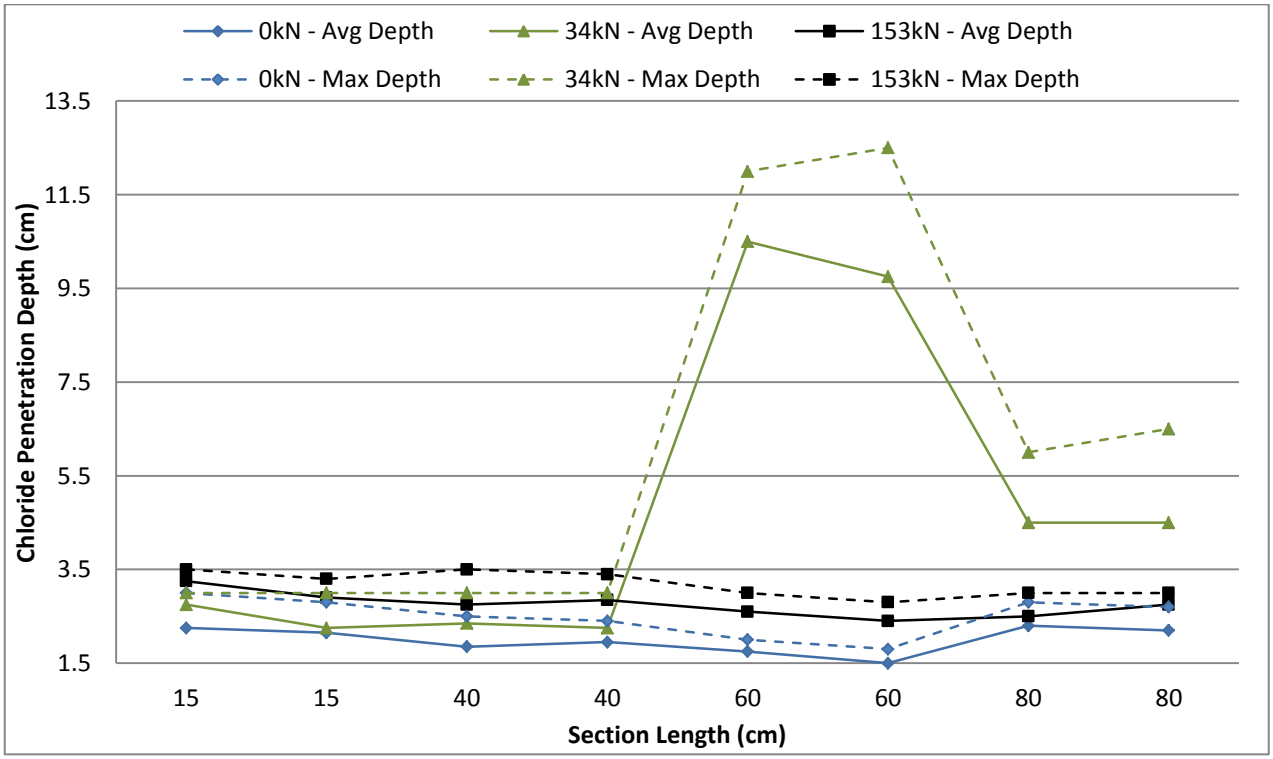

Figure 4.3: Average and maximum chloride penetration depths for compressive face (w/c = 0.35)

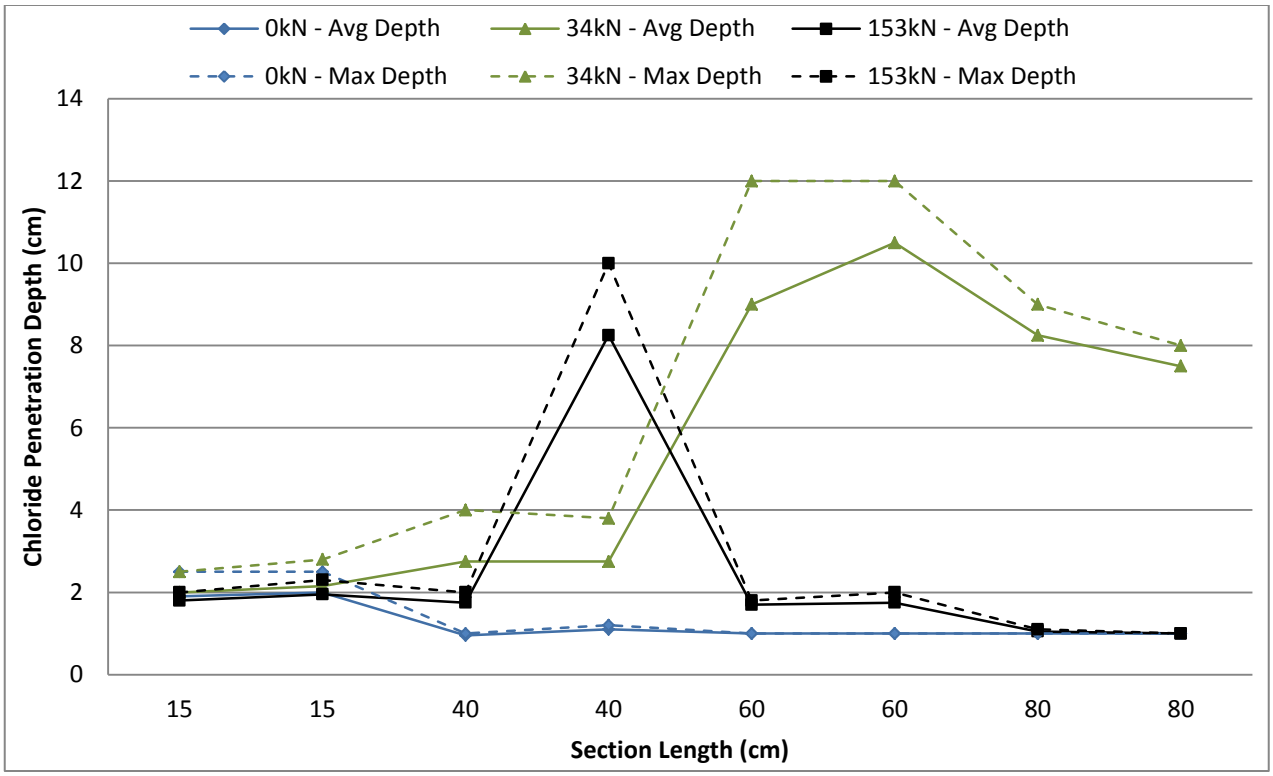

Figure 4.4: Average and maximum chloride penetration depths for tensile face (w/c = 0.35)

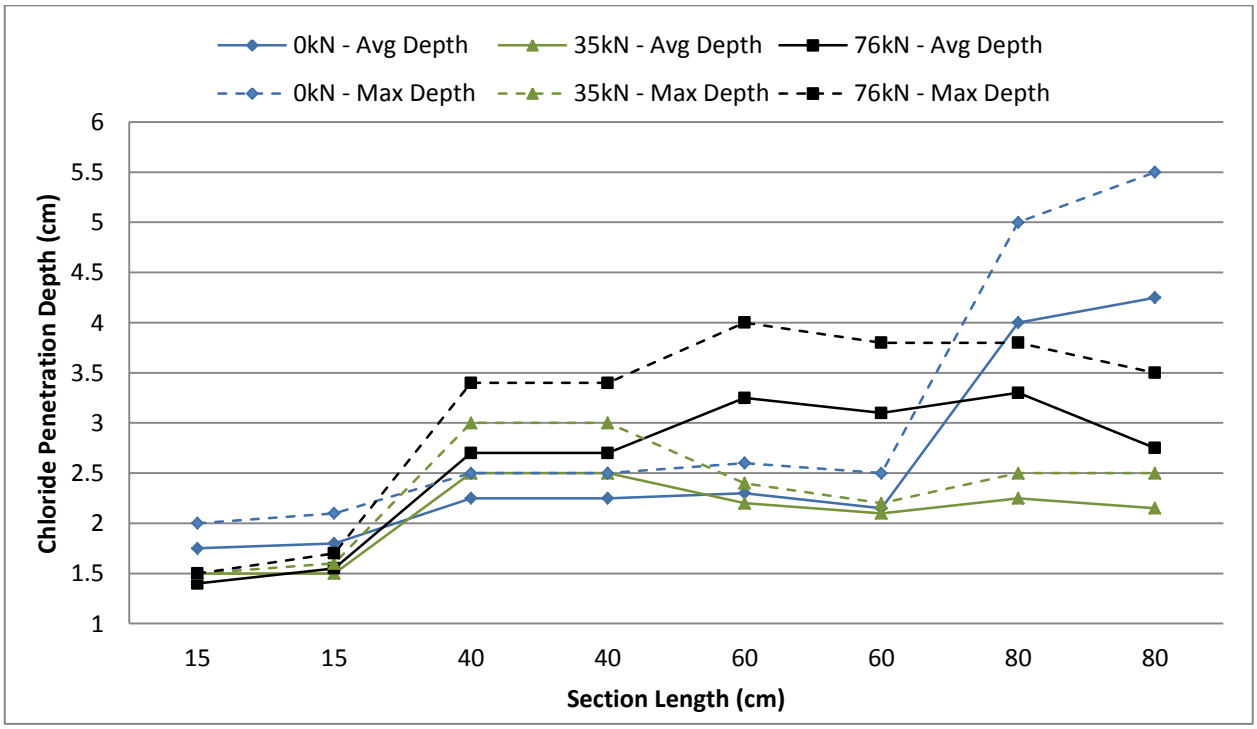

Figure 4.5: Average and maximum chloride penetration depths for compressive face (w/c = 0.40)

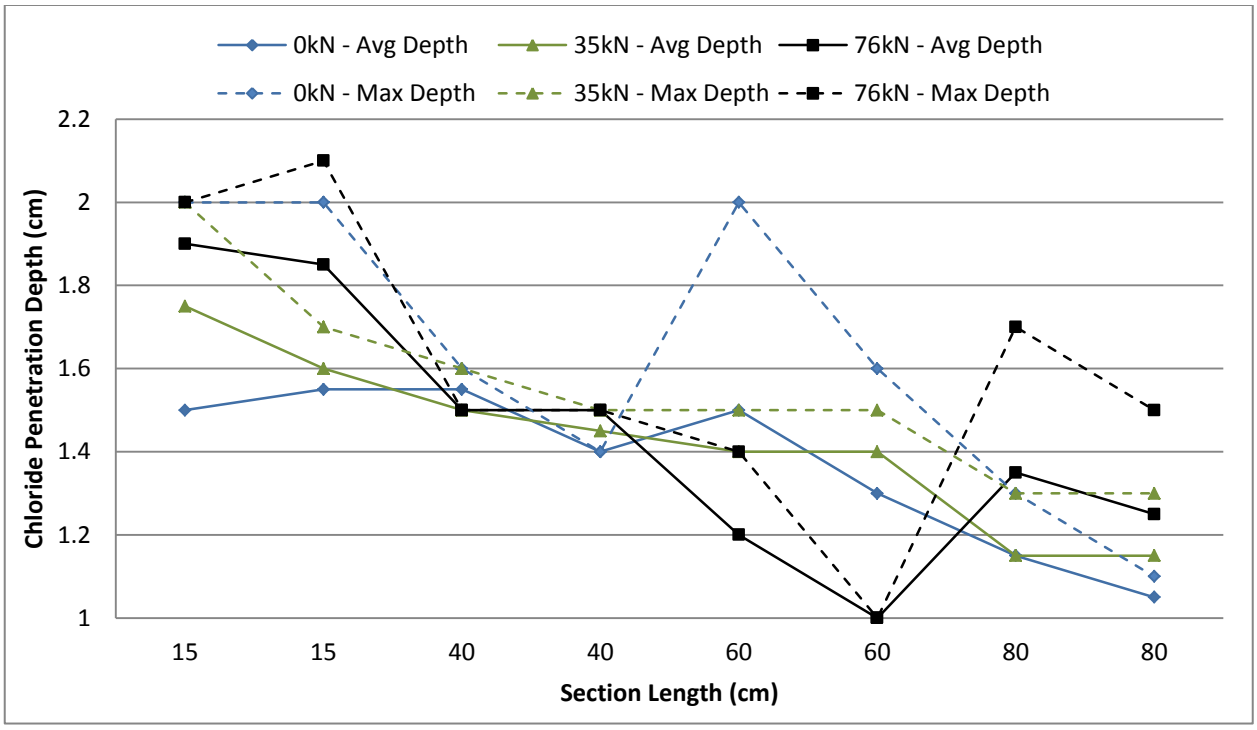

Figure 4.6: Average and maximum chloride penetration depths for tensile face (w/c = 0.40)

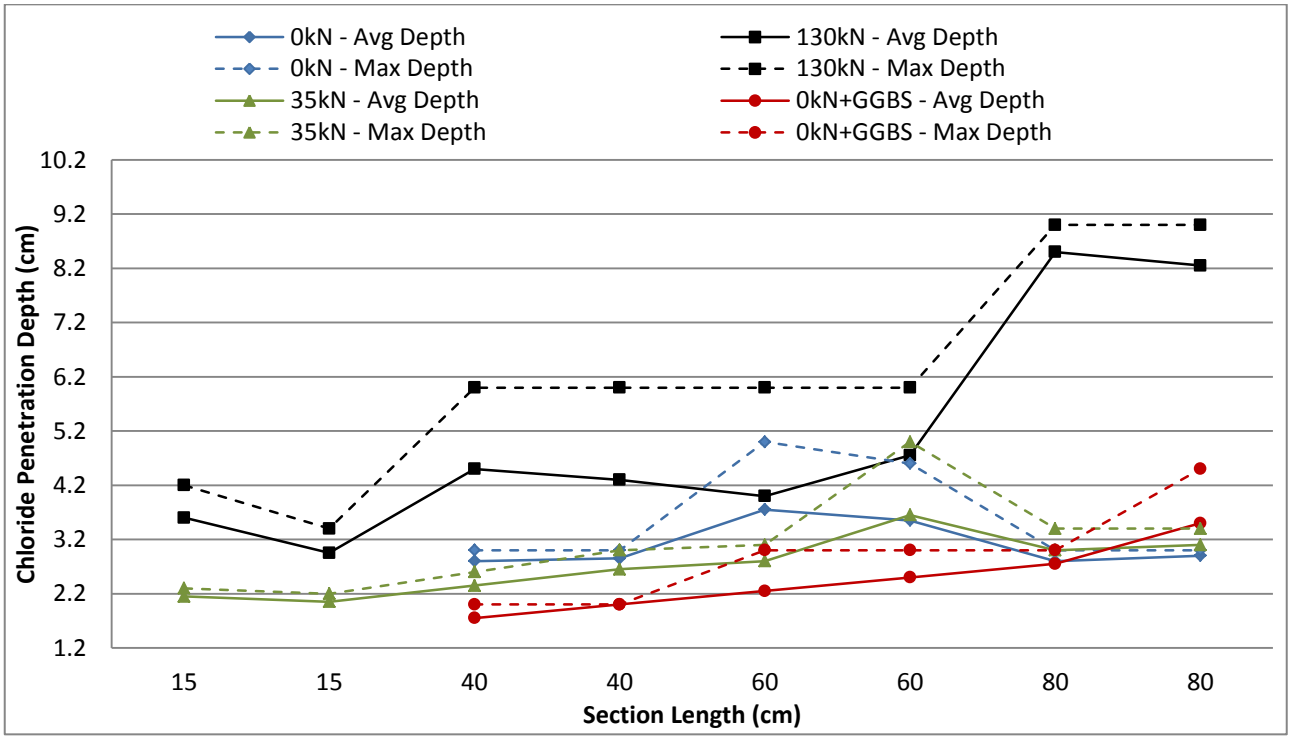

Figure 4.7: Average and maximum chloride penetration depths for compressive face (w/c = 0.50)

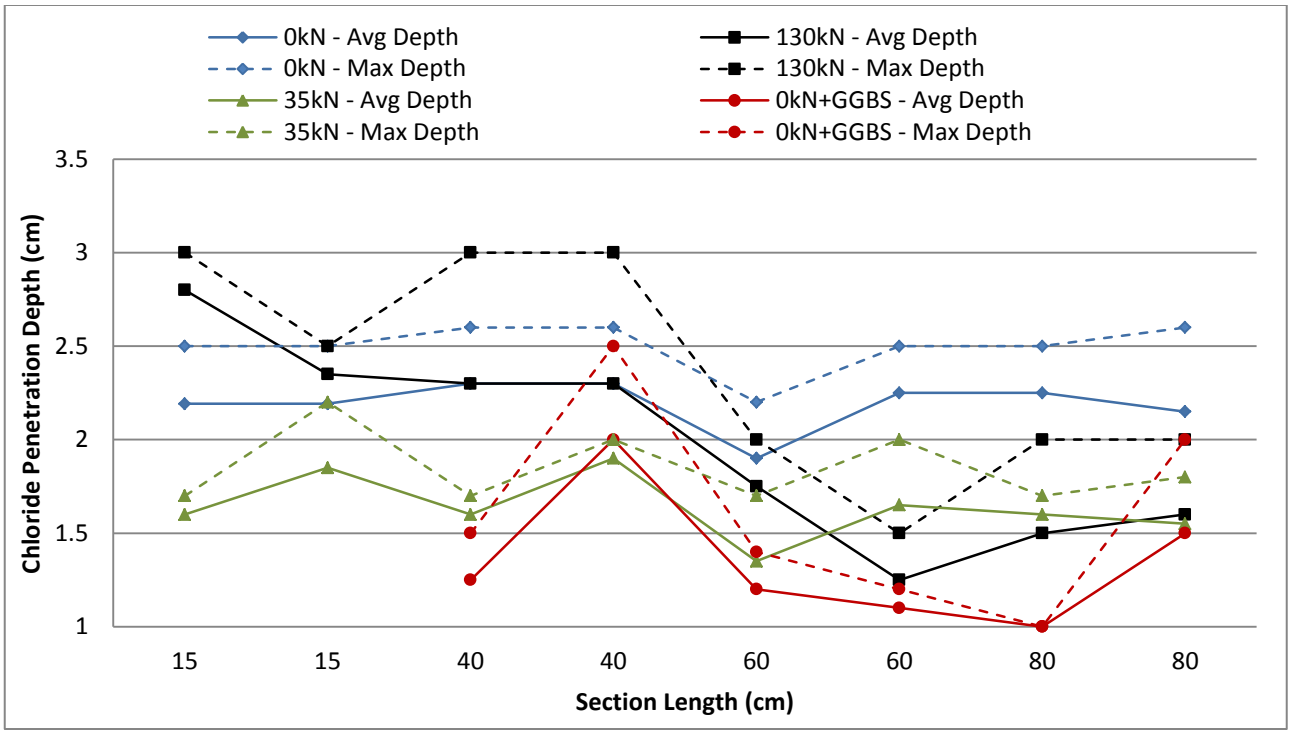

Figure 4.8: Average and maximum chloride penetration depths for tensile face (w/c = 0.50)

4.2.2 Potentiometric Titration Method

This section presents the results from the potentiometric titrations on the concrete power obtained for the selected concentration profiles as outlined in Table 3.8. The total chloride content is given in % by weight of the concrete sample and was calculated according to Eq. (3.9), as seen in the ASTM 1152/C 1152M-04 and ASTM C114-07 standards. The total chloride content from the powder sample obtained from grinding concrete at 5-mm intervals represents the average value for that 5-mm depth interval, and therefore the concentration values for a given depth are plotted at the mid-way depth of that interval. Concrete powder was obtained by profile grinding, as discussed in Section 3.4.3, in 5-mm depth intervals. Bound chlorides in the concrete, that do not react with the silver nitrate spray to form a white precipitate, are acid soluble and are released with the addition of nitric acid. Therefore, the preselected concrete sections were grinded to a depth of 5 mm below the observable average chloride penetration boundary.

The total chloride concentration profiles obtained for the compressive face of each beam as a function of w/c and applied load can be seen in Figures 4.9 through 4.14. Two concentration profiles were obtained from the bottom face of each unstressed control beam; profiles

corresponding to the control beams have two entries instead of just one. According to the results, the effect of compressive stress on chloride ingress and concentration is different for each w/c. Generally, for a w/c of 0.35 and 0.40, an increase of compressive stress does not seem to affect chloride concentration results; however, for a w/c of 0.50 an increase in compressive stress usually causes a decrease in chloride concentrations. This probably has to do with the fact that concrete with a high w/c ratio has a higher porosity and is more compressible. Generally, the lower the w/c the lower the chloride concentration is; this can be seen clearly in the lower compressive stress profiles of Figure 4.13. Concrete with GGBS have higher chloride concentrations close to the surface; however, it seems to have a greater impact on chloride concentration reduction the deeper into the section it goes, giving very low chloride concentrations than its comparable control counterpart at a depth of 1.5 cm and beyond. As a supplementary material, GGBS acts to reduce the pore size distribution (permeability) in concrete by filling in the voids and increase compressive strength by having a higher proportion of calcium silicate hydrates.

The total chloride concentration profiles obtained for the tensile face of each beam as a function of w/c and applied load can be seen in Figures 4.15 through 4.20. To save time, only one concentration profile was obtained for the top face of each unstressed control beam. While chloride concentration profiles for a w/c of 0.40 do not seem to have a clear dependency on the applied tensile stress, the concentration profiles for a w/c of 0.35 and 0.5 decrease and increase with the increase in tensile stress, respectively; this effect is more pronounced at larger depths. Again, it is observed that the lower the w/c the lower the chloride concentration is, which can be seen clearly in the higher tensile stress profiles of Figure 4.20. The effect of GGBS is more noticeable in reducing the chloride concentrations for the top face (Figure 4.18) of the control beams than the bottom face (Figure 4.12); the top face was subjected to a less concentrated chloride solution, and therefore a lower concentration gradient.

The effect of different concrete water-to-cement ratios on chloride ingress and concentration is very apparent in this study; as expected, a lower w/c generally gave lower chloride concentrations and penetration depths for both the compressive and tensile faces of each beam. However, the effect of compressive and tensile stress on chloride concentrations is not as clear; trends are observed, but they are not consistent, even in the same profile.

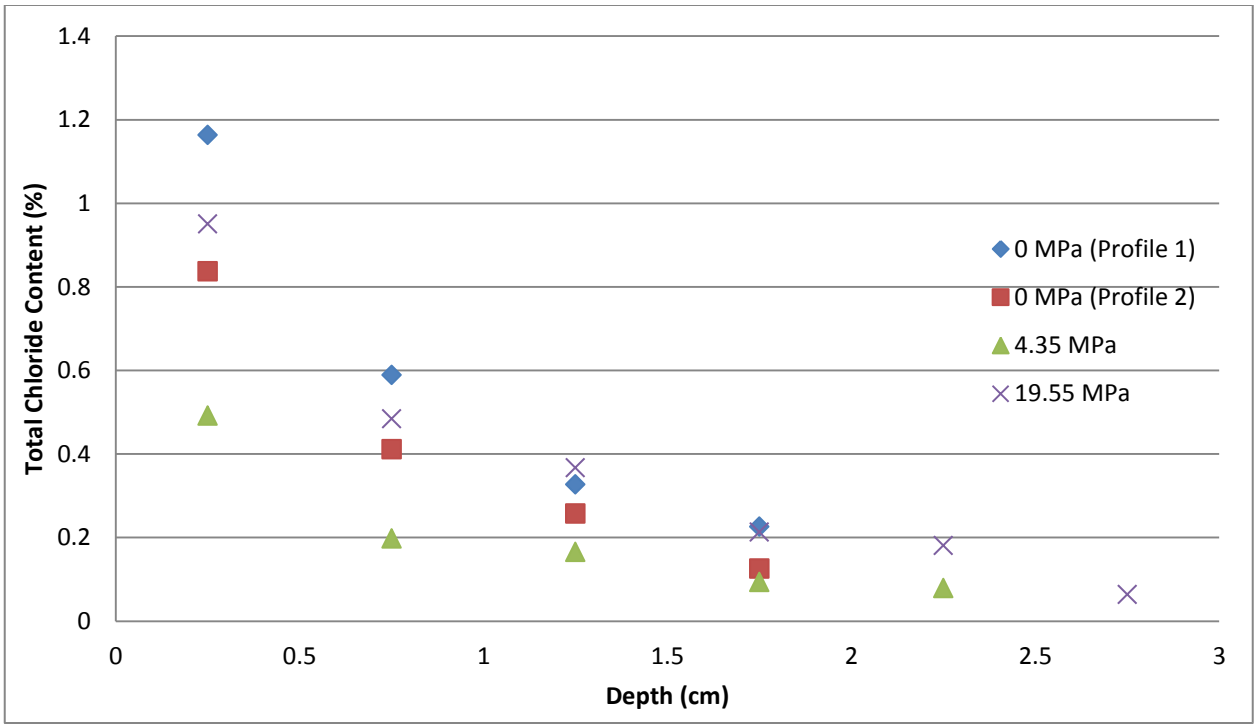

Figure 4.9: Chloride concentration profiles for compression face of beams with w/c =0.35

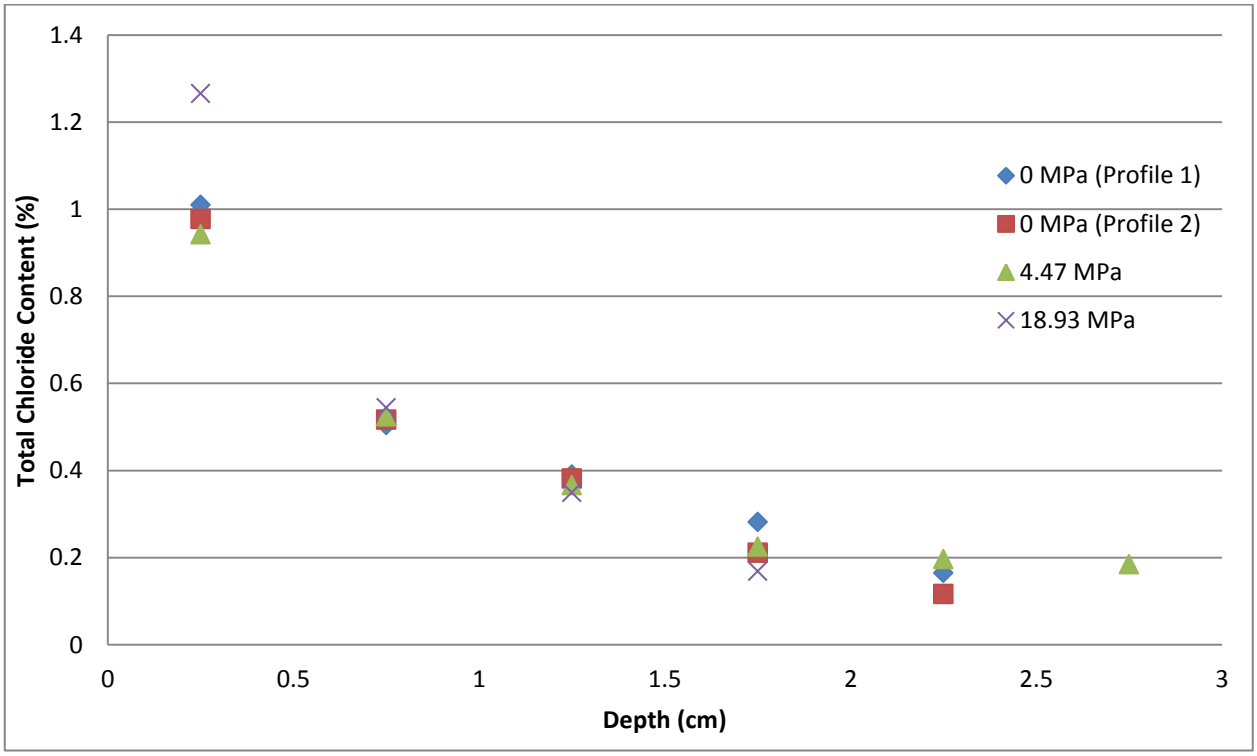

Figure 4.10: Chloride concentration profiles for compression face of beams with w/c =0.40

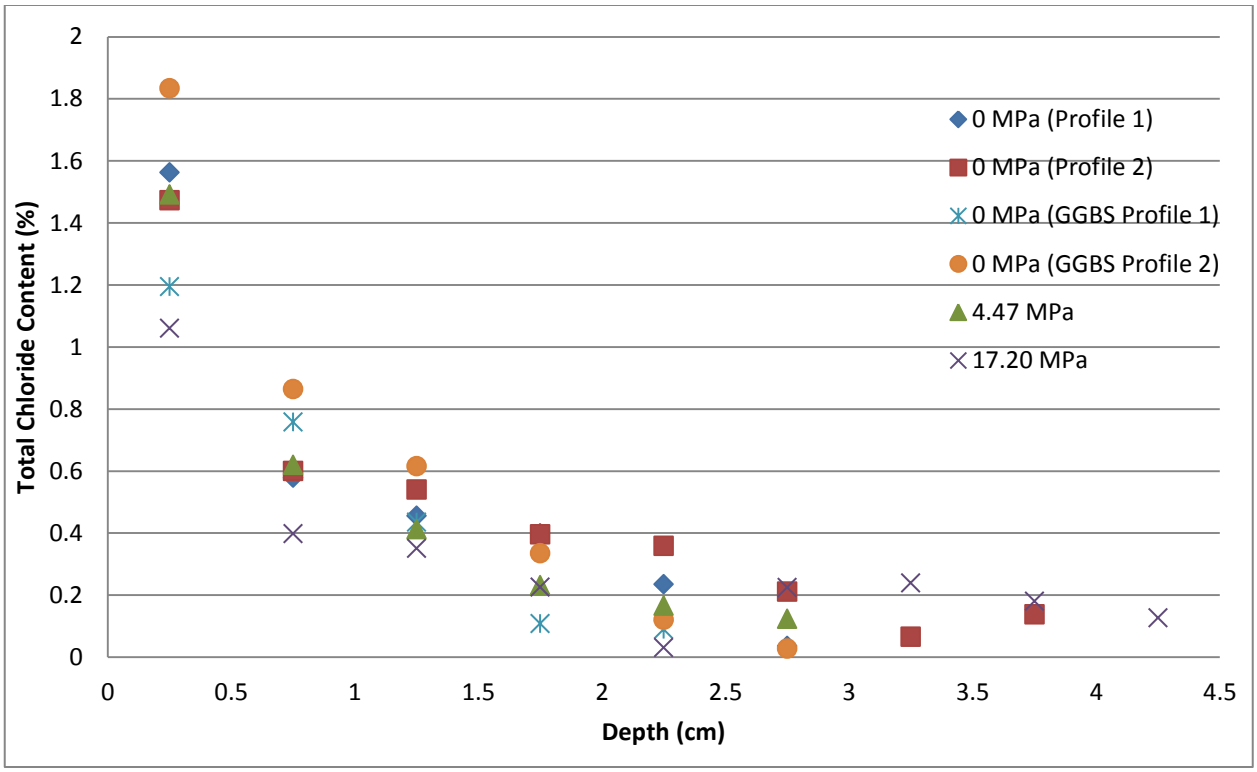

Figure 4.11: Chloride concentration profiles for compression face of beams with w/c =0.50

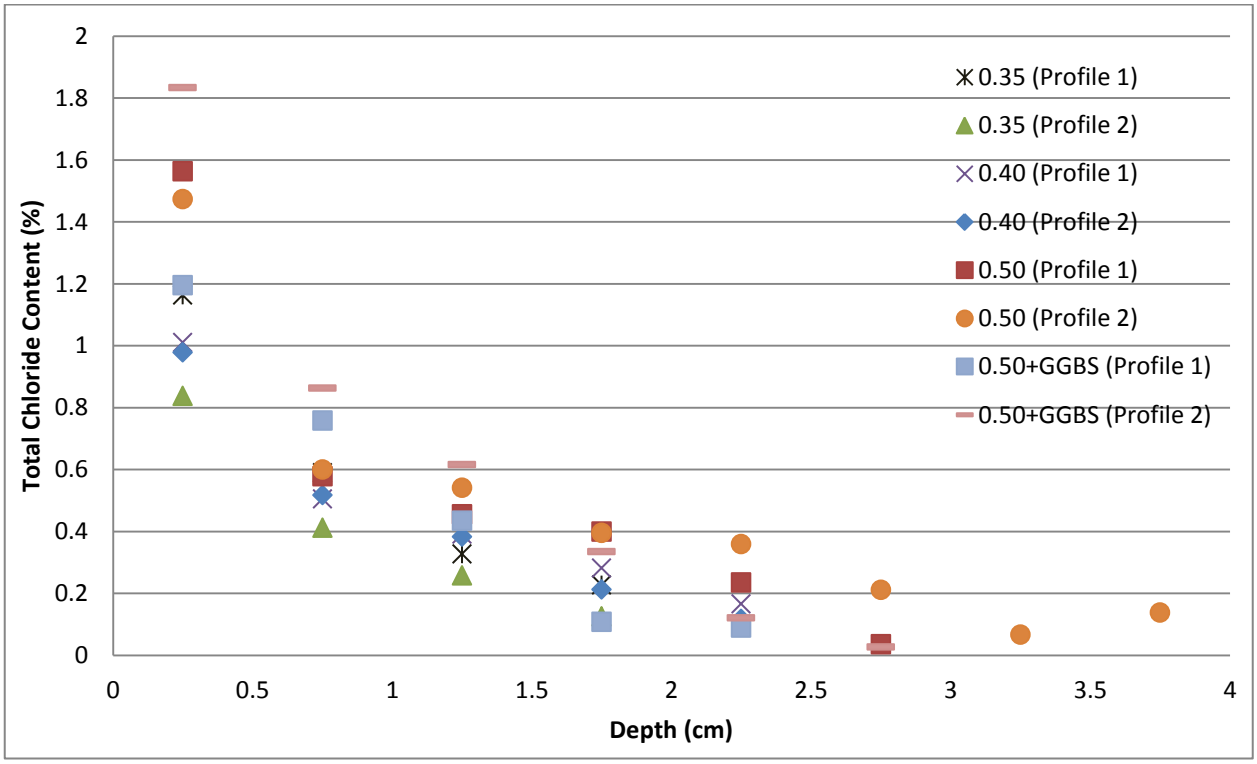

Figure 4.12: Chloride concentration profiles for bottom face of control beams

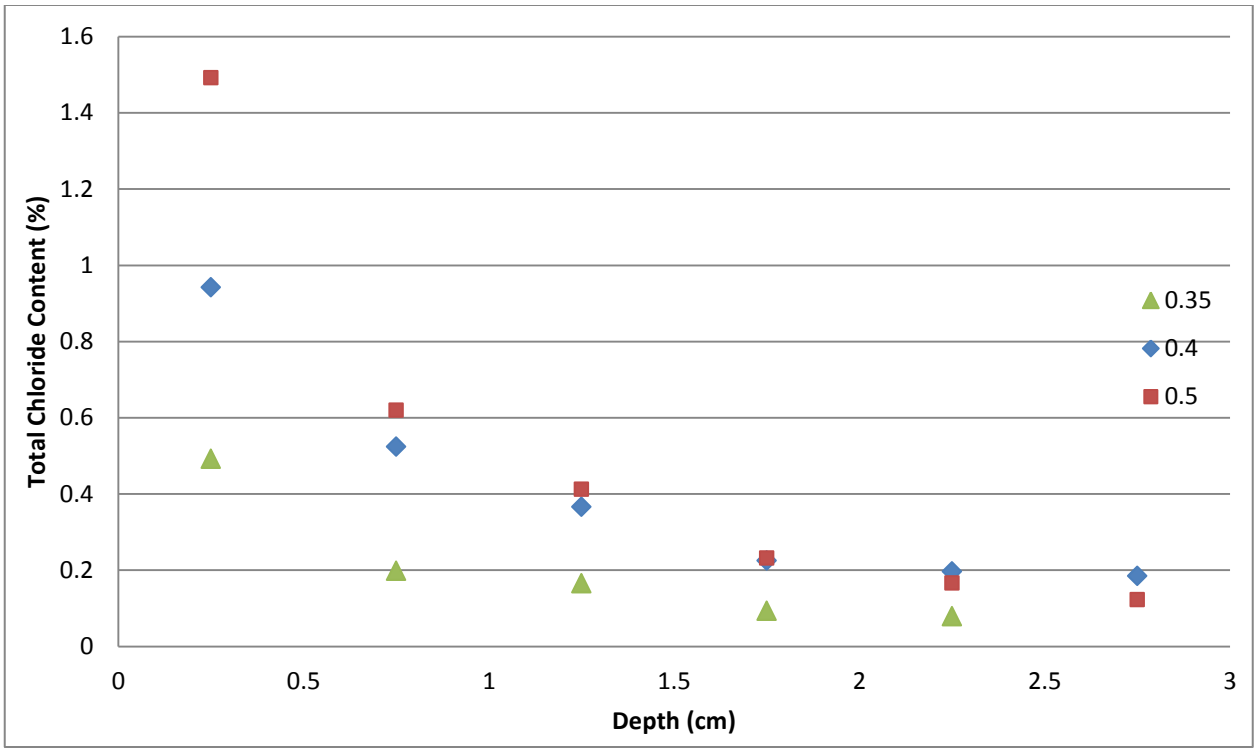

Figure 4.13: Chloride concentration profiles for beams sustaining 4.47 MPa compressive stress

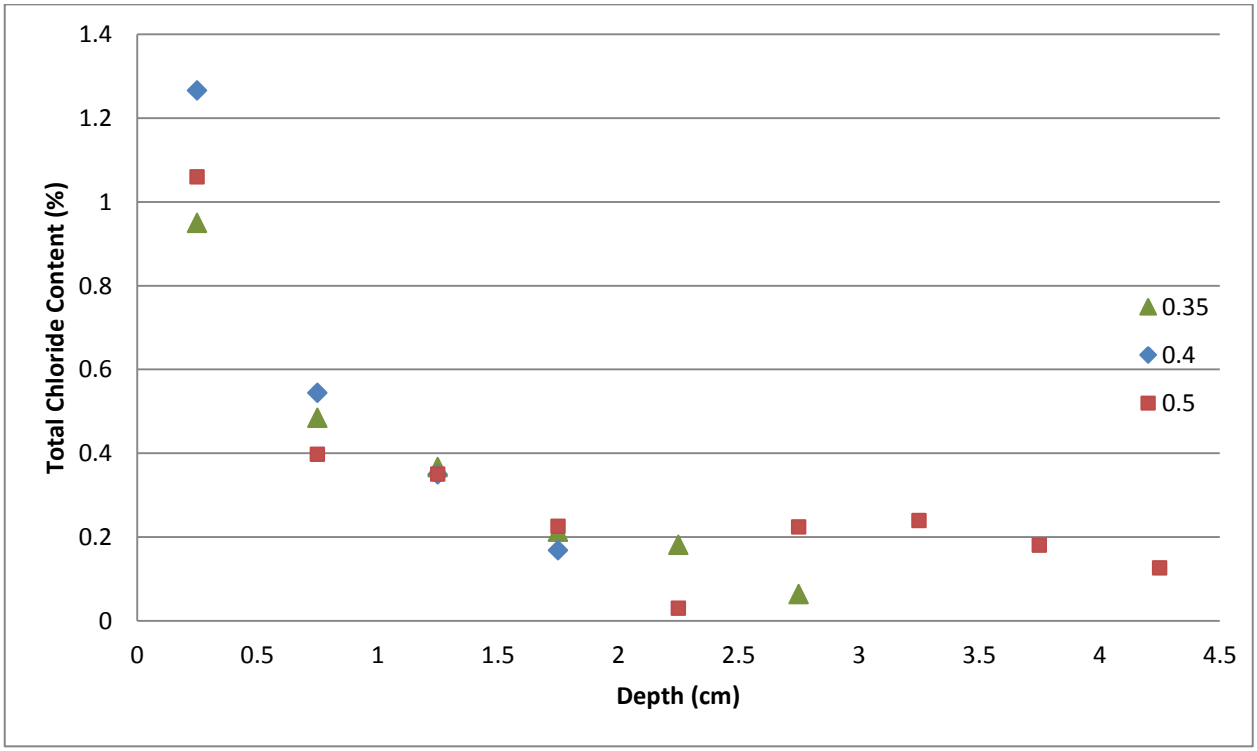

Figure 4.14: Chloride concentration profiles for beams sustaining 19.00 MPa compressive stress

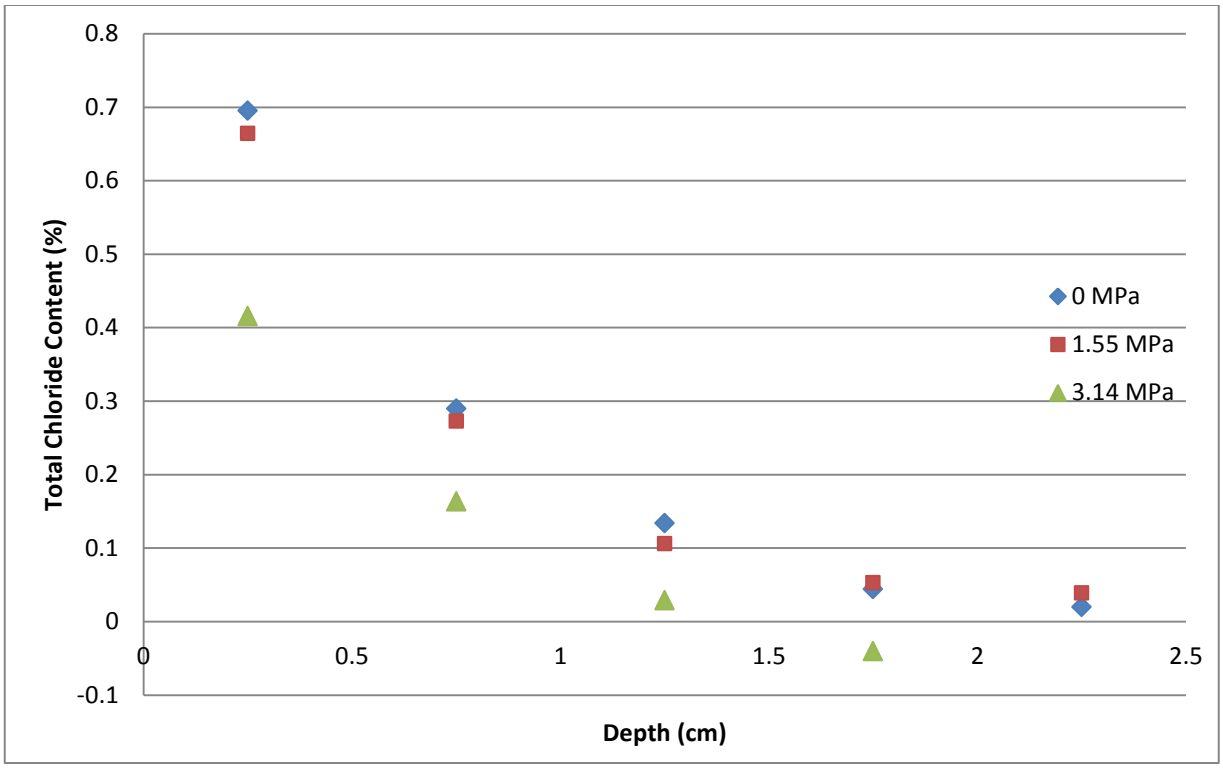

Figure 4.15: Chloride concentration profiles for tensile face of beams with w/c =0.35

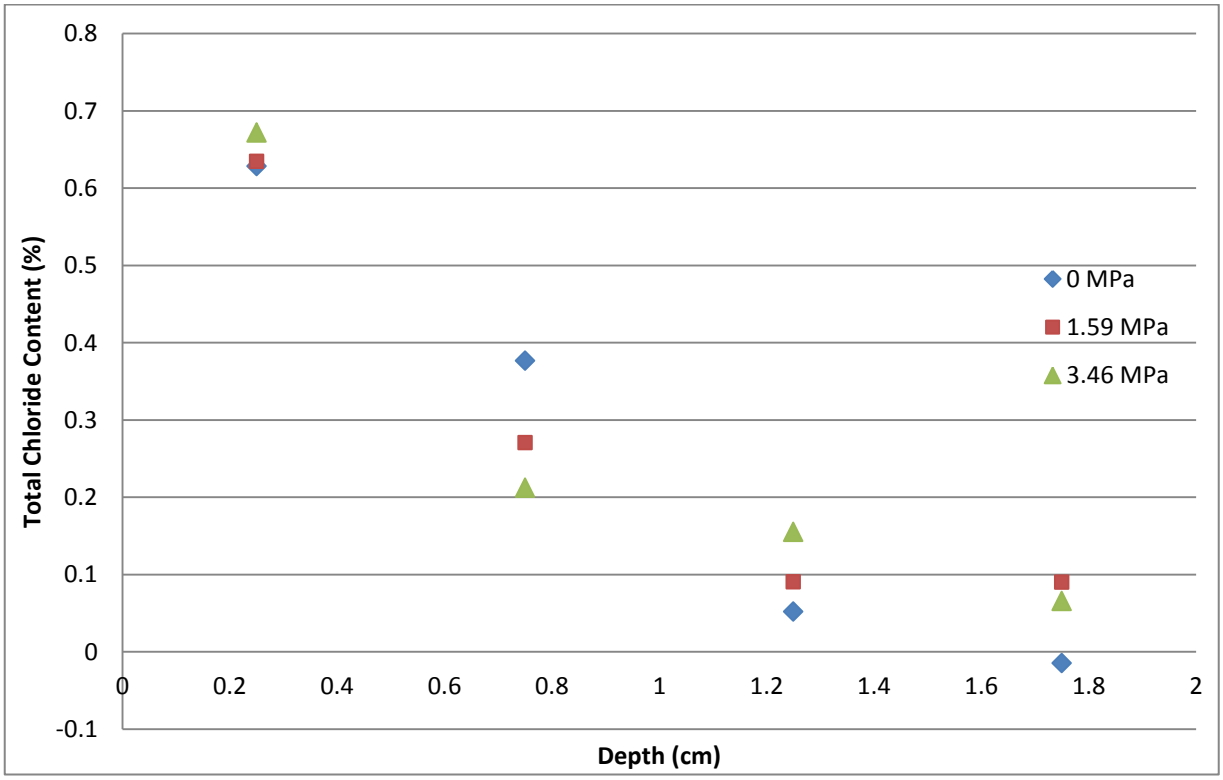

Figure 4.16: Chloride concentration profiles for tensile face of beams with w/c =0.40

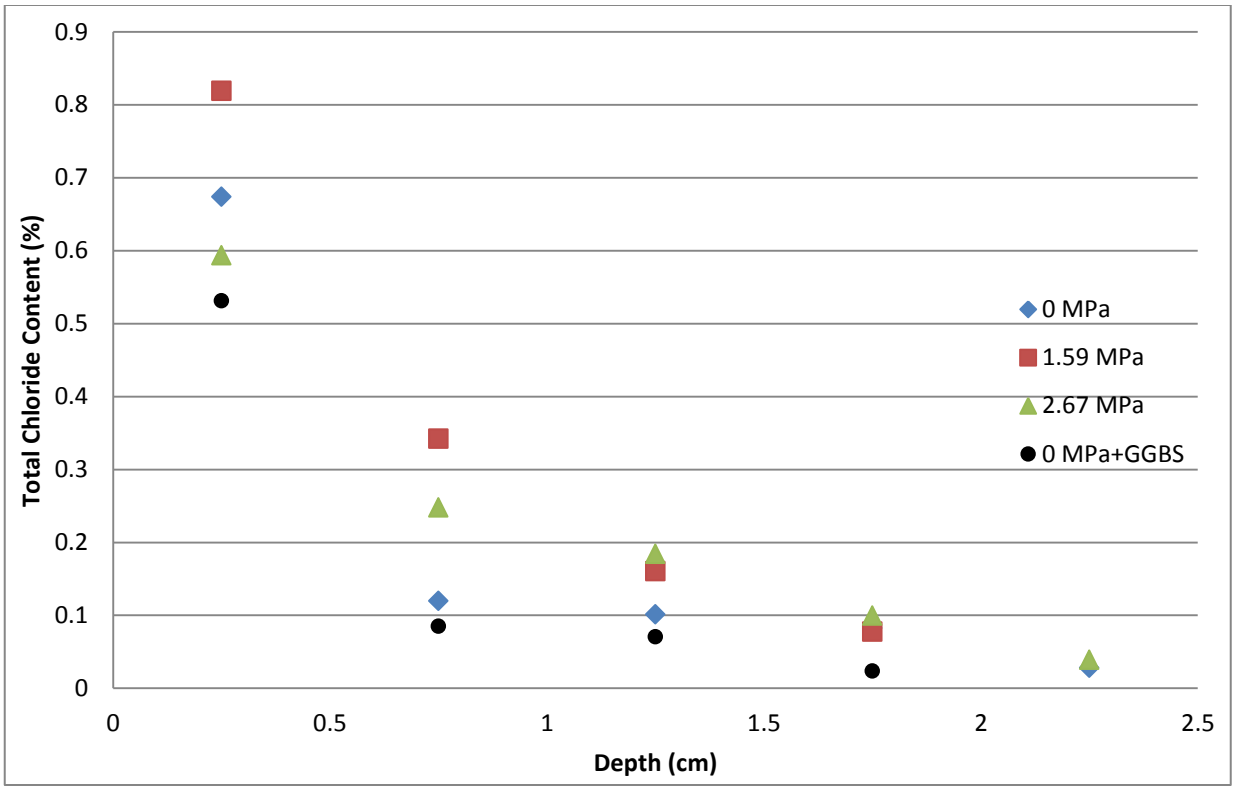

Figure 4.17: Chloride concentration profiles for tensile face of beams with w/c =0.50

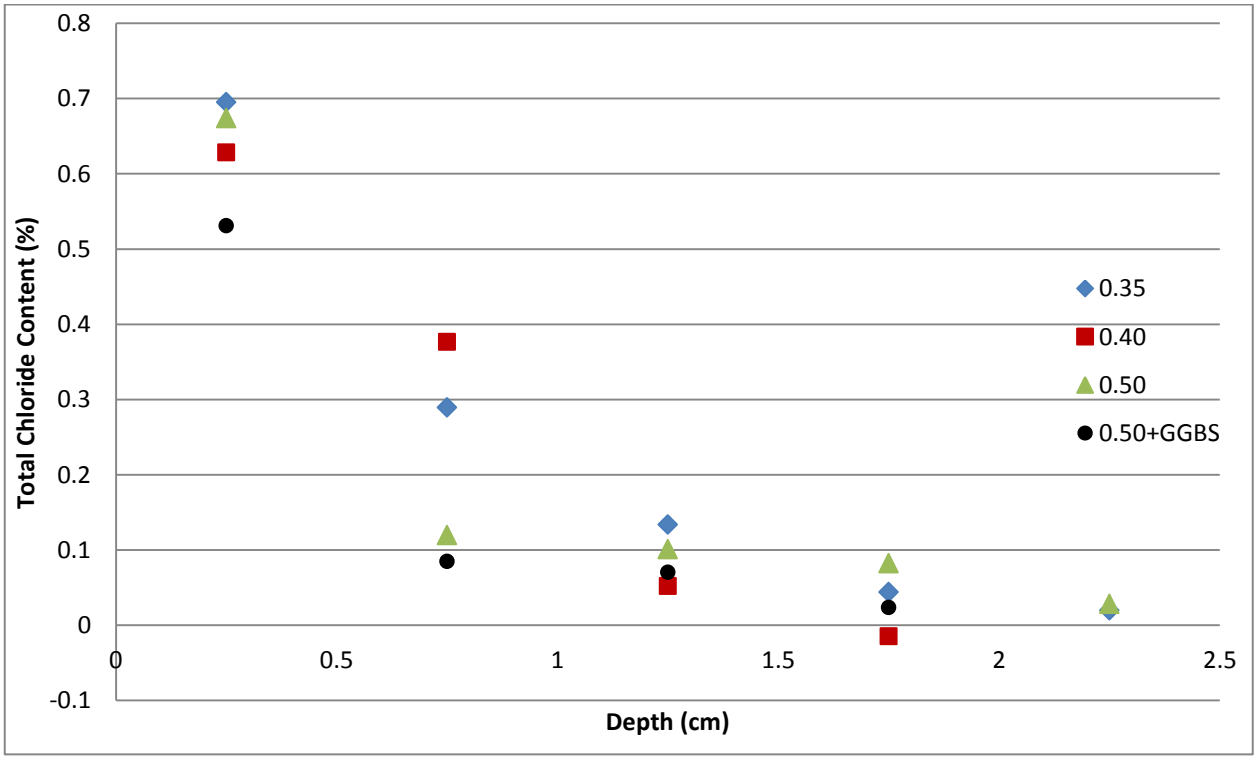

Figure 4.18: Chloride concentration profiles for top face of control beams

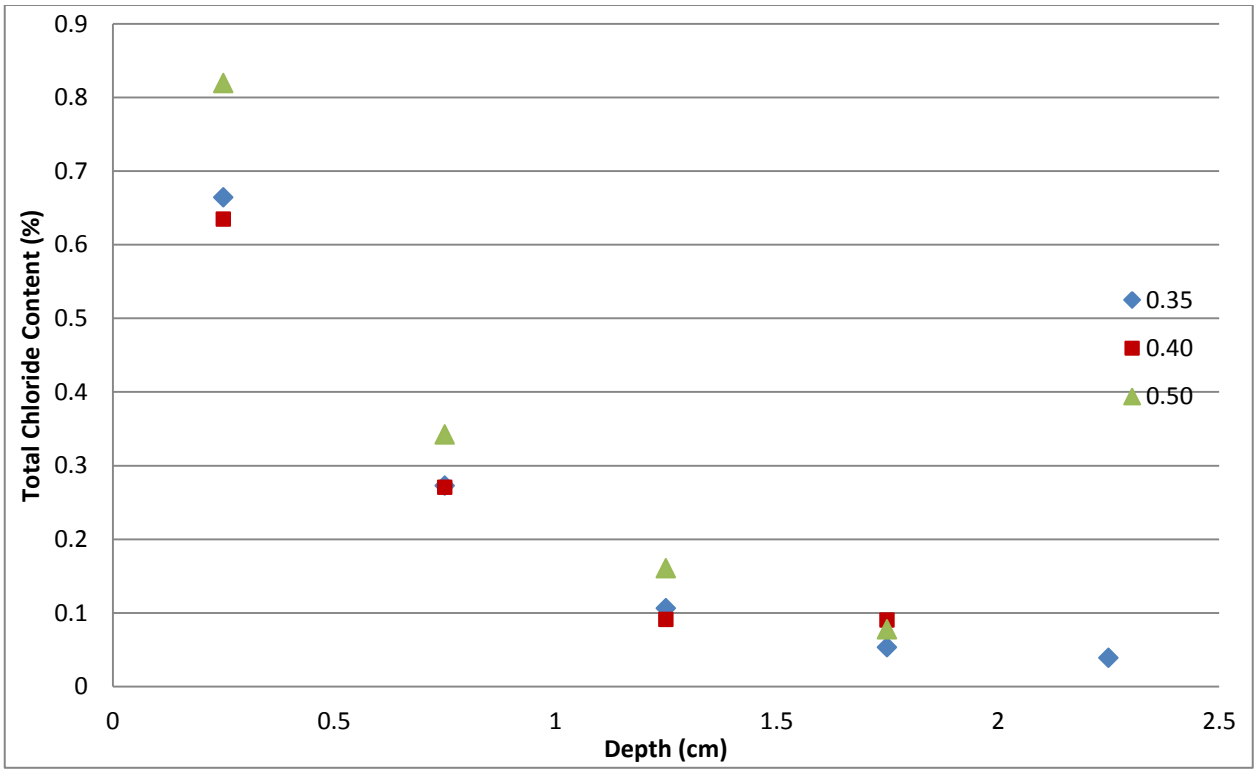

Figure 4.19: Chloride concentration profiles for beams sustaining 1.59 MPa tensile stress

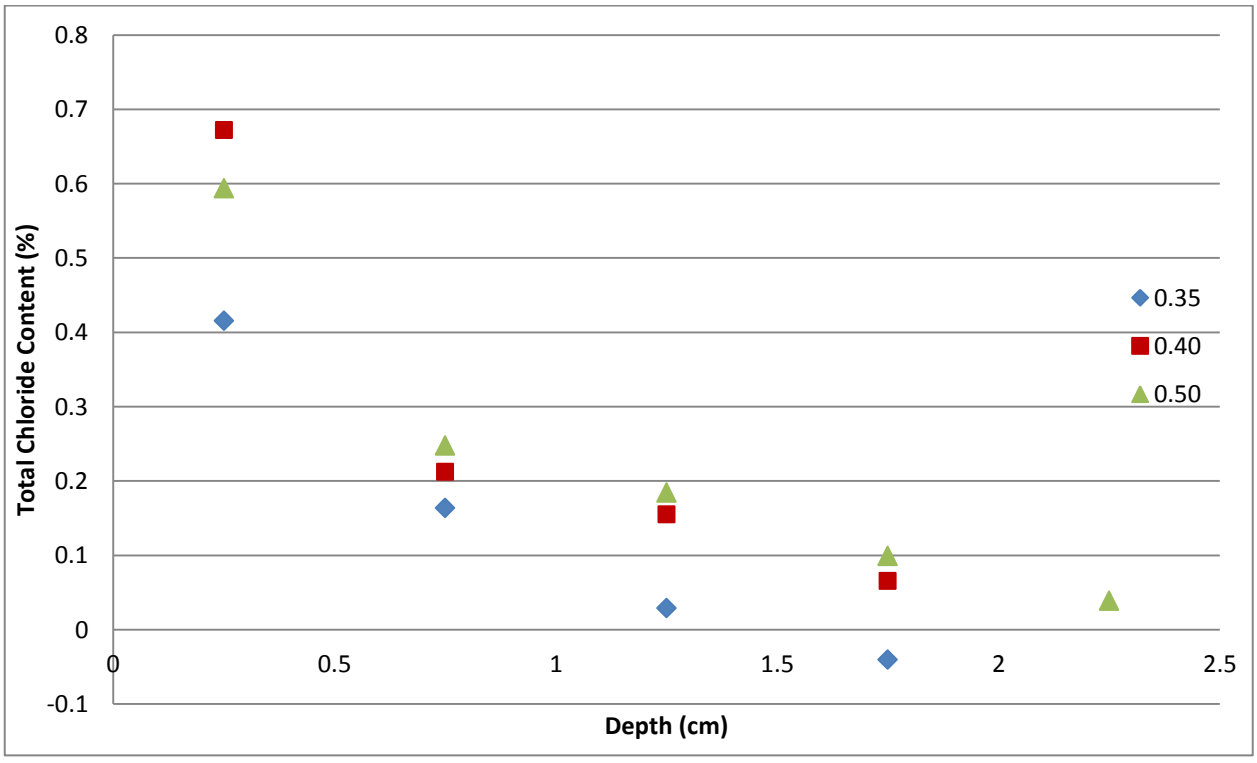

Figure 4.20: Chloride concentration profiles for beams sustaining 3.46 MPa tensile stress

Chapter 5 – Assessment of Chloride Ingress

5.1 Introduction

This chapter presents the analysis of chloride concentration data and profiles presented in Chapter 4. Section 5.2.1 gives chloride apparent diffusion coefficients determined by fitting chloride concentration data into Crank's error function solution, while Section 5.2.2 gives relative diffusivities obtained from average penetration depths. Results from both potentiometric titration and silver nitrate spraying are compared to establish the reliability of the $AgNO_3$ spray indicator in Section 5.2.3. Finally, the effect of stress and w/c on the chloride diffusivity of concrete is discussed in Section 5.3 and 5.4, respectively.

5.2 Chloride Diffusivity

As previously discussed in Chapter 2, there are many different chloride transport mechanisms that govern the ingress of chlorides into concrete. In reality, the chloride ion transport mechanisms discussed do not act in isolation; however, since the concrete specimens in this study were completely submerged and fully saturated, chloride ingress is assumed to be governed by pure diffusion as mathematically described in Fick's second law of diffusion (see Eq. (2.2)). Therefore, Crank's error function solution to Fick's second law of diffusion (Eq. (2.6)) is used to obtain the diffusivities of concrete for chloride content profiles obtained in Chapter 4.

5.2.1 Determination of Diffusivity from Chloride Profiles

There are several methods to quantify chloride diffusivity in concrete, but the current practice is to fit acid-soluble chloride concentration profiles with Crank's solution to Fick's second law of diffusion (Bentur, Diamond, & Berke, 1998). Fitting the obtained chloride concentration profile data to Eq. (2.6) was done with the non-linear least squares regression software developed by Pezzullo (2013); after analysis, the profile specific apparent diffusion coefficient (D_{app}) and chloride surface concentration (C_S) are given for 12 weeks of exposure. Crank's solution is only valid when both the D_{app} and C_S values are constant in time and space during pure diffusion; however, this is usually not the case in concrete exposed to field conditions, where diffusion rates and surface concentrations are fluctuating over time. Therefore, apparent values for diffusion coefficients and surface concentrations are used to account for these assumptions.

Tables 5.1 and 5.2 tabulate the D_{app} and C_S (by % weight of concrete) values obtained from the non-linear regression analysis of each concentration profile for each beam along with its corresponding compressive and tensile stresses values. The correlation factors (R^2) determined by the non-linear regression software are also given. Based upon the high R^2 values, Crank's solution to Fick's 2nd law provides an accurate description of the variation of chloride concentration over depth for beams sustaining both compressive and tensile stresses. However, beams 7 and 9 give relatively low R^2 values under sustained compression; for reasons unknown, the chloride concentration of both beams fluctuate as depth increases. Tables 5.1 and 5.2 also report the maximum penetration depth of 5-mm below the visible colour change boundary (from the silver nitrate spray) for each chloride profile; profiles with higher chloride penetration depths generally have higher diffusion coefficients. This is expected as a higher diffusion coefficient will lead to deeper chloride ingress into the concrete given the same time of exposure; therefore, as seen in Figures 5.1 and 5.2, the rate of diffusion for each w/c ratio (obtained from fitting chloride profiles to Crank´s solution) is related to the chloride penetration depth obtained from the colourimetric method (silver nitrate spray method).

In the study done by Wang et al. (2011), diffusivity was plotted against a stress level index (λ_σ) defined by the ratio between the applied stresses and the measured strength of the concrete, for both compressive and tensile stresses; this was done to normalize the stress data to the specific concrete material strength. This parameter has also been calculated and reported in Tables 5.1 and 5.2. Compressive stresses were normalized by the corresponding compressive strength f'_c, while tensile stresses resulting from flexural loading were normalized by the corresponding modulus of rupture. A more in-depth analysis of the effect of stress and w/c on the D_{app} values will be seen in Sections 5.3 and 5.4, respectively, of this chapter.

Table 5.1: Surface chloride content C_S, apparent diffusion coefficient D_{app}, and correlation factor R^2 obtained by fitting chloride profiles for the bottom face of control beams and beams under compression

w/c	Beam	C_S (%)	D_{app} ($x10^{-12}$ m^2/s)	R^2	Stress (MPa)	λ_σ	Max Penetration Depth (cm)
0.35	1	1.193	7.645	0.975	0.00	0.000	2.0
	2	0.547	9.039	0.895	4.35	0.078	2.5
	3	1.034	12.675	0.951	19.55	0.351	3.0
0.4	4	1.096	12.171	0.950	0.00	0.000	2.5
	5	0.995	15.991	0.922	4.47	0.078	3.0
	6	1.544	6.176	0.965	18.93	0.332	2.0
0.5	7	1.575	12.875	0.873	0.00	0.000	4.0
	8	1.755	7.000	0.944	4.47	0.101	3.0
	9	1.146	9.594	0.739	17.20	0.388	4.5
	10	1.795	8.672	0.982	0.00	0.000	3.0

Table 5.2: Surface chloride content C_S, apparent diffusion coefficient D_{app}, and correlation factor R^2 obtained by fitting chloride profiles for the top face of control beams and beams under tension

w/c	Beam	Cs (%)	D_{app} ($x10^{-12}$ m^2/s)	R^2	Stress (MPa)	λ_σ	Max Penetration Depth (cm)
0.35	1	0.906	4.490	0.997	0.00	0.000	2.5
	2	0.876	4.212	0.989	1.55	0.347	2.5
	3	0.593	3.019	0.982	3.14	0.704	2.0
0.4	4	0.856	4.602	0.962	0.00	0.000	2.0
	5	0.830	4.433	0.975	1.59	0.414	2.0
	6	0.880	3.946	0.944	3.46	0.901	2.0
0.5	7	1.090	1.704	0.946	0.00	0.000	2.5
	8	1.058	4.672	0.987	1.59	0.398	2.0
	9	0.696	7.281	0.950	2.67	0.668	2.5
	10	0.892	1.515	0.972	0.00	0.000	2.0

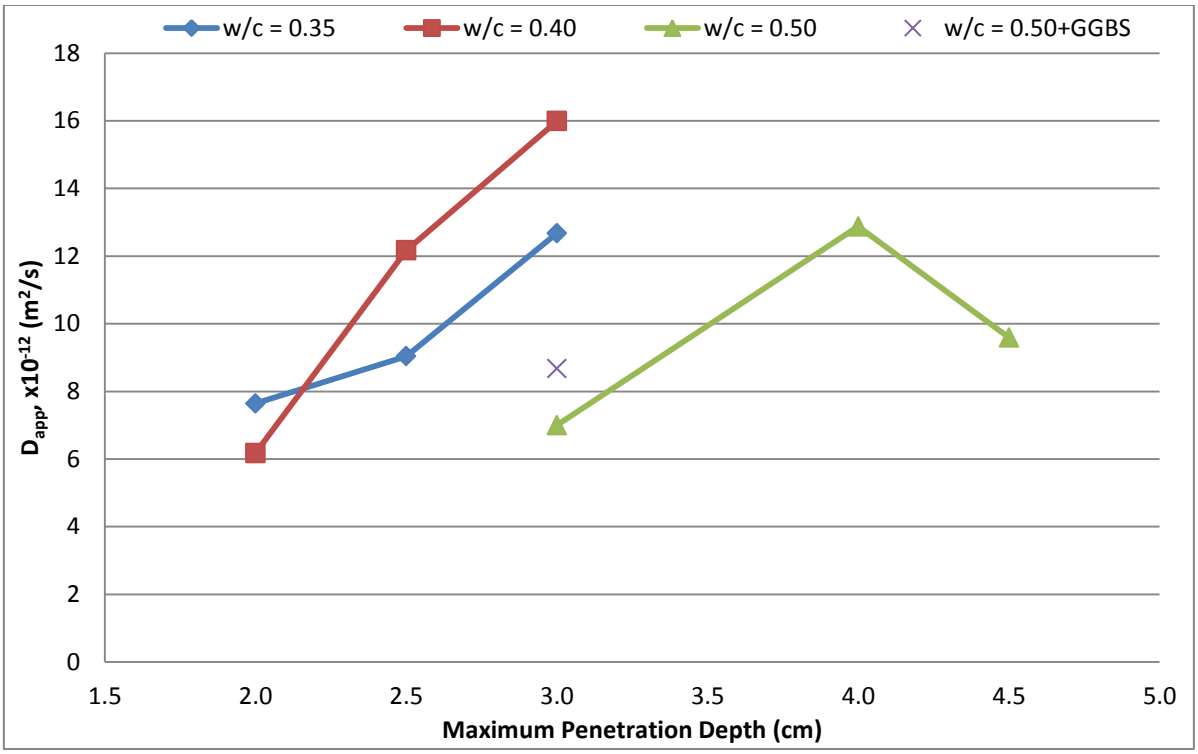

Figure 5.1: Diffusion coefficient versus max penetration depth for concrete under compression

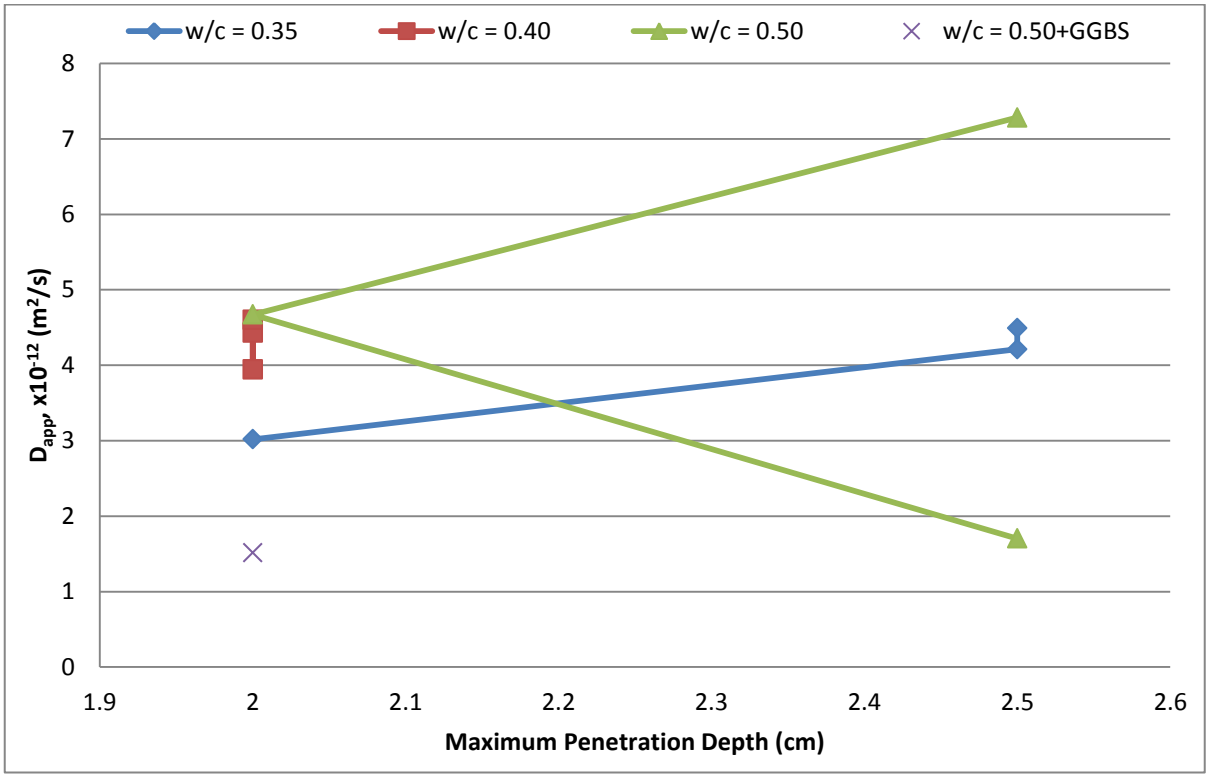

Figure 5.2: Diffusion coefficient versus max penetration depth for concrete under tension

The theoretical surface chloride concentrations C_S in Tables 5.1 and 5.2 range from 0.55 to 1.79% by weight of concrete (mean value μ= 1.27%, standard deviation σ = ±0.39%, and coefficient of variation of 31%) for concrete under sustained compression, and 0.59 to 1.09% by weight of concrete (mean value μ= 0.87%, standard deviation σ = ±0.15%, and coefficient of variation of 17%) for concrete under sustained tension. This further reinforces that concrete under compression and tension were subjected to different boundary conditions during the entire duration of exposure. In fact, it was observed that the compression faces of the beams, which were placed at the bottom of the tank where salt grains deposited, were subjected to a chloride solution with higher concentration. Furthermore, the C_s values in Tables 5.1 and 5.2 are much lower than the average chloride concentrations in the tank solution obtained experimentally and reported in Table 3.7. Deviations of these values are attributed to localized areas of higher NaCl concentration in the tank solution. Surface concentration data plotted against w/c can be seen in Figures 5.3 (compression) and 5.4 (tension). Generally, an increase in w/c causes an increase in the C_S values for concrete both under compression and tension.

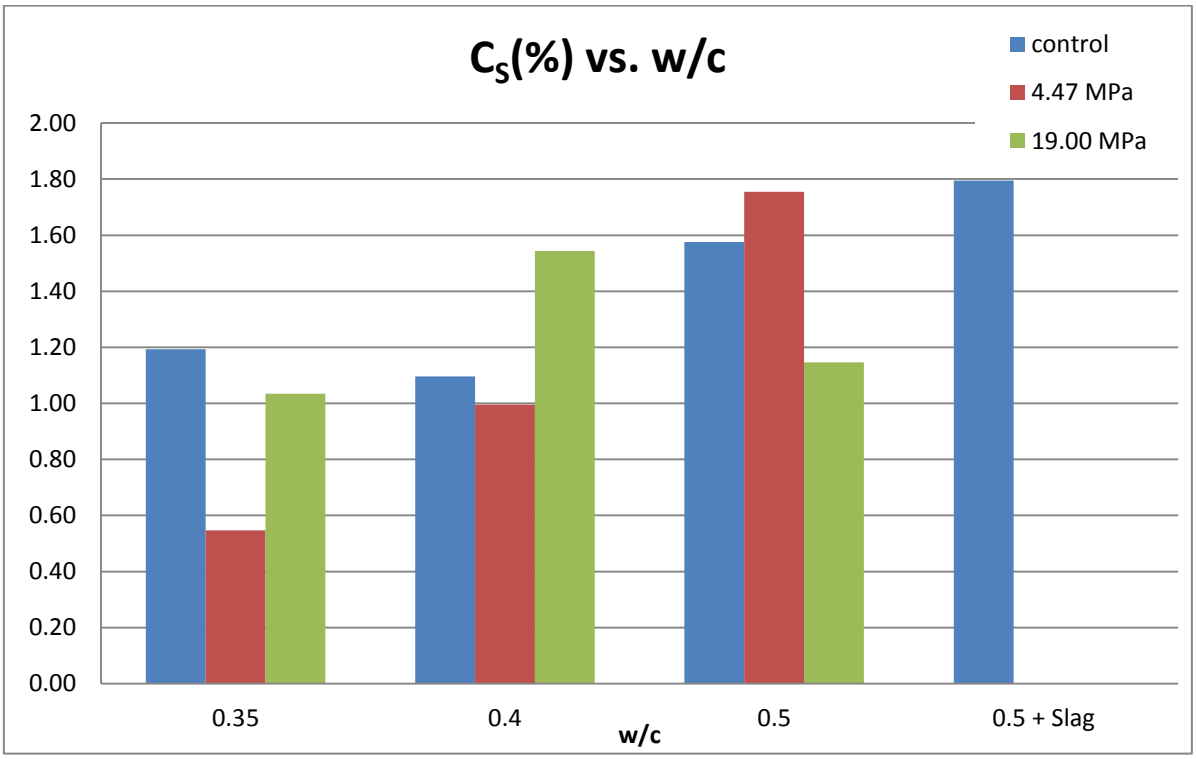

Figure 5.3: Theoretical surface concentrations for all beams under compression

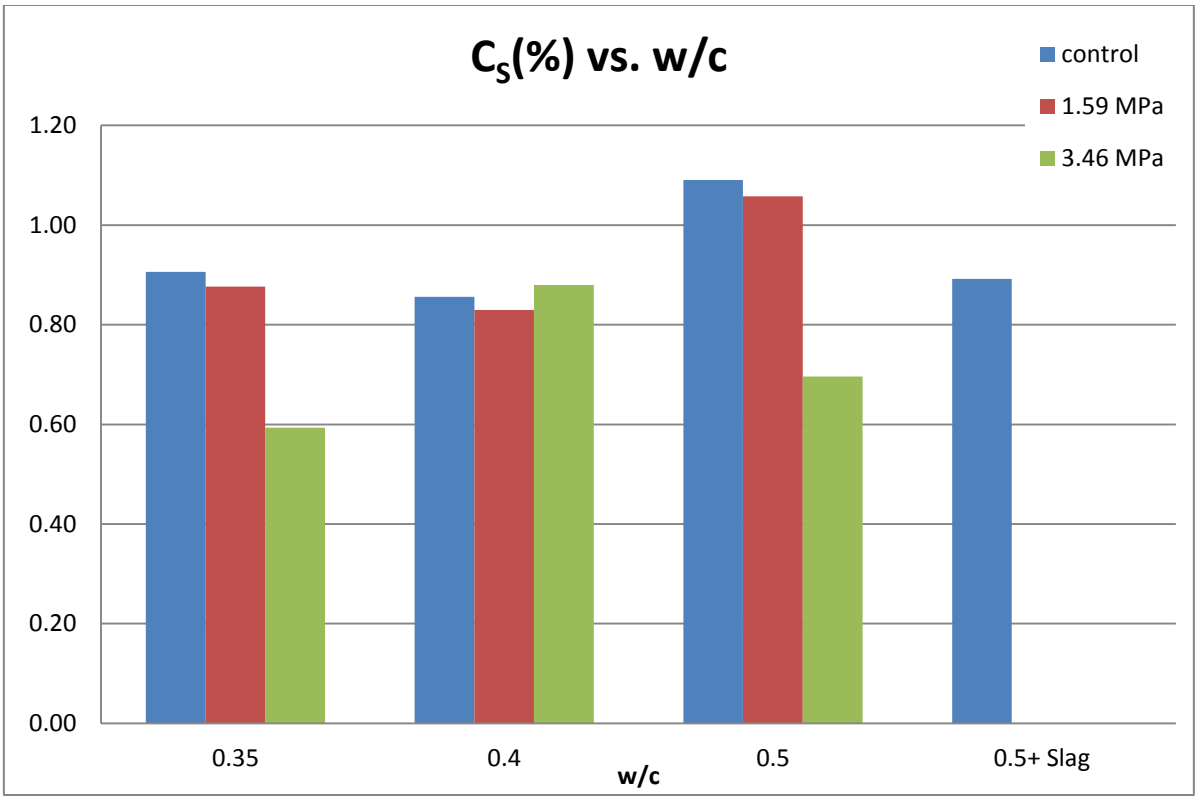

Figure 5.4: Theoretical surface concentrations for all beams under tension

The D_{app} and C_S values presented in Tables 5.1 and 5.2 are used with Eq. (2.6) to model the theoretical chloride concentrations for the profiles seen in Chapter 4, assuming that the initial concentration (C_0) is zero. Since the chloride concentration to which each of the beams was exposed varied, each individual chloride profile is normalized to the corresponding calculated C_s value to allow for comparisons among different load types and levels and w/c. Crank's error function solution to Fick's second law correlates well to the experimentally obtained chloride profiles, as seen in Figures 5.5 through 5.16 and the high R^2 values of Tables 5.1 and 5.2. Figures 5.5 to 5.7 show chloride profiles (normalized with respect to the corresponding C_s) taken from the compressive faces of the beams with a w/c of 0.35, 0.40 and 0.50, respectively. Compressive stresses increase the chloride penetration for the concrete with a w/c of 0.35 (Figure 5.5), although at a low compressive stress of 4.35 MPa, the increase is marginal with respect to the unloaded specimen. However, as the w/c increases to 0.40 and 0.5 (Figures 5.6 and 5.7), with a corresponding increase of the porosity of the concrete, an increase in compressive stress reduces the penetration of chlorides. This is likely attributed to closing of concrete pores by the compressive loading

(Guoping et al. 2011). The effect of w/c on the penetration of chlorides is observed on the chloride profiles obtained from unloaded specimens and illustrated in Figure 5.8. As expected, as the w/c of the concrete is decreased, the corresponding chloride profile reflects a lower contamination of chlorides. From this figure, it is also observed that the addition of GGBS to a concrete with a w/c of 0.5 results in less chloride penetration, since adding GGBS reduces the capillary porosity of the concrete. The effect of the level of compressive stress on each beam with different w/c is illustrated in Figures 5.9 and 5.10, for stress levels of 4.47 MPa and 19.00 MPa, respectively. As noted before, compressive stresses reduce chloride ingress in concretes with a w/c of 0.40 and 0.50, the effect being stronger for the higher w/c.

Figures 5.11 to 5.13 show chloride profiles (normalized with respect to the corresponding C_s) taken from the tensile faces of the beams with a w/c of 0.35, 0.40 and 0.50, respectively. The effect of tensile stresses on the beams with a w/c of 0.35 and 0.40 (Figures 5.11 and 5.12) is only minimal. However, as tensile stresses are increased, so do the chloride penetration fronts for the beam with a w/c of 0.5 (Figure 5.13). The effect of w/c on the penetration of chlorides is observed on the chloride profiles obtained from the top face of unloaded specimens and illustrated in Figure 5.14. Unlike the observations made from Figure 5.8, the concrete with the higher w/c shows the lower chloride penetration. This is observed too from the calculate D_{app} reported in Table 5.2, which is much lower than the corresponding values for the beams with w/c of 0.35 and 0.40. The effect of the level of tensile stress on each beam with different w/c is illustrated in Figures 5.15 and 5.16, for stress levels of 1.59 MPa and 3.46 MPa, respectively. At a tensile stress level of 1.59 MPa (Figure 5.15), there is no difference in the chloride profiles from the beams with different w/c. However, as the tensile stress is increased to 3.46 MPa (Figure 5.16), chloride penetration is greater as the w/c is increased, as expected.

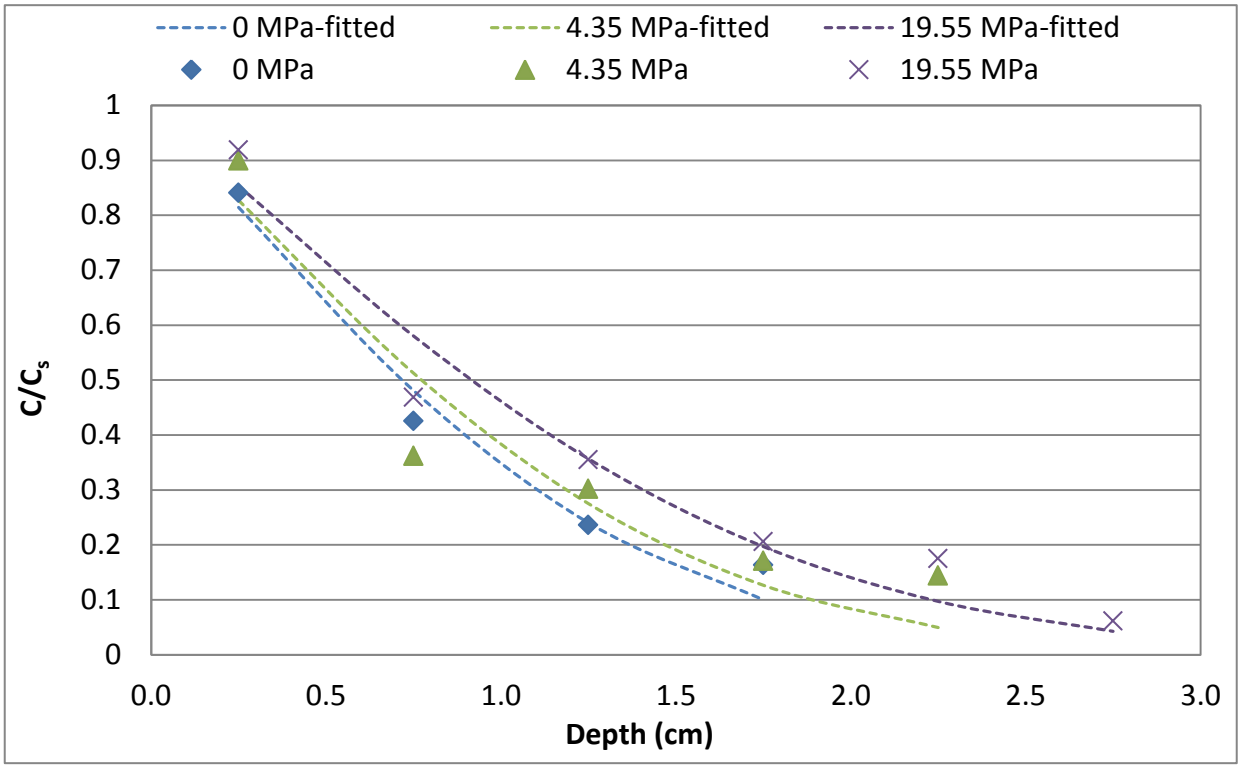

Figure 5.5: Fitted chloride concentration profiles for compression face of beams with w/c = 0.35

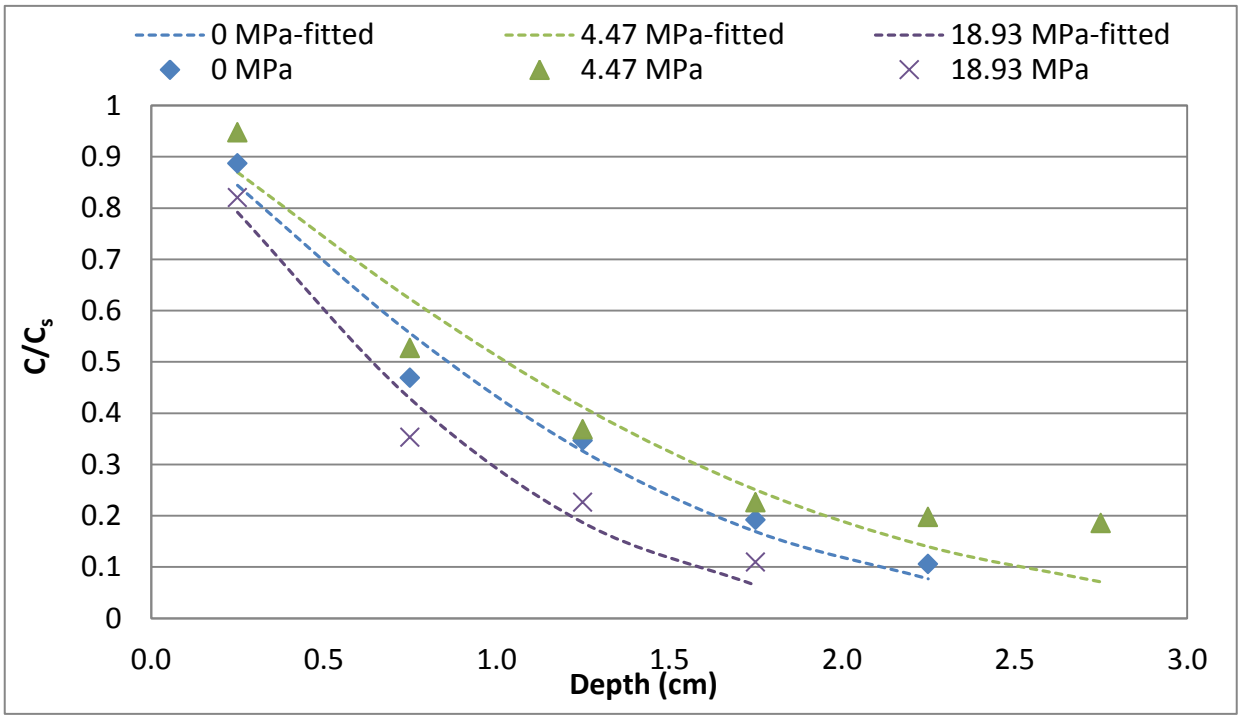

Figure 5.6: Fitted chloride concentration profiles for compression face of beams with w/c = 0.40

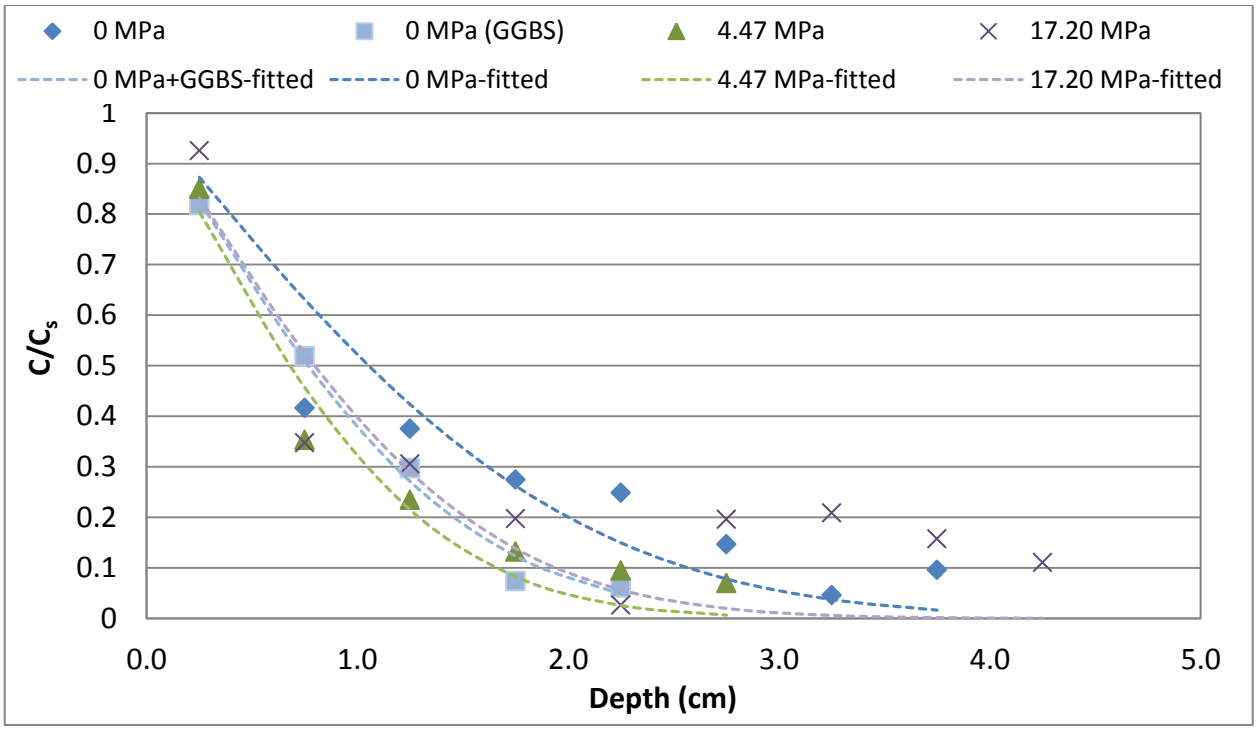

Figure 5.7: Fitted chloride concentration profiles for compression face of beams with w/c = 0.50

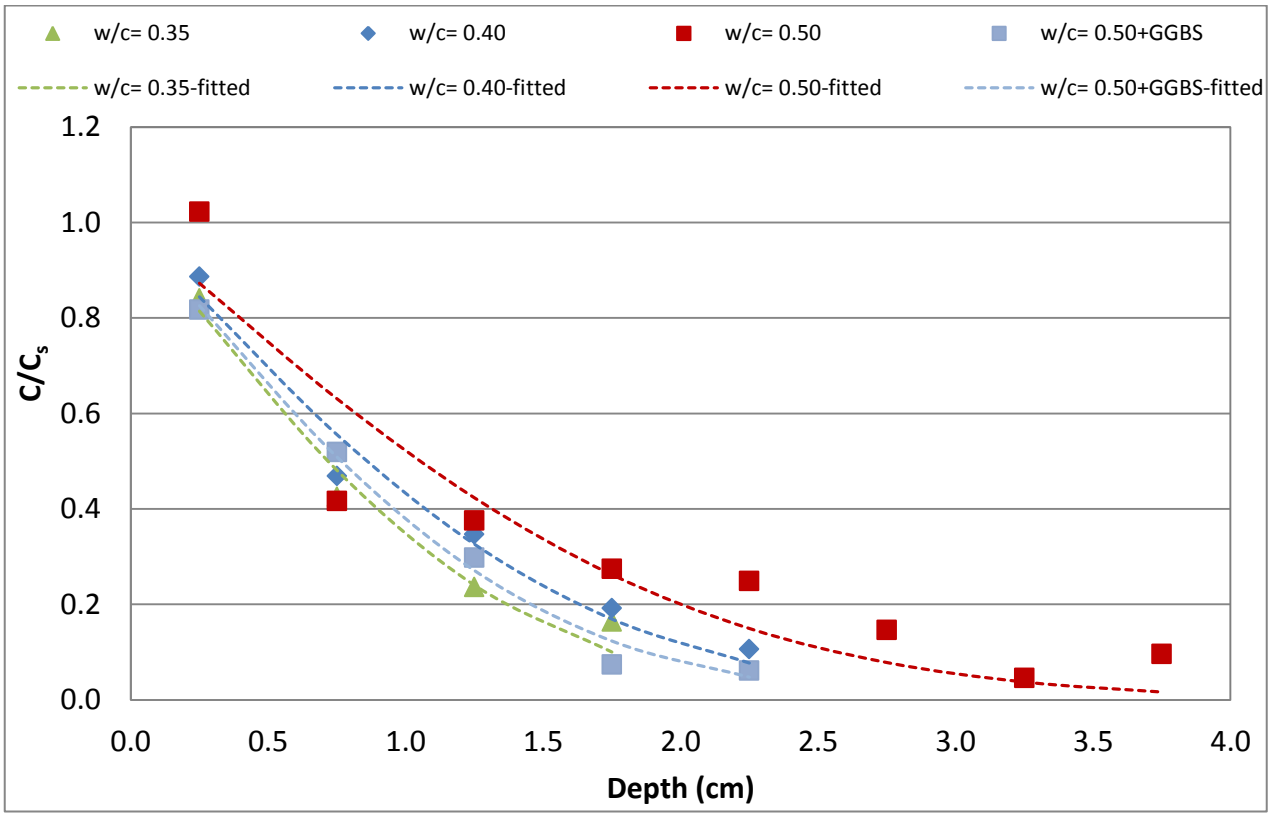

Figure 5.8: Fitted chloride concentration profiles for bottom face of control beams

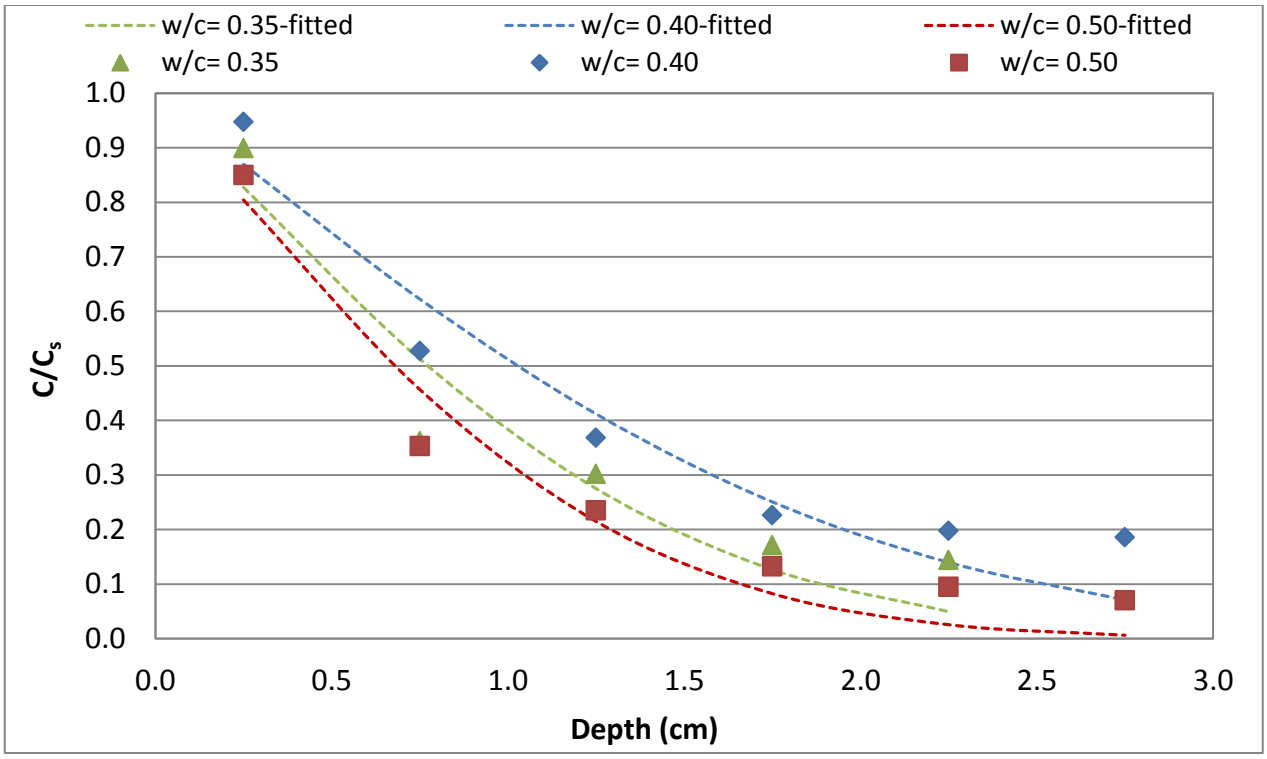

Figure 5.9: Fitted chloride concentration profiles for beams sustaining 4.47 MPa compressive stress

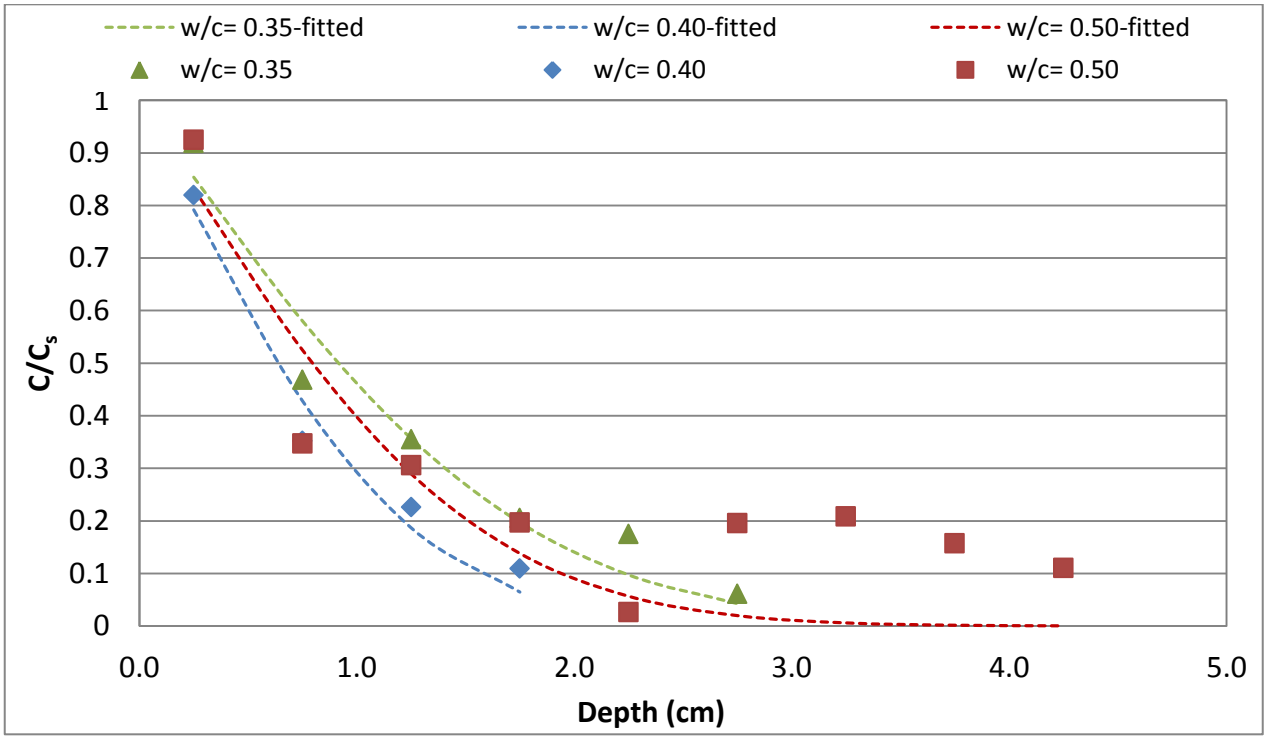

Figure 5.10: Fitted chloride concentration profiles for beams sustaining 19.00 MPa compressive stress

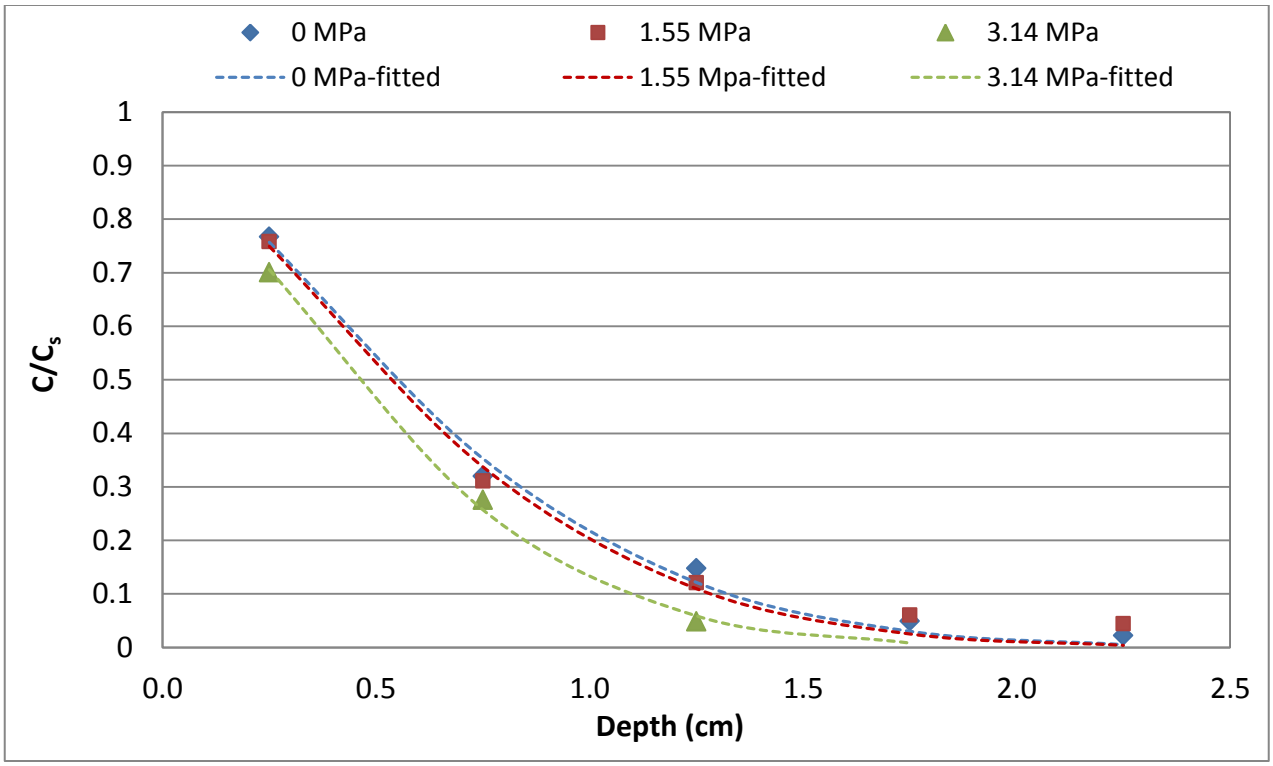

Figure 5.11: Fitted chloride concentration profiles for tensile face of beams with w/c = 0.35

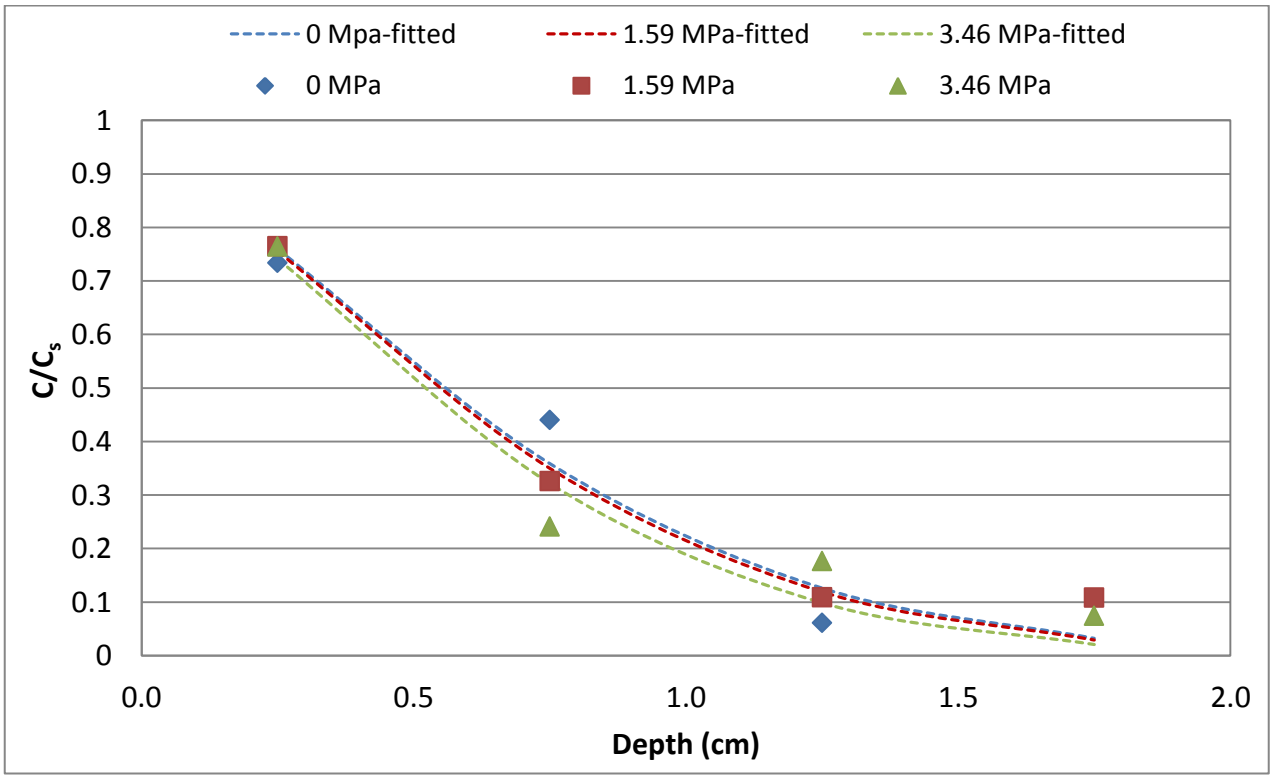

Figure 5.12: Fitted chloride concentration profiles for tensile face of beams with w/c = 0.40

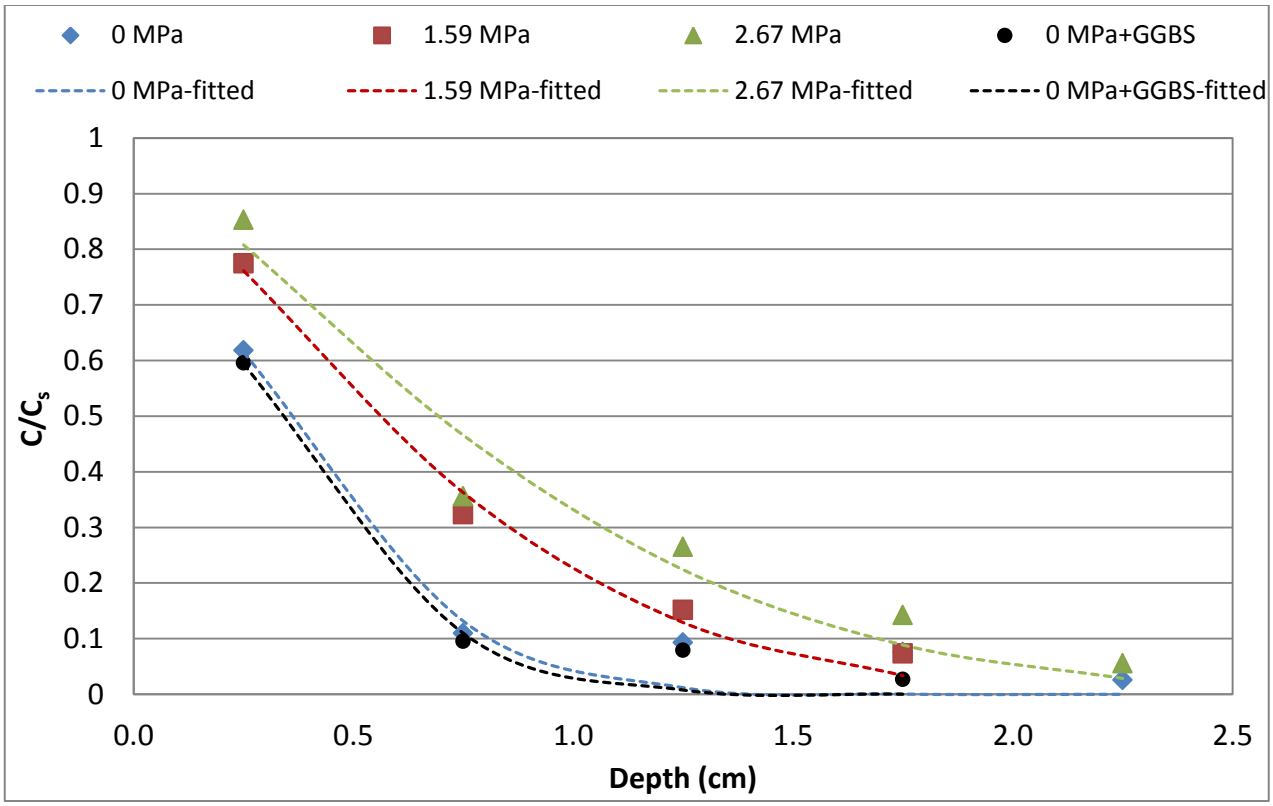

Figure 5.13: Fitted chloride concentration profiles for tensile face of beams with w/c = 0.50

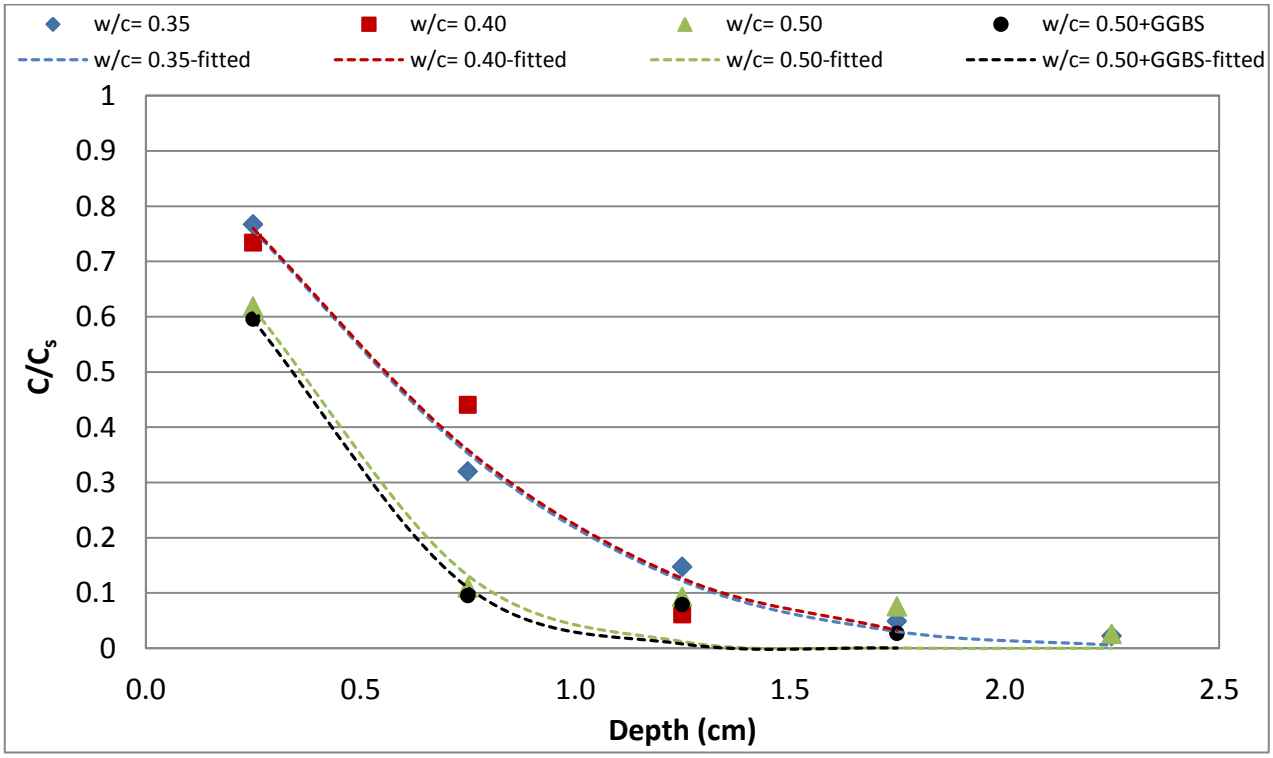

Figure 5.14: Fitted chloride concentration profiles for top face of control beams

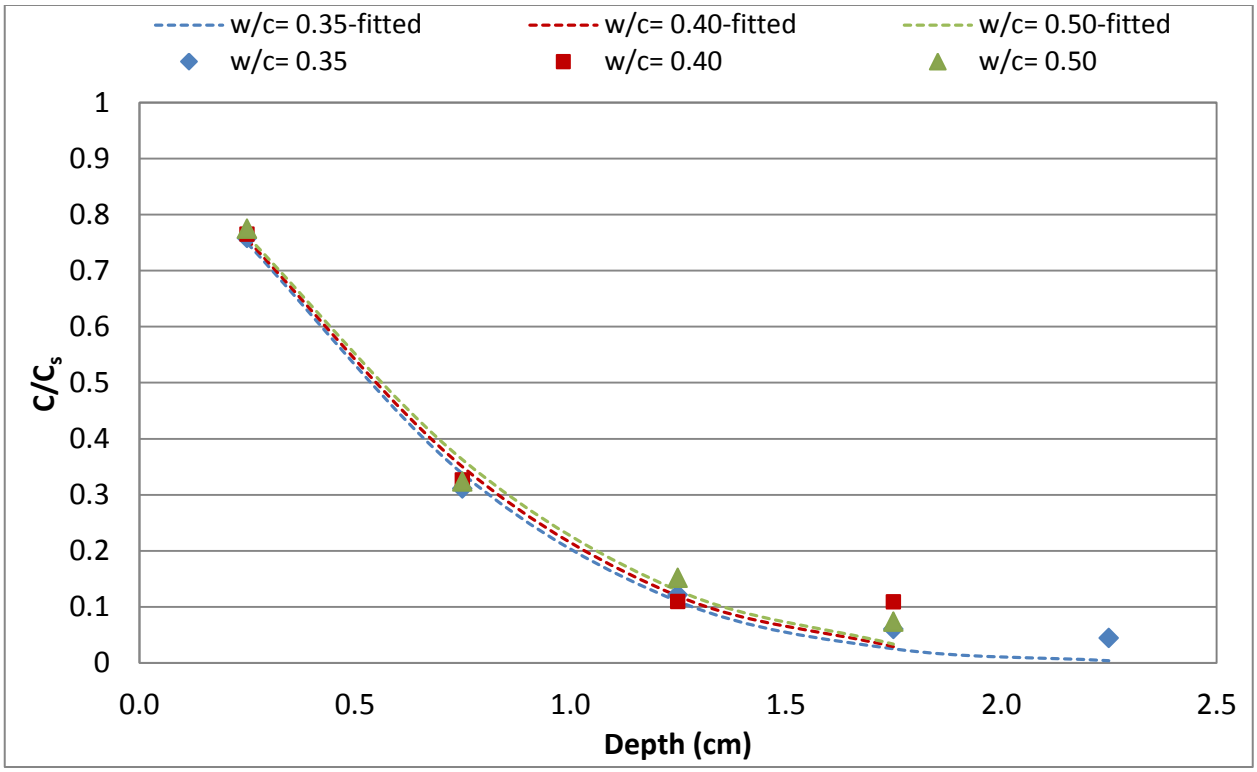

Figure 5.15: Fitted chloride concentration profiles for beams sustaining 1.59 MPa tensile stress

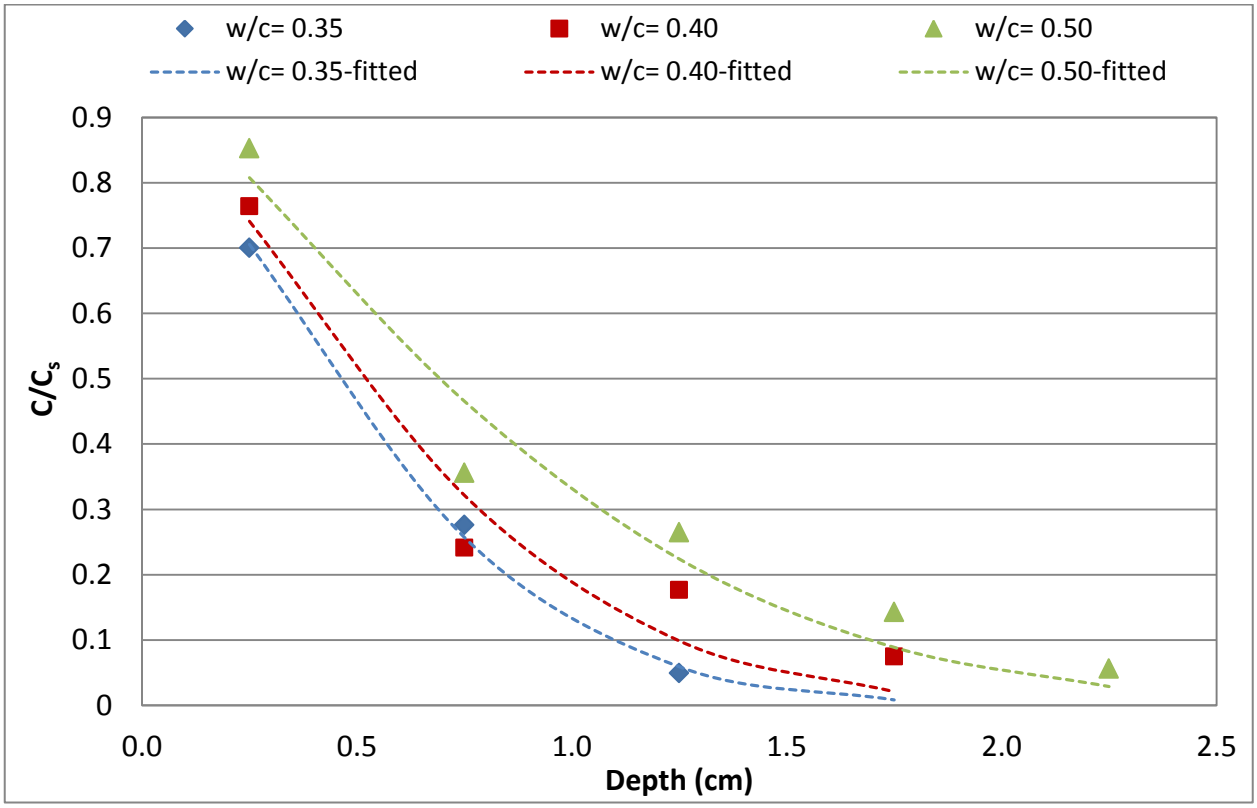

Figure 5.16: Fitted chloride concentration profiles for beams sustaining 3.46 MPa tensile stress

5.2.2 Determination of Diffusivity from $AgNO_3$ Spraying

As seen in Chapter 2, another way to determine chloride relative diffusivities is with the model proposed by Deif (2010). The model is based on the assumptions that the chloride concentration at the boundary of colour change caused by the free chloride interaction with silver nitrate (colourimetric method) is the same for each sample, regardless of applied external loads. The relative value of the diffusivity for different sections of loaded and unloaded control specimens can be determined solely by using the penetration data in Appendix C obtained from the colourimetric method; this relation can be seen in Eq. (2.8).

Using the relation tested by Deif (2010), average relative diffusivities (with corresponding standard deviation values) for all sections were obtained with Eq. (2.8) and can be seen in Tables 5.3, 5.4, and 5.5 for a w/c of 0.35, 0.40, and 0.50, respectively. The subscript *o* refers to the control beam of the specific w/c, and the subscript *i* refers to the beam number; therefore, D_2/D_o is the relative diffusivity for average penetration depths of beam 2. Large relative diffusivities can be seen in the compressive and tensile face of beam 2 and a random spike in the tensile face of beam 3; as mentioned before, beam 2 is very inconsistent in terms of quality, and the outliers in the data set were accordingly discarded from analysis. It is interesting to note that in Table 5.4 there is less variability in concrete with a w/c ratio of 0.40 in both compression and tension. This is attributed to the quality and consistency of concrete from batch 2 (w/c = 0.40) giving very consistent average penetration depths.

Generally, relative diffusivity values in Table 5.3 are all above the control section value of 1.00 and have relatively high standard deviations when compared to other w/c ratios; as mentioned before, batch 1 (w/c = 0.35) was poorly mixed giving unreliable results. For this reason many of the data points in Table 5.3 have been omitted in the trend analysis of Figures 5.17 and 5.18 with respect to the colourimetric method.

Table 5.3: Relative diffusivity obtained from average chloride penetration depths (w/c = 0.35)

	Section Cut	X_2/X_o	$(D_2/D_o)_{avg}$	λ_σ	X_3/X_o	$(D_3/D_o)_{avg}$	λ_σ
Compression	A-A	1.22	1.30 (±0.195)	0.152	1.44	1.96 (±0.135)	0.684
		1.05			1.35		
	B-B	1.27	1.47 (±0.14)	0.078	1.49	2.18 (±0.035)	0.351
		1.15			1.46		
	C-C	6.00	39.13 (±3.13)	0.056	1.49	2.39 (±0.175)	0.253
		6.50			1.60		
	D-D	1.96	4.00 (±0.175)	0.044	1.09	1.37 (±0.19)	0.197
		2.05			1.25		
Tension	A-A	1.05	1.14 (±0.025)	0.347	0.95	0.925 (±0.025)	1.561
		1.08			0.98		
	B-B	2.89	7.32 (±1.07)	0.157	1.84	29.82 (±26.43)	0.705
		2.50			7.50		
	C-C	9.00	95.63 (±14.63)	0.108	1.70	2.98 (±0.085)	0.484
		10.50			1.75		
	D-D	8.25	62.16 (±5.91)	0.082	1.05	1.05 (±0.05)	0.368
		7.50			1.00		

Table 5.4: Relative diffusivity obtained from average chloride penetration depths (w/c = 0.40)

	Section Cut	X_5/X_o	$(D_5/D_o)_{avg}$	λ_σ	X_6/X_o	$(D_6/D_o)_{avg}$	λ_σ
Compression	A-A	0.86	0.71 (±0.02)	0.153	0.80	0.69 (±0.05)	0.332
		0.83			0.86		
	B-B	1.11	1.23 (±0.0)	0.078	1.20	1.44 (±0.0)	0.170
		1.11			1.20		
	C-C	0.96	0.93 (±0.02)	0.056	1.41	2.04 (±0.04)	0.123
		0.98			1.44		
	D-D	0.56	0.29 (±0.03)	0.044	0.83	0.55 (±0.13)	0.096
		0.51			0.65		
Tension	A-A	1.17	1.22 (±0.145)	0.415	1.27	1.51 (±0.09)	0.901
		1.03			1.19		
	B-B	0.97	1.00 (±0.065)	0.187	0.97	1.05 (±0.105)	0.407
		1.04			1.07		
	C-C	0.93	1.01 (±0.145)	0.129	0.80	0.62 (±0.025)	0.279
		1.08			0.77		
	D-D	1.00	1.1 (±0.01)	0.098	1.17	1.4 (±0.02)	0.212
		1.10			1.19		

Table 5.5: Relative diffusivity obtained from average chloride penetration depths (w/c = 0.50)

	Section Cut	X_8/X_o	$(D_8/D_o)_{avg}$	λ_σ	X_9/X_o	$(D_9/D_o)_{avg}$	λ_σ
Compression	A-A	-	-	0.196	-	-	0.729
		-			-		
	B-B	0.84	0.78 (±0.08)	0.101	1.61	2.43 (±0.15)	0.374
		0.93			1.51		
	C-C	0.75	0.81 (±0.25)	0.072	1.07	1.46 (±0.325)	0.269
		1.03			1.34		
	D-D	1.07	1.145 (±0.005)	0.057	3.04	8.66 (±0.565)	0.210
		1.07			2.84		
Tension	A-A	0.73	0.62 (±0.09)	0.398	1.28	1.39 (±0.24)	1.479
		0.84			1.07		
	B-B	0.70	0.58 (±0.10)	0.180	1.00	1.00 (±0.00)	0.668
		0.83			1.00		
	C-C	0.71	0.52 (±0.02)	0.124	0.92	0.58 (±0.27)	0.459
		0.73			0.56		
	D-D	0.71	0.515 (±0.005)	0.094	0.67	0.50 (±0.06)	0.349
		0.72			0.74		

Omitting exceptionally high relative diffusivities, results from Tables 5.3, 5.4, and 5.5 are plotted in Figures 5.17 and 5.18 against normalized compressive and tensile stresses (stress index, λ_σ), respectively. Beams with similar w/c ratios are plotted together to isolate for the effect of stress on relative diffusivities. Figure 5.17 shows a general trend that concrete sustaining low values of compressive stresses (up to approximately 20% of f'_c) have lower relative diffusivities, and the trend is more apparent the higher the w/c is. This can be attributed to the reduction of porosity at low compressive stress levels. However, as the compressive stress is increased, an increase of the relative diffusivity over the value of 1 is observed. This is likely due to the increase in microcracking as the compression increases. Similar observations have been reported by Guoping et al. (2011).

Figure 5.18 illustrates that only a marginal increase in the relative diffusivity occurs for tensile stresses above the modulus of rupture of the material. The increase in relative diffusivity for concrete subjected to a tensile stress above the stress index ($\lambda_{\sigma t}$) of 1.00 can be attributed to the fact that concrete is cracked, because it is theoretically being subjected to a tensile stress larger than the experimentally obtained tensile strength of the concrete. This also explains why in Figure 5.18 that data points to the left of the dotted line (uncracked) have lower relative diffusivity values.

Depending on the w/c ratio, the obtained results reported in Figures 5.17 and 5.18 are not in full agreement with the findings from studies done by Gowripalan et al. (2000), Lim et al. (2000), and Wang et al. (2011), which conclude that with an increase in stress level, the chloride diffusivity D_{app} decreases in the compression zone (as long as the applied stress is below 55% of f'_c), and marginally increased in the tension zone.

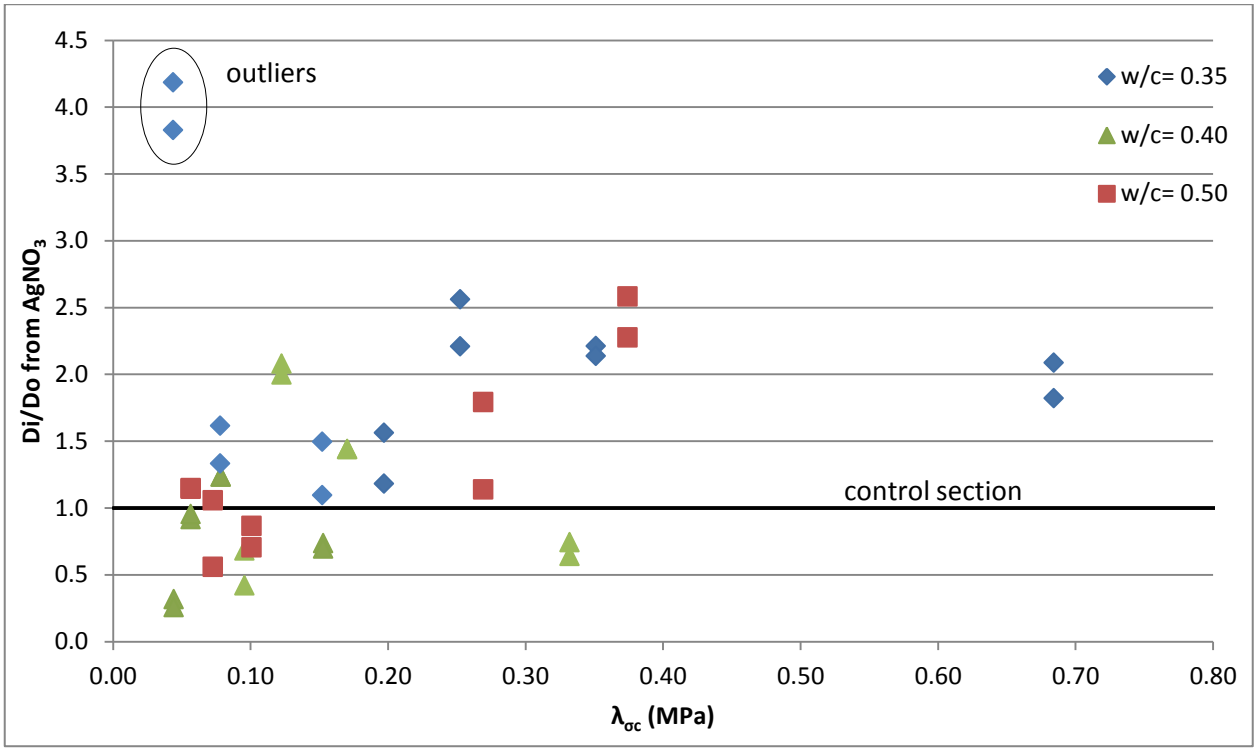

Figure 5.17: Relative diffusivities from colourimetric method for concrete under compression (normalized)

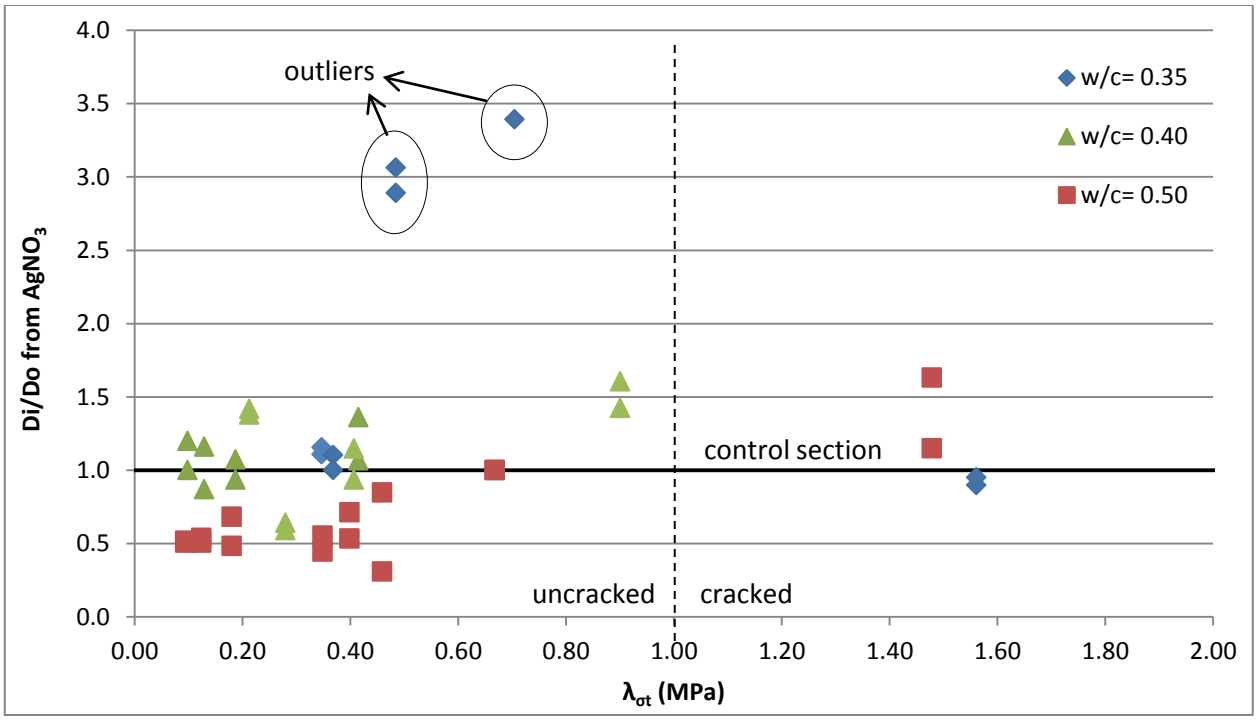

Figure 5.18: Relative diffusivities from colourimetric method for concrete under tension (normalized)

5.2.3 Comparison between both Methods

In order to establish the reliability and accuracy of determining diffusion coefficients by spraying chloride contaminated concrete with silver nitrate (colourimetric method), a comparison between the relative diffusivities obtained from the colourimetric and potentiometric titration method must be done. During comparison, the more data points that converge to a 45-degree line, the more accurate the colourimetric method is in determining the rate of chloride penetration in concrete; the closer the differences in numerical values are to each other the more reliable the results are. The study done by Deif (2010) illustrates that since the differences in the ratios of both methods seem to converge as the time of exposure increases, the colourimetric method could be used as a quick analytical tool to detect average chloride penetration fronts after at least one year of exposure (Deif, 2010). Figure 5.19 shows the comparison of relative diffusivities between the colourimetric and potentiometric titration methods for the third wetting and drying cycle (270 days) of his experiment.

Relative diffusivities from the titration results are calculated from the D_{app} values in Tables 5.1 and 5.2 for compression and tension, respectively; however, only a select few of relative diffusivities

calculated in Tables 5.3, 5.4, and 5.5 were used for comparison, since specifically chosen (Table 3.8) concentration profiles were analyzed by potentiometric titration. Figures 5.20 and 5.21 show the comparison between the relative diffusivities obtained from both methods for compression and tension, respectively; each w/c data point represents a control, a lower stress, and a higher stress section. Generally, the ratios obtained for concrete under compression give more accurate comparisons, converging to the 45-degree line better than the ratios for concrete under tension. In general, relative diffusivity ratios obtained from the colourimetric method are larger than those obtained from titration for both concrete under compression and tension.

In order to quantify the accuracy of the colourimetric method, the magnitude of deviation (normal distances) of each D_i/D_o ratio from the 45-degree line for concrete under compression and tension are plotted in Figures 5.22 and 5.23, respectively. Again, ratios for concrete in compression show less deviation than ratios for concrete under tension. Notably, concrete with a w/c of 0.40 shows the least amount of deviation in compression and tension; the reason for this is the higher quality and consistency of concrete obtained from properly mixing batch 2 (w/c = 0.40).

To determine apparent diffusion coefficients from in-situ concrete samples sprayed with silver nitrate, relative diffusivities can be multiplied by a reference chloride diffusion coefficient (D_{ref}) as recommended by the ACI Committee 365 service life prediction model (Bentz & Thomas, 2001). The D_{ref}, as seen in Eq. (5.1), takes into account the effect of the w/c ratio and curing time of concrete (t_O); the curing time is specified as 28 days by Life-365. Rearranging Eq. (2.8) and substituting D_{ref} as the uncracked unstressed D_o section, the D_{app} from the silver nitrate spray can be successfully calculated with Eq. (5.2).

$$D_{ref}(W/C\,, t_o) = D_{t_{o=28days}} = 1 \times 10^{(-12.06+2.40W/C)}\ (m^2/s) \tag{5.1}$$

$$D_{app} = D_{ref}\left(\frac{x_i}{x_o}\right)^2\ (m^2/s) \tag{5.2}$$

In order to test the validity of determining apparent diffusion coefficients from the silver nitrate spray and the ACI Life-365 equation for D_{ref}, Figures 5.24 and 5.25 plot the D_{app} values obtained from potentiometric titration against the D_{app} values obtained from Eq. (5.2). With the exception of a single data point, results for concrete under compression (Figure 5.24) show that there is a good agreement between both methods, and that Eq. (5.1) is suitable for replacing uncracked concrete control sections (D_o). However, results are not as promising for concrete under tension (Figure

5.25), where D_{app} values obtained from Eq. (5.2) are higher than the values obtained from titration; the poor agreement between both methods can be explained by the low surface concentrations and D_{app} values for concrete under tension, as seen in Tables 5.1 and 5.2. As mentioned before, a lower chloride concentration gradient near the surface of the exposure tank acted to skew results for concrete under tension; D_{app} values from potentiometric titration are 25% lower than those obtained from Eq. (5.1).

Therefore, based on the aforementioned observations, it can be concluded that using a silver nitrate spray to predict and determine apparent chloride diffusivity values for concrete is most accurate and acceptable for use on durable, well mixed, and consistent concrete that is sustaining compressive stress. The simple and quick method of spraying silver nitrate on in-situ samples can effectively replace the need for time consuming potentiometric titrations. However, further validation is required to confirm this since this experiment only provides limited data.

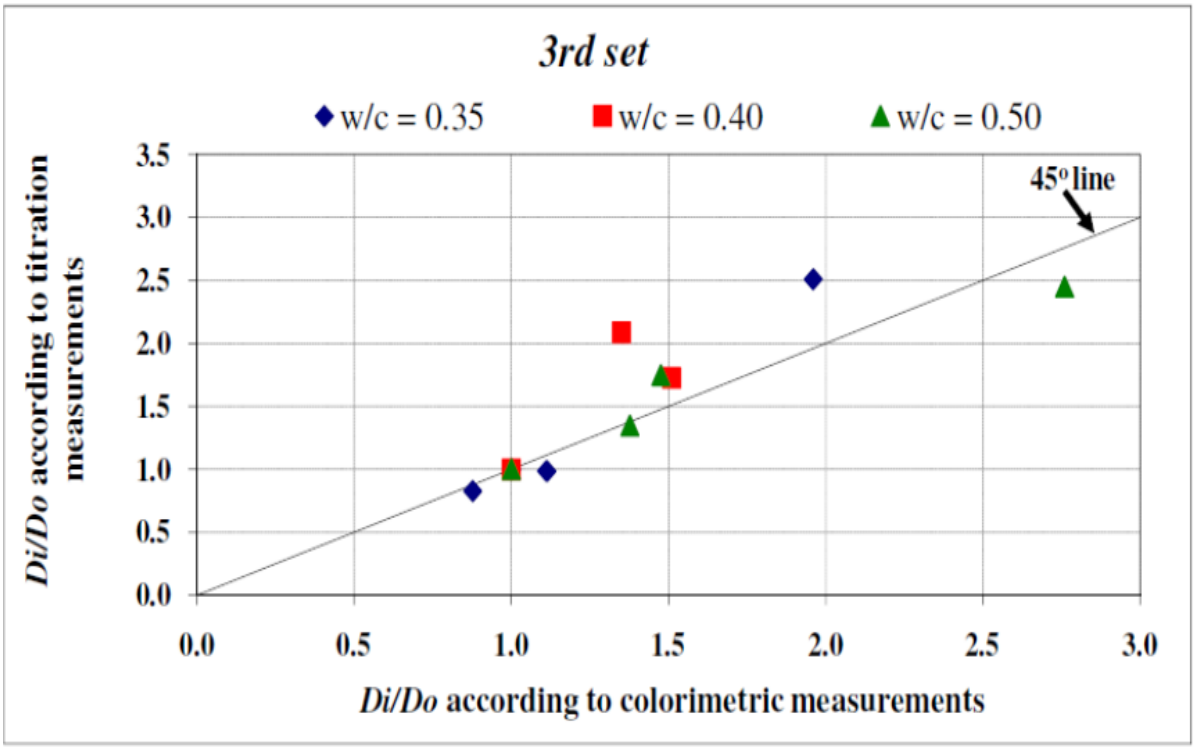

Figure 5.19: D_i/D_o from titration versus D_i/D_o from colourimetric method for the third cycle (Deif, 2010)

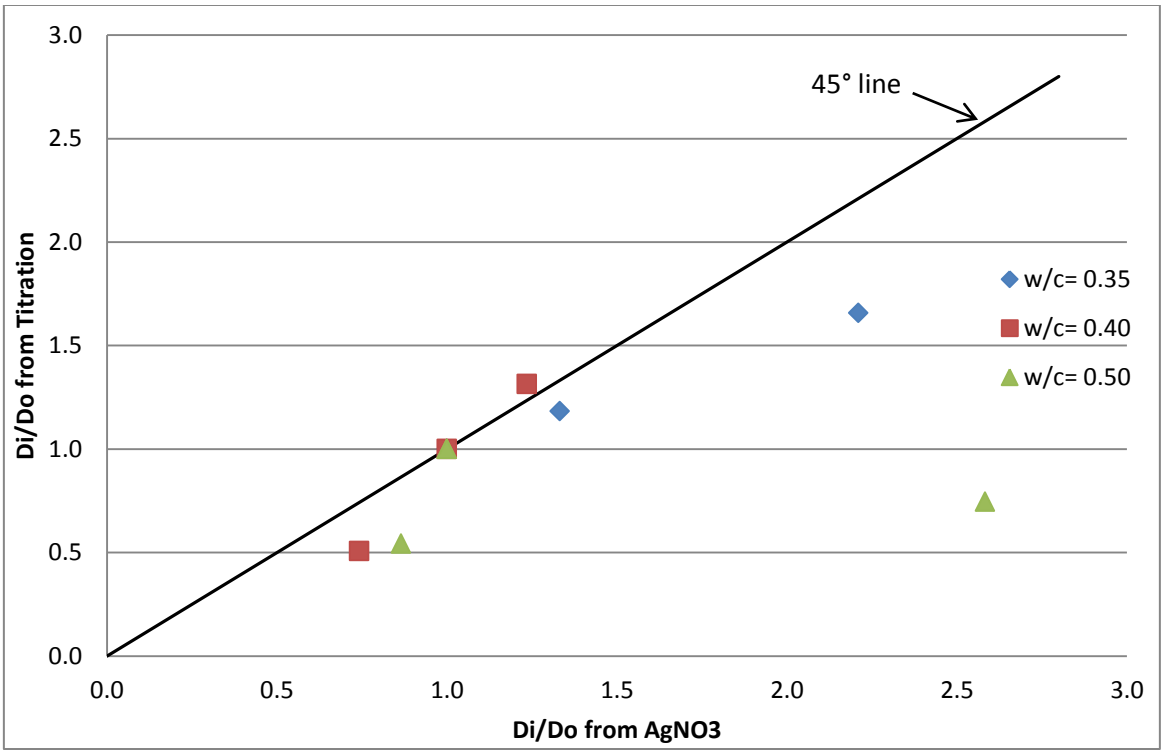

Figure 5.20: D_i/D_o from titration versus D_i/D_o from colourimetric method for concrete under compression

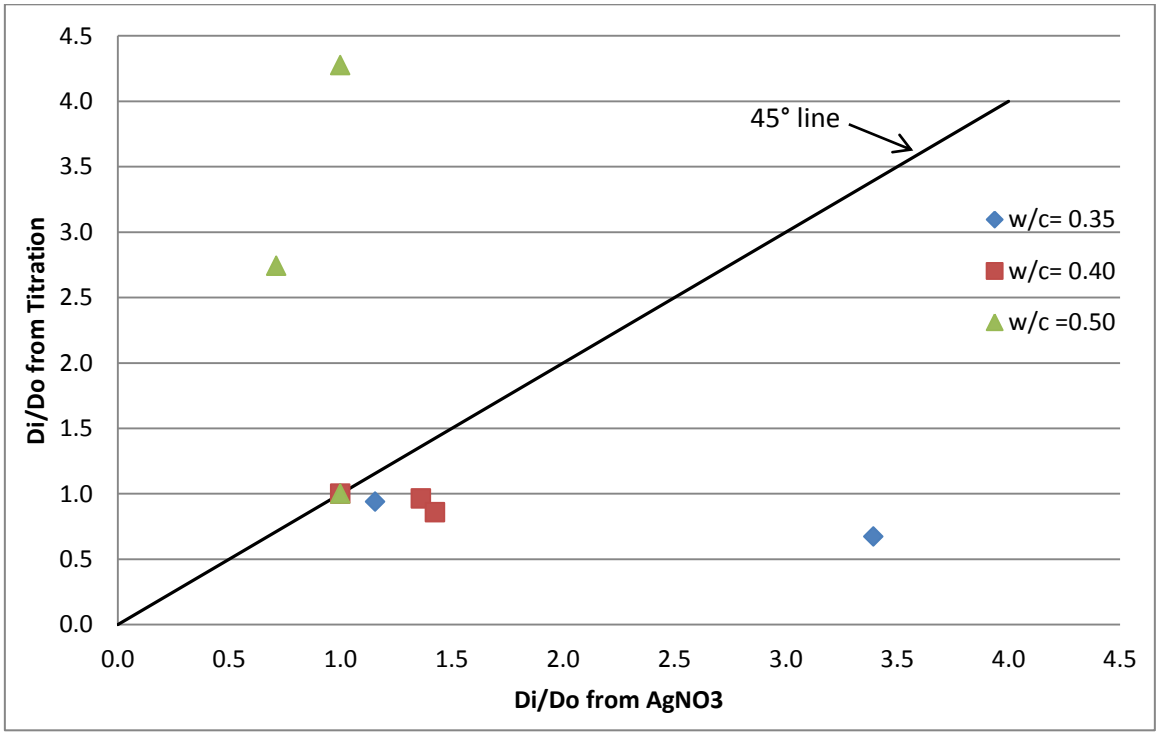

Figure 5.21: D_i/D_o from titration versus D_i/D_o from colourimetric method for concrete under tension

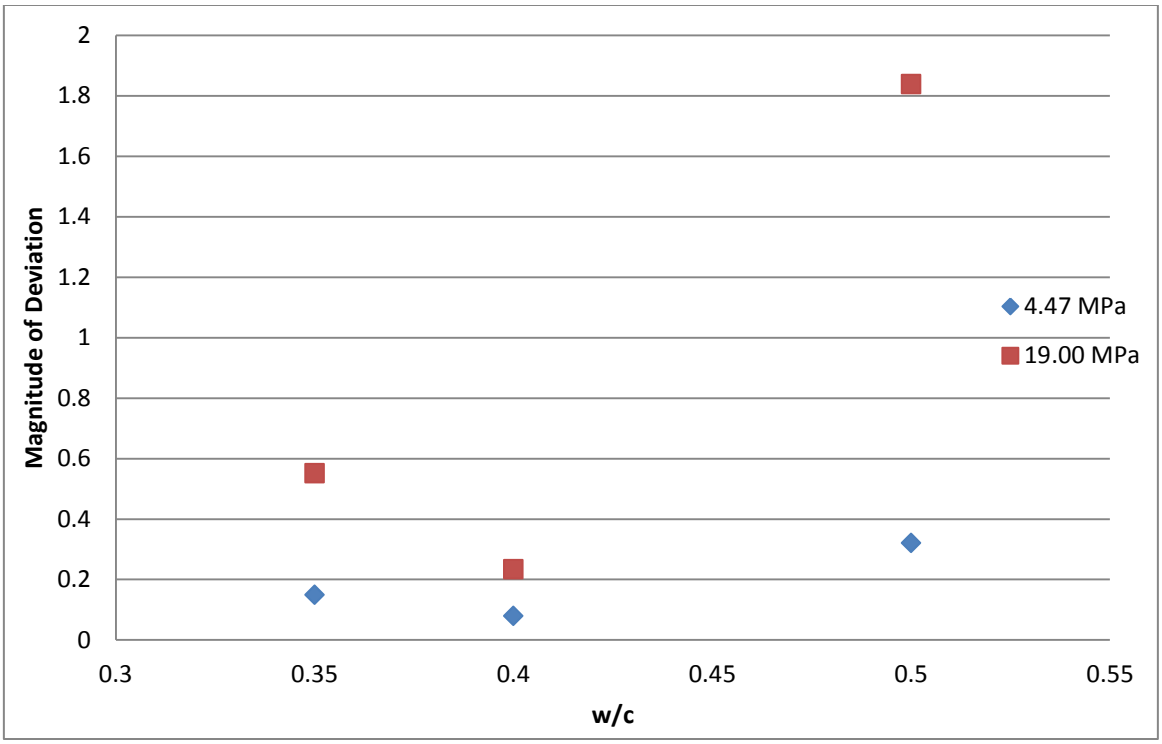

Figure 5.22: Magnitude of normal deviation from 45° line for concrete under compression

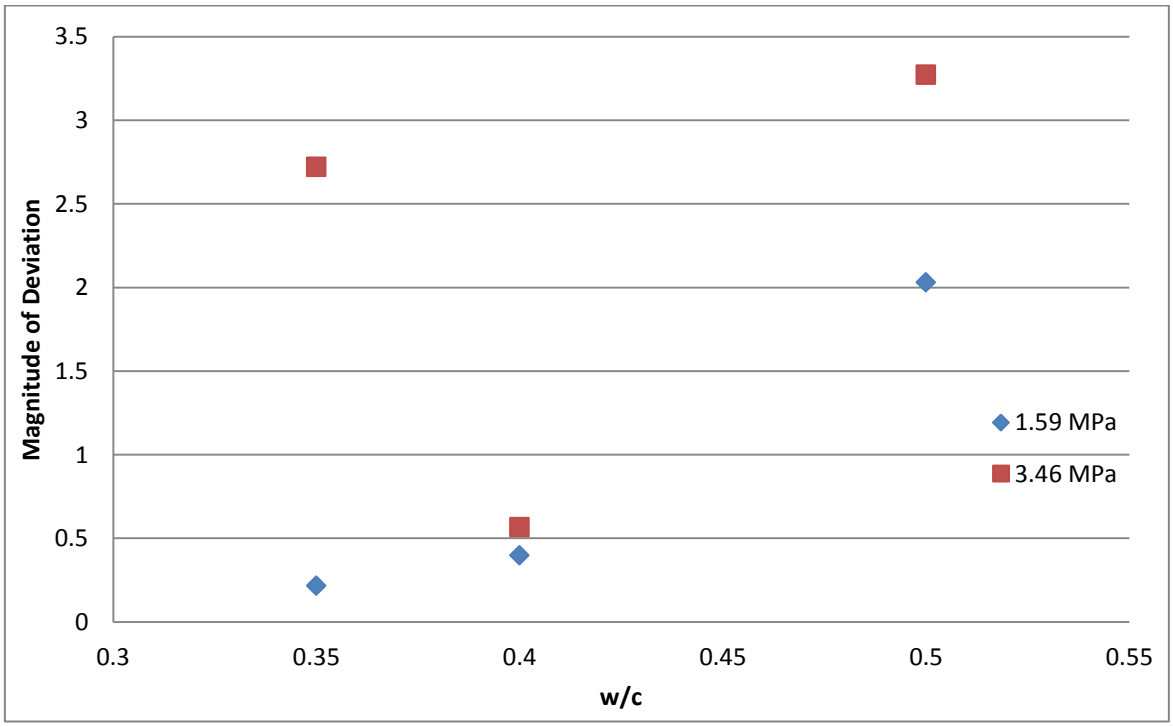

Figure 5.23: Magnitude of normal deviation from 45° line for concrete under tension

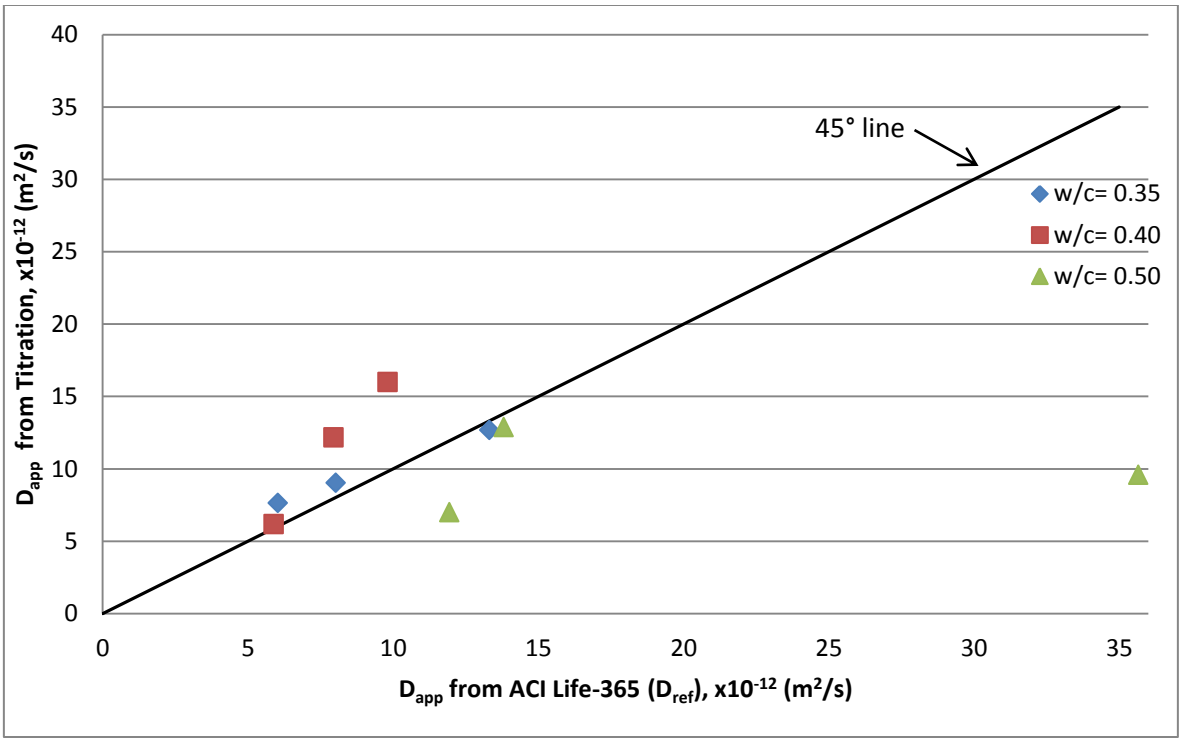

Figure 5.24: D_{app} from titration versus D_{app} from ACI Life-365 (D_{ref}) for concrete under compression

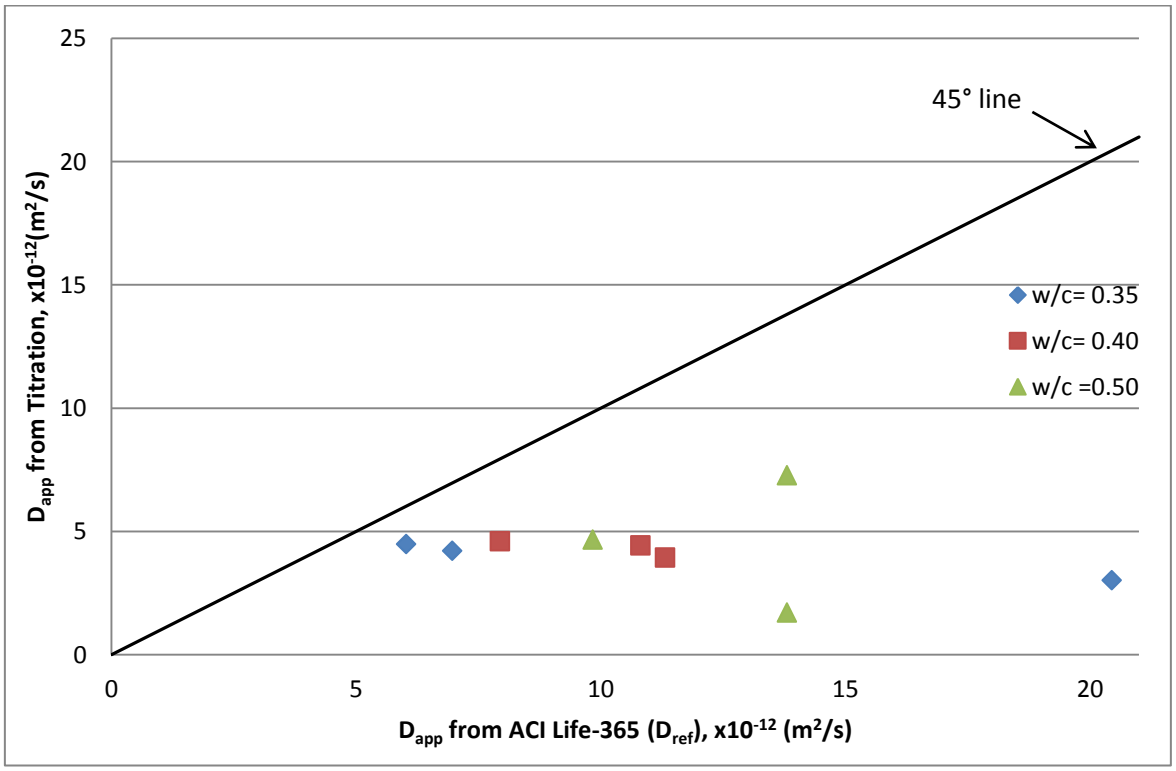

Figure 5.25: D_{app} from titration versus D_{app} from ACI Life-365 (D_{ref}) for concrete under tension

5.3 Chloride Diffusivity as a Function of Stress

Before the relative diffusivities obtained from the colourimetric method and potentiometric titration are evaluated as a function of compressive and tensile stresses, the stress as a function of average penetration depths should be analyzed. Figures 5.26 through 5.28 show the average chloride penetration depths with increasing normalized compressive stress values for each w/c, while Figures 5.29 through 5.31 show the average chloride penetration depths with increasing normalized tensile stress values for each w/c. Seeing that the squared of the average penetration depth obtained by spraying silver nitrate is directly related to the diffusivity of concrete by Eq. (2.8), similar trends are observed as in Figures 5.17 and 5.18. However, for Figures 5.26 through 5.31 stresses are isolated for specific beams and w/c ratios for both concrete under compression and tension.

Generally, an increase in compressive stress (up to $0.2f'_c$) causes a slight decrease in average penetration depths for all beams and an increase in the penetration fronts at higher levels of compressive stresses. An increase in tensile stress causes an increase in average penetration depths for all beams, particularly at values of $\lambda_\sigma > 1$. With the exclusion of the poorly constructed beam 2, it is interesting to note that for concrete under compression, beams with a higher post-tensioning load of the same w/c ratio always have higher average penetration depths when subjected to similar stress as its lower post-tensioned counterpart (e.g., see blue points of B9 over red points of B8 in Figure 5.28). Beams may be similar in stress conditions; however, the cross-sectional area and tendon eccentricity are different, which accounts for the slight variations in average penetration depth. The opposite is true for beams subjected to tensile stress, where a higher post-tensioning load gives lower average penetration depths under similar stress conditions. The overall increase of average penetration depths for increasing tensile stress values is expected; according to the 28-day f'_t material strengths reported in Chapter 3, concrete cracking due to the load should have occurred.

According to Lim et al. (2000), the critical compressive stress level to induce microcrack formation is between $0.80\text{-}0.95f'_c$; however, only beam 9 comes close with a value of $0.73\ f'_c$. If critical compressive microcracks developed, then a sudden jump in average penetration depth should have occurred at the highest compressive stress values, but it did not. Figures 5.27 and 5.28 show a decrease in average penetration depths for each respected beam as levels of compressive stress

increase. These results can also be seen in the experiment done by Wang et al. (2011) and Lim et al. (2000), where compressive stresses below the critical stress level act to reduce chloride penetration and concentration in concrete.

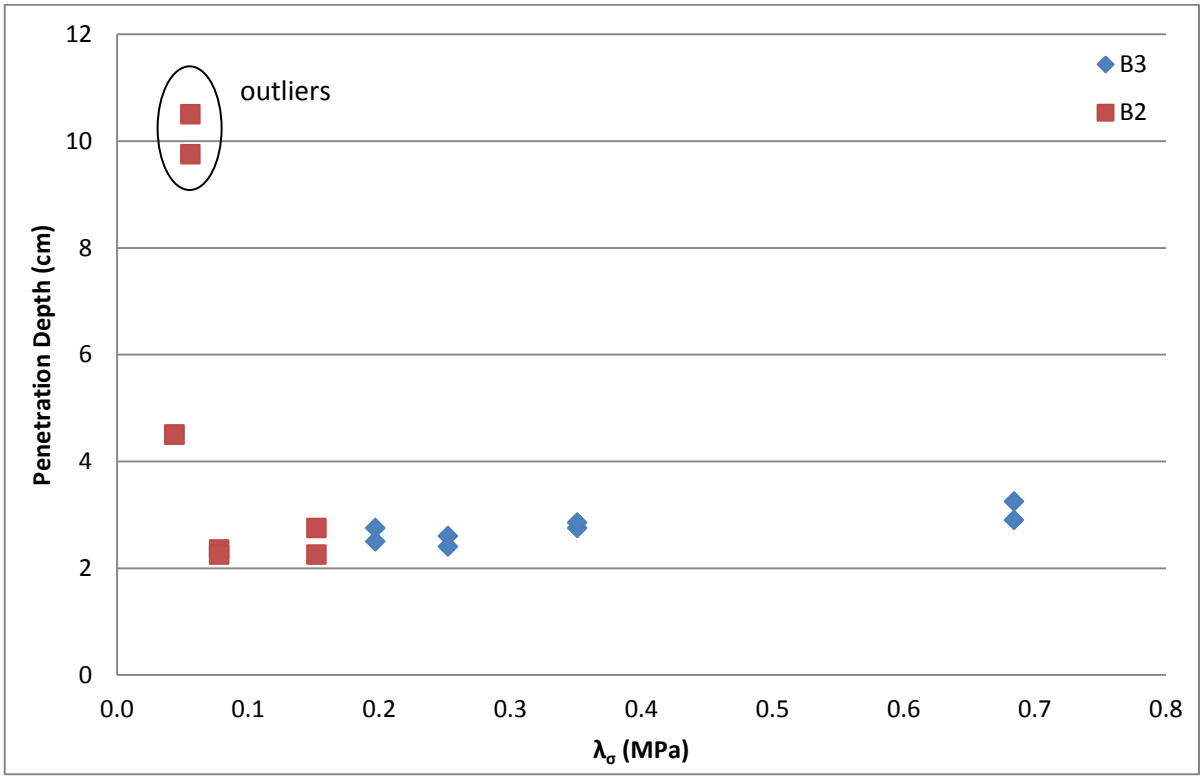

Figure 5.26: Average penetration depths versus compressive stress for beams 2 & 3 (w/c = 0.35)

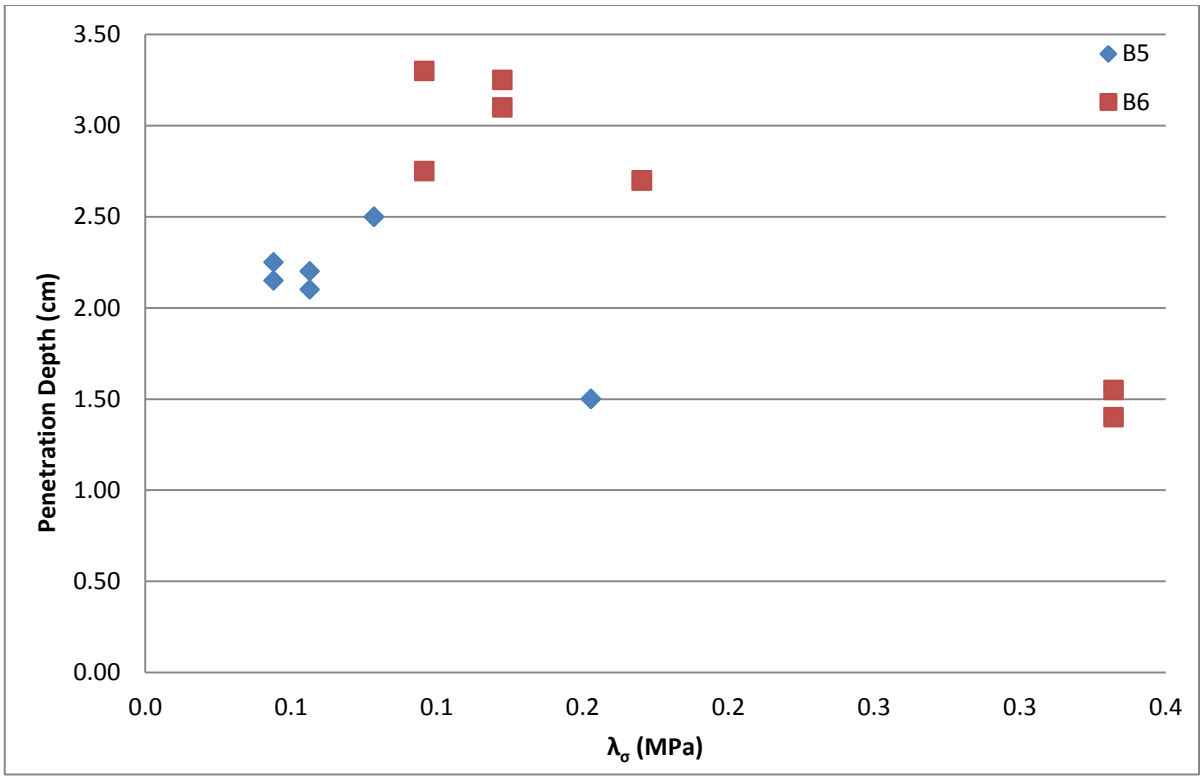

Figure 5.27: Average penetration depths versus compressive stress for beams 5 & 6 (w/c = 0.40)

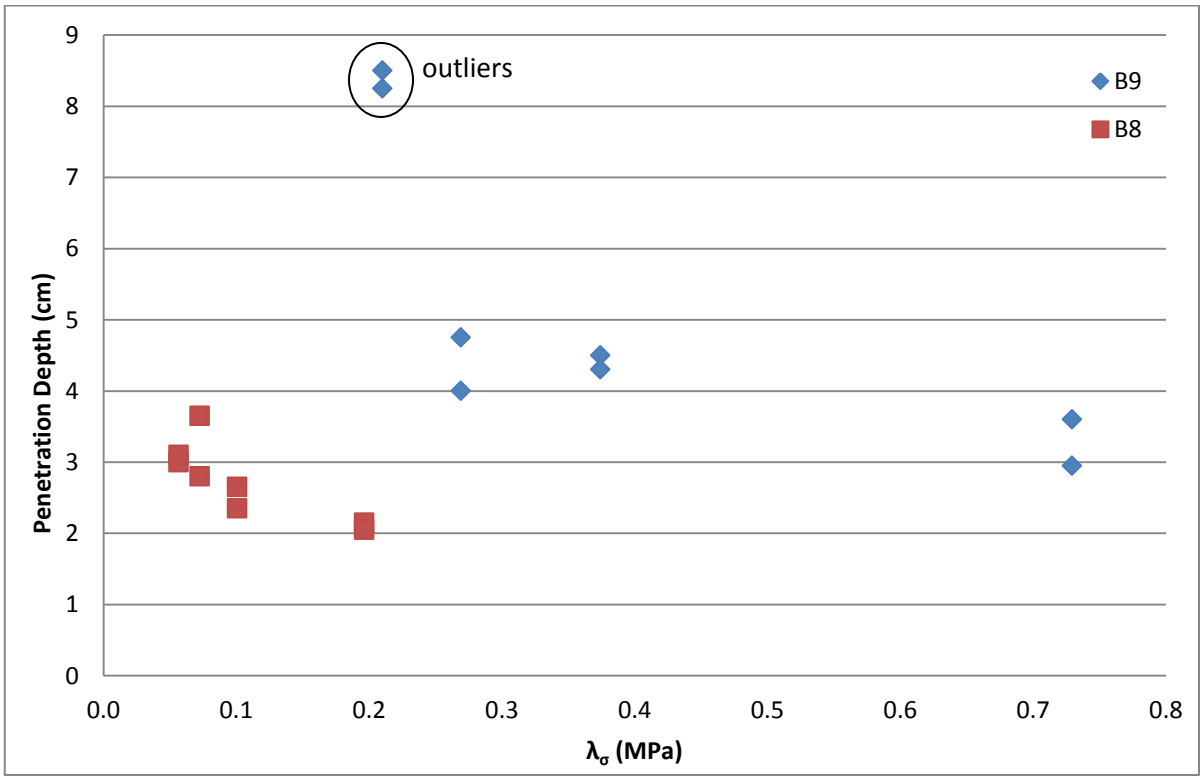

Figure 5.28: Average penetration depths versus compressive stress for beams 8 & 9 (w/c = 0.50)

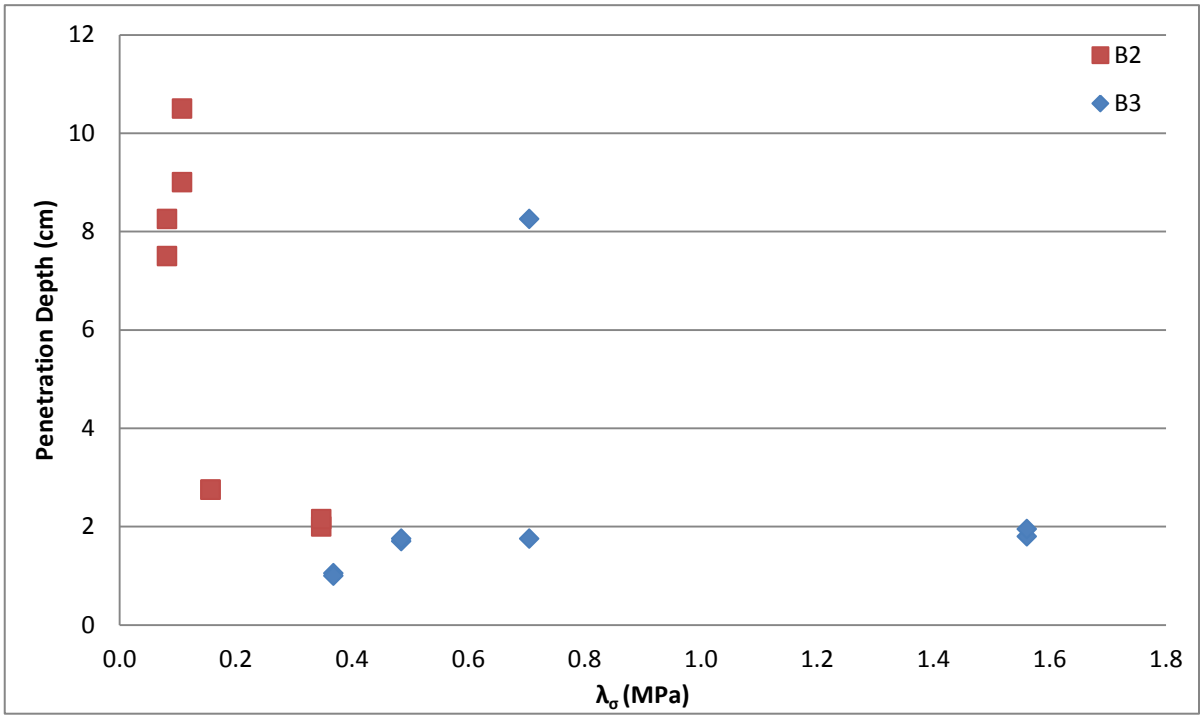

Figure 5.29: Average penetration depths versus tensile stress for beams 2 & 3 (w/c = 0.35)

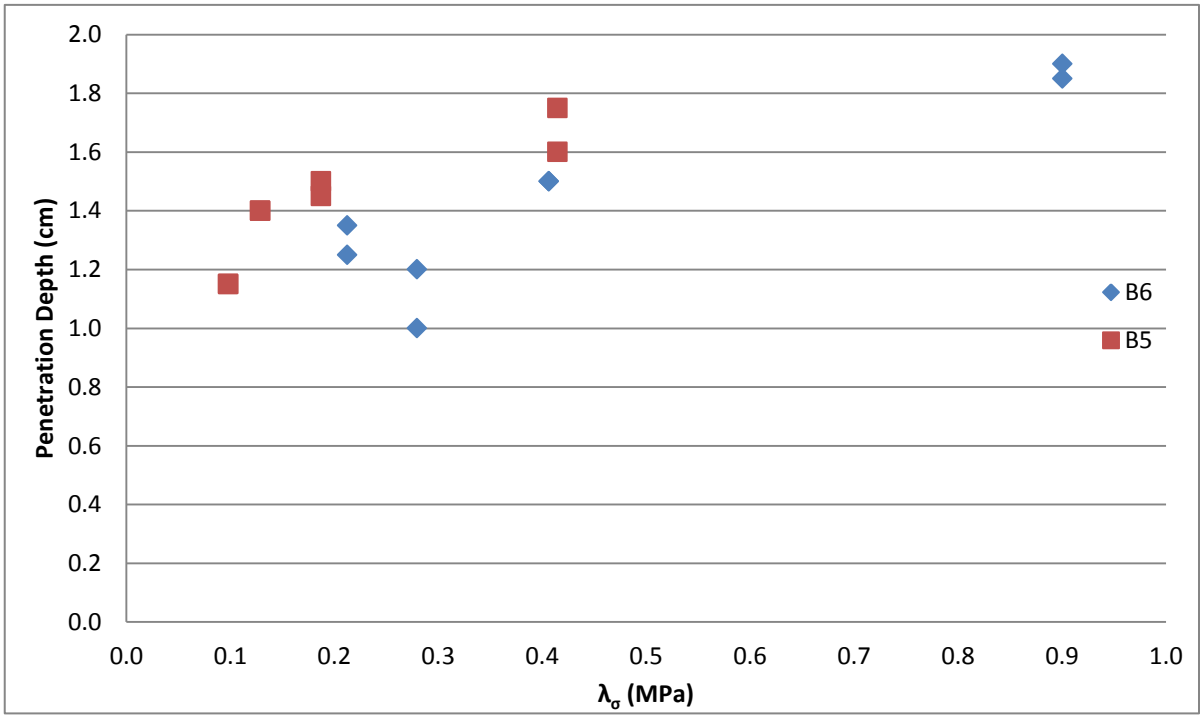

Figure 5.30: Average penetration depths versus tensile stress for beams 5 & 6 (w/c = 0.40)

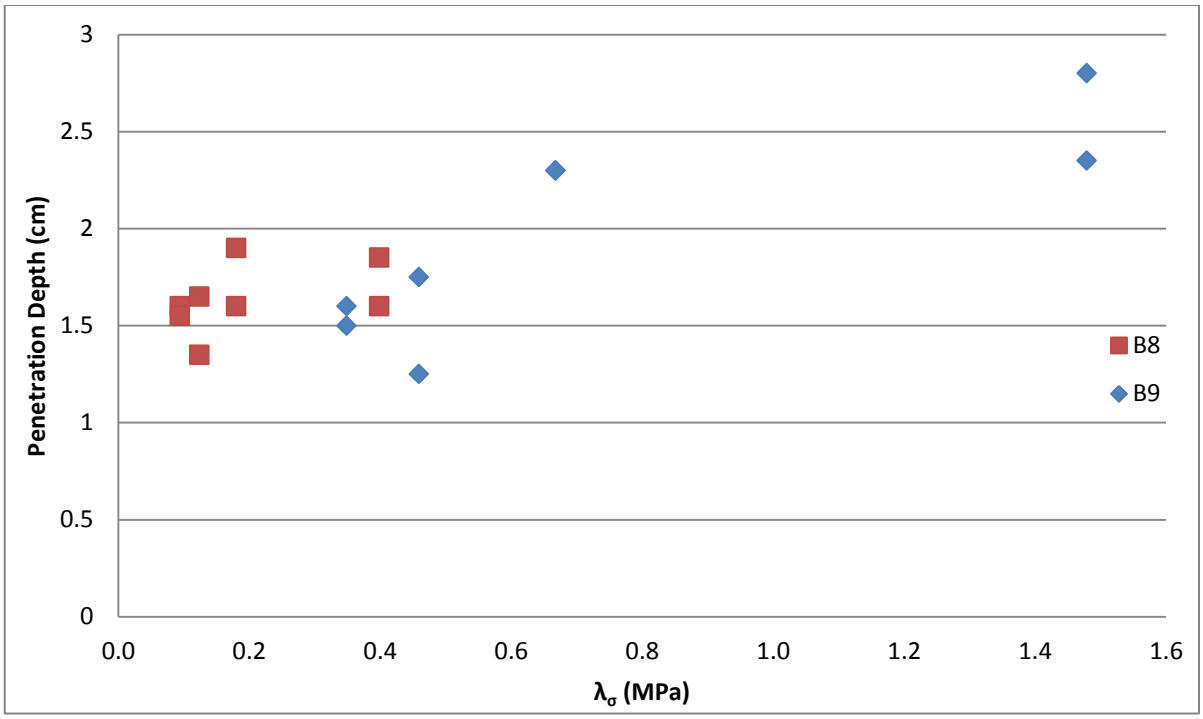

Figure 5.31: Average penetration depths versus tensile stress for beams 8 & 9 (w/c = 0.50)

Similar to Figures 5.17 and 5.18, the ratio of diffusivity of a stressed section to that unstressed (obtained from chloride concentration profiles) is plotted against the stress index ratio λ_σ in Figures 5.32 and 5.33 as a function of normalized compressive and tensile stress, respectively. Accuracy and numerical deviation between both methods has already been discussed; however, similar conclusions can be drawn about the effect of compressive and tensile stress on relative diffusivity as were drawn in the previous figures in this section regarding average penetration depths. Only values corresponding to uncracked concrete are shown in Figures 5.32 and 5.33. As it can be observed, stress does indeed have an effect on the relative diffusivities of uncracked concrete. Generally, relative diffusivities obtained from titration are lower than those obtained from spraying silver nitrate. Under compressive stress, an increase in stress causes an increase in relative diffusivity for a w/c of 0.35, while compressive stresses tend to reduce the relative diffusivity for higher w/c (0.40 and 0.5), likely by closing its pores. Under tensile stress, an increase in stress causes an increase in relative diffusivity for higher w/c (0.5); the effect of tensile stresses on the other two w/c (0.35 and 0.4) is only marginal for uncracked concrete.

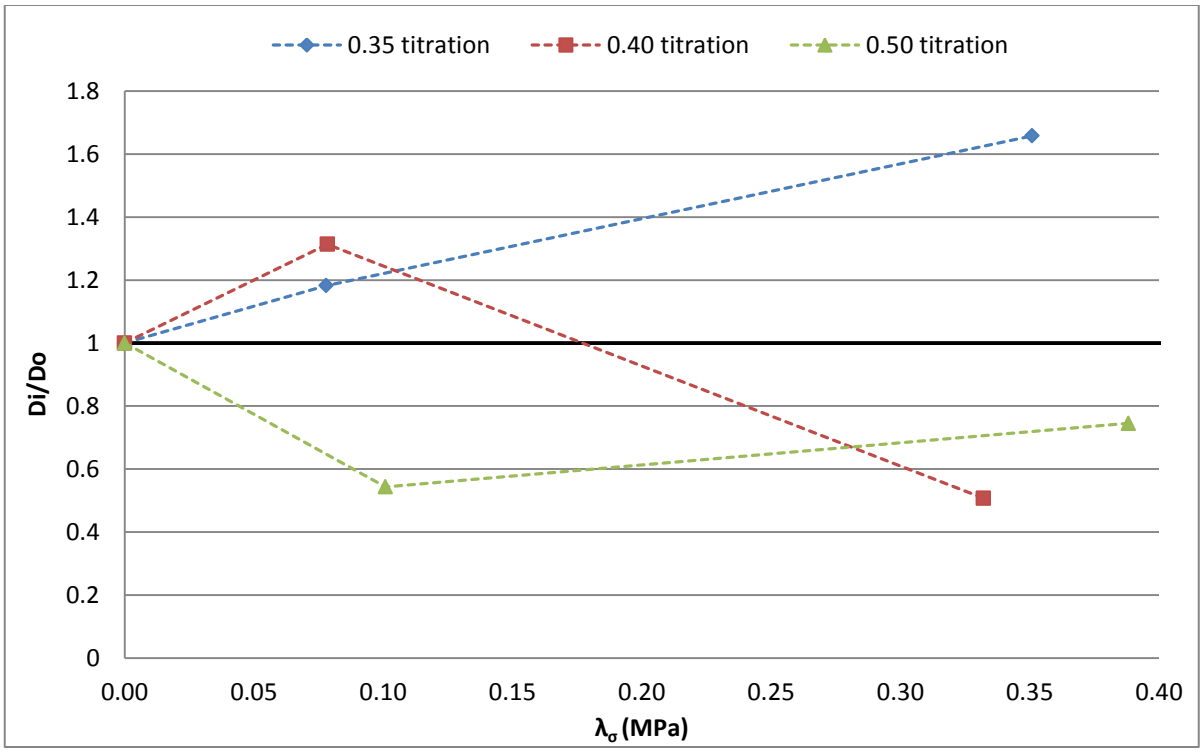

Figure 5.32: Comparison of relative diffusivities from chloride profiles versus normalized compressive stress

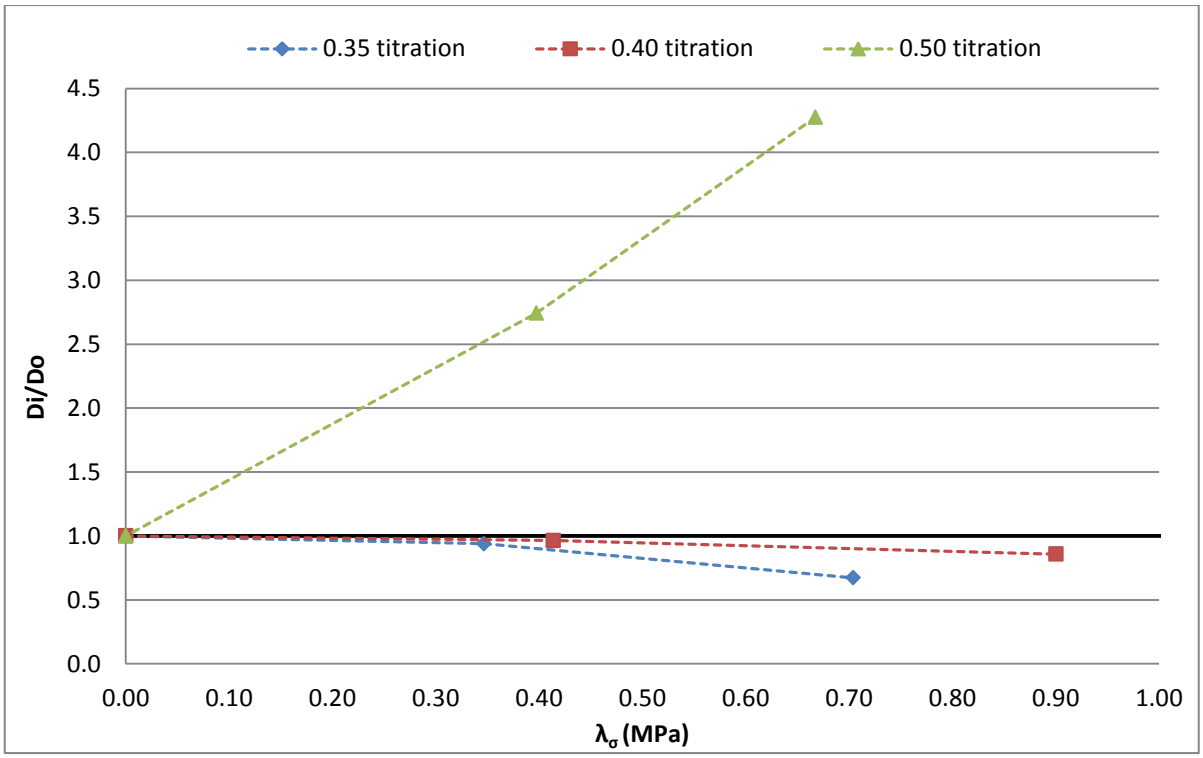

Figure 5.33: Comparison of relative diffusivities from chloride profiles versus normalized tensile stress

5.4 Chloride Diffusivity as a Function of w/c

There is no doubt that the diffusivity of chlorides into concrete depends on the composition and mix proportions of said concrete; the water-to-cement ratio being the deciding factor affecting the capillary porosity of a concrete. Each beam was constructed with the same amount of hydrating cement, allowing the w/c ratio to be governed directly by the amount of mixing water added. The chloride diffusivity data obtained by non-linear regression curve fitting, as seen in Tables 5.1 and 5.2, are analyzed as a function of the three w/c ratios used in this study.

With some exceptions, Figures 5.34 and 5.35 illustrate that an increasing w/c ratio does indeed cause an increase in D_{app} values as expected; with the effect of GGBS being more apparent in reducing diffusivity for the bottom face of control beams (compression), where diffusion was influenced by a larger chloride concentration gradient. Major exceptions in the lower compressive stress values and top face of control beams seem puzzling and unexpected; the D_{app} value for both cases dramatically drops for a w/c of 0.50.

The effect of stress on D_{app} values obtained with Crank's error function solution can also been seen in Figures 5.34 and 5.35. An increase in compressive stress causes an increase in D_{app} values for a w/c of 0.35, while the effect of compressive stress on w/c ratio 0.40 and 0.50 do not seem to have a clear trend. Also, an increase in tensile stress for a w/c ratio 0.35 and 0.40 causes a minor decrease in D_{app} values, while a major increase can be seen for a w/c ratio of 0.50.

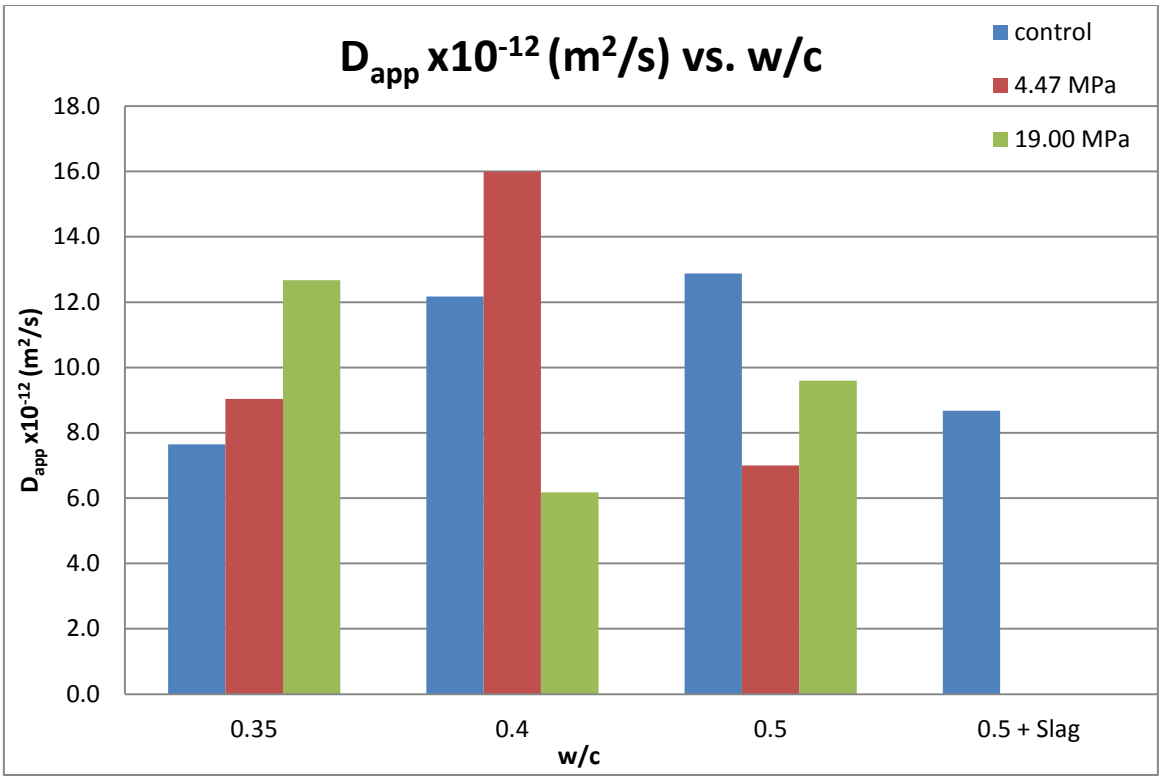

Figure 5.34: Diffusion coefficient versus w/c ratio for concrete under compression

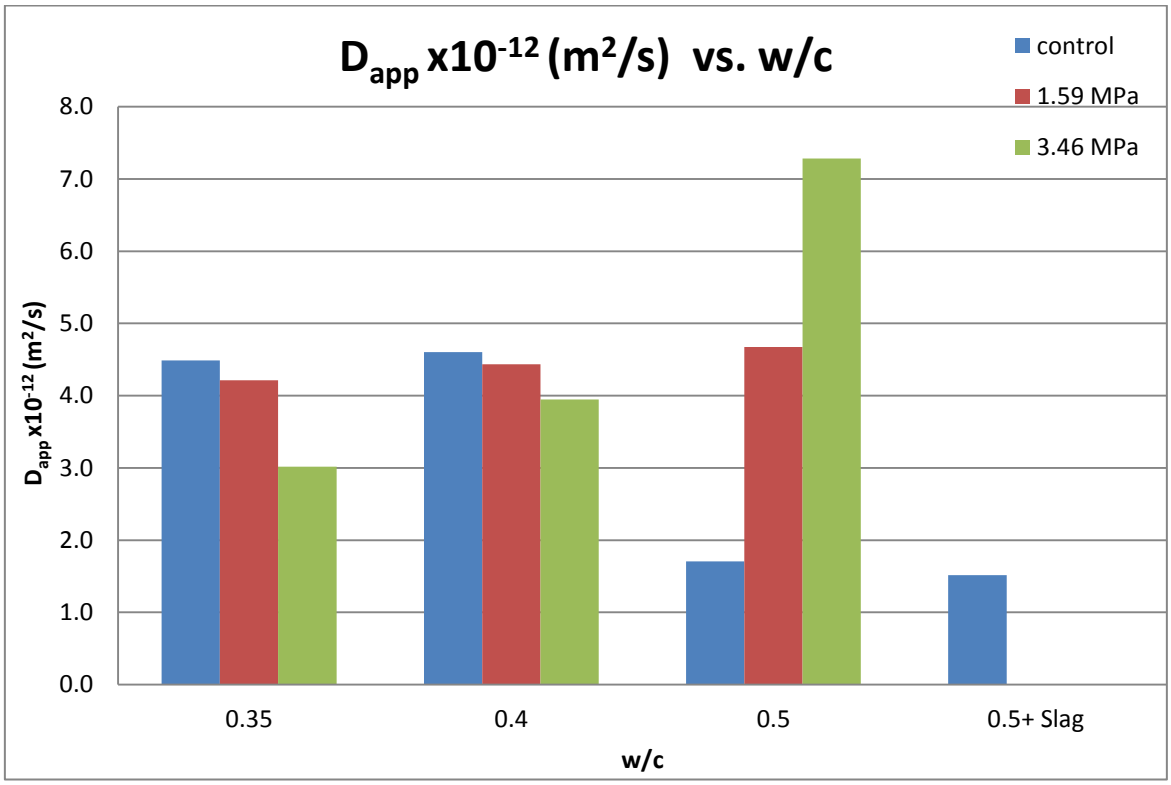

Figure 5.35: Diffusion coefficient versus w/c ratio for concrete under tension

Chapter 6 – Concluding Remarks

6.1 Summary and Conclusions

The effects of sustained compressive and tensile stresses on the ingress of chlorides into concrete were investigated in this study. Six post-tensioned and four non-reinforced control concrete beams were submerged in a 4-5% NaCl de-icing salt solution for 12 weeks, allowing chloride transfer to be completely governed by continuous diffusion. Water-to-cement ratios of 0.35, 0.40, and 0.50 were used; three concrete beams of each ratio were constructed along with a single beam of w/c of 0.50 with the addition of GGBS to study the effects of supplementary cementing material on chloride ingress. Lastly, out of the three beams with similar w/c ratios, one was used as an unloaded control sample, while the other two beams were post-tensioned, inducing variable sustained compressive and tensile stresses along the beam. The applied post-tensioning loads range from 16-73% of the compressive strength of concrete.

After 12 weeks of exposure, each beam was fractured at specific cross sections and analyzed for chloride content by spraying silver nitrate (colourimetric method) to determine average penetration depths, and by conducting potentiometric titrations on extracted concrete powder to determine chloride concentrations. The pre-selected concentration profiles based on upper and lower compressive and tensile stress levels were then fitted to Crank's error function solution to determine the D_{app} and C_S values for each profile. The effects of sustained stress on chloride penetration depth, chloride concentration by % weight of concrete, and apparent diffusion coefficients were evaluated and compared to results of unloaded control specimens.

From the analysis of the colourimetric and potentiometric titration results, the following conclusions can be made:

1. For the majority of sections, chloride penetration depths obtained from spraying silver nitrate were reasonable and expected. The high likelihood of compressive and tensile microcracks in concrete sustaining high levels of stress can explain the large depths obtained. Generally, an increase in compressive stress causes a slight decrease in average penetration depths for the beams with higher w/c, while an increase in tensile stress causes an increase in average penetration depths for all beams. Due to the exposure tank solution

having higher chloride concentrations at the bottom of the tank, where the compressive face was situated for all beams, penetration depths for beams under compression were always higher than beams under tension; this error must be avoided in the future.

2. Chloride penetration depths, concentration, and apparent diffusion coefficients cannot be accurately determined in poorly mixed inconsistent concrete, as seen in the skewed results of beam 2 (w/c = 0.35, 34 kN).
3. According to the results, the effect of compressive stress on chloride ingress and concentration is different for each w/c. Generally, for a w/c of 0.35 and 0.40, an increase of compressive stress does not seem to affect chloride concentration results; however, for a w/c of 0.50 an increase in compressive stress usually causes a decrease in chloride concentrations. While chloride concentration profiles for a w/c of 0.35 and 0.40 do not seem to have a clear dependency on the applied tensile stress, the concentration profiles for a w/c of 0.5 increase with the increase in tensile stress; this effect is more pronounced at larger depths.
4. Crank's error function solution to Fick's second law correlates well to the experimentally obtained chloride profiles, giving high R^2 values for all profiles.
5. The effect of different concrete water-to-cement ratios on chloride ingress and concentration is apparent in this study for unloaded specimens; as expected, a lower w/c generally gave lower chloride concentrations and penetration depths. Likewise, although with some exceptions, an increasing w/c ratio does indeed cause an increase in D_{app} values.
6. The effect of stress on D_{app} values obtained with Crank's error function solution gave different results for each w/c ratio. An increase in compressive stress causes an increase in D_{app} values for a w/c of 0.35, while the effect of compressive stress on the beams with a w/c ratio of 0.40 and 0.50 is to reduce the diffusivity, likely due to closing of concrete pores. Also, an increase in tensile stress for a w/c ratio 0.35 and 0.40 has a marginal effect on D_{app} values, while a major increase of approximately 400% can be seen for a w/c ratio of 0.50 as the tensile stress is raised.
7. There are good agreements between the colourimetric and titration methods with respect to comparing relative diffusivities; the magnitude of deviation is the lowest in concrete with a w/c of 0.40, and relative diffusivity ratios for concrete in compression show less deviation than ratios for concrete under tension. The results from both methods were plotted against each other, and it was found that generally, the ratios obtained for concrete under

compression give more accurate comparisons, converging to the 45-degree line better than the ratios for concrete under tension. In general, relative diffusivity ratios obtained from the colourimetric method are larger than those obtained from titration for concrete under compression and tension. Knowing this, the simple and quick method of spraying silver nitrate on in-situ samples can effectively replace the need for time consuming potentiometric titrations to determine the D_{app} of a concrete for a particular period of time; D_{app} for concrete in field can be calculated with Eq. (5.2).

8. The relative diffusivities obtained from the colourimetric and titration method were plotted against stress. Generally, relative diffusivities obtained from titration are lower than those obtained from spraying silver nitrate. Under compressive stress, an increase in stress causes an increase in relative diffusivity for a w/c of 0.35, while a decrease for a w/c of 0.40 and 0.50, likely due to the reduction of porosity because of compression. Under tensile stress, an increase in stress causes an increase in relative diffusivity for the highest w/c, while it shows a minimal effect on the beams with a w/c of 0.35 and 0.40.
9. The effect of GGBS is very apparent and can be seen in average penetration depths, chloride concentrations, and D_{app} results; when compared to its similar control counterpart, the addition of GGBS acts to reduce average chloride penetration depths, chloride concentrations, and apparent diffusion coefficients for the top and bottom faces.
10. The results obtained can be considered a source of knowledge in the field of chloride ingress into submerged concrete sustaining compressive and tensile stresses. The effect of sustained compressive and tensile stresses on chloride ingress and apparent diffusion coefficients should not be overlooked; the aforementioned trends and conclusions made above prove this.

6.2 Recommendations for Future Work

The work completed in this study successfully applied and took into consideration past experiences and suggestions from similar experiments done by Dr. Bruno Cousin of the Université Montpellier, France. However, according to the experience and results obtained from the current study, new suggestions and recommendations to improve the results of future work are described below:

Materials:

- In order to accurately compare results for each beam, it is important that all concrete undergoes quality control to meet the material quality and durability standards set by CSA A23.1-04; effort to try and minimize any apparent inconsistences in concrete should be taken.
- It is recommended that ready-mix concrete be used for future work in light of the aforementioned comment.
- It would be interesting to study chloride ingress into cracked concrete while steel reinforcement is corroding, much like deteriorated structures behave in field conditions; monitoring the increase of strains in reinforcement and stresses in concrete and noting their effects.

Post-Tensioning (Loading):

- To ensure the most accurate post-tensioning load readings, the application of strain gauges on concrete and post-tensioning strands (if possible) would help to monitor experimental stresses in the concrete and strains in the steel tendon during and after post-tensioning.
- Also, it is important to monitor strains in the steel tendon to determine if tendon relaxation has occurred; re-adjustment of post-tensioning loads would need to be done to maintain compressive and tensile stress levels.
- It is preferable if material testing of concrete be done the on the day of post-tensioning to take into account concrete strength increasing as it ages.
- It is preferable that the lower and higher bound post-tensioning loads for each w/c ratio be similar to each other to reduce variability and uncertainty in comparing the results; higher bound post-tensioning loads for this experiment were different for each w/c ratio. Care must be taken to try and achieve similar stress index values for comparison.

- It would be interesting to study the combined effects of shear, torsion, tension, and compression on the chloride ingress of chlorides into concrete.

Chloride Exposure Conditions:

- To accurately compare the effects of compressive and tensile stresses on chloride ingress, it is important that the concentration of the chloride (de-icing salt) solution in the exposure tank be as consistent as possible in all areas of the tank. The possibility of using a more uniform salt fog solution can avoid this error.
- It is recommended that before submerging the concrete beams into the de-icing salt solution that the solution be consistent and mixed thoroughly; an initial concentration should be taken experimentally followed by monitoring, to ensure that chloride concentrations in the tank are constant during chloride ingress.
- It would be interesting to study the combined effects of permeation and diffusion on chloride ingress when concrete is fully submerged; permeation being a minor secondary transport mechanism to diffusion.
- It is preferable for the exposure time to be longer than 12 weeks, as 12 weeks is not enough time to develop meaningful trends on the effect of stress on chloride ingress.

Data Collection:

- It is important to take at least three concrete powder samples sustaining the same amount of stress for each profile to reduce the variability and increase the accuracy of the results.
- It would be interesting to experimentally determine the amount of compressive and tensile microcracking that occurred instead of estimating based on applied load and chloride penetration data. Non-destructive methods such as mercury intrusion porosimetry (pore structure analysis) or surface electrical resistivity could be used.

Miscellaneous:

- Analysis of diffusivity into concrete was done after 12 weeks of exposure to chlorides; it would be interesting to see the effects of exposure time on diffusivity using the same experimental grid, but testing more specimens at different time intervals.

- Since there are variable compressive and tensile stresses along the length of each beam, post-tensioning loads could be identical for both beams of each w/c ratio; this allows for the effect of time, stress, and w/c ratio on chloride ingress to be studied.
- Instead of estimating the occurrence of microcracking based on applied loads, compressive and tensile microcracking could have been quickly analyzed with an optical microscope and the equations developed by Loo (1992). This would help to further explain trends with more accuracy.

References

Andrade, C., Castellote, M., Alonso, C., & Gonzalez, C. (1999). "Relation Between Colourimetric Chloride Penetration Depth and Charge Passed in Migration Tests of the Type of Standard ASTM C1202-91". *Cement and Concrete Research, 29*(3), 417-421.

Angst, U., Vennesland, O., Elsener, B., & Larsen, C. K. (2009). "Critical Chloride Content in Reinforced Concrete - A Review". *Cement and Concrete Research, 39*(12), 1122-1138.

ASTM C 114-11b. (2007). *"Standard Test Methods for Chemical Analysis of Hydraulic Cement".* West Conshohocken, PA: ASTM International.

ASTM C 1152/C 1152M-04. (2004). *"Standard Test Methods for Acid-Soluble Chloride in Mortar and Concrete".* West Conshohocken, PA: ASTM International.

ASTM C469/C469M-10. (2010). "Standard Test Method for Static Modulus of Elasticity and Poisson's Ratio of Concrete in Compression". West Conshohocken, PA: ASTM International.

Bentur, A., Diamond, S., & Berke, N. (1998). *Steel Corrosion in Concrete: Fundamentals and Civil Engineering Practice.* London, UK: E & FN Spon.

Bentz, E., & Thomas, M. (2001). Life-365: Service Life Prediction Model™ and Computer Program for Predicting the Service Life and Life-Cycle Costs of RC Exposed to Chlorides. Cleveland: American Concrete Institute.

Bioubakhsh, S. (2011). *"The Penetration of Chloride in Concrete Subject to Wetting and Drying: Measurement and Modelling".* Ph.D Thesis, University College London, London, England.

Broomfield, J. P. (2007). *Corrosion of Steel in Concrete: Understanding, Investigation, and Repair, 2nd ed.* New York: Taylor & Francis.

Buckley, L. J., Carter, M. A., Wilson, M. A., & Scantlebury, J. D. (2007). "Methods of Obtaining Pore Solution from Cement Pastes and Mortars for Chloride Analysis". *Cement and Concrete Research, 37*(11), 1544-1550.

Cement Association of Canada. (2002). *Design and Control of Concrete Mixtures 7th Edition.* Ottawa: First Printing.

Claisse, P. A., Ganjian, E., & Adham, T. A. (2003). "In Situ Measurement of the Intrinsic Permeability of Conrete". *Magazine of Concrete Research, 55*(2), 125-132.

Climent, M., de Vera, G., Viqueira, E., & Lopez-Atalaya, M. (2004). "Generalization of the Possibility of Eliminating the Filtration Step in the Determination of Acid-Soluble Chloride Content in Cement and Concrete by Potentiometric Titration". *Cement and Concrete Research, 34*(12), 2291-2295.

Cousin, B., & Martin-Perez, B. (2010). "Chloride Ingress in Pre-Tensioned Prestressed Concrete Beams and the Effect of Corrosion on Their Structural Behaviour". *Sixth International Conference on Concrete under Service Conditions, Environment & Loading (CONSEC'10), Castro-Borges, Moreno, Sakai, Gjorv, and Banthia, eds.* (pp. 247-256). London, Mérida, Yucatan, México: CRC Press/Balkema Taylor & Francis Group.

CSA A23.1-04/A23.2-04. (2005). *"Concrete Materials and Methods of Concrete Construction/Methods of Test and Standard Practices for Concrete".* Mississauga, ON, Canada: Canadian Standards Association.

CSA A23.3-04. (2004). *"Design of Concrete Structures".* Mississauga, ON, Canada: Canadian Standards Association.

Deif, A. (2010). *"Chloride Ingress into Reinforced Concrete Sustaining In-Service Loads".* Ph.D Thesis, University of Ottawa, Department of Civil Engineering, Ottawa, Canada.

Djerbi, A., Bonnet, S., Khelidj, A., & Baroghel-bouny, V. (2008). "Influence of transversing crack on chloride diffusion into concrete". *Cement and Concrete Research, 38*(6), 877-883.

Environment Canada. (2006, May). *Winter Road Maintenance Activities and the Use of Road Salts in Canada*. Retrieved June 2013, from Environment Canada's World Wide Web Site: https://www.ec.gc.ca/nopp/roadsalt/reports/en/winter.cfm

Francois, R., & Arliguie, G. (1999). "Effect of Microcracking and Cracking on the Development of Corrosion in Reinforced Concrete Members". *Magazine of Concrete Research, 51*(2), 143-150.

Gowripalan, N., Sirivivatnanon, V., & Lim, C. (2000). "Chloride Diffusivity of Concrete Cracked in Flexure". *Cement and Concrete Research, 30*(5), 725-730.

Guoping, L., Fangjian, H., & Yongxian, W. (2011). "Chloride Ion Penetration in Stressed Concrete". *Journal of Materials in Civil Engineering, 23*(8), 1145-1153.

Hach Company. (2013). *Chloride QuanTab® Test Strips, 300-6000 mg/L*. Retrieved August 2013, from http://www.hach.com/chloride-quantab-test-strips-300-6000-mg-l/product?id=7640211608#

Hoseini, M., Bindiganavile, V., & Banthia, N. (2009). "The effect of mechanical stress on permeability of concrete". *Cement and Concrete Research, 31*(4), 213-220.

Jacobsen, S., Marchand, J., & Boisvert, L. (1996). "Effect of Cracking and Healing on Chloride Transport in OPC Concrete". *Cement and Concrete Research, 26*(6), 869-881.

Jin, W. L., Yan, Y. D., & Wang, H. L. (2010). "Chloride Diffusion in the Cracked Concrete". *Proceedings of FraMCoS-7-05*, (pp. 880-886). Jeju, South Korea.

Kermani, A. (1991). "Permeability of Stressed Concrete". *Building Research & Information, 19*(6), 360-366.

Kim, A. T., & Stewart, M. G. (2000). "Structural Reliability of Concrete Bridges Including Improved Chloride-Induced Corrosion Models". *Structural Safety, 22*(4), 313-333.

Kuter, A., Geiker, M., Olesen, J., & Al, e. (2005). "Chloride ingress in concrete cracks under cyclic loading". *Proceedings of ConMat'05.* Vancouver, BC, Canada: August 22-24.

Lim, C., Gowripalan, N., & Sirivivatnanon, V. (2000). "Microcracking and Chloride Permeability of Concrete Under Uniaxial Compression". *Cement and Concrete Composites, 22*(5), 353-360.

Loo, Y. (1992). "A New Method for Microcrack Evaluation in Concrete Under Compression". *Materials and Structures, 25*(10), 573-578.

Manual of 794 Basic Titrino. (2002). *Instruction for use - 8.794.1003.* Metrohm Ltd.

Martin-Perez, B., Deif, A., & Cousin, B. (2009). "Experimental Study of Chloride Penetration in an RC Slab Sustaining In-Service Loads". (T. Tanabe, K. Sakata, H. Mihashi, R. Sato, K. Maekawa, & H. Nakamura, Eds.) *Creep, Shrinkage and Durability Mechanics of Concrete and Concrete Structures*, 1107-1113.

Mehta, P., & Monteiro, P. (2006). "Microstructure and Properties of Hardened Concrete". *Concrete: Microstructure, Properties and Materials*, 41-80.

Nagi, M., & Kilgour, R. (2008). Service Life Prediction of Concrete Structures. *CANMET/ACI.* Dubai: GHD Global Pty Ltd.

Otieno, M., Alexander, M., & Beushausen, H. (2010). *Corrosion of Steel in Concrete (Initiation, propagation & factors affecting).* University of Cape Town, Department of Civil Engineering. Cape Town: Concrete Materials and Structural Integrity Research Group (CSIRG).

Pezzullo, J. C. (2013). *Nonlinear Least Squares Regression (Curve Fitter)*. Retrieved July 2013, from Interactive Statistics: http://statpages.org/nonlin.html

Poulsen, E., & Mejlbro, L. (2006). *Diffusion of Chloride in Concrete - Theory and Applications* (1st ed.). Taylor & Francis.

Poursaee, A., & Hansson, C. M. (2008). "The influence of longitudinal cracks on the corrosion protection afforded reinforcing steel in high performance concrete". *Cement and Concrete Research, 38*(8-9), 1098-1105.

Richardson, M. G. (2002). *Fundamentals of Durable Concrete, Modern Concrete Technology.* London: Spon Press.

Saito, M., & Ishimori, H. (1995). "Chloride Permeability of Concrete Under Static and Repeated Compressive Loading". *Cement and Concrete Research, 25*(4), 803-808.

Samaha, H., & Hover, K. (1992). "Influence of Microcracking on the Mass Transport Properties of Concrete". *ACI Materials Journal, 89*(4), 416-424.

Schweitzer, P. A. (2009). *Fundamentals of Corrosion: Mechanisms, Causes, and Preventative Methods.* Boca Raton: CRC Press.

Tullmin, M. (2002). *Rebar Corrosion*. Retrieved June 2013, from Corrosion-Club: http://www.corrosion-club.com/concretecorrosion.htm

Tutti, K. (1982). "Corrosion of Steel in Concrete". *Swedish Cement and Concrete Research Institute, 82*(4).

Wang, H., Lu, C., Jin, W., & Bai, Y. (2011). "Effect of External Loads on Chloride Transport in Concrete". *Journal of Materials in Civil Engineering, 23*(7), 1043-1049.

Appendix A - Concrete Mix Design

Aggregate Properties

Coarse Aggregate (C.A.)

Pan = 19.0 g

Normal free aggregate = 2124.5 – 19.0 = 2105.5 g

Oven-dry aggregate = 2088.0 – 19.0 = 2069.0 g

Start time: October 15, 2012 @ 3:12pm

End time: October 16, 2012 @ 1:45pm

$$*Moisture\ Content\ (MC) = \frac{2105.5-2069.0}{2069.0} \times 100\% = \mathbf{1.76}\% \qquad (A.1)$$

SSD aggregate = 2093.0 – 19.0 = 2074.0 g

Start time = October 16, 2012 @ 2:20pm

End time: October 17, 2012 @ 2:10pm

Weight of water + container = 2894.0 g

Wet aggregate in air = 2164.0 g

Submerged aggregate = 4964.5 – 2894.0 = 2070.5 g

$$*Absorption\ Content\ (AC) = \frac{B-A}{A} \times 100\% = \frac{2074.0-2069.0}{2069.0} \times 100\% = \mathbf{0.24}\% \qquad (A.2)$$

$$Bulk\ relative\ density = \frac{B}{B-C} = \frac{2069.0}{2069.0-2070.5} = \mathbf{1379}\boldsymbol{kg/m^3} \qquad (A.3)$$

$$Apparent\ relative\ density = \frac{A}{A-C} = \frac{2074.0}{2074.0-2070.5} = \mathbf{593}\boldsymbol{kg/m^3} \qquad (A.4)$$

where:

A = mass of oven-dry aggregate in air (g)
B = mass of SSD aggregate in air (g)
C = mass of submerged aggregate (g)

* It was decided that C.A. would be washed and dried (24 hr) to SSD, giving a MC = AC = 0%

Fine Aggregate (F.A.)

Pan = 19.0 g

Normal free aggregate = 650.0 – 19.0 = 631.0 g

Oven-dry agg = 646.0 – 19.0 = 627.0 g

Start time: October 15, 2012 @ 3:20pm

End time: October 16, 2012 @ 1:45pm

$$MC = \frac{631.0 - 627.0}{627.0} \times 100\% = \mathbf{0.64}\% \qquad (A.5)$$

SSD aggregate = 656.0 – 19.0 = 634.0 g

Start time = October 16, 2012 @ 2:20pm

End time: October 17, 2012 @ 2:10pm

$$AC = \frac{Mf - A}{A} \times 100\% = \frac{634.0 - 627.0}{627.0} \times 100\% = \mathbf{1.12}\% \qquad (A.6)$$

where:

A= mass of oven-dry aggregate in air (g)
Mf = mass of SSD aggregate in air (g)

Table A.1: Fine aggregate gradation results

Sieve Size (mm)	Weight Retained (g)	% Retained	Cumulative % Retained
4.75 (Sieve 4)	0.0	0.00	0.00
2.36 (Sieve 8)	1.0	0.20	0.20
1.18 (Sieve 16)	3.0	0.60	0.80
0.60 (Sieve 30)	29.0	5.79	6.59
0.30 (Sieve 50)	215.0	42.96	49.55
0.15 (Sieve 100)	213.5	42.66	92.21
Pan	39.0	**Total**	149.35
Total	500.5	**FM**	**1.49**

Concrete Mix Design (w/c = 0.35)

Non air-entrained normal exposure class concrete

Cement: Holcim Type 10 (GU) with relative density of 3.15

Blast Furnace Slag: Relative density of 2.9, usage of 15% of cementing materials (used in Batch 4 only)

Coarse Aggregate (C.A.): Well-graded, 20 mm nominal maximum-size rounded gravel (CSA A23.1) with an ovendry relative density of 2.68, absorption and moisture content of 0% (washed and dried to SSD), and ovendry rodded bulk density of 1600 kg/m^3.

Fine Aggregate (F.A.): Natural sand (CSA A23.1) with an ovendry relative density of 2.66 and absorption of 1.12%. The laboratory sample moisture content is 0.64%. Since the sand in the laboratory is too fine, select a fineness modulus (FM) of 2.4.

Plasticizer: dosage of 4-10 g per kg of cementing materials; similar density as water.

Cement= **400 kg/m^3** (preselected value for each preselected w/c ratio)

Water = 400*(0.35) = 140 kg/m^3

(Plasticizer water demand reduction of 5%) → water **=** 133 kg/m^3

Plasticizer = (10 g/kg)*(400) = **4 kg/m^3**

C.A. = (1600 kg/m^3)*0.66 = **1056 kg/m^3** (SSD, no adjustment needed)

$$F.A. = 1 - \left\lfloor \frac{133}{1(998)} + \frac{400}{3.15(998)} + \frac{1056}{2.68(998)} \right\rfloor = 0.3387\ m^3$$

$$F.A. = 0.3387 m^3 \times \frac{998 kg}{m^3} \times 2.66 = 899 kg/m^3$$

$F.A. = 899 kg/m^3 \times (1.0064) = \mathbf{905 kg/m^3}$ (Moisture content adjustment)

Corrected water demand (absorption) = 133 - 0 – 889*(0.0064-0.011) – 4 = **133 kg/m^3**

Total density (with absorption) = 400 + 133 + 4 + 1056 + 905 = **2498 kg/m^3**

Table A.2: Summary of actual concrete mix proportions for 0.05 m^3 batches

	Batch 1a	Batch 1b	Batch 2a	Batch 2b	Batch 3a	Batch 3b	Batch 4
Water (kg)	6.50	6.45	7.68	7.66	9.66	**9.40	9.52
Cement (kg)	20.2	20.0	20.0	20.0	20.0	20.1	17.0
C.A. (kg)	52.8	52.8	52.8	52.8	52.8	52.8	52.8
F.A. (kg)	48.0	48.0	42.6	42.6	37.8	37.9	37.2
Blast furnace Slag (kg)	-	-	-	-	-	-	3.0
*Plasticizer (L)	0.6	0.6	0.3	0.3	0.2	-	-
w/c	0.35	0.35	0.40	0.40	0.50	0.50	0.50

* More plasticizer was needed than calculated to allow for a workable concrete for all w/c except for 0.5

** Aggregates were still a bit wet from washing, water reduced by visual estimation

Casting Notes

Batch 1a) & b)

- Extra water and plasticizer was needed to improve the low workability from original w/c = 0.30
- Some F.A. was left over and did not mix properly (more in 1a than 1b)
- Both concrete prisms were from 1a)

Batch 2a) & b)

- No extra water added, actual design proportions were used
- Small shrinkage cracks were found on the top face of beam 4 and 6 before burlap curing
- Concrete prism from 2b)

Batch 3a) & b)

- Plasticizer was not needed in 3a); it became too watery. Plasticizer was not used in 3b)
- Excess water was removed from the surface of beams 7, 8, and 9
- Everything mixed well, good workability
- Concrete prism from 3a)

Batch 4)

- C.A. was still a bit wet from the morning
- Some F.A. was left over, it was a bit watery but very consistent
- Blast furnace slag did not change the colour of the concrete

Appendix B - Raw Material Testing Data

Table B.1: Concrete cylinder compression test data for all batches

	Specimen	Failure Load (kN)	Type of Failure	Notes
7d compression (w/c = 0.35)	1 (Batch 1b)	344.6	Crushing	-
	2 (Batch 1a)	212.2	Shear	Not rodded; rough and uneven top surface
	3 (Batch 1a)	355.5	Shear	-
28d compression (w/c = 0.35)	1 (Batch 1b)	407.8	Brittle shear	Not rodded; inconsistent and sandy
	2 (Batch 1a)	467.4	Sudden brittle shear	Top surface was not perfectly leveled
	3 (Batch 1a)	371.8	Slow crush	Not rodded; very inconsistent and porous
7d compression (w/c = 0.40)	1 (Batch 2b)	401.8	Shear	Some shrinkage cracks
	2 (Batch 2a)	348.0	Crushing	-
	3 (Batch 2a)	354.3	Shear/crushing	-
28d compression (w/c = 0.40)	1 (Batch 2b)	461.5	Explosive shear	Uneven top surface
	2 (Batch 2a)	472.0	Brittle shear	Rough surface
	3 (Batch 2b)	406.2	Shear	Premature failure
7d compression (w/c = 0.50)	1 (Batch 3a)	192.1	Shear/crushing	Uneven top surface
	2 (Batch 3b)	256.8	Brittle shear	-
	3 (Batch 3a)	224.1	Shear	-
28d compression (w/c = 0.50)	1 (Batch 3a)	358.9	Brittle shear	-
	2 (Batch 3b)	337.8	Complete crush	-
	3 (Batch 3a)	267.7	Crushing	-
7d compression (w/c = 0.50)	1 (Batch 4)	255.0	Brittle shear	-
	2 (Batch 4)	288.1	Shear	-
	3 (Batch 4)	257.8	Cone/shear/crush	-
28d compression (w/c = 0.50)	1 (Batch 4)	390.0	Brittle shear	-
	2 (Batch 4)	377.7	Brittle shear	Slightly off centered
	3 (Batch 4)	391.6	Brittle shear	-

Figure B.1: Failure patterns of cylinders from all batches (7d compression)

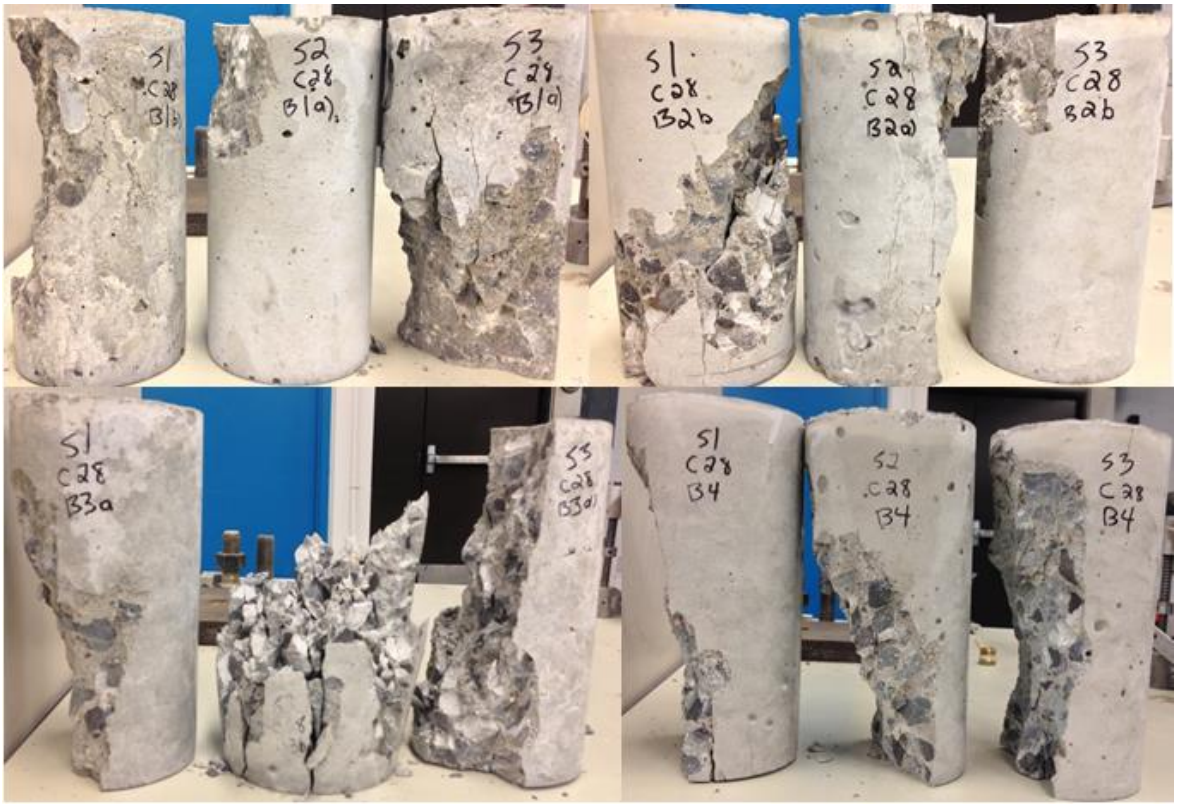

Figure B.2: Failure patterns of cylinders from all batches (28d compression)

Table B.2 uses Eq. (B.1) to calculate the splitting tensile strength of a concrete specimen:

$$T = \frac{2P}{\pi l d} \qquad (B.1)$$

where T is the splitting tensile strength (MPa), P is the maximum applied loaded indicated by the testing machine (N), l is the length of the cylinder (mm), and d is the diameter of the cylinder (mm).

Table B.2: Concrete cylinder tensile splitting test data

	Specimen	Failure Load (kN)	Splitting Tensile Strength (MPa)	Notes
38d splitting (w/c = 0.35)	1 (Batch 1b)	54.8	1.74	Not rodded, very porous and inconsistent
	2 (Batch 1b)	95.6	3.04	-
	3 (Batch 1a)	94.0	2.99	-
33d splitting (w/c = 0.40)	1 (Batch 2a)	78.4	2.50	-
	2 (Batch 2b)	107.0	3.41	-
	3 (Batch 2a)	63.0	2.00	Cylinder not loaded evenly
27d splitting (w/c = 0.50)	1 (Batch 3b)	53.8	1.71	Cylinder not loaded evenly
	2 (Batch 3a)	89.0	2.83	-
	3 (Batch 3b)	104.0	3.31	-

Table B.3 uses Eqs. (B.2) and (B.3) to calculate the modulus of rupture, where Eq. (B.2) is used if the fracture occurs within the middle third of the span length, and Eq. (B.3) is used if the fracture occurs outside of the middle third of the span length by not more than 5% of the span length.

$$R = \frac{Pl}{bd^2} \qquad (B.2)$$

$$R = \frac{3Pa}{bd^2} \qquad (B.3)$$

where R is the modulus of rupture (MPa), P is the maximum applied load indicated by the testing machine (N), l is the span length (mm), b is the average width of the specimen (mm), d is the average depth of the specimen (mm), and *a* is the distance between the fracture and the nearest support (mm).

Table B.3: Concrete prism modulus of rupture test data

	Specimen	Failure Load (kN)	Modulus of Rupture (MPa)	Notes
40d rupture (w/c = 0.35)	Batch 1a	15.5	4.46	Crack was outside middle third of span length, loading was not fully symmetrically
35d rupture (w/c = 0.40)	Batch 2b	12.8	3.84	-
29d rupture (w/c = 0.50)	Batch 3a	12.5	-	Loaded rapidly by accident, discard results and use CSA equation

Table B.4: Values obtained from compressometer (135 mm span length) and loading machine

	Load (kN)	Stress (MPa)	Deformation (mm)	Strain (mm/mm)
Batch 2 w/c = 0.40 28day	0	0.00	0	0.00E+00
	40.20	5.12	0.005	3.70E-05
	81.84	10.42	0.036	2.67E-04
	129.76	16.52	0.067	4.96E-04
	160.92	20.49	0.091	6.74E-04
	199.64	25.42	0.109	8.07E-04
Batch 4 w/c = 0.50 7day	0	0.00	0	0.00E+00
	39.48	5.03	0.015	1.11E-04
	64.72	8.24	0.028	2.07E-04
	85.16	10.84	0.045	3.33E-04
	110.00	14.01	0.063	4.67E-04
	132.68	16.89	0.089	6.59E-04

Table B.5: Load cell calibration readings

Load Cell Readings	Load Machine Readings (kN)
0	0
11.0	5
21.9	10
31.8	15
42.4	20
62.0	30
83.6	40
104.5	50
209.0	100

Appendix C - Chloride Penetration Depths

Figure C.1: Chloride penetration depths for beam 1; section B1-A (w/c = 0.35, 0 kN)

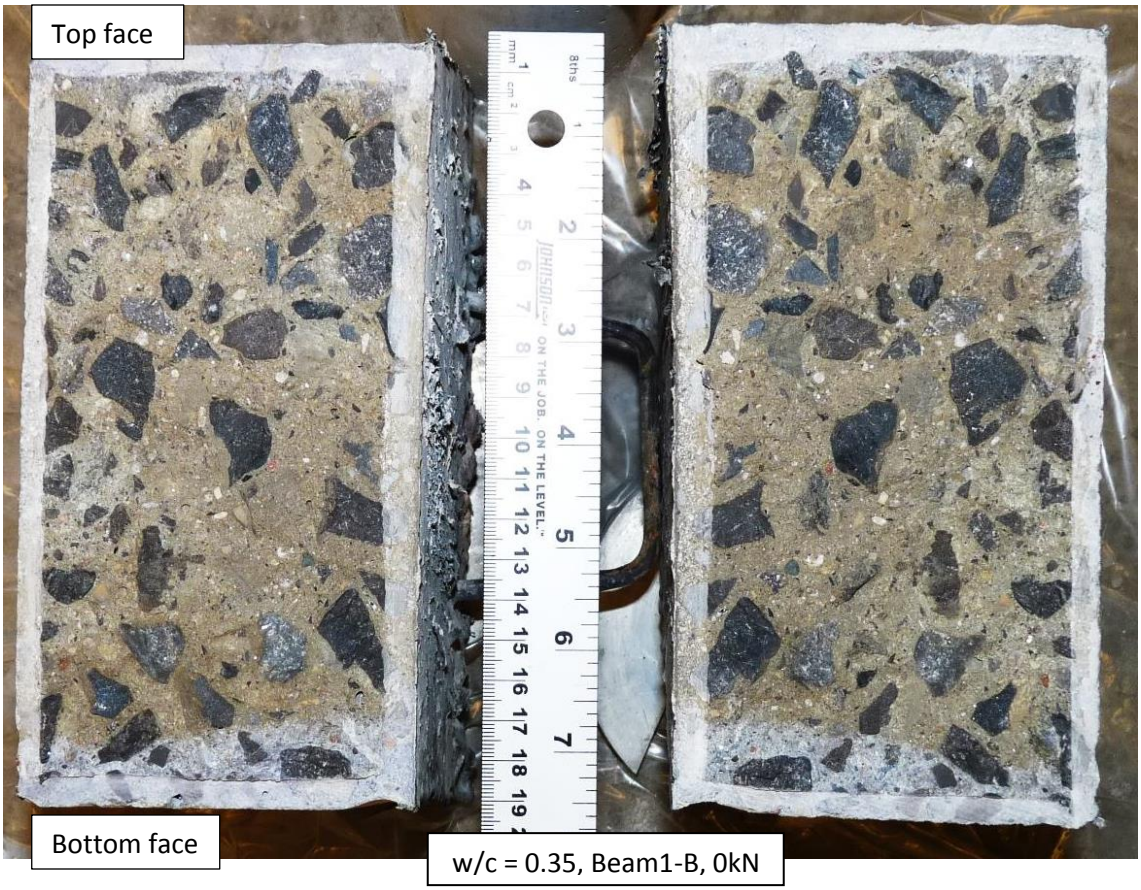

Figure C.2: Chloride penetration depths for beam 1; section B1-B (w/c = 0.35, 0 kN)

Figure C.3: Chloride penetration depths for beam 1; section B1-C (w/c = 0.35, 0 kN)

Figure C.4: Chloride penetration depths for beam 1; section B1-D (w/c = 0.35, 0 kN)

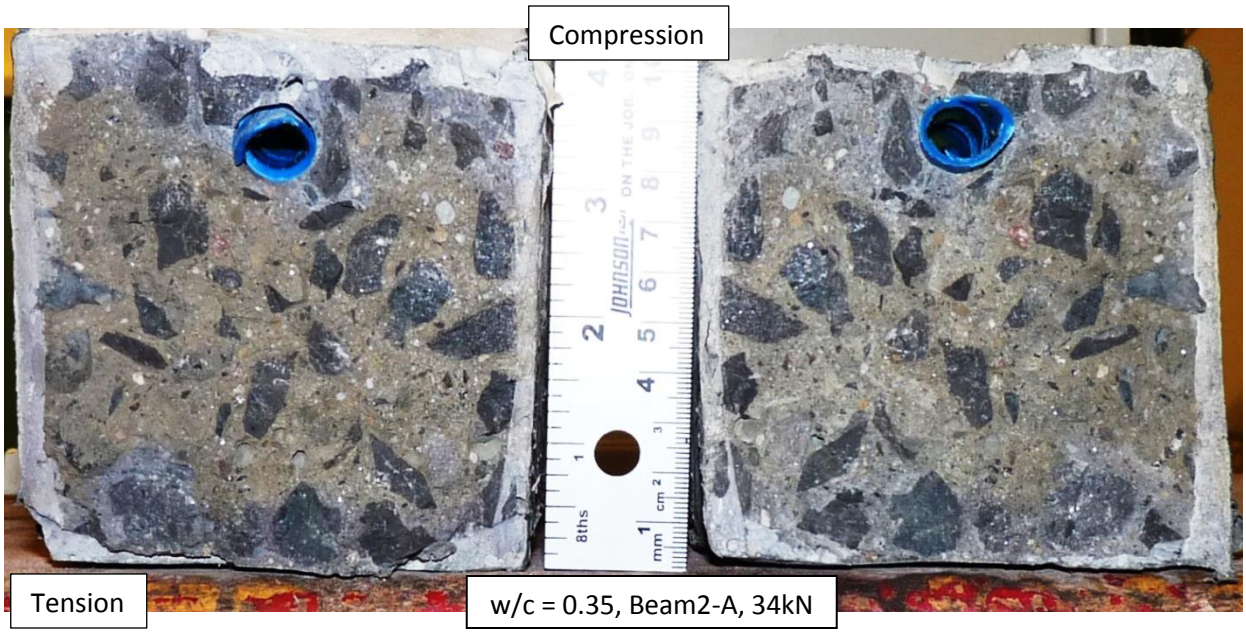

Figure C.5: Chloride penetration depths for beam 2; section B2-A (w/c = 0.35, 34 kN)

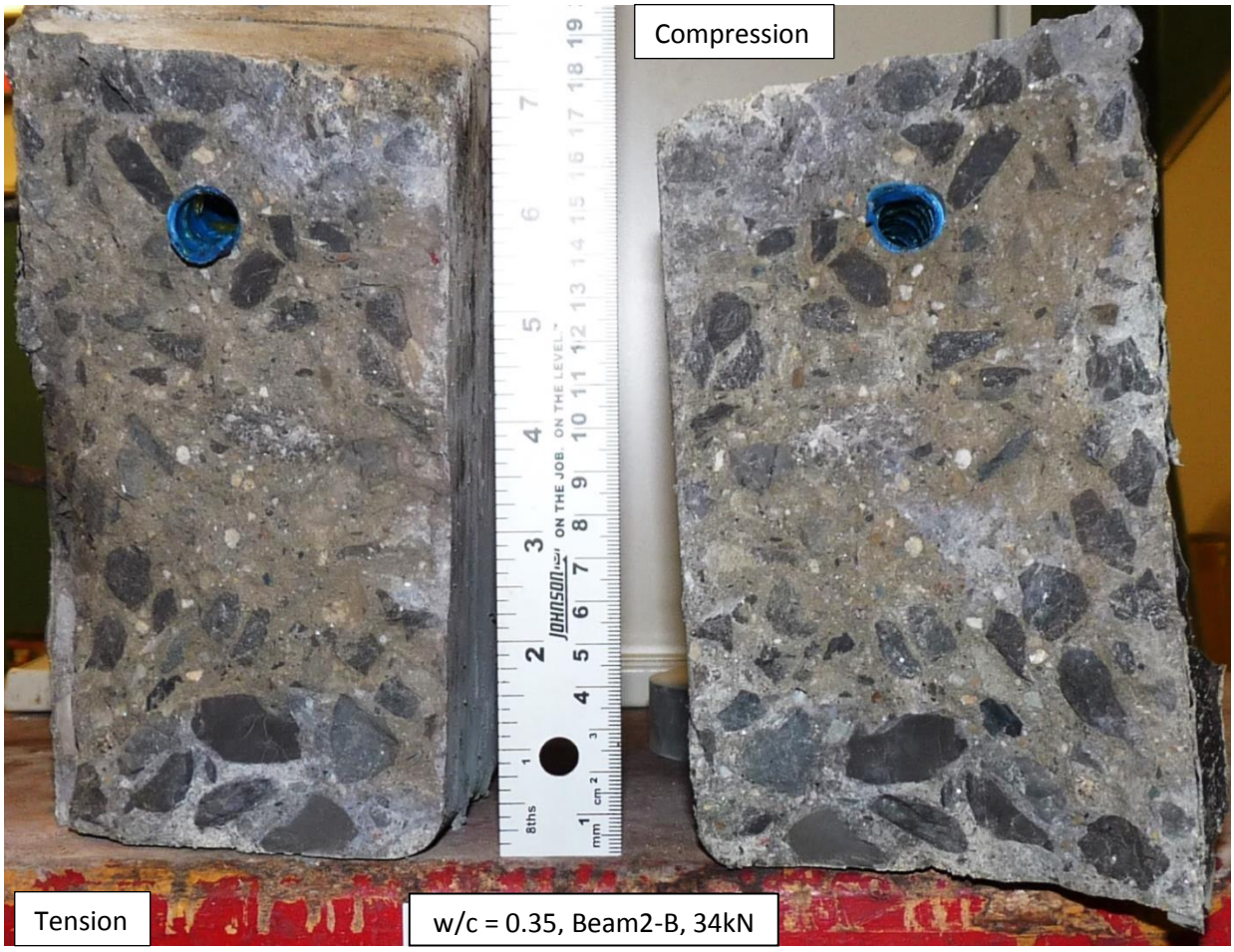

Figure C.6: Chloride penetration depths for beam 2; section B2-B (w/c = 0.35, 34 kN)

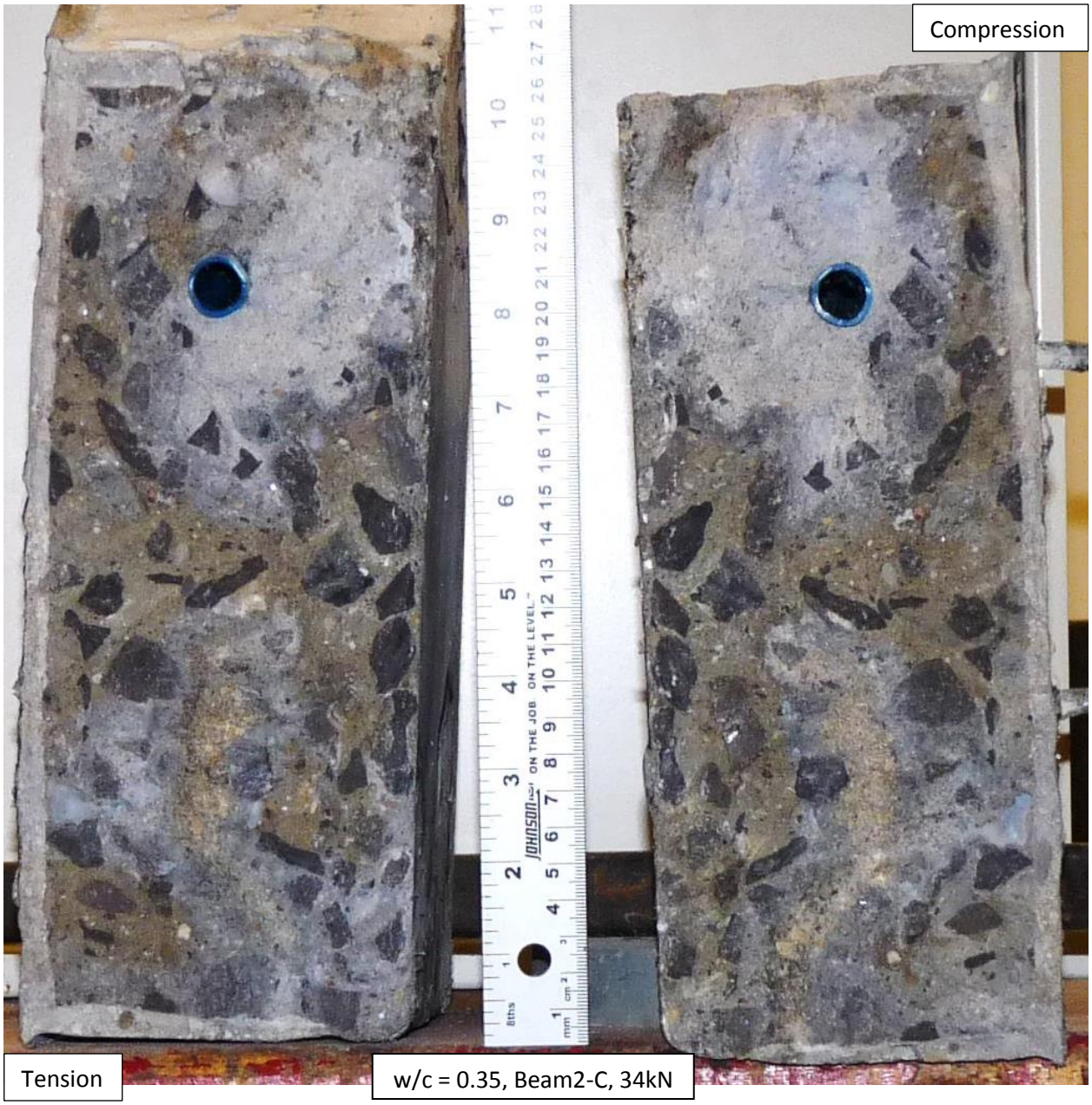

Figure C.7: Chloride penetration depths for beam 2; section B2-C (w/c = 0.35, 34 kN)

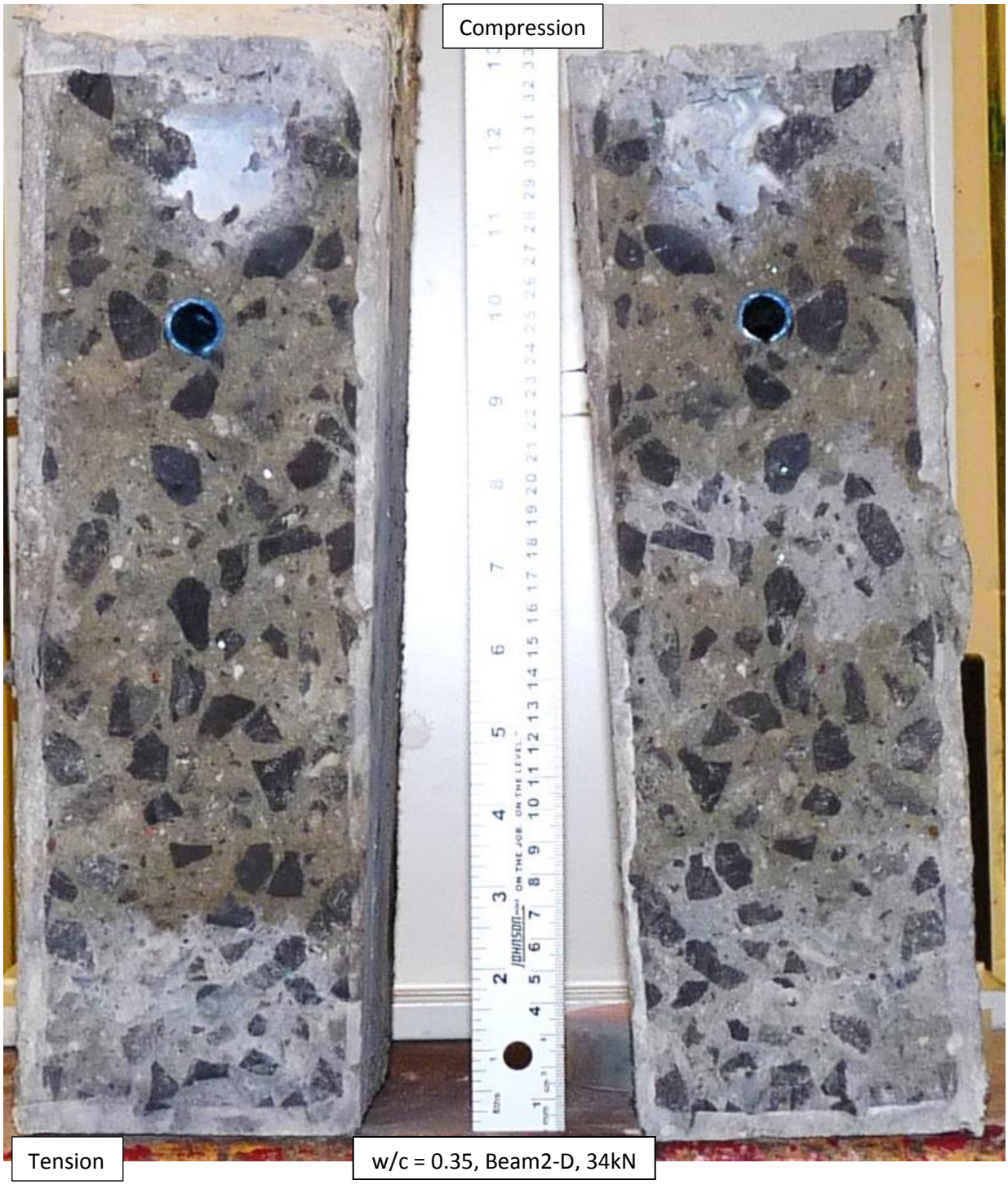

Figure C.8: Chloride penetration depths for beam 2; section B2-D (w/c = 0.35, 34 kN)

Figure C.9: Chloride penetration depths for beam 3; section B3-A (w/c = 0.35, 153 kN)

Figure C.10: Chloride penetration depths for beam 3; section B3-B (w/c = 0.35, 153 kN)

Figure C.11: Chloride penetration depths for beam 3; section B3-C (w/c = 0.35, 153 kN)

Figure C.12: Chloride penetration depths for beam 3; section B3-D (w/c = 0.35, 153 kN)

Figure C.13: Chloride penetration depths for beam 4; section B4-A (w/c = 0.40, 0 kN)

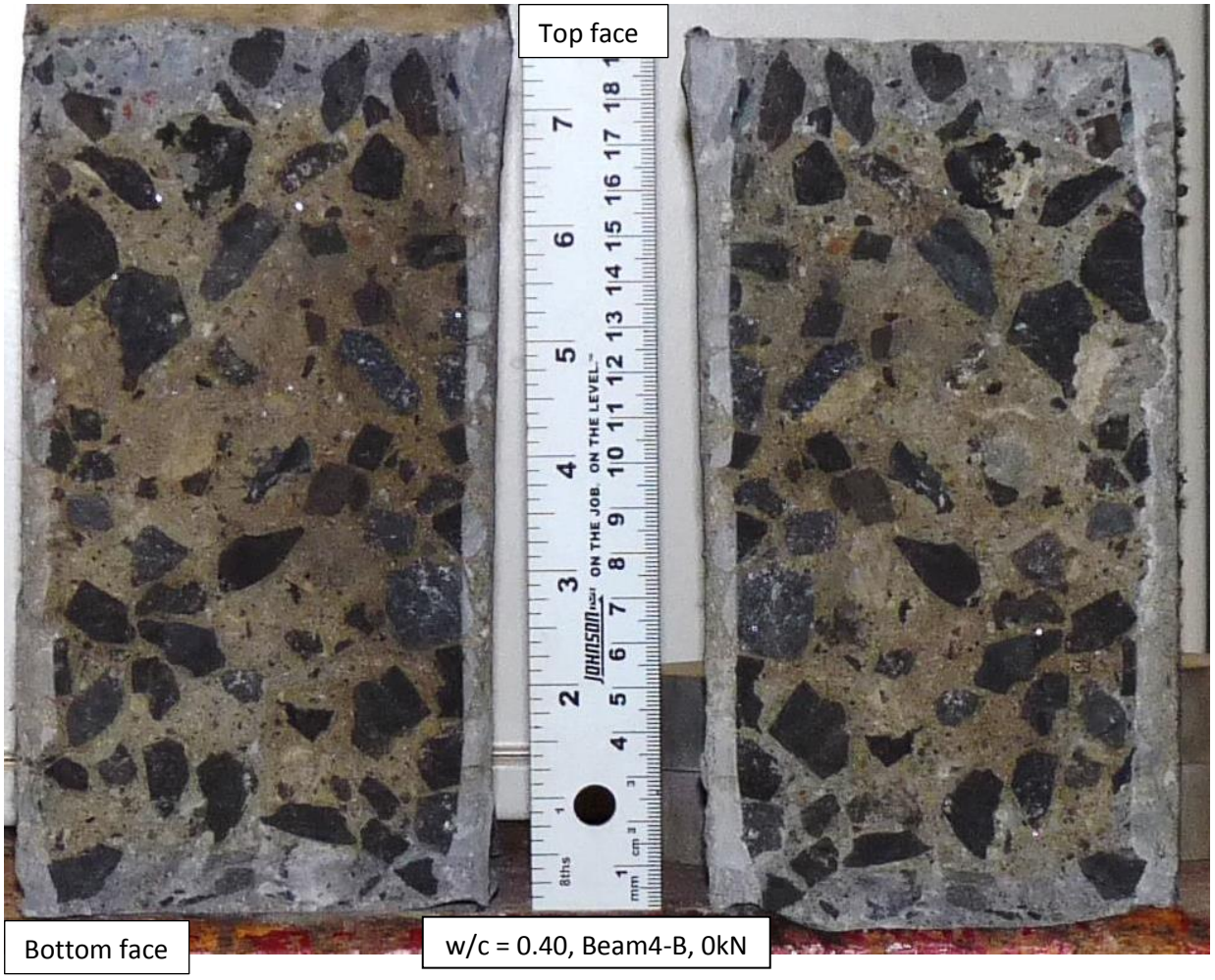

Figure C.14: Chloride penetration depths for beam 4; section B4-B (w/c = 0.40, 0 kN)

Figure C.15: Chloride penetration depths for beam 4; section B4-C (w/c = 0.40, 0 kN)

Figure C.16: Chloride penetration depths for beam 4; section B4-D (w/c = 0.40, 0 kN)

Figure C.17: Chloride penetration depths for beam 5; section B5-A (w/c = 0.40, 35 kN)

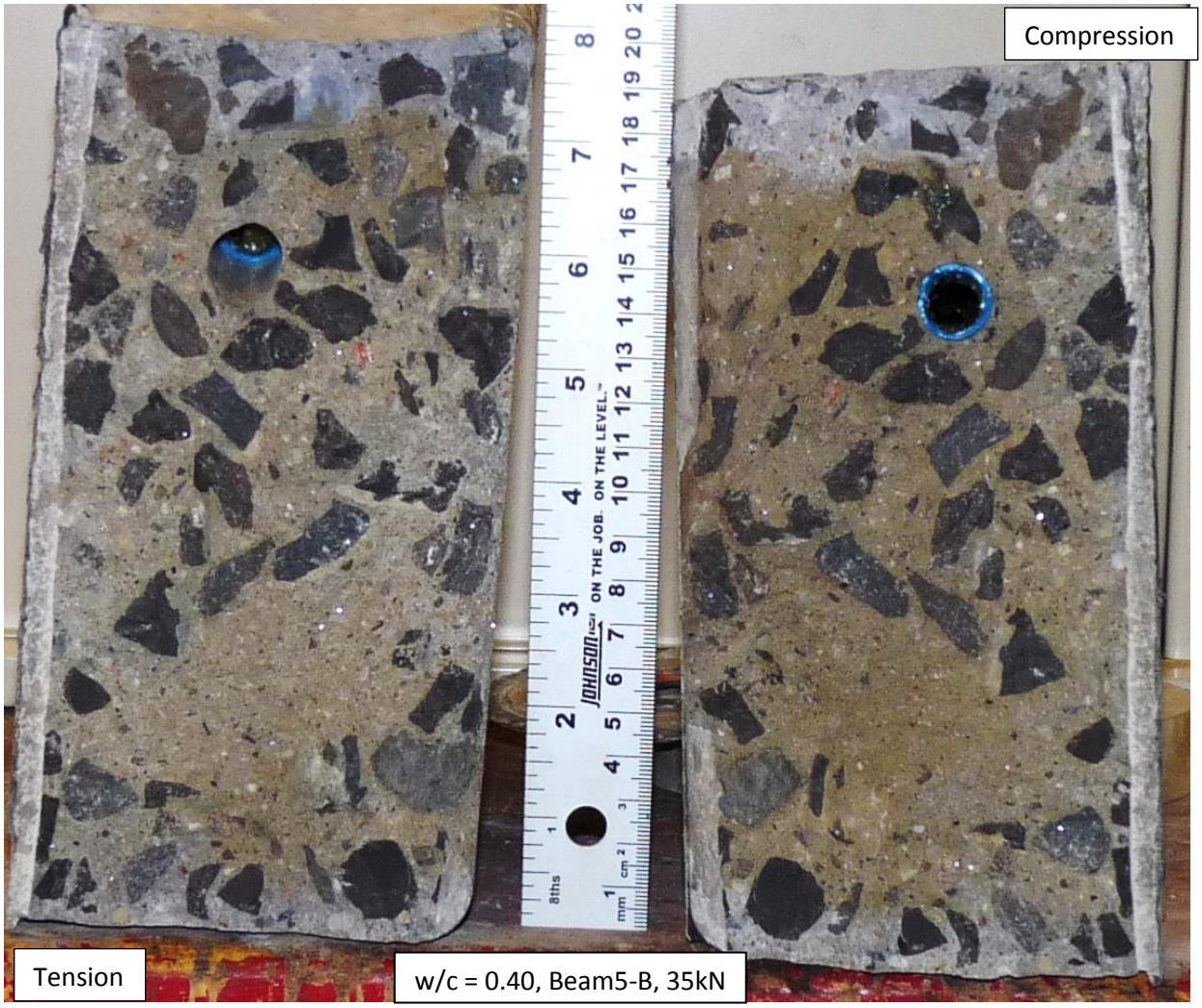

Figure C.18: Chloride penetration depths for beam 5; section B5-B (w/c = 0.40, 35 kN)

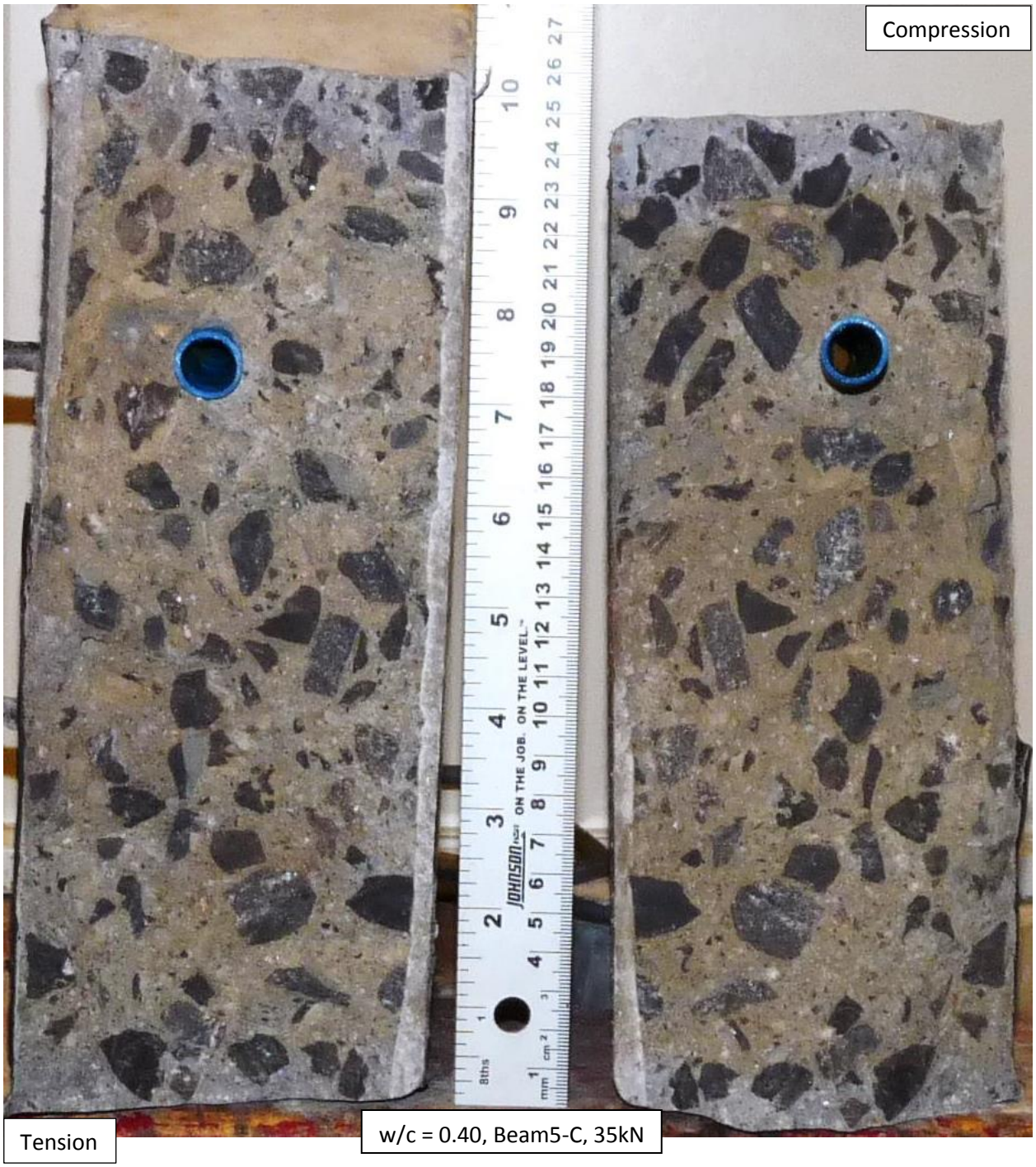

Figure C.19: Chloride penetration depths for beam 5; section B5-C (w/c = 0.40, 35 kN)

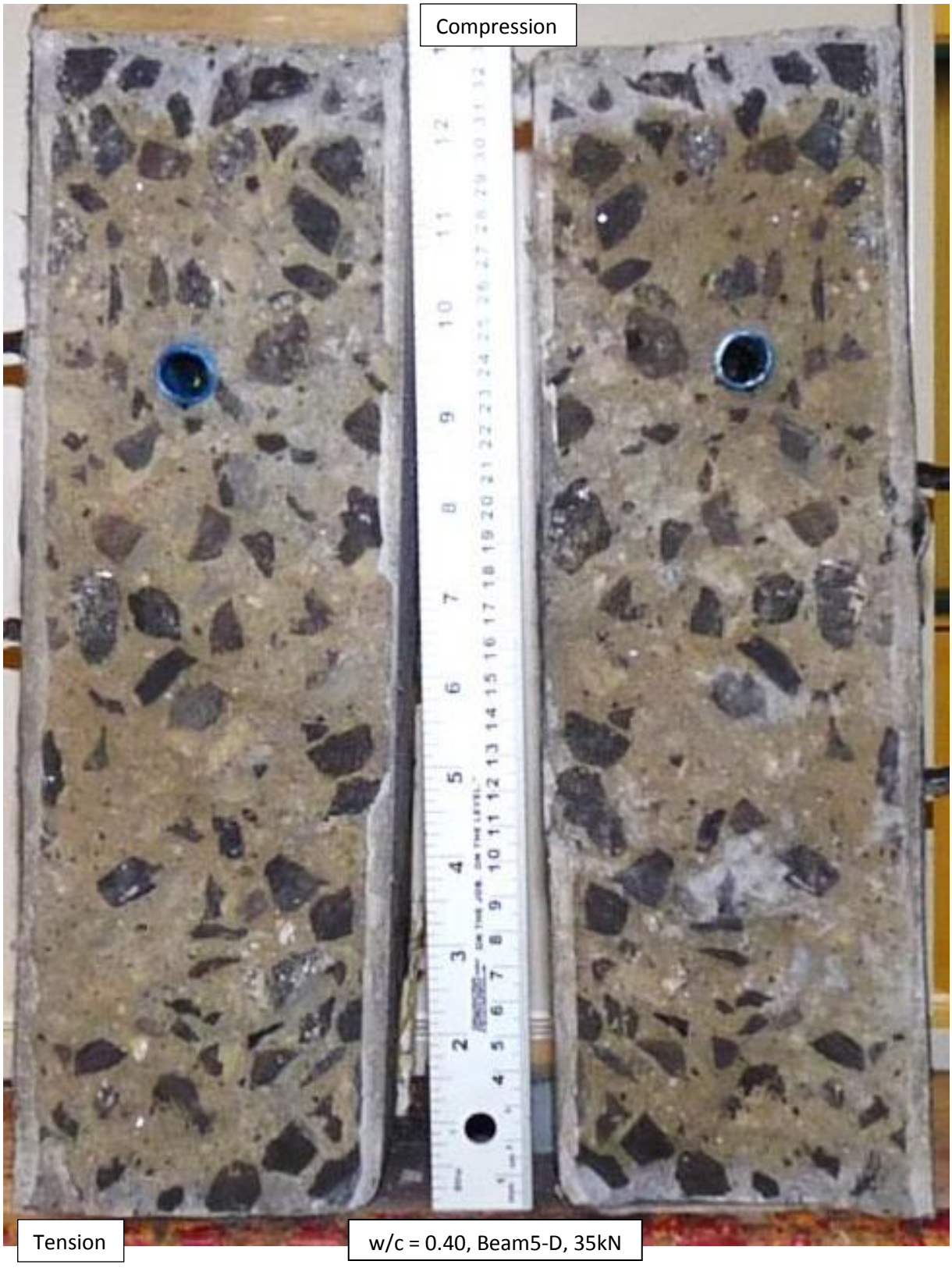

Figure C.20: Chloride penetration depths for beam 5; section B5-D (w/c = 0.40, 35 kN)

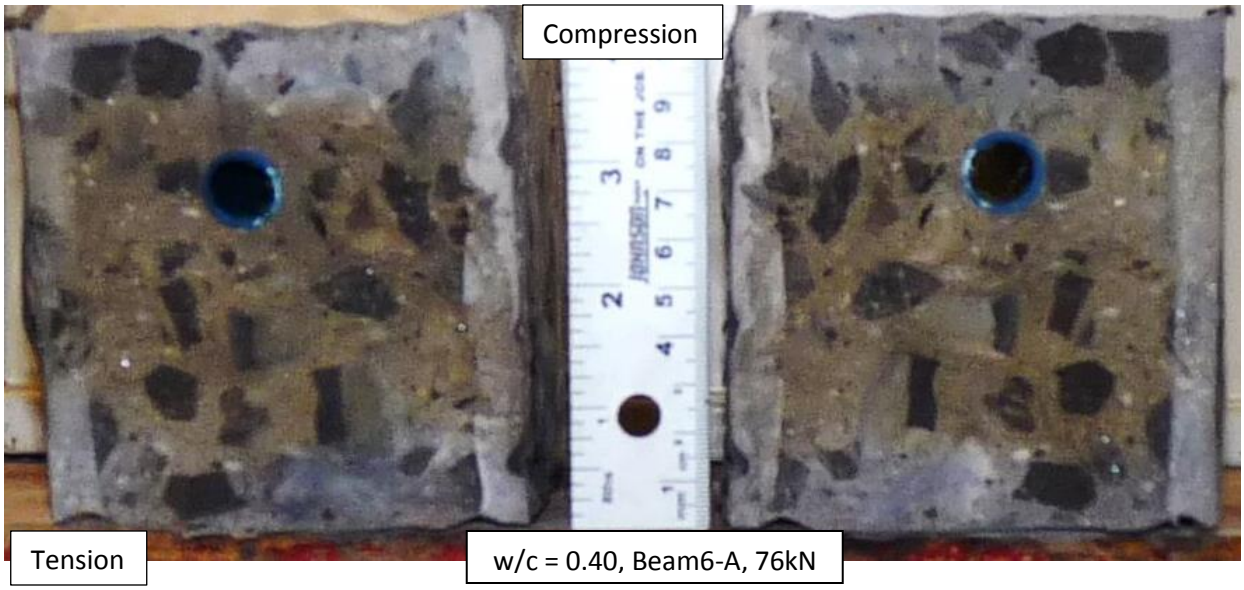

Figure C.21: Chloride penetration depths for beam 6; section B6-A (w/c = 0.40, 76 kN)

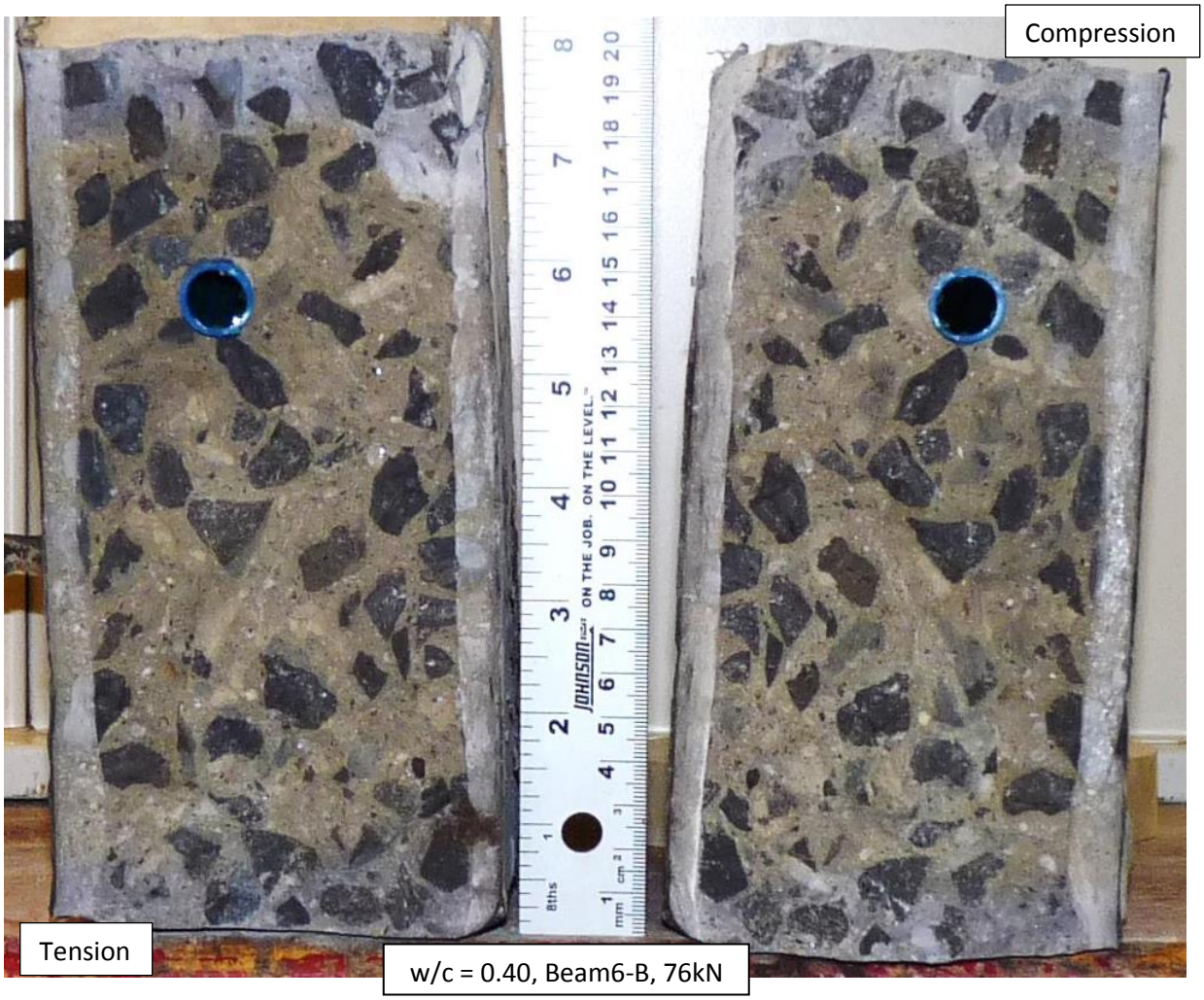

Figure C.22: Chloride penetration depths for beam 6; section B6-B (w/c = 0.40, 76 kN)

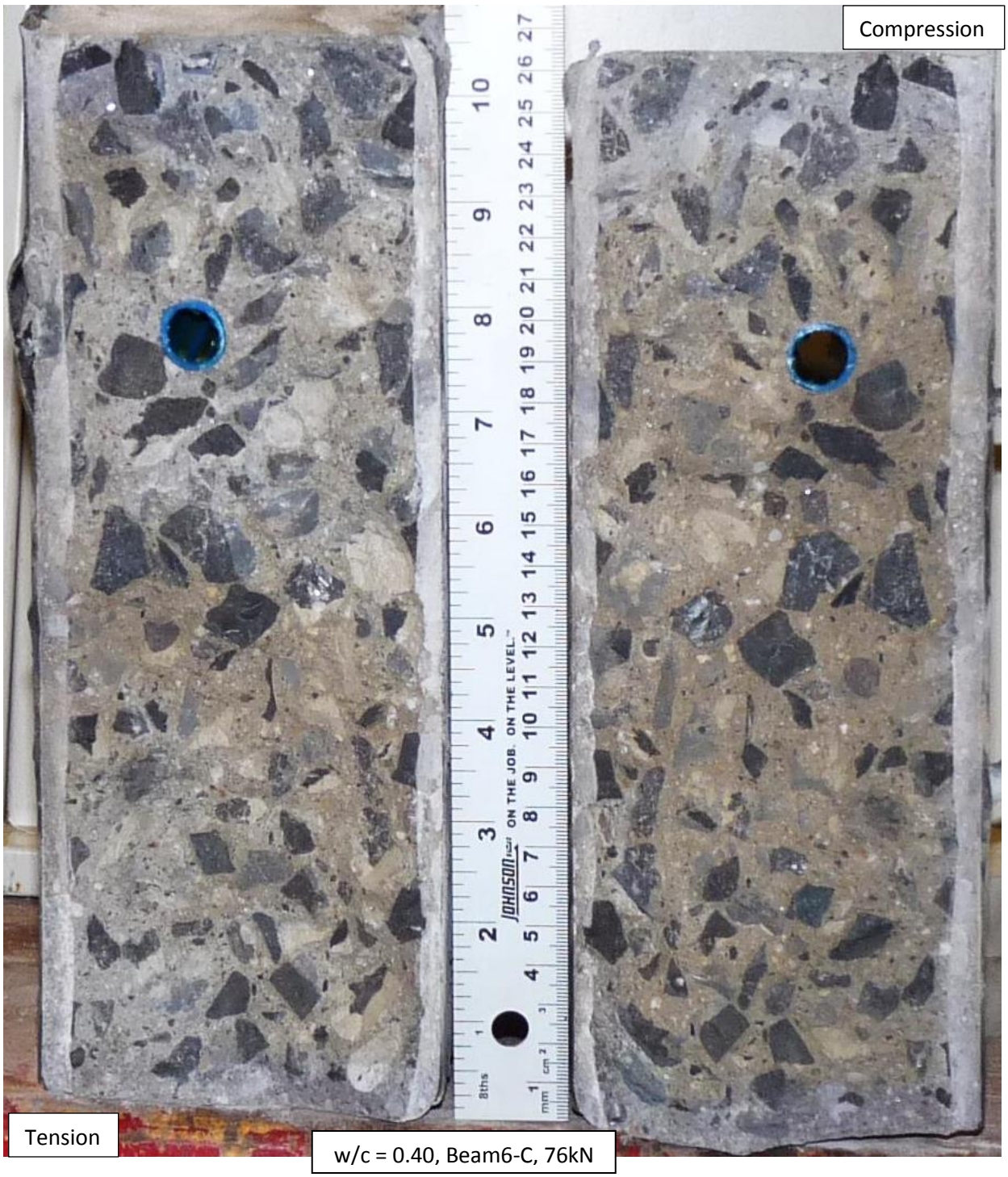

Figure C.23: Chloride penetration depths for beam 6; section B6-C (w/c = 0.40, 76 kN)

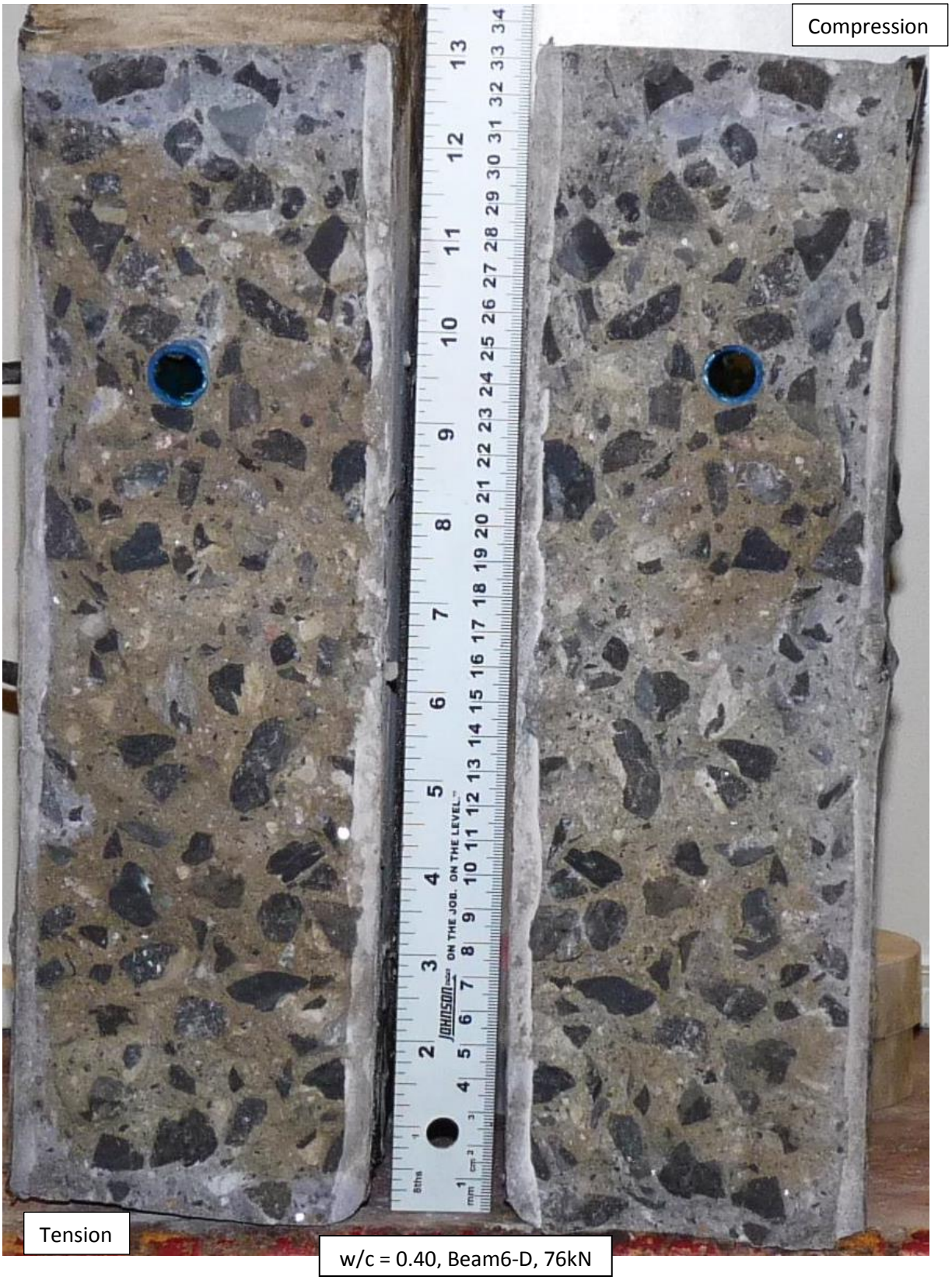

Figure C.24: Chloride penetration depths for beam 6; section B6-D (w/c = 0.40, 76 kN)

Figure C.25: Chloride penetration depths for beam 7; section B7-A (w/c = 0.50, 0 kN)

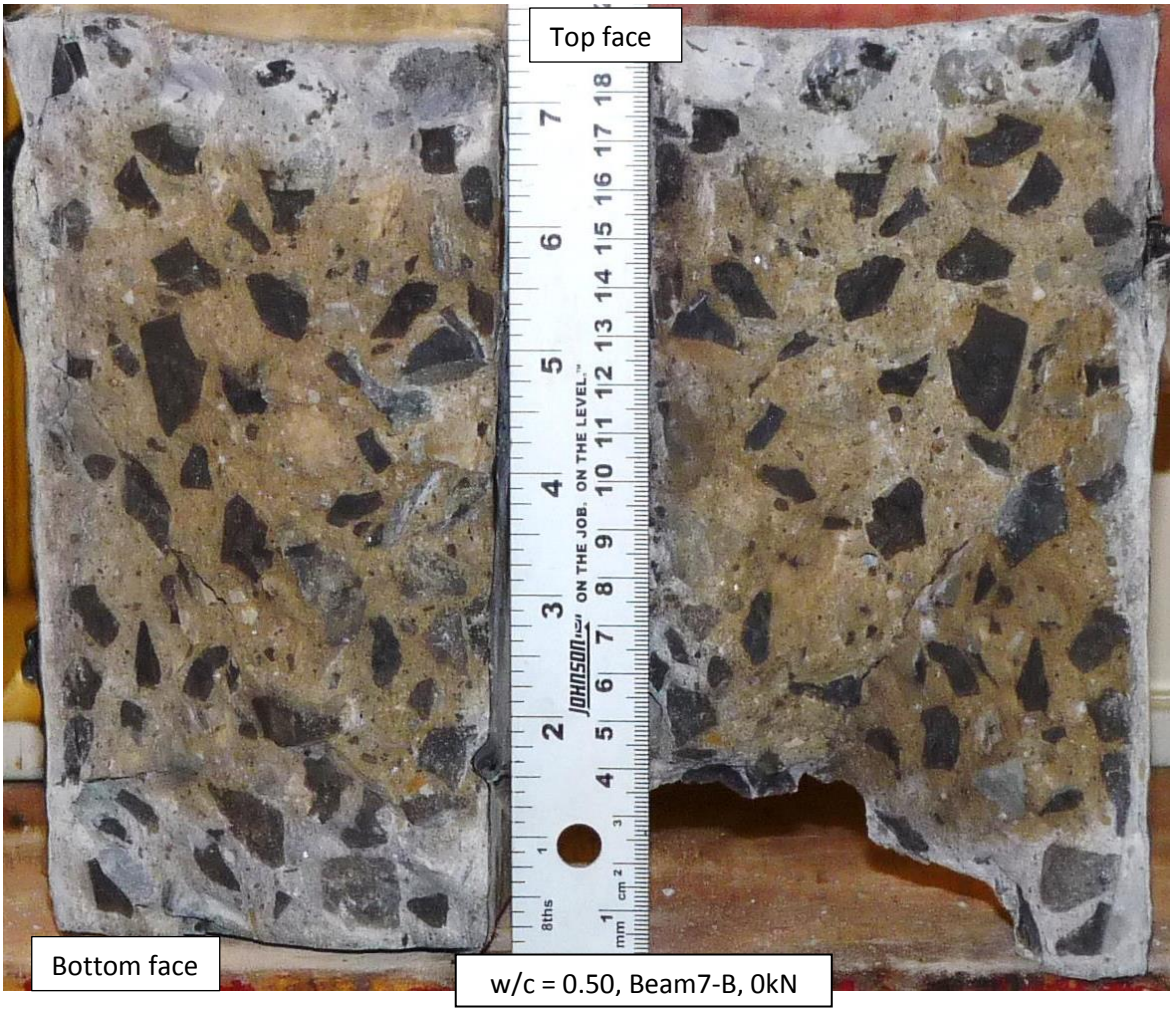

Figure C.26: Chloride penetration depths for beam 7; section B7-B (w/c = 0.50, 0 kN)

Figure C.27: Chloride penetration depths for beam 7; section B7-C (w/c = 0.50, 0 kN)

Figure C.28: Chloride penetration depths for beam 7; section B7-D (w/c = 0.50, 0 kN)

Figure C.29: Chloride penetration depths for beam 8; section B8-A (w/c = 0.50, 35 kN)

Figure C.30: Chloride penetration depths for beam 8; section B8-B (w/c = 0.50, 35 kN)

Figure C.31: Chloride penetration depths for beam 8; section B8-C (w/c = 0.50, 35 kN)

Figure C.32: Chloride penetration depths for beam 8; section B8-D (w/c = 0.50, 35 kN)

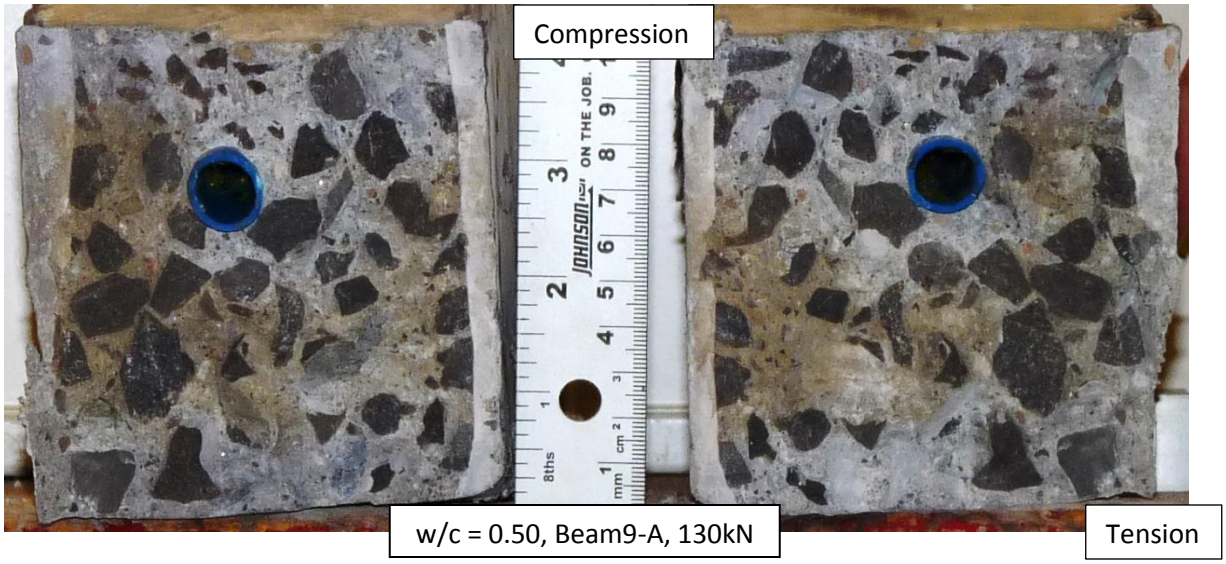

Figure C.33: Chloride penetration depths for beam 9; section B9-A (w/c = 0.50, 130 kN)

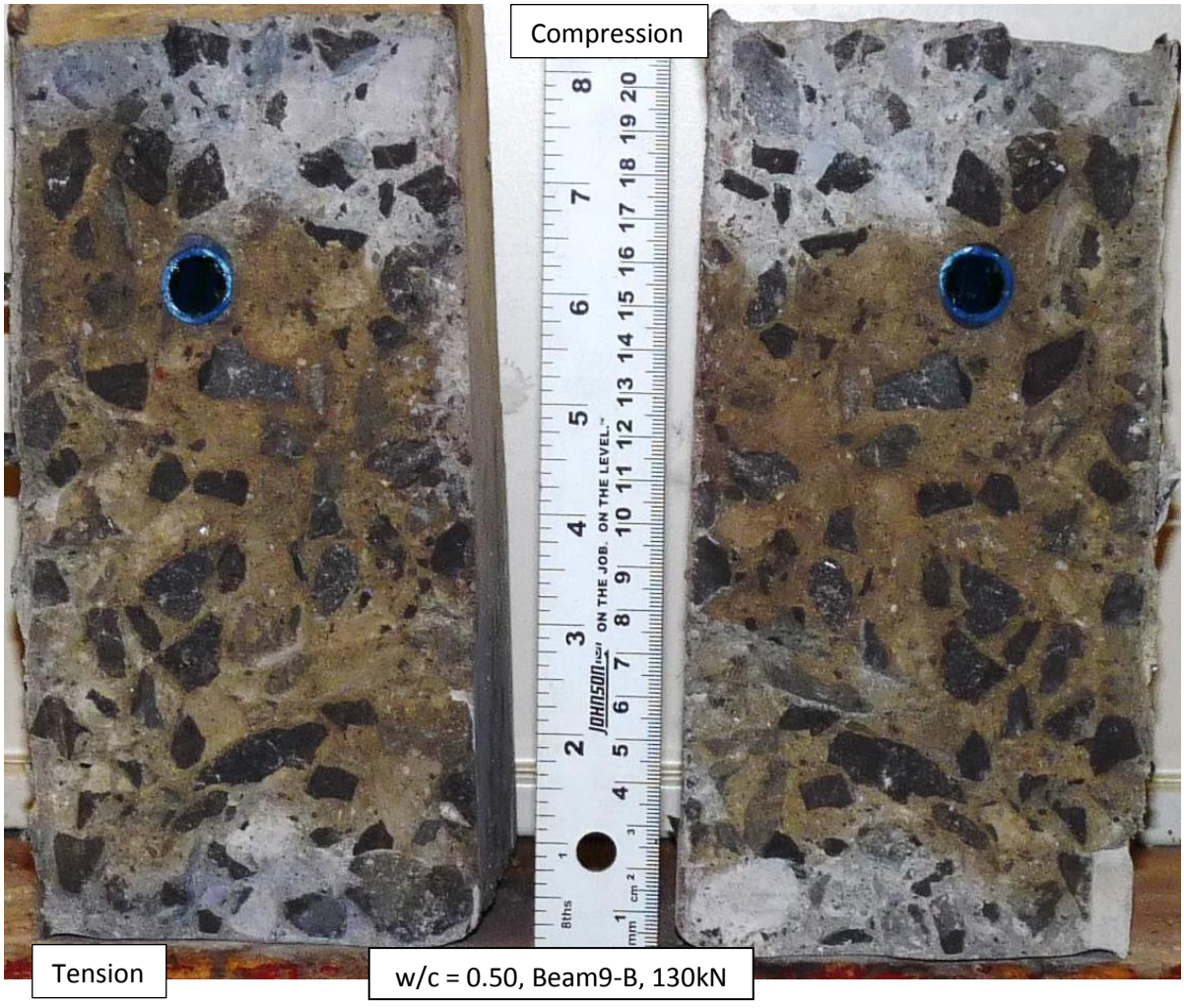

Figure C.34: Chloride penetration depths for beam 9; section B9-B (w/c = 0.50, 130 kN)

Figure C.35: Chloride penetration depths for beam 9; section B9-C (w/c = 0.50, 130 kN)

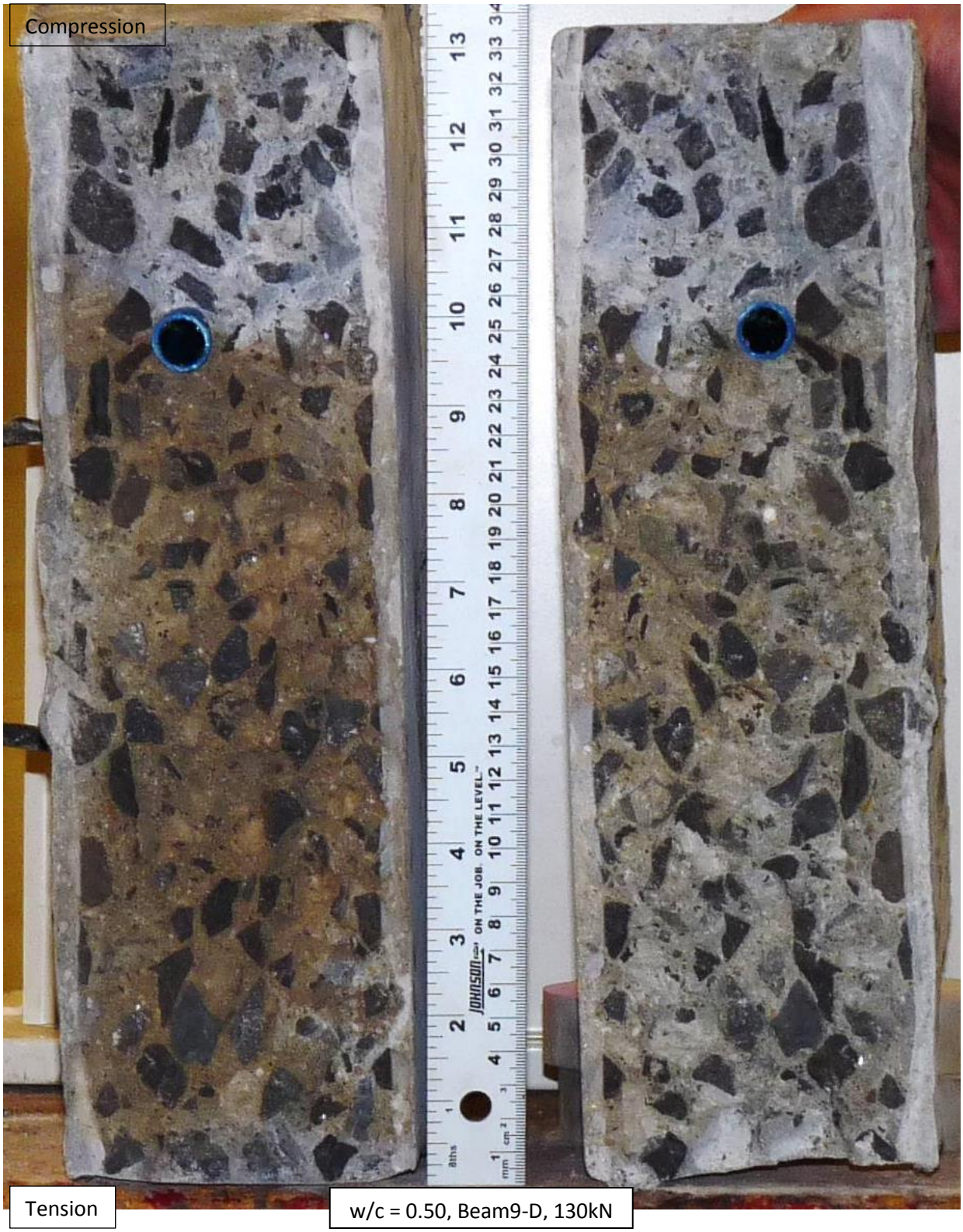

Figure C.36: Chloride penetration depths for beam 9; section B9-D (w/c = 0.50, 130 kN)

Figure C.37: Chloride penetration depths for beam 10; section B10-A (w/c = 0.50, 0 kN)

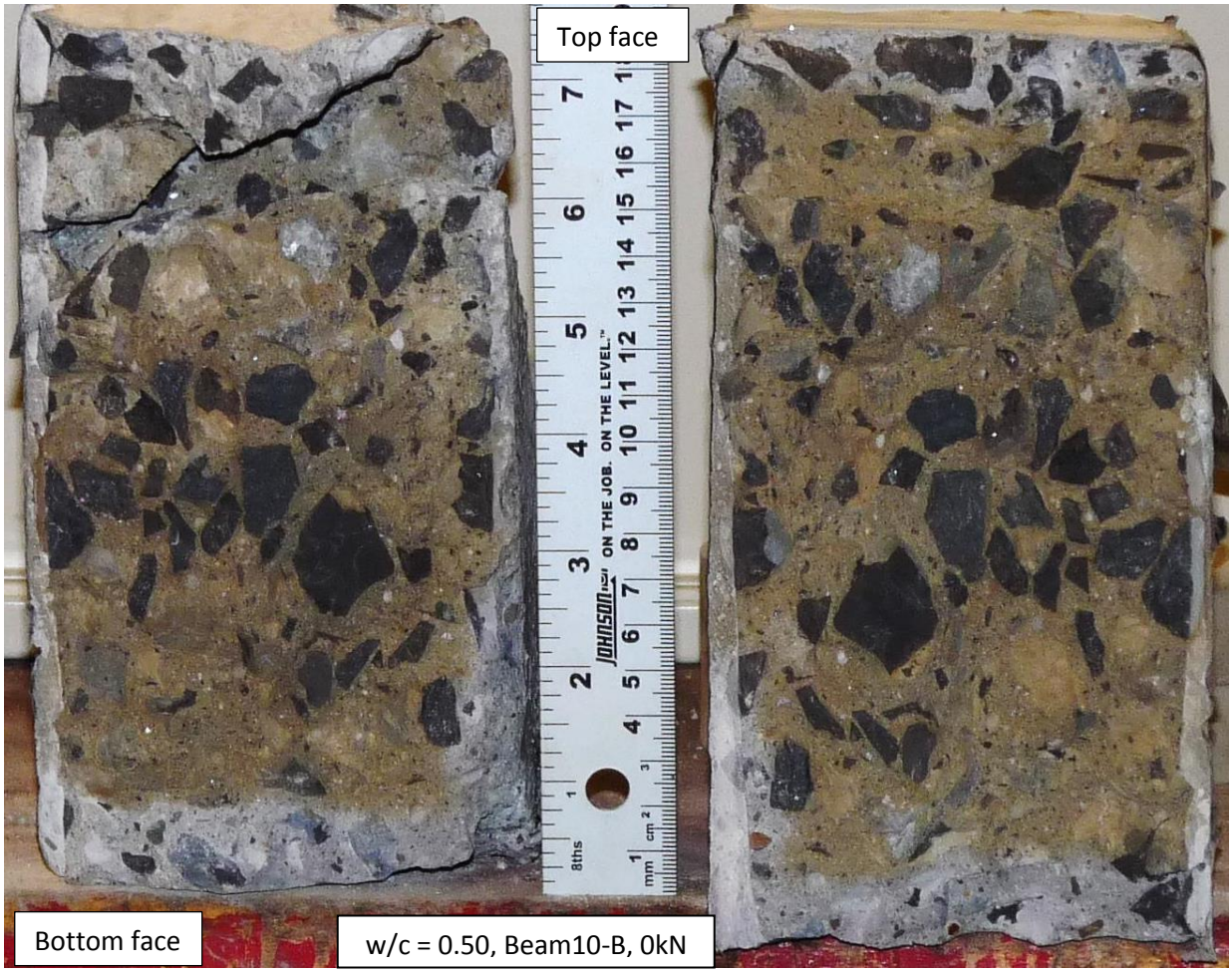

Figure C.38: Chloride penetration depths for beam 10; section B10-B (w/c = 0.50, 0 kN)

Figure C.39: Chloride penetration depths for beam 10; section B10-B (w/c = 0.50, 0 kN)

Figure C.40: Chloride penetration depths for beam 10; section B10-D (w/c = 0.50, 0 kN)

Table C.1: Average chloride penetration depths for Beam 1 (w/c = 0.35; 0 kN)

Section Cut	Section Side	Compression (cm)			Tension (cm)			Position of Section (cm)
		Max	Min	Average	Max	Min	Average	
B1-A	B1-1	3.0	1.5	2.25	2.5	1.3	1.9	15
	B1-2	2.8	1.5	2.15	2.5	1.5	2.0	15
B1-B	B1-2	2.5	1.2	1.85	1.0	0.9	0.95	40
	B1-3	2.4	1.5	1.95	1.2	1.0	1.1	40
B1-C	B1-3	2.0	1.5	1.75	1.0	1.0	1.0	60
	B1-4	1.8	1.2	1.5	1.0	1.0	1.0	60
B1-D	B1-4	2.8	1.8	2.3	1.0	1.0	1.0	80
	B1-5	2.7	1.7	2.2	1.0	1.0	1.0	80

Table C.2: Average chloride penetration depths for Beam 2 (w/c = 0.35; 34 kN)

Section cut	Section Side	Compression (cm)			Tension (cm)			Position of Section (cm)	Stress (MPa)	
		Max	Min	Average	Max	Min	Average		σ_c	σ_t
B2-A	B2-1	3.0	2.5	2.75	2.5	1.5	2.0	15	8.46	-1.54
	B2-2	3.0	1.5	2.25	2.8	1.5	2.15	15	8.46	-1.54
B2-B	B2-2	3.0	1.7	2.35	4.0	1.5	2.75	40	4.34	-0.69
	B2-3	3.0	1.5	2.25	3.8	1.7	2.75	40	4.34	-0.69
B2-C	B2-3	12.0	9.0	10.5	12.0	6.0	9.0	60	3.12	-0.48
	B1-4	12.5	7.0	9.75	12.0	9.0	10.5	60	3.12	-0.48
B2-D	B1-4	6.0	3.0	4.5	9.0	7.5	8.25	80	2.44	-0.36
	B1-5	6.5	2.5	4.5	8.0	7.0	7.5	80	2.44	-0.36

Table C.3: Average chloride penetration depths for Beam 3 (w/c = 0.35; 153 kN)

Section Cut	Section Side	Compression (cm)			Tension (cm)			Position of Section (cm)	Stress (MPa)	
		Max	Min	Average	Max	Min	Average		σ_c	σ_t
B3-A	B3-1	3.5	3.0	3.25	2.0	1.6	1.8	15	38.11	-6.96
	B3-2	3.3	2.5	2.9	2.3	1.6	1.95	15	38.11	-6.96
B3-B	B3-2	3.5	2.0	2.75	2.0	1.5	1.75	40	19.55	-3.14
	B3-3	3.4	2.3	2.85	10.0	6.5	8.25	40	19.55	-3.14
B3-C	B3-3	3.0	2.2	2.6	1.8	1.6	1.7	60	14.06	-2.16
	B3-4	2.8	2.0	2.4	2.0	1.5	1.75	60	14.06	-2.16
B3-D	B3-4	3.0	2.0	2.5	1.1	1.0	1.05	80	10.98	-1.64
	B3-5	3.0	2.5	2.75	1.0	1.0	1.0	80	10.98	-1.64

Table C.4: Average chloride penetration depths for Beam 4 (w/c = 0.40; 0 kN)

Section Cut	Section Side	Compression (cm)			Tension (cm)			Position of Section (cm)
		Max	Min	Average	Max	Min	Average	
B4-A	B4-1	2.0	1.5	1.75	2.0	1.0	1.5	15
	B4-2	2.1	1.5	1.8	2.0	1.1	1.55	15
B4-B	B4-2	2.5	2.0	2.25	1.6	1.5	1.55	40
	B4-3	2.5	2.0	2.25	1.4	1.4	1.4	40
B4-C	B4-3	2.6	2.0	2.3	2.0	1.0	1.5	60
	B4-4	2.5	1.8	2.15	1.6	1.0	1.3	60
B4-D	B4-4	5.0	3.0	4.0	1.3	1.0	1.15	80
	B4-5	5.5	3.0	4.25	1.1	1.0	1.05	80

Table C.5: Average chloride penetration depths for Beam 5 (w/c = 0.40; 35 kN)

Section Cut	Section Side	Compression (cm)			Tension (cm)			Position of Section (cm)	Stress (MPa)	
		Max	Min	Average	Max	Min	Average		σ_c	σ_t
B5-A	B5-1	1.5	1.5	1.5	2.0	1.5	1.75	15	8.71	-1.59
	B5-2	1.6	1.4	1.5	1.7	1.5	1.6	15	8.71	-1.59
B5-B	B5-2	3.0	2.0	2.5	1.6	1.4	1.5	40	4.47	-0.71
	B5-3	3.0	2.0	2.5	1.5	1.4	1.45	40	4.47	-0.71
B5-C	B5-3	2.4	2.0	2.2	1.5	1.3	1.4	60	3.21	-0.49
	B5-4	2.2	2.0	2.1	1.5	1.3	1.4	60	3.21	-0.49
B5-D	B5-4	2.5	2.0	2.25	1.3	1.0	1.15	80	2.51	-0.37
	B5-5	2.5	1.8	2.15	1.3	1.0	1.15	80	2.51	-0.37

Table C.6: Average chloride penetration depths for Beam 6 (w/c = 0.40; 76 kN)

Section Cut	Section Side	Compression (cm)			Tension (cm)			Position of Section (cm)	Stress (MPa)	
		Max	Min	Average	Max	Min	Average		σ_c	σ_t
B6-A	B6-1	1.5	1.3	1.4	2.0	1.8	1.9	15	18.93	-3.45
	B6-2	1.7	1.4	1.55	2.1	1.6	1.85	15	18.93	-3.45
B6-B	B6-2	3.4	2.0	2.7	1.5	1.5	1.5	40	9.71	-1.56
	B6-3	3.4	2.0	2.7	1.5	1.5	1.5	40	9.71	-1.56
B6-C	B6-3	4.0	2.5	3.25	1.4	1.0	1.2	60	6.98	-1.07
	B6-4	3.8	2.4	3.1	1.0	1.0	1.0	60	6.98	-1.07
B6-D	B6-4	3.8	2.8	3.3	1.7	1.0	1.35	80	5.45	-0.81
	B6-5	3.5	2.0	2.75	1.5	1.0	1.25	80	5.45	-0.81

Table C.7: Average chloride penetration depths for Beam 7 (w/c = 0.50; 0 kN)

Section Cut	Section Side	Compression (cm)			Tension (cm)			Position of Section (cm)
		Max	Min	Average	Max	Min	Average	
B7-A	B7-1	-	-	-	-	-	*2.19	15
	B7-2	-	-	-	-	-	*2.19	15
B7-B	B7-2	3.0	2.6	2.8	2.6	2.0	2.3	40
	B7-3	3.0	2.7	2.85	2.6	2.0	2.3	40
B7-C	B7-3	5.0	2.5	3.75	2.2	1.6	1.9	60
	B7-4	4.6	2.5	3.55	2.5	2.0	2.25	60
B7-D	B7-4	3.0	2.6	2.8	2.5	2.0	2.25	80
	B7-5	3.0	2.8	2.9	2.6	1.7	2.15	80

*Critical section at cut B7-A was split before being submerged and therefore data was inconclusive. An average of the average tensile depths was used (standard deviation = 0.153)

Table C.8: Average chloride penetration depths for Beam 8 (w/c = 0.50; 35 kN)

Section Cut	Section Side	Compression (cm)			Tension (cm)			Position of Section (cm)	Stress (MPa)	
		Max	Min	Average	Max	Min	Average		σ_c	σ_t
B8-A	B8-1	2.3	2.0	2.15	1.7	1.5	1.6	15	8.71	-1.59
	B8-2	2.2	1.9	2.05	2.2	1.5	1.85	15	8.71	-1.59
B8-B	B8-2	2.6	2.1	2.35	1.7	1.5	1.6	40	4.47	-0.71
	B8-3	3.0	2.3	2.65	2.0	1.8	1.9	40	4.47	-0.71
B8-C	B8-3	3.1	2.5	2.8	1.7	1	1.35	60	3.21	-0.49
	B8-4	5.0	2.3	3.65	2.0	1.3	1.65	60	3.21	-0.49
B8-D	B8-4	3.4	2.6	3.0	1.7	1.5	1.6	80	2.51	-0.37
	B8-5	3.4	2.8	3.1	1.8	1.3	1.55	80	2.51	-0.37

Table C.9: Average chloride penetration depths for Beam 9 (w/c = 0.50; 130 kN)

Section Cut	Section Side	Compression (cm)			Tension (cm)			Position of Section (cm)	Stress (MPa)	
		Max	Min	Average	Max	Min	Average		σ_c	σ_t
B9-A	B9-1	4.2	3.0	3.6	3.0	2.6	2.8	15	32.38	-5.91
	B9-2	3.4	2.5	2.95	2.5	2.2	2.35	15	32.38	-5.91
B9-B	B9-2	6.0	3.0	4.5	3.0	1.6	2.3	40	16.61	-2.67
	B9-3	6.0	2.6	4.3	3.0	1.6	2.3	40	16.61	-2.67
B9-C	B9-3	6.0	2.0	4.0	2.0	1.5	1.75	60	11.95	-1.83
	B9-4	6.0	3.5	4.75	1.5	1.0	1.25	60	11.95	-1.83
B9-D	B9-4	9.0	8.0	8.5	2.0	1.0	1.5	80	9.33	-1.39
	B9-5	9.0	7.5	8.25	2.0	1.2	1.6	80	9.33	-1.39

Table C.10: Average chloride penetration depths for Beam 10 (w/c = 0.50; 0 kN)

Section Cut	Section Side	Compression (cm)			Tension (cm)			Position of Section (cm)
		Max	Min	Average	Max	Min	Average	
B10-A	B10-1	*-	-	-	-	-	-	15
	B10-2	-	-	-	-	-	-	15
B10-B	B10-2	2.0	1.5	1.75	1.5	1.0	1.25	40
	B10-3	2.0	2.0	2.0	2.5	1.5	2.0	40
B10-C	B10-3	3.0	1.5	2.25	1.4	1.0	1.2	60
	B10-4	3.0	2.0	2.5	1.2	1.0	1.1	60
B10-D	B10-4	3.0	2.5	2.75	1.0	1.0	1.0	80
	B10-5	4.5	2.5	3.5	2.0	1.0	1.5	80

*Critical section at cut B10-A was split before being submerged and therefore data was inconclusive

Appendix D - Titration Results

Table D.1: Potentiometric results for blanks of deionized distilled water

Date	V_2, mL	mV	Average, mL
Jun-24	3.693	180	2.223
Jun-24	1.957	178	
Jun-24	2.488	166	
Jun-25	1.647	197	1.647
Jun-26	2.489	173	2.230
Jun-26	1.971	185	
Jun-27	2.299	191	2.299
Jul-03	2.154	180	2.154
Jul-04	1.995	155	1.979
Jul-04	1.963	167	
Jul-12	2.275	162	2.275

Table D.2: Potentiometric results of total chloride content (% weight of concrete) for bottom face of unloaded control beams

Section	Depth, cm	Weight, g	mV	V_1, mL	Cl, %
Cut B1-C Section B1-3	0.25	4.969	184	34.832	1.163
	0.75	4.793	129	18.144	0.588
	1.25	6.086	133	13.442	0.326
	1.75	4.936	170	8.519	0.226
Cut B1-B Section B1-3	0.25	4.318	157	22.611	0.836
	0.75	4.686	154	13.088	0.410
	1.25	4.312	143	8.481	0.257
	1.75	4.748	144	5.583	0.125
Cut B4-B Section B4-2	0.25	4.940	164	29.803	1.010
	0.75	4.789	142	15.286	0.504
	1.25	4.607	139	11.797	0.390
	1.75	5.188	157	9.884	0.281
	2.25	5.627	120	6.888	0.165
Cut B4-C Section B4-3	0.25	4.869	212	28.514	0.978
	0.75	4.637	210	15.165	0.516
	1.25	4.963	241	12.345	0.382
	1.75	4.371	157	6.863	0.211
	2.25	4.993	220	4.934	0.116

Cut B7-B Section B7-3	0.25	5.365	185	49.537	1.562
	0.75	4.528	137	16.998	0.578
	1.25	5.466	134	16.267	0.455
	1.75	5.717	117	15.107	0.399
	2.25	5.450	138	9.449	0.234
	2.75	5.620	231	3.356	0.0355
Cut B7-C Section B10-3	0.25	4.509	231	39.706	1.473
	0.75	4.590	144	17.767	0.599
	1.25	5.439	140	18.819	0.540
	1.75	6.053	124	15.734	0.395
	2.25	5.448	128	13.244	0.358
	2.75	5.890	120	9.230	0.210
	3.25	5.523	136	4.289	0.066
	3.75	6.334	165	7.163	0.138
Cut B10-B Section B7-4	0.25	5.056	151	36.31	1.194
	0.75	4.906	141	23.213	0.758
	1.25	5.140	125	14.836	0.434
	1.75	4.595	161	5.028	0.108
	2.25	4.894	176	4.693	0.089
Cut B10-D Section B10-4	0.25	4.888	161	52.866	1.833
	0.75	4.995	130	26.639	0.863
	1.25	4.622	139	18.355	0.615
	1.75	5.626	129	12.936	0.335
	2.25	5.238	122	5.861	0.120
	2.75	5.222	143	3.108	0.027

Table D.3: Potentiometric results of total chloride content (% weight of concrete) for top face of unloaded control beams

Section	Depth, cm	Weight, g	mV	V_1, mL	Cl, %
Cut B1-A Section B1-2	0.25	4.644	134	20.369	0.695
	0.75	4.560	140	9.605	0.289
	1.25	4.674	129	5.679	0.133
	1.75	4.215	133	3.207	0.044
	2.25	4.538	142	2.665	0.0199
Cut B4-B Section B4-2	0.25	4.451	127	17.776	0.628
	0.75	4.523	142	11.611	0.376
	1.25	4.814	120	3.414	0.052
	1.75	5.290	223	1.561	-0.014
Cut B7-C Section B7-4	0.25	4.735	161	19.968	0.674
	0.75	4.644	209	5.099	0.119
	1.25	4.792	124	4.697	0.101
	1.75	5.695	135	4.605	0.082
	2.25	5.642	122	2.860	0.028
Cut B10-D Section B10-5	0.25	4.847	120	16.486	0.531
	0.75	5.048	206	4.387	0.085
	1.25	4.640	138	3.812	0.070
	1.75	4.322	129	2.540	0.023

Table D.4: Potentiometric results of total chloride content (% weight of concrete) for the compression face of post-tensioned beams

Section	Depth, cm	Weight, g	mV	V_1, mL	Cl, %
Cut B2-B Section B2-3	0.25	4.522	143	14.775	0.492
	0.75	4.189	161	6.903	0.198
	1.25	5.360	130	7.220	0.165
	1.75	4.776	139	4.743	0.093
	2.25	4.720	155	4.321	0.078
Cut B3-B Section B3-2	0.25	4.360	151	25.594	0.950
	0.75	4.661	137	14.958	0.484
	1.25	4.906	158	12.385	0.367
	1.75	4.378	136	7.475	0.212
	2.25	5.963	146	8.313	0.181
	2.75	4.983	140	4.004	0.063
Cut B5-B Section B5-3	0.25	4.417	234	25.130	0.942
	0.75	4.377	147	14.595	0.524
	1.25	4.285	135	10.509	0.366
	1.75	4.093	148	6.843	0.225
	2.25	4.131	159	6.223	0.196
	2.75	5.328	170	7.200	0.184
Cut B6-A Section B6-2	0.25	4.567	155	34.264	1.265
	0.75	4.267	157	14.744	0.544
	1.25	5.064	159	11.629	0.349
	1.75	5.395	170	6.777	0.168
Cut B8-A Section B8-2	0.25	4.272	154	38.185	1.491
	0.75	4.840	237	19.149	0.619
	1.25	4.932	134	13.698	0.412
	1.75	5.660	145	9.638	0.231
	2.25	5.584	126	7.466	0.166
	2.75	6.577	124	6.794	0.123
Cut B9-B Section B9-2	0.25	4.77	149	30.825	1.060
	0.75	5.40	210	14.408	0.397
	1.25	4.92	155	12.019	0.350
	1.75	5.204	123	8.929	0.225
	2.25	5.057	237	3.161	0.030
	2.75	4.828	156	8.410	0.224
	3.25	4.44	125	8.288	0.239
	3.75	4.593	132	6.974	0.180
	4.25	4.126	139	5.249	0.126

Table D.5: Potentiometric results of total chloride contents (% weight of concrete) for the tensile face of post-tensioned beams

Section	Depth, cm	Weight, g	mV	V_1, mL	Cl, %
Cut B2-A Section B2-2	0.25	4.566	211	19.109	0.664
	0.75	5.092	145	9.826	0.272
	1.25	4.760	139	4.846	0.106
	1.75	5.528	127	3.649	0.053
	2.25	5.354	124	3.171	0.038
Cut B3-B Section B3-2	0.25	4.82	124	13.296	0.415
	0.75	4.945	139	6.56	0.163
	1.25	4.825	166	2.784	0.028
	1.75	5.206	134	0.809	-0.040
Cut B5-A Section B5-1	0.25	4.64	177	18.608	0.634
	0.75	4.919	166	9.505	0.270
	1.25	4.522	147	4.31	0.090
	1.75	4.487	128	4.275	0.090
Cut B6-A Section B6-2	0.25	4.416	124	18.739	0.672
	0.75	4.437	210	7.309	0.212
	1.25	5.076	136	6.442	0.155
	1.75	4.654	124	3.718	0.065
Cut B8-A Section B8-2	0.25	4.783	104	24.384	0.819
	0.75	4.811	97	11.56	0.342
	1.25	5.968	123	7.684	0.160
	1.75	5.261	114	4.574	0.077
Cut B9-B Section B9-3	0.25	4.52	118	17.104	0.593
	0.75	4.459	106	8.195	0.247
	1.25	5.37	81	7.55	0.184
	1.75	4.75	70	4.625	0.099
	2.25	5.724	97	3.216	0.038